



**Performance of Ti-6Al-4V by laser powder bed fusion:
powder feedstock and heat treatment considerations**

Xi Du, MEng

**Thesis submitted to the University of Nottingham for the
degree of Doctor of Philosophy**

February 2024

Abstract

Laser powder bed fusion (LPBF) has received significant attention in the past decade due to its capacity to produce complex shaped 3D metallic parts from digital models. Ti and Ti alloys exhibit high potential for medical and aerospace applications due to their low density, high specific strength, good corrosion properties, and good biocompatibility. Among these Ti alloys, Ti-6Al-4V ($\alpha+\beta$ type) is the most common titanium alloy for various applications. The fabrication of Ti-6Al-4V by LPBF has received extensive attention in recent years. However, the performance of Ti-6Al-4V by LPBF with powder feedstock and heat treatment considerations is not fully understood. This thesis aims at understanding and optimising the performance of Ti-6Al-4V by LPBF considering the role of powder feedstock (including particle size distribution (PSD) and chemical composition) and heat treatment.

First, the PSD changes of reused powder were examined by laser diffraction and scanning electron microscope (SEM) image method. PSD coarsening of reused powder was observed. The PSD coarsening mechanisms were systematically investigated by analysing various types of powder collected in different locations of the build chamber. PSD of various collected powders and interactions between laser and powder material were analysed. There are three main reasons for coarsening mechanisms, namely, layer thickness, spatter formation, and sintered powder after laser scanning borders. Besides, the effect of PSD coarsening of reused powder on the porosity and surface quality of as-built parts was investigated. After that, three different PSD powder feedstocks were obtained via the sieving method with a 38 μm sieve mesh. The effect of different PSD powder feedstocks on in-process powders, single-track formability, and the performance of Ti-6Al-4V by LPBF was systematically studied. A link can be established between different PSD powder feedstocks, in-process powders, and the performance of Ti-6Al-4V. It is suggested that fine powder feedstock (PSD range $\sim 15\text{-}38 \mu\text{m}$) presents better surface quality and relative density. Significant differences in the microstructure and mechanical performance of Ti-6Al-4V by different PSD powder feedstocks cannot be found.

As-built Ti-6Al-4V by LPBF typically shows columnar prior- β grain boundaries with fine martensite α' inside, resulting in high strength (tensile strength more than 1200 MPa) but poor ductility (elongation less than 10%). Due to the limitations of PSD on tailoring

the microstructure and mechanical performance of Ti-6Al-4V, chemical composition modification and heat treatment were considered to tune the microstructure and achieve balanced strength-ductility. In-situ chemical composition modification of Ti-6Al-4V via CP Ti additions was employed in this thesis. After diluting Ti-6Al-4V with different CP Ti additions, different nominal Ti-4.5Al-3V (with 25 wt.% CP Ti, called PT25), Ti-3Al-2V (with 50 wt.% CP Ti, called PT50) alloys can be obtained. Microstructure, mechanical properties, and related mechanisms of Ti-6Al-4V, nominal Ti-4.5Al-3V, and nominal Ti-3Al-2V were studied. It is found that the martensite α' size is increased, and the crystal lattice parameters c/a ratio is decreased when CP Ti addition increases. A trend of decreasing strength and increasing ductility can be observed with increasing addition of CP Ti. PT50 presents a well-balanced strength (tensile strength ~ 1000 MPa) and ductility ($\sim 13\%$) in the as-built state without post heat treatment. The decreased c/a ratio promoting the dislocation slip may mainly make contribute to the increased ductility.

Since balanced strength and ductility can also be achieved by common heat treatment, heat treatment was employed in the thesis to compare with the chemical composition tailoring approach. Microstructure and mechanical properties of Ti-6Al-4V at stress relief temperature (730 °C, called HT730) and annealing temperature (900 °C, called HT900) were investigated. The main work focused on the heat treatment of Ti-6Al-4V in this thesis was to investigate the deformation behaviour of heat treated Ti-6Al-4V after tensile testing using electron backscatter diffraction (EBSD). Deformation twins can be observed in heat treated Ti-6Al-4V, especially in HT900. Deformation twinning behaviour of heat treated Ti-6Al-4V was further analysed, including twin variants and the Schmid factor. More deformation twins, more twin variants, and more twin-twin intersections can be found in HT900 compared to HT730. Besides dislocation slip, twinning-induced plasticity (TWIP) may also contribute to increased ductility after heat treatment, in contrast to chemical composition modification. The differences in microstructure and mechanical properties mechanisms for chemical composition modification and heat treatment were discussed.

Publications associated with the thesis

Published paper

X. Du, M. Simonelli, J.W. Murray, A.T. Clare, Facile manipulation of mechanical properties of Ti-6Al-4V through composition tailoring in laser powder bed fusion, *J. Alloys Compd.* 941 (2023) 1–12. <https://doi.org/10.1016/j.jallcom.2023.169022>.

CRedit authorship contribution statement

Xi Du: Conceptualization, Methodology, Investigation, Formal analysis, Writing – original draft. **Marco Simonelli**: Conceptualization, Resources, Formal analysis, Writing – review & editing, Supervision. **James W. Murray**: Conceptualization, Formal analysis, Writing – review & editing, Supervision. **Adam T. Clare**: Conceptualization, Formal analysis, Writing – review & editing, Supervision, Funding acquisition.

Acknowledgements

I am very grateful for my primary supervisor, Prof. Adam Clare. He gave me the opportunity to be a PhD student. He is knowledgeable in the non-traditional manufacturing field. He fully understands the innovation and contribution of additive manufacturing research, which helps me to think about the core contributions of my work. Many thanks for his efforts in my PhD research. Next, thanks my supervisor Assistant Prof. Marco Simonelli. He is an expert in the field of Ti-6Al-4V by LPBF. He can always provide professional comments and suggestions for my experiments, which promotes my PhD progress. Many thanks for his guidance on my PhD research. Finally, I thank my supervisor Dr James Murray. He is well-experienced in non-traditional manufacturing (such as additive manufacturing). When it comes to supervisor meetings and paper corrections, he is always positive and helpful. Many thanks for his kind support of my PhD research. I wish him good luck on his new journey. Thank you all for PhD research and thesis support and help.

Besides, I would like to thank the technical help of technicians, without their help and support, it is hard for me to finish my PhD. First, many thanks to the technicians in the additive manufacturing lab, Mr. Mark East, Mr. Mark Hardy, and Mr. Adam Whitbread. My sample fabrication and powder characterisation are well supported by them. I thank technicians in Wolfson building for sample preparation and materials characterisation, Mr. Jason Greaves, Dr Hannah Constantin, Mr. Kieran Orange, Mr. Richard Homer, Ms. Rebecca Saint, Mr. Daniel Flower, Mr. John Kirk. I thank technicians at nmRC, Mr. Martin Roe, Dr Richard Cousins and Dr Nigel Neate. I would like to give special thanks to Dr Nigel Neate for his kind training in SEM and EBSD. He is always helpful when I have EBSD measurement problems. I thank the technician in our ACEL lab, Mr. Alex Jackson-Crisp, for his mechanical machining of my samples for tensile testing. Additionally, I would like to thank other technicians who are not listed here.

During my PhD research, I also received support from staff and students. Prof. Chris Tuck, Associate Prof. Zhirong Liao, Assistant Prof. Alistair Speidel, Dr Zhiyi Zou, Dr Julan Wu, Dr Peifeng Li, Dr Zhao Wang, Dr Yue Yang, Dr Qi Liu, Mr. Huseyin Hizli, Mr. Shusong Zan, Dr Giuseppe Del Guercio, Dr Lewis Newton, are acknowledged.

I would like to give special thanks to my PhD sponsor, China Scholarship Council. Without this sponsorship, I would not have the opportunity to pursue a PhD.

Lastly, my special thanks to my family. I much appreciate my wife Ms. Xin Wen for her selfless understanding and support. She is dedicating and great for my family. Special thanks to my lovely son, Xiuqi Du, his coming to my family gives me happiness and positive energy. Thanks to my parents for backing me up and always respecting my decisions, I thank you for your support.

Contents

Abstract	1
Publications associated with the thesis	3
Acknowledgements	4
List of figures	10
List of tables	16
List of abbreviations	17
1 Introduction	18
1.1 Aims of thesis	19
1.2 Outline of thesis	20
2 Literature review	23
2.1 Metal additive manufacturing	23
2.2 Laser powder bed fusion (LPBF)	25
2.2.1 Introduction	25
2.2.1.1 Machine used in LPBF	25
2.2.1.2 Materials used in LPBF	26
2.2.2 Powder feedstock	27
2.2.2.1 Powder manufacturing.....	27
2.2.2.2 Powder morphology	30
2.2.2.3 Powder particle size distribution (PSD)	31
2.2.2.4 Chemical composition	34
2.2.2.5 Powder flowability	35
2.2.2.6 Powder reusing (recycling).....	36
2.2.3 Interactions between laser and powder materials.....	37
2.2.4 Microstructure of Ti-6Al-4V	40
2.2.5 Relative density, surface quality, and mechanical properties	46
2.3 The role of powder feedstock on performance of Ti-6Al-4V alloy by LPBF	50
2.3.1 Effect of powder morphology on parts performance	50
2.3.2 Effect of PSD on parts performance	52
2.3.3 Effect of chemical composition on parts performance	55
2.4 The role of heat treatment on performance of Ti-6Al-4V alloy by LPBF.....	61
2.4.1 Stress relief and annealing	62
2.4.2 Solution treatment and aging (STA)	64
2.4.3 Hot isostatic pressing (HIP)	65

2.4.4 Novel heat treatment	68
2.4.5 Deformation behaviour of heat treated Ti-6Al-4V	69
2.5 Summary of research gaps	71
2.5.1 PSD	71
2.5.2 Chemical composition.....	72
2.5.3 Heat treatment	72
3 Experimental.....	73
3.1 Introduction.....	73
3.2 Powder characterisation and preparation.....	75
3.2.1 Powder characterisation	75
3.2.1.1 Morphology	75
3.2.1.2 PSD.....	75
3.2.1.3 Chemical composition	76
3.2.1.4 Flowability.....	77
3.2.2 Powder preparation	77
3.3 Sample fabrication by LPBF	78
3.3.1 Sample fabrication for PSD coarsening mechanisms analysis of reused powder.....	79
3.3.2 Sample fabrication for the effect of different PSD powder feedstocks on build quality	81
3.3.3 Sample fabrication for the chemical composition modification of Ti-6Al-4V by CP Ti addition.....	82
3.3.4 Sample fabrication conditions for heat treatment experiments.....	82
3.4 Sample characterisation	83
3.4.1 Optical microscopy	83
3.4.2 Alicona G4	83
3.4.3 X-ray diffraction (XRD).....	84
3.4.4 Scanning electron microscope (SEM).....	84
3.4.5 Electron backscatter diffraction (EBSD).....	85
3.4.6 Microhardness	86
3.4.7 Tensile testing.....	86
4 PSD coarsening mechanisms of reused Ti-6Al-4V powder by LPBF.....	87
4.1 Introduction.....	87
4.2 Experimental.....	87
4.3 Results.....	88

4.3.1 Effect of powder reuse on PSD changes	88
4.3.2 Characteristics of particle size evolution by classification of the build chamber	90
4.3.3 Effect of PSD coarsening on the performance of as-fabricated parts	95
4.4 Discussion.....	97
4.4.1 Coarsening mechanisms responsible for PSD changes.....	97
4.4.2 Practical implications of powder management	101
4.4.2.1 Effect of measurement technique on the PSD	101
4.4.2.2 Strategies to minimise PSD changes	101
4.5 Conclusions.....	102
5 The role of PSD on the performance of Ti-6Al-4V alloy by LPBF	103
5.1 Introduction.....	103
5.2 Experimental.....	104
5.3 Results.....	104
5.3.1 Powder properties of three powder feedstocks	104
5.3.2 In-process powders.....	106
5.3.3 Single-track morphology.....	108
5.3.4 Surface quality and relative density of the as-built parts	112
5.3.5 Microstructure and mechanical properties	115
5.4 Discussion.....	117
5.4.1 Relationship between in-process powders and powder feedstocks.....	117
5.4.1.1 Spatter.....	117
5.4.1.2 Powder from powder bed and overflow	118
5.4.2 Single-track evolution	119
5.4.3 The link between parts performance and in-process powders and single-track formability.....	119
5.5 Conclusions.....	121
6 Chemical composition modification of Ti-6Al-4V alloy via CP Ti addition by LPBF	122
6.1 Introduction.....	122
6.2 Experimental.....	123
6.3 Results.....	123
6.3.1 Relative density and homogeneity	123
6.3.2 Microstructure analysis	126
6.3.3 Mechanical performance	130

6.4 Discussion.....	133
6.4.1 Chemical homogeneity.....	134
6.4.2 Composition-dependent microstructure	135
6.4.3 Composition-dependent mechanical properties	136
6.4.3.1 Mechanisms of ductile behaviour.....	136
6.4.3.2 Strength mechanisms.....	138
6.4.4 Materials adaption for Ti alloys by LPBF	140
6.4.5 Comparison with PSD work.....	141
6.5 Conclusions.....	142
7 Heat treatment of Ti-6Al-4V alloy by LPBF with stress relief and annealing. 144	
7.1 Introduction.....	144
7.2 Experimental.....	145
7.3 Results.....	146
7.3.1 Microstructure and elemental distribution	146
7.3.2 Mechanical properties	149
7.3.3 EBSD analysis before and after tensile testing	152
7.3.3.1 The deformation twinning formation	152
7.3.3.2 The deformation twinning behaviour	158
7.4 Discussion.....	167
7.4.1 Deformation mechanisms.....	167
7.4.2 Twinning behaviour	169
7.4.3 Comparison with composition modified Ti alloys.....	171
7.4.3.1 Chemical homogeneity and microstructure.....	171
7.4.3.2 Strength and ductility mechanisms.....	171
7.5 Conclusions.....	172
8 Conclusions	174
8.1 General conclusions.....	174
8.1.1 PSD findings	174
8.1.2 Chemical composition findings.....	175
8.1.3 Heat treatment findings	176
8.2 Benefits of the study to academia	177
8.3 Benefits of the study to the industry	177
8.4 Future work.....	178
Appendix-PSD measurements.....	181
References	188

List of figures

Fig. 2.1 Machine architectures for three common metal AM techniques, (a) DED, (b) LPBF, (c) EBM [10,11]	23
Fig. 2.2 Schematics of the atomising processes (a) WA, (b) GA, (c) PA and (d) PREP [41,42].	28
Fig. 2.3 SEM images of Ti-6Al-4V powder by different atomisation techniques, (a) GA, (b) PREP, (c) PA [41].	30
Fig. 2.4 (a) Effect of powder shape on apparent density (b) effect of particle aspect ratio on mass flow rate [51,52].	30
Fig. 2.5 (a) A typical schematic diagram of a laser diffraction system [39,59], (b) projected area for particle size measurement by image analysis method [39,60], (c) particle size measured by micro XCT [57,61].	32
Fig. 2.6 (a) Formation and ejection of droplet ejection spatter, including a protuberance, elongated neck, escapes as a spherical droplet, (b) schematic of particle entrainment (hot and cold spatter) mechanism of the powder bed by an induced argon gas flow with the effect of laser beam [90].	39
Fig. 2.7 (a) Phase diagram of Ti-6Al-4V [12] (b) phase transformation diagram under different cooling rates [95] (c) prior- β grain structure of Ti-6Al-4V by LPBF [96] (d) typical martensite α' structure of Ti-6Al-4V by LPBF [97].	42
Fig. 2.8 Optical microscopy images of Ti-6Al-4V (a) LoF pores, (b) keyhole pores [131].	46
Fig. 2.9 (a) Slip planes and slip directions in the HCP structure, (b) schematic of Schmid factor [38,133].	48
Fig. 2.10 (a) Morphology of Powders 1 (Gas atomised), 2 (Plasma atomised) and 3 (Plasma atomised) by SEM images, (b) cumulative particle size distributions of Powders 1 (20–53 μm), 2 (20–53 μm) and 3 (15–45 μm), (c) the comparison of rheological properties of three powders using Radar diagram, (d) powder bed density and (e) relative density of as-printed parts by three powders with two layer thicknesses (30 μm and 60 μm) [61].	51
Fig. 2.11 (a) 15-53 μm (coarse) powder feedstock, (b) 15-45 μm (fine) powder feedstock, (c) 3D visualizations of defect population in the parts by coarse and fine powder feedstock using XCT [153].	53
Fig. 2.12 Microstructure of as-built samples with different Fe contents by optical micrographs (a) Ti-6Al-4V, (b) Ti-6Al-4V-2Fe, (c) Ti-6Al-4V-3Fe, and (d) Ti-6Al-4V-4Fe, white arrows show the build direction (i.e., Z direction) [154].	56
Fig. 2.13 Microstructure and mechanical properties of the as-built Ti-6Al-4V with 316L additions, (A) tensile properties of Ti-6Al-4V-2wt.% 316L, Ti-6Al-4V-4.5wt.% 316L and Ti-6Al-4V-6wt.%316L, (B) mechanical properties comparison between as-built Ti-6Al-4V with 316L additions and Ti-6Al-4V alloy fabricated by different AM methods and conventional technologies, (C) XRD results of modified Ti alloys, (D to I) EBSD phase maps and IPF maps of modified Ti alloys [8].	57
Fig. 2.14 (a) SEM image of Ti-6Al-4V powder with CNTs planted, (b) SEM image in the marked area of (a), (c) SEM image of the as-built sample in high magnification, (d) XRD result of the as-printed sample, (e) mechanical properties of as-built Ti-6Al-4V	

alloy and composite, (f) schematic diagram of the strengthening mechanisms of the as-built composite [161].	59
Fig. 2.15 Inverse pole figure (IPF) maps of the reconstructed prior- β grains in (a) Ti-6Al-4V (Ti64), (b) Ti-4Al-4V (Ti44), (c) mechanical properties of the Ti44-H, Ti44-V, Ti64-H and Ti64-V, (d) elongation along H and V directions of as-built Ti44 compared to other literature [167].	60
Fig. 2.16 (a) SEM image of as-built Ti-6Al-4V, (b-e) SEM images of heat treated Ti-6Al-4V by 700 °C/2h, 800 °C/2h, 900 °C/2h, 950 °C/2h, respectively, (f) lamellar width of Ti-6Al-4V by different heat treatment temperatures and holding times [171].	63
Fig. 2.17 The influence of solution temperature (920 °C, 940 °C, 960 °C, 980 °C) and time (2h, 10h, 100h) on Ti-6Al-4V microstructure [178].	65
Fig. 2.18 The X-ray tomography results to present the effect of HIP on pores elimination, (a) keyhole pores elimination, (b) LoF pores elimination [183].	66
Fig. 2.19 (a-d) Microstructural evolution of as-printed and HIP sample with fully dense (FD) and LoF parameters, (e-g) inverse pole figure maps and (h-j) maps of reconstructed prior- β grains, (k) schematic diagram of the dislocation evolution in a LoF sample during HIP treatment, (l) tensile properties of Ti-6Al-4V in as-printed and HIP [181].	67
Fig. 2.20 The refinement of prior- β grains through rapid heat treatment, (a, b, e) IPF map, reconstructed prior- β grain map, misorientation boundary of as-built Ti-6Al-4V, (c, d, f) IPF map, reconstructed prior- β grain map, misorientation boundary of Ti-6Al-4V by rapid heat treatment [192].	68
Fig. 2.21 (a) In situ HEXRD experimental setup, evolution of the lattice strains during deformation of (b) as-built Ti-6Al-4V, (c) HT-730, and (d) HT-900 [101].	70
Fig. 3.1 Flowchart of the research including powder feedstock and heat treatment considerations.	73
Fig. 3.2 Flowchart of experimental methodology.	74
Fig. 3.3 SEM images of cross-sections of virgin Ti-6Al-4V powder feedstock.	75
Fig. 3.4 Morphology of powder feedstock observed by SEM (a) PT0, (b) CP Ti, (c) PT25, and (d) PT50.	78
Fig. 3.5 Schematic diagram of modulated laser pulse used in this thesis (a) point distance between two melt pools (b) hatch distance [27].	79
Fig. 3.6 (a) Schematic diagram of powder change under the laser and material interaction during LPBF, (b) designed parts (small holder and large holder) with different geometry for powder analysis around borders of parts, (c) build chamber after completing a build.	80
Fig. 3.7 Single-track experiments and in-process powders including spatter, powder from powder bed and overflow in the build chamber.	82
Fig. 3.8 Schematic illustration of the EBSD process and basic principle [94].	85
Fig. 4.1 PSD curves of virgin and reused powders using laser diffraction method.	88
Fig. 4.2 SEM images of (a) virgin powder and (b) reused powder (12x).	89
Fig. 4.3 PSD curves of virgin powder, P-PB, and powder from overflow using laser diffraction.	90
Fig. 4.4 PSD results of virgin powder, P-PB, and P-GO spatter using laser diffraction method.	91

Fig. 4.5 SEM images of P-GO (a, c) and P-GI (b, d) spatter at two different magnifications, EDS point analysis of a particle showing oxygen presence in (e).....	93
Fig. 4.6 SEM images and EDS analysis of powder morphology and composition change in the build envelope, (a) spatter on parts, (b) spatter in the powder bed, (c) Al elemental content in point 1, point 2, and point 3, (d) O elemental content in point 1, point 2, and point 3, (e) EDS results in different positions.	94
Fig. 4.7 (a) and (b) Sintered powder in small holder, (c) and (d) sintered powder in outer borders of the small holder.	95
Fig. 4.8 Effect of particle size evolution on as-built parts, porosity (relative density) in (a, b) Build 1 and (c, d) Build 12, surface roughness on the top surface (e) and side surface (f) of Build 1 and Build 12, the surface topography of side surface in (g) Build 1 and (h) Build 12.....	96
Fig. 4.9 (a) Schematic of the effect of layer thickness on powder coarsening: powder from overflow shows larger particle size than that of powder from the powder bed, (b) schematic of interactions between laser and powder material including various spatters during LPBF: this schematic presents the spatter formation and spatter locations, (c) schematic of the effect of sintered powder by laser scanning borders on powder coarsening.....	98
Fig. 5.1 SEM images (a-c) of three powder feedstocks and PSD results (d) measured by laser diffraction.....	105
Fig. 5.2 PSD comparison of powder feedstock, powder from the powder bed, and overflow, (a) 15-45 μm powder, (b) 15-38 μm powder, (c) 38-45 μm powder.	107
Fig. 5.3 SEM images of three spatters generated by (a) and (d) 15-45 μm powder, (b) and (e) 15-38 μm powder, (c) and (f) 38-45 μm powder.	107
Fig. 5.4 (a) PSD curves of spatter generated by three powder feedstocks, (b) collected spatter weight generated by three powder feedstocks.	108
Fig. 5.5 Single-track formability with different processing parameters (power from 100 W to 200 W, and exposure time from 40 μs to 90 μs) by three powder feedstocks, (a1-a5) 15-45 μm powder feedstock, (b1-b5) 15-38 μm powder feedstock, (c1-c5) 38-45 μm powder feedstock.....	109
Fig. 5.6 The average width of single tracks fabricated by (a) 15-45 μm powder feedstock, (b) 15-38 μm powder feedstock, (c) 38-45 μm powder feedstock, (d) width comparison by different powder feedstocks.	110
Fig. 5.7 Height profile of single tracks with laser power 125 W (a, b, c) and 200 W (d, e, f) by three powders, (a) and (d) 15-45 μm powder feedstock, (b) and (e) 15-38 μm powder feedstock, (c) and (f) 38-45 μm powder feedstock.....	112
Fig. 5.8 Surface morphology of as-built parts for the (a, b, c) top surface and (d-i) side surface by three powders (a, d, g) 15-45 μm powder feedstock, (b, e, h) 15-38 μm powder feedstock, (c, f, i) 38-45 μm powder feedstock.	113
Fig. 5.9 Surface texture and roughness results of the as-built parts for the top surface by three powders, (a) 15-45 μm powder feedstock, (b) 15-38 μm powder feedstock, and (c) 38-45 μm powder feedstock.	114
Fig. 5.10 Surface texture and roughness results of the as-built parts for the side surface by three powders, (a) 15-45 μm powder feedstock, (b) 15-38 μm powder feedstock, and (c) 38-45 μm powder feedstock.....	114

Fig. 5.11 OM images to show pores by (a, d) 15-45 μm powder feedstock, (b, e) 15-38 μm powder feedstock, (c, f) 38-45 μm powder feedstock.....	115
Fig. 5.12 Optical microscopy and SEM images by (a) and (d) 15-45 μm powder feedstock, (b) and (e) 15-38 μm powder feedstock, (c) and (f) 38-45 μm powder feedstock, respectively.....	116
Fig. 5.13 (a) Microhardness results of as-built samples by different PSD powder feedstocks, (b) mechanical properties of tensile bars by 15-45 μm powder feedstock, 15-38 μm powder feedstock, 38-45 μm powder feedstock.....	116
Fig. 5.14 Fractured morphology of tensile bars by (a) and (d) 15-45 μm powder feedstock, (b) and (e) 15-38 μm powder feedstock, (c) and (f) 38-45 μm powder feedstock.....	117
Fig. 6.1 Porosity (relative density) of as-fabricated PT0, PT25, and PT50 captured by optical microscopy images.	124
Fig. 6.2 Backscattered electron (BSE) images and EDS area maps of as-fabricated (a1-a4) PT0, (b1-b4) PT25, and (c1-c4) PT50.....	125
Fig. 6.3 XRD results of as-fabricated PT0, PT25 and PT50.....	127
Fig. 6.4 Microstructure of as-fabricated (a, d, g) PT0, (b, e, h) PT25, and (c, f, i) PT50 by OM and SEM. An increasing trend in martensite α' thickness can be observed in SEM images when CP Ti addition increases. Numbers 1-18 in (g-i) are EDS points for elemental composition analysis.....	128
Fig. 6.6 Grain boundary distribution (LAGB, HAGB) and KAM maps of as-fabricated (a, d) PT0, (b, e) PT25, and (c, f) PT50.....	130
Fig. 6.7 Microhardness results of the as-fabricated PT0, PT25 and PT50 exhibit a reduction in microhardness when CP Ti addition increases, error bars are standard deviation of 48 indentations in each sample.....	131
Fig. 6.8 (a) Tensile properties of as-fabricated PT0, PT25, PT50 and (b) comparison with as-fabricated and heat-treated Ti-6Al-4V by LPBF from literature [12,101–103,120,136,169,170,192,193,229,236–241] indicating comparable mechanical properties in PT50 with Ti-6Al-4V by heat treatment.....	132
Fig. 6.9 Fracture surface morphologies of as-fabricated (a, d) PT0, (b, e) PT25, and (c, f) PT50, indicating the fracture mode transferred from brittle to mixed brittle-ductile to ductile mode.	133
Fig. 6.10 The summary of composition-microstructure relationship by using simply mixed feedstock.....	136
Fig. 6.11 The comparison of grain boundary distribution (a) and (d), and KAM (b) and (e), and band contrast + special boundaries maps in as-fabricated (c) PT0 and (f) PT50 after tensile testing.....	138
Fig. 6.12 The relationships between (a) ductility, (b) tensile and yield strength, (c) microhardness, (d) c/a ratio, (e) martensite α' thickness, (f) the inverse square root of martensite α' thickness and CP Ti addition.....	140
Fig. 7.1 XRD results (a) 2θ from 30° to 90° and (b) 2θ from 34° to 44° (show the main peaks) of as-built Ti-6Al-4V, HT730, and HT900.....	147
Fig. 7.2 Optical microscopy images of etched microstructure for (a) and (d) as-built Ti-6Al-4V, (b) and (e) HT730, and (c) and (f) HT900.....	148

Fig. 7.3 SEM images of etched microstructure for (a) and (d) as-built Ti-6Al-4V, (b) and (e) HT730, and (c) and (f) HT900. β phase can be observed in HT730 and HT900, and a small amount of globular α can be found in HT900.....	148
Fig. 7.4 BSE images and EDS area maps of (a1-a4) as-built Ti-6Al-4V, (b1-b4) HT730, and (c1-c4) HT900.	149
Fig. 7.5 Tensile properties of three samples (as-built Ti-6Al-4V, HT730 and HT900).	150
Fig. 7.6 Fracture surface morphology of (a, d) as-built Ti-6Al-4V, (b, e) HT730, and (c, f) HT900, showing obvious ductile mode in HT900 compared to brittle mode in as-built Ti-6Al-4V.....	151
Fig. 7.7 Phase maps of as-built Ti-6Al-4V, HT730, and HT900 before (a-c) and (d-f) after tensile testing.....	152
Fig. 7.8 Misorientation distribution of as-built Ti-6Al-4V, HT730, and HT900 before (a-c) and after (d-f) tensile testing. The misorientation axis with 80° - 90° is inserted in misorientation maps.....	153
Fig. 7.9 Band contrast + special boundary maps for all three samples (a-c) before and (d-f) after tensile testing. Twins $85^\circ\langle 11\bar{2}0 \rangle$ (tension twinning), $35^\circ\langle 10\bar{1}0 \rangle$ (tension twinning), $65^\circ\langle 10\bar{1}0 \rangle$ (compression twinning) are marked with red, green, blue, respectively.....	154
Fig. 7.10 Grain boundary maps of as-built Ti-6Al-4V, HT730, and HT900 before and after tensile testing, LAGB (2 - 10°) marked with red colour, HAGB ($>10^\circ$) marked with blue colour.	155
Fig. 7.11 Inverse pole figure (IPF//Z0) + special boundaries maps of as-built Ti-6Al-4V, HT730, and HT900 before (a-c) and (d-f) after tensile testing.	156
Fig. 7.12 Pole figure (PF) maps of as-built Ti-6Al-4V (a, d), HT730 (b, e), and HT900 (c, f) before (a-c) and after (d-f) tensile testing.	157
Fig. 7.13 KAM maps of (a, d) as-built Ti-6Al-4V, (b, e) HT730, and (c, f) HT900 (a-c) before and (d-f) after tensile testing.	157
Fig. 7.14 IPF maps (//X0) of (a) HT730 and (c) HT900, and All Euler maps of (b) HT730 and (d) HT900 after tensile testing.....	158
Fig. 7.15 Twin variants and Schmid factor analysis with c-axis of parent grains nearly paralleling to tensile direction in HT730, subset 1 to subset 3 (a1, b1, c1) All Euler maps, (a2, b2, c2) point-to-point misorientation maps with twins and parent grains, (a3, b3, c3) discrete pole figures of each twin and parent grain for twinning plane $\{10\bar{1}2\}$	159
Fig. 7.16 Twin variants and Schmid factor analysis with c-axis of parent grains offsetting tensile direction around 45° in HT730, subset 4 to subset 6 (a1, b1, c1) All Euler maps, (a2, b2, c2) point-to-point misorientation maps with twins and parent grains, (a3, b3, c3) discrete pole figures of each twin and parent grain for twinning plane $\{10\bar{1}2\}$	161
Fig. 7.17 Twin variants and Schmid factor analysis with c-axis of parent grains nearly paralleling to tensile direction in HT900, subset 7 to subset 9 (a1, b1, c1) All Euler maps, (a2, b2, c2) point-to-point misorientation maps with twins and parent grains, (a3, b3, c3) discrete pole figures of each twin and parent grain for twinning plane $\{10\bar{1}2\}$	162
Fig. 7.18 Twin variants and Schmid factor analysis with c-axis of parent grains offsetting tensile direction around 45° in HT900, subset 10 to subset 12 (a1, b1, c1) All Euler maps, (a2, b2, c2) point-to-point misorientation maps with twins and parent grains, (a3, b3, c3) discrete pole figures of each twin and parent grain for twinning plane $\{10\bar{1}2\}$	164

Fig. 7.19 Schmid factor maps of (a-d) HT730 and (g-j) HT900 after deformation in $\{0001\}\langle 11\bar{2}0\rangle$ basal $\langle\alpha\rangle$ slip, $\{10\bar{1}0\}\langle 11\bar{2}0\rangle$ prismatic $\langle\alpha\rangle$ slip, $\{10\bar{1}1\}\langle 11\bar{2}0\rangle$ pyramidal $\langle\alpha\rangle$ slip, $\{11\bar{2}2\}\langle 11\bar{2}3\rangle$ pyramidal $\langle\alpha + c\rangle$ slip, $\{10\bar{1}2\}\langle 10\bar{1}\bar{1}\rangle$ twinning deformation of (e) HT730 and (k) HT900, IPF//X0 of (f) HT730 and (l) HT900, showing the complementary relationship between dislocation slip and deformation twinning.

..... 166

Fig. 7.20 KAM maps plus the special boundary (i.e., deformation twins, marked with red colour) for (a) as-built Ti-6Al-4V, (b) HT730 and (c) HT900 after tensile testing.

..... 168

List of tables

Table 2.1 Comparison of three common metal AM techniques [3,13–18].	25
Table 2.2 The chemical composition of Ti-6Al-4V Grade 5 and Grade 23 (ELI) [37].	27
Table 2.3 Comparison with different PSD measurements [39,56,57].	34
Table 4.1 PSD results of virgin and 5x and 12x reused powder measured by laser diffraction.	89
Table 4.2 PSD results of virgin and reused powder measured by SEM image analysis.	90
Table 4.3 PSD metrics for virgin powder and P-PB, as well as a powder from overflow, were measured by laser diffraction.	91
Table 4.4 PSD metrics for virgin powder, P-PB, and P-GO spatter, measured by laser diffraction.	92
Table 4.5 PSD of P-GI spatter by SEM images method with 300X, circularity 0.5-1.0, and comparison with virgin powder and reused powder.	92
Table 5.1 PSD results of three powder feedstocks measured by laser diffraction (standard deviation obtained by measuring at least three powder samples).	106
Table 5.2 Flowability and apparent density of three powder feedstocks measured by Hall flowmeter.	106
Table 5.3 PSD results of spatter using three powder feedstocks.	108
Table 5.4 The average width and standard deviation of single tracks by different processing parameters in three powder feedstocks, unit: P (power), W; ET (exposure time), μs ; track width, μm .	111
Table 5.5 Ra values of single tracks by different processing parameters (power (P), exposure time (ET)) and different PSD powder feedstocks.	112
Table 6.1 The average elemental content for PT0, PT25 and PT50 from the EDS area maps in Fig. 6.2.	125
Table 6.2 The point analysis (in Fig. 6.4(g-i)) of EDS for as-fabricated PT0, PT25 and PT50.	126
Table 6.3 XRD data of as-fabricated PT0, PT25, and PT50.	127
Table 6.4 Young's modulus, tensile strength, yield strength, elongation at break of as-fabricated PT0, PT25 and PT50.	132
Table 7.1 XRD data (peak position, c/a ratio) of as-built Ti-6Al-4V, HT730, and HT900.	147
Table 7.2 Microhardness results of as-built Ti-6Al-4V, HT730 and HT900, errors are standard deviation of 48 indentations in each sample.	150
Table 7.3 Mechanical properties of as-built Ti-6Al-4V, HT730 and HT900 (errors are standard deviation, two samples are used for each alloy).	151
Table 7.4 Schmid factors of all six possible twin variants (Schmid factor bold for observed twin variants) in HT730 (C0 means c-axis of parent grains nearly along tensile direction, C45 means c-axis of parent grains offsetting tensile direction $\sim 45^\circ$).	160
Table 7.5 Schmid factors of all six possible twin variants (Schmid factor bold for observed twin variants) in HT900 (C0 means c-axis of parent grains nearly along tensile direction, C45 means c-axis of parent grains offsetting tensile direction $\sim 45^\circ$).	163
Table 7.6 Elemental content by EDS results of HT730 and HT900 for α phase.	170

List of abbreviations

AM: Additive Manufacturing
ASTM: American Society for Testing and Materials
BCC: Body-Centered Cubic
BSE: Backscatter Electron
CRSS: Critical Resolved Shear Stress
DED: Direct Energy Deposition
DMLS: Direct Metal Laser Sintering
EBSD: Electron Backscatter Diffraction
EBM: Electron Beam Melting
EDS: Energy Dispersive X-Ray Spectrometry
FCC: Face-Centered Cubic
HAGB: High Angle Grain Boundary
HCP: Hexagonal Close-Packed
HIP: Hot Isostatic Pressing
IPF: Inverse Pole Figure
KAM: Kernel Average Misorientation
LAGB: Low Angle Grain Boundary
LPBF: Laser Powder Bed Fusion
LoF: Lack of Fusion
OM: Optical Microscopy
PF: Pole Figure
PSD: Particle Size Distribution
SB: Special Boundary
SE: Secondary electron
SEM: Scanning Electron Microscope
SLM: Selective Laser Melting
TWIP: Twinning-Induced Plasticity
XRD: X-Ray Diffraction

1 Introduction

Metal additive manufacturing (AM) has gained wide attention in academic and industrial areas due to its ability to rapidly build complex structures and customised parts. Metal AM includes multiple techniques. These mainly include laser powder bed fusion (LPBF, also called selective laser melting (SLM), direct metal laser sintering (DMLS)), electron beam melting (EBM), and direct energy deposition (DED). LPBF can produce complex parts with high mechanical properties and high feature resolution. Due to the layer-by-layer melting and multiple thermal cycles with rapid cooling for LPBF parts, LPBF parts usually present some unique characteristics (such as non-equilibrium microstructure), which may affect the final performance. The common overall performance of parts by LPBF includes surface quality, relative density (porosity), and mechanical properties (including hardness, strengths, ductility, fatigue, etc). In some cases, other performances like dimensional accuracy, corrosion resistance, and magnetic properties should also be considered. The parts performance is largely affected by the interactions between laser and powder feedstock and post heat treatment.

Metal powders are commonly employed as feedstock materials during LPBF. The powder feedstock characteristics have a crucial influence on the performance of the final LPBF parts. For example, different particle size distribution (PSD) ranges of powder may affect the flowability and powder bed density and then influence the parts relative density. Powders with different chemical compositions induce different microstructures and mechanical properties of as-built parts. It is essential to investigate the effect of powder feedstock on final LPBF parts and improve the parts performance through powder feedstock optimisation. Post heat treatment is a powerful way to tailor the microstructure and achieve desired mechanical properties, which is also interesting and significant when compared with the powder feedstock effect. This thesis aims to investigate the effects of powder feedstock and heat treatment on the performance of Ti-6Al-4V parts by LPBF and understand the interactions between laser and powder feedstock, modified microstructure and balanced strength-ductility via powder feedstock and heat treatment considerations. Through a systematic study of the effects of powder feedstock and post heat treatment on the performance of Ti-6Al-4V parts by LPBF, it provides a deep understanding of Ti-6Al-4V parts under different conditions by LPBF. This will allow the performance of LPBF parts to be improved and help to

understand the strength-ductility mechanisms and thus improve the strength-ductility of LPBF Ti-6Al-4V parts.

1.1 Aims of thesis

The aims of this thesis are to investigate the effects of powder feedstock and heat treatment on the performance of LPBF titanium alloy parts. Among powder feedstock characteristics, PSD and chemical composition may be the most important factors as they influence almost all other powder properties and play a crucial role in the properties of final parts. Currently, many related studies have been reported, mainly focused on stainless steel powder feedstock. However, few studies pay attention to lightweight Ti-6Al-4V alloy powder feedstock, especially with the systematic work to understand the role of powder feedstock. Ti-6Al-4V is the base material in this thesis as it is the most important titanium alloy in academia and industry. Ti-6Al-4V is widely used in the aerospace and medical industry due to its excellent specific strength and low density, good corrosion resistance, and good biocompatibility. This study will be crucial for the improvement of lightweight alloy parts properties by understanding the interaction between the laser and Ti-6Al-4V powder with different powder characteristics (such as PSD and chemical composition). The thesis will study three areas based on these aims:

- I. The PSD coarsening mechanisms in reused powder have not yet been fully understood. This study aims to explain the mechanisms of PSD coarsening in reused powder through a collection of various powders in different positions of the build chamber after LPBF build and understand the particle size evolution during LPBF. The role of different PSD powder feedstocks on performance and related mechanisms of Ti-6Al-4V parts by LPBF is also not fully understood. Different PSD powder feedstocks work aims to establish a link between PSD, in-process powders, and parts performance. Single-track formability and spatter collection are used to analyse the effect of PSD on the performance of Ti-6Al-4V parts by LPBF. Such a study is crucial for understanding and controlling the PSD for better powder life management (such as controlling the powder degradation for PSD) and good performance (such as relative density and surface quality) of Ti-6Al-4V parts through PSD understanding and optimisation.

- II. As-built Ti-6Al-4V parts by LPBF typically present martensitic structures and thus high strength but poor ductility, which may be difficult to tune via PSD consideration. Achieving balanced and controllable strength-ductility of Ti-6Al-4V parts is desired. In this thesis, a simple way via mixing Ti-6Al-4V powder and CP Ti powder to rapidly tune the composition was aimed at modifying the microstructure and achieving good balanced strength and ductility. By combining common commercial powder feedstocks, this study opens the possibility of rapidly changing the composition of powder feedstock and has economic benefit due to the lower price of CP Ti compared to Ti-6Al-4V.
- III. Heat treatment is a common way to decompose martensite α' into stable $\alpha+\beta$ phase to achieve balanced strength and ductility. Despite numerous heat treatment studies of Ti-6Al-4V by LPBF, dislocation slip is reported as the main mechanism during deformation. For hexagonal close-packed (HCP) structure dominated Ti-6Al-4V alloy with limited dislocation slip systems compared to body-centered cubic (BCC) or face-centered cubic (FCC) alloy, exploring the possible deformation twinning mechanism during plastic deformation is also important. Deformation twinning (twinning-induced plasticity, TWIP) that can benefit deformation and increase ductility is significantly found in this thesis by high temperature heat treatment. The microstructure and mechanical properties of as-built Ti-6Al-4V, stress relief Ti-6Al-4V, and annealing Ti-6Al-4V were investigated. The main aim is to study the deformation behaviour (in particular for deformation twinning behaviour) of heat treated Ti-6Al-4V. Strength and ductility mechanisms were demonstrated and understood. Deformation twinning behaviour was also analysed. Also, the microstructure and mechanical properties mechanisms were compared between the composition tailoring method and the heat treatment way.

1.2 Outline of thesis

Chapter 2 is a literature review that describes the fundamentals and progress of the LPBF process and describes the research gaps in detail, which will be addressed in this thesis. The LPBF technique is presented with more details, including powder feedstock,

interactions between laser and powder materials, defects, surface quality, microstructure, and mechanical properties. The effect of powder feedstock (including morphology, PSD, and chemical composition) on the performance of Ti-6Al-4V parts by LPBF is summarised and discussed. The effect of heat treatment on the microstructure and strength-ductility performance of Ti-6Al-4V by LPBF and related mechanisms are also reviewed. Finally, research gaps are proposed.

Chapter 3 describes experimental methods and materials characterisation. It contains three sections. Firstly, powder characterisation and preparation methods are introduced. Then, sample fabrication by LPBF and heat treatment are described. Finally, various sample characterisation methods are employed in this thesis.

Chapter 4 is the first research chapter. This chapter systematically studies the PSD coarsening of reused powder in LPBF and the effect of reused powder on the performance of Ti-6Al-4V parts by LPBF. PSD coarsening mechanisms are discussed through partitioning the build chamber.

Chapter 5 investigates the role of different PSD powder feedstocks on the performance of Ti-6Al-4V parts by LPBF. The relationships between PSD, in-process powders, and parts performance are established.

Chapter 6 focuses on microstructure modification and mechanical properties manipulation through composition tailoring of Ti-6Al-4V. In this chapter, Ti-6Al-4V mixing with different CP Ti contents to develop Ti-Al-V alloys is investigated. Relative density, chemical homogeneity, microstructure, and mechanical properties are studied. The relationship between composition, microstructure, and mechanical properties is discussed. The strength and ductility mechanisms for Ti-6Al-4V and modified Ti-Al-V alloys are also explained based on the chemical composition and microstructure.

Chapter 7 presents microstructure tailoring and manipulation of mechanical properties of Ti-6Al-4V through heat treatment. A systematic study is carried out by analysis of microstructure and mechanical properties. The strength and ductility mechanisms are also explained. The ductility mechanism with deformation twinning (TWIP) is demonstrated. The deformation twinning behaviour of Ti-6Al-4V by heat treatment is also particularly analysed. Finally, the differences in microstructure and mechanical

properties mechanisms between chemical composition tailoring and heat treatment work are compared.

Finally, Chapter 8 includes the general conclusions and proposed future work to extend the current research.

2 Literature review

2.1 Metal additive manufacturing

Over the last few decades, additive manufacturing (AM) has gained importance as a technology known as 3D printing. AM is a process of joining materials to make parts from 3D model data, usually layer upon layer, as opposed to subtractive manufacturing and formative manufacturing methodologies, based on the ISO/ASTM 52900:2021(en) [1]. Both academia and industry have great interests in additive manufacturing with the capability of building complex and high performance parts [2,3]. Some exciting achievements have been made based on this technology in recent years, such as rebuilding components of the human heart by 3D bioprinting of collagen [4], multi-material multi-nozzle 3D printing for voxelated soft matter [5], high-strength crack-free aluminium alloys by 3D printing [6], ultrafine-grained high-strength titanium alloys by additive manufacturing [7], in situ design of advanced titanium alloy with concentration modulations to achieve high mechanical properties by additive manufacturing [8].

Metal AM uses metallic materials as raw materials, which allows wide applications in aerospace, medical implants, die or casting molds, and automotive [3]. There are several techniques developed for metal AM, including laser powder bed fusion (LPBF), direct energy deposition (DED), electron beam melting (EBM, also called electron beam powder bed fusion (EB-PBF)), binder jetting, sheet lamination (ultrasonic additive manufacturing) [3,9]. The three common metal AM techniques are LPBF, EBM, and DED. The machine architectures for three common metal AM techniques are shown in Fig. 2.1.

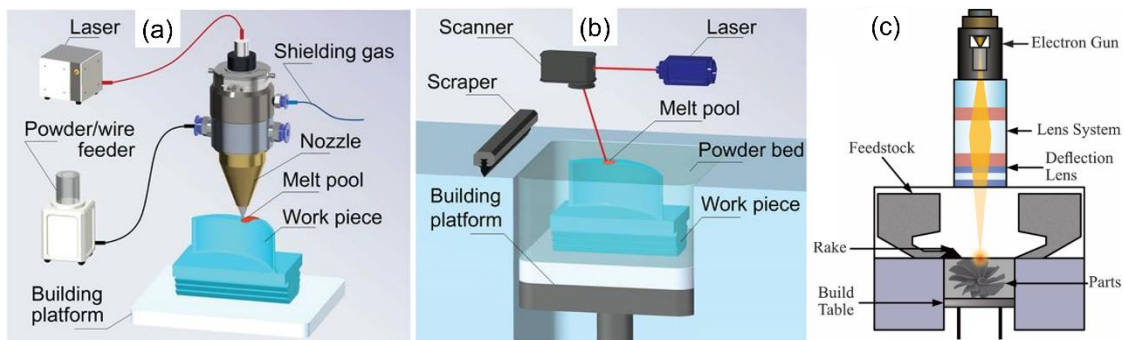


Fig. 2.1 Machine architectures for three common metal AM techniques, (a) DED, (b) LPBF, (c) EBM [10,11].

DED is an additive manufacturing process in which focused thermal energy is used to fuse materials by melting as they are being deposited based on the ISO/ASTM 52900:2021(en) [1]. DED process uses a laser beam (or electron beam or electric arc) and powder (delivered by a nozzle) or wire simultaneously to create melt paths and molten pools in each layer, and then materials are deposited layer by layer to fabricate the final parts on a substrate or a built part [3]. Based on the nature of the DED process, two points should be noticed [12]. One is that composite materials or compositionally graded materials can be fabricated using DED. Another is that DED can repair worn or damaged thin-wall parts. LPBF is an additive manufacturing process in which thermal energy (using a laser(s)) selectively fuses regions of a powder bed based on the ISO/ASTM 52900:2021(en) [1]. The LPBF process is that a thin layer (typically 30-60 μm) of powder is spread by a recoater to form a powder bed, and laser melts along the defined scan path in the powder bed. This powder spreading and laser melting are repeated layer by layer, and the build envelope drops after building each layer on the Z-axis. The LPBF technique is suitable for parts with high resolution features due to the small laser spot size and thin layer thickness employed. EBM is an additive manufacturing process in which thermal energy (using an electron beam(s)) selectively fuses regions of a powder bed based on ISO/ASTM 52900:2021(en) [1]. EBM is also a powder bed technique similar to LPBF, but it uses an electron beam as a heat source in a vacuum chamber. The high build temperature of 600–750 °C in EBM can release residual stress for Ti-6Al-4V. All three metal AM techniques usually use powder feedstock to build parts (DED can also use wire as feedstock). [Table 2.1](#) shows the main differences between LPBF, EBM, and DED [3,13]. Therefore, each technique has unique characteristics to meet different application needs.

Table 2.1 Comparison of three common metal AM techniques [3,13–18].

Metal AM	LPBF	EBM	DED
Feedstock	Powder (typical 15-45 μm)	Powder (typical 45-106 μm)	Powder (typical 45-106 μm)/wire
Heat source	Laser beam (LB)	Electron beam (EB)	LB/EB/Electric arc
Atmosphere	Inert gas	Vacuum	Shielding gas
Power (W)	50-1000 (typical 100-400)	50-3000	100-3000 (typical over 500)
Scan speeds	Limited by galvanometer inertia	Very fast, magnetically-driven	Slow
Surface roughness	Moderate	High	High
Feature resolution	Excellent	Moderate	Bad

2.2 Laser powder bed fusion (LPBF)

2.2.1 Introduction

2.2.1.1 Machine used in LPBF

In comparison to other metal AM techniques, LPBF has the potential to produce high-performance, complex, and customised parts, especially with high strength and high surface quality. Metallic part fabrication using LPBF dates back to the early 1990s [13]. From the perspective of the machine, currently, there are more and more companies that are manufacturing the LPBF machine, such as EOS, GE, Renishaw, and Bright Laser Technologies (BLT) [16,19–21]. Fig. 2.1(b) shows the schematic diagram of the LPBF machine [10]. The laser source can be expanded from one laser to two lasers or even multiple lasers (such as four lasers), and multiple galvanometers can be used, which can significantly improve productivity. The monitoring system has been developed, especially for melt pool and powder spreading monitoring, which can help to find the reasons for build failure and improve the quality of built parts. The auto-sieving system

inserted in the machine has been achieved for industrial production by Renishaw [16]. Meanwhile, computer technology accelerates the development of the LPBF technique, such as software for optical control and build preparation file processing [16,20].

2.2.1.2 Materials used in LPBF

After the introduction of the LPBF machine, common materials such as steels [22], Ti-6Al-4V [12], AlSi10Mg [23], superalloys [11], Cu alloys [24] are employed for LPBF. Other materials, such as Ti-6.5Al-2Zr-1Mo-1V (TA15) [25,26], Ti-10V-2Fe-3Al [27,28], Maraging stainless steel CX [29,30], have been employed for LPBF in recent years. For example, TA15 is a near α titanium alloy with a good high-temperature resistance compared to Ti-6Al-4V [25,26,31]. More and more materials have been employed and developed with good performance [6,32–36].

Titanium-based alloys are of particular interest to the AM community due to their high strength-to-weight ratios, good biocompatibility, and high corrosion resistance [12]. Among these titanium-based alloys, $\alpha+\beta$ Ti-6Al-4V alloy accounts for 50% of the whole applications. Al (main α stabiliser with typical 6 wt.%) and V (main β stabiliser with typical 4 wt.%) are the main alloying elements. There are two typical Ti-6Al-4V types, Grade 5 (UNS R56400) and Grade 23 (UNS R56407) based on ASTM B348/B348M-21 [37]. Grade 23 is a higher purity grade of Ti-6Al-4V with extra low interstitial (ELI) elements compared to Grade 5, presenting lower iron, oxygen, nitrogen, and hydrogen content. The composition specification for Grade 5 and Grade 23 (ELI) is shown in [Table 2.2](#). Ti-6Al-4V usually presents a microstructure with a mixture of $\alpha+\beta$ phase at room temperature. Due to the high strength and high fatigue resistance requirements for various applications (such as aerospace, medical, and marine applications), Ti-6Al-4V alloy should be used rather than CP Ti [38]. The Ti-6Al-4V alloy fabricated by LPBF has received great interest in academia and industry as it meets the high demand for complex parts in aerospace and medical applications. The characteristics and properties of powder feedstock have significant effects on the performance of LPBF parts, which is one of the main considerations in this thesis and will be reviewed in sections 2.2 and 2.3. Besides powder feedstock, post heat treatment is also crucial for the performance of LPBF parts (see section 2.4).

Table 2.2 The chemical composition of Ti-6Al-4V Grade 5 and Grade 23 (ELI) [37].

Content (wt.%)	Ti	Al	V	Fe	N	O	C	H	Other Elements
									Total \leq
Grade 5	Bal.	5.50- 6.75	3.50- 4.50	\leq 0.40	\leq 0.05	\leq 0.20	\leq 0.08	\leq 0.015	0.40 Each \leq 0.10
									Total \leq
Grade 23 (ELI)	Bal.	5.50- 6.50	3.50- 4.50	\leq 0.25	\leq 0.03	\leq 0.13	\leq 0.08	\leq 0.0125	0.40 Each \leq 0.10

2.2.2 Powder feedstock

2.2.2.1 Powder manufacturing

Powder feedstock characteristics are critical to the performance of the LPBF process and therefore the parts [3]. These characteristics of powder feedstock mainly include surface morphology, flowability, PSD, and chemical composition [9]. Therefore, it is important to evaluate the manufacturing routes of metal or alloy powders [3]. Atomisation is a common method to produce powders to meet LPBF requirements [39]. There are four main common manufacturing methods: water atomisation (WA), gas atomisation (GA), plasma atomisation (PA), and plasma rotating electrode process (PREP) [3,39]. Each method has its own features, such as powder properties and suitable material categories. Besides the common atomisation techniques to produce powders, other mechanical methods like hydride-dehydride (HDH) [40] are also used to produce cost-effective AM powder.

[Fig. 2.2](#) shows the atomising processes of WA, GA, PREP, and PA [41,42]. In the WA process, molten metal droplets are atomised and solidified as powders through a high-pressure water jet ([Fig. 2.2\(a\)](#)) [43]. Due to the fast cooling rate for the WA process, powders are usually irregular and have rough surfaces, resulting in a lower flowability and oxide formation on the powder surface [39,44].

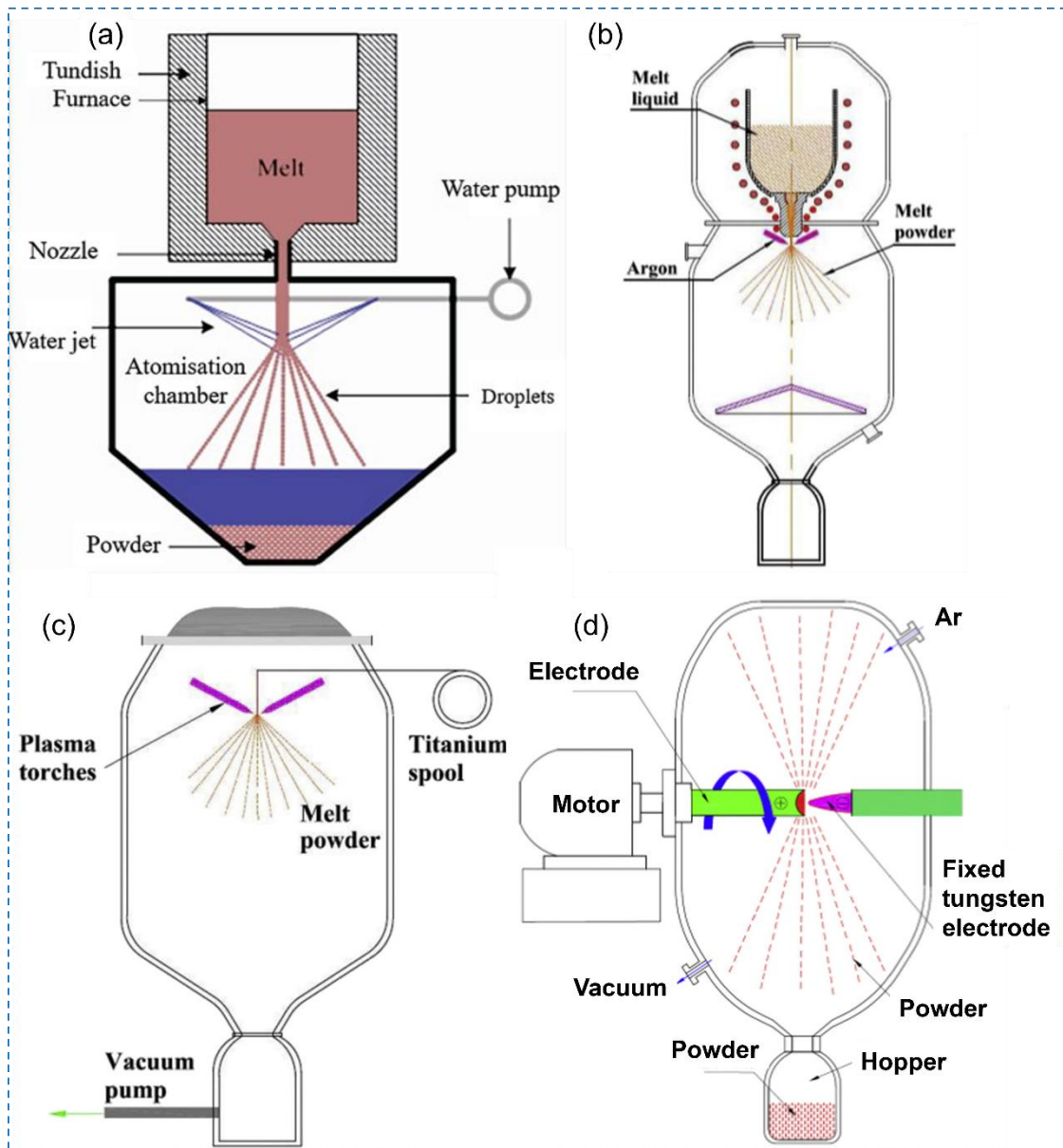


Fig. 2.2 Schematics of the atomising processes (a) WA, (b) GA, (c) PA and (d) PREP [41,42].

GA is a method for atomising molten metal droplets using a high-pressure flow of nitrogen or argon gases (Fig. 2.2(b)) [45]. The GA process can produce more materials, especially reactive alloys than the WA process. This is because the GA process using the inert gas (Ar, N₂) can yield better spherical and low oxygen content powders [39,46]. Therefore, powders from the WA process are limited in use compared to powders from the GA process because of their shortcomings, especially for reactive materials [39,46]. WA process generally produces non-reactive materials (oxide formation in reactive materials), such as steels [46]. However, powders from both WA and GA processes

present satellites with wide particle size distributions because of the existence of a large number of fine particles (less than 15 μm) [39].

PA process uses a plasma torch that rapidly heats, melts, and solidifies the feed materials to produce highly spherical and narrow PSD powders (Fig. 2.2(c)) [39,46]. Powder with less number of fine particles can be obtained by the PA process than the GA and WA process due to the employment of high-pressure gas and water jet (high cooling rate), respectively [39,43,45]. Bars or wires, as well as particles, can be directly used as feed materials for the PA process, while GA and WA use melt alloy (i.e., melt liquid) as feed materials [46]. Highly spherical Ti-6Al-4V particles can be achieved by the PA process because of the extremely high temperature of a plasma and modest gas flows with a low cooling rate compared to WA and GA processes [40,46,47]. Besides the feed material, another main difference between GA and PA is that wire is melted and atomised simultaneously by high-temperature plasma in the PA process, while feedstock material is first melted and then atomised by high-pressure gas in GA [48]. Meanwhile, PA powders usually show high purity as liquid metal or alloy does not contact any other solid materials (such as crucible) to make it free of contamination before solidification. PREP is different from PA for feedstock [40]. PREP uses a bar of rotating metal feedstock and plasma torches melt the end of the bar to eject material and form powders in the atomisation chamber (Fig. 2.2(d)). Powders produced by PREP are highly spherical with smooth surfaces but low productivity [3,39]. PREP powders also present high purity, which is consistent with PA. It is noteworthy that the internal porosity of the powder by PREP is significantly low. This is because the metal droplets are formed by centrifugal forces rather than by high-pressure gas [48]. Chen et al. [41] compared the internal porosity of Ti-6Al-4V powder produced by GA, PA, and PREP. The results indicate that GA powder shows a higher internal porosity while PREP powder presents a lower internal porosity compared to PA powder.

In summary, from the perspective of powder quality, PREP powders have excellent quality, followed by PA and GA powders, and WA powders are bad quality. However, the cost, production rate, and powder quality are in conflict. Powders by the WA process have many issues (like irregular particle shape and high oxygen level), which makes it unsuitable to produce Ti-6Al-4V. Therefore, GA, PREP, and PA are the main processes to produce Ti-6Al-4V (see Ti-6Al-4V powder SEM images in Fig. 2.3). However, Ti-6Al-4V powder by PREP process is not cost-effective (low productivity and high cost)

for industrial applications, and most powder suppliers provide Ti-6Al-4V powder by GA and PA. Hence, GA and PA are the common methods for manufacturing reactive Ti-6Al-4V powder with low oxide formation levels and high sphericity.

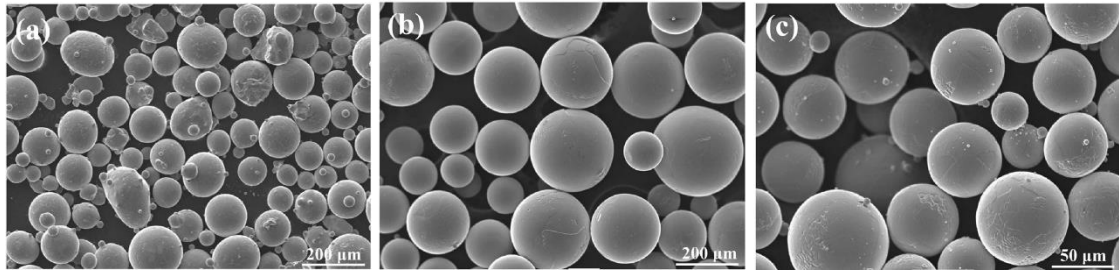


Fig. 2.3 SEM images of Ti-6Al-4V powder by different atomisation techniques, (a) GA, (b) PREP, (c) PA [41].

2.2.2.2 Powder morphology

It is also crucial to characterise the powder feedstock used in LPBF due to the importance of powder feedstock in the LPBF process and final parts performance. Powder morphology is one of the most critical concerns for powder feedstock as it affects flowability and packing density [49]. Powder morphology (particle shape) can be spherical, angular/irregular, rod-like, dendritic [39,50,51]. Highly spherical powder is desired for LPBF as it can increase apparent density and flowability [51,52], which benefits powder spreading during LPBF, as shown in Fig. 2.4.

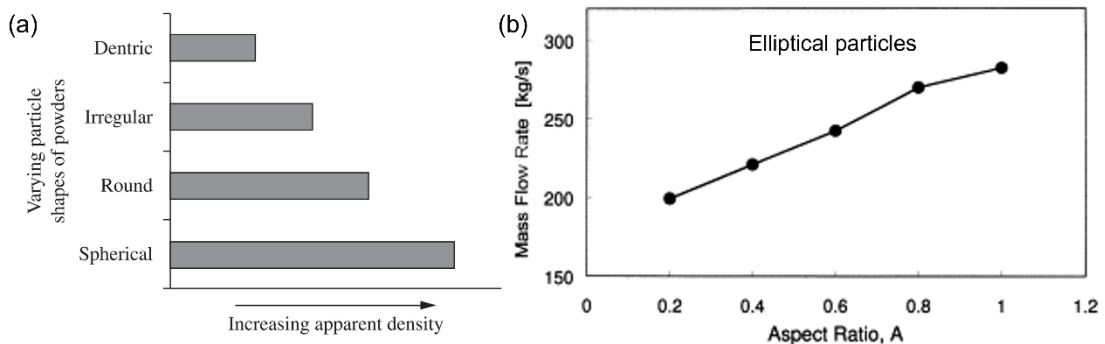


Fig. 2.4 (a) Effect of powder shape on apparent density (b) effect of particle aspect ratio on mass flow rate [51,52].

Powder morphology can be characterised by optical microscopy (OM), scanning electron microscope (SEM), and X-ray computed tomography (XCT) scans [49]. Powder surface roughness also plays a significant role in powder behaviour and part properties. Low surface roughness (smooth) of powder can reduce interparticle friction

between particles and increase flowability [39]. Atomic force microscopy (AFM) and confocal laser scanning microscopy can be used for powder surface roughness characterisation [50].

2.2.2.3 Powder particle size distribution (PSD)

Particle size distribution (PSD) is one of the most crucial powder characteristics as it has significant effects on powder properties (flowability, packing density, thermal properties) and various stages of the LPBF process (powder storage, powder spreading on the powder bed, recycling) [49,53]. For example, powders with narrow PSDs with fewer fine particles usually show better flowability than those with wide PSDs with more fine particles [54]. This is because fine particles tend to be agglomerated and show high cohesion due to the inter-particle force [49]. However, wide PSD may present a higher packing density than narrow PSD due to the gaps between particles filled with fine particles [54]. Hence, it is crucial to choose suitable PSD to balance the flowability and packing density. Commercial powders use a typical particle size range of 15-45 μm following a Gaussian distribution or an approximately Gaussian distribution [40,49]. However, according to the powder cohesion effect related to particle size and powder density, different materials with different densities may have different suitable PSD ranges for LPBF [49,55]. Therefore, further investigation is essential to obtain suitable PSD for different density materials. PSD curve can be modified by adding (mixing two powders) or removing powder (sieving method) [49]. As a result, right- and left-skewed distributions may be obtained with higher fractions in coarse and fine particles, respectively. Besides the skewed distributions, multimodal distributions may also be observed with two or more distinct peaks at discrete particle sizes. Three terms of size gauges (D10, D50, D90) are usually used to represent PSD results. For example, D10 = 18 μm means that 10% volume percentage of the powder is less than 18 μm .

Currently, there are several methods to measure PSD for LPBF powder feedstock [39,56,57], mainly including laser diffraction, image analysis method, sieving method, and XCT. Laser diffraction is commonly employed for PSD analysis owing to its convenience and theoretically high accuracy for spherical powder [39,49]. The PSD of spheres (or equivalent spheres) can be calculated through the mathematical inversion of the scattering or diffracted light pattern [58] (see [Fig. 2.5](#)).

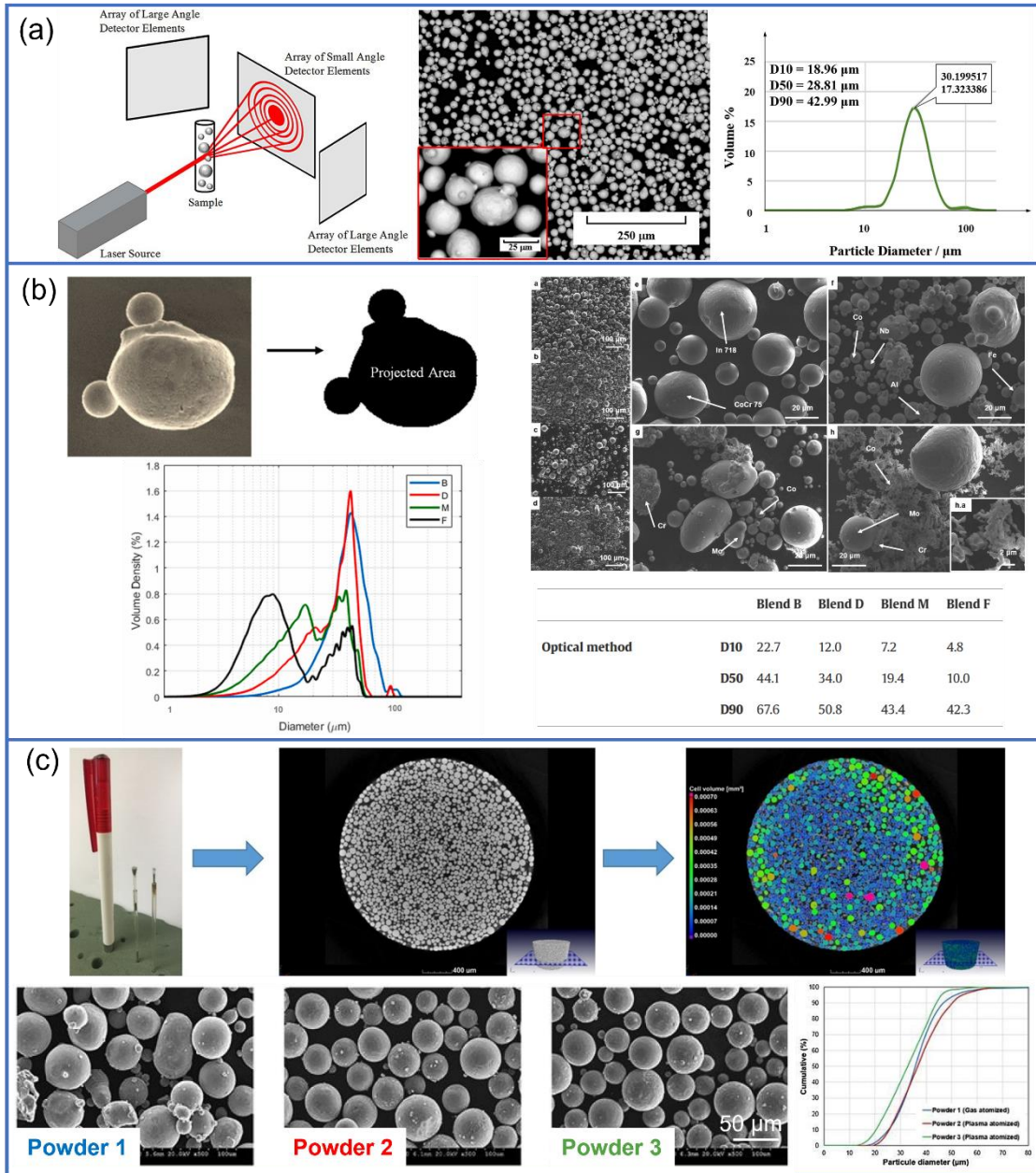


Fig. 2.5 (a) A typical schematic diagram of a laser diffraction system [39,59], (b) projected area for particle size measurement by image analysis method [39,60], (c) particle size measured by micro XCT [57,61].

Laser diffraction is fast and repeatable but is the most accurate when modelling powder as spheres, and may not be the best for powder with fine agglomerates [39,49]. The image analysis method can not only quantitatively measure PSD but also qualitatively observe particle size and particle shape [39]. SEM image analysis has the ability to directly measure powder sizes at higher resolution than other image analysis methods due to the capability of high magnification and high depth of field of SEM [62], which

may make it a powerful tool for qualitative particle size analysis and quantitative PSD measurement. Hence, the SEM image analysis method provides higher resolution and visual dispersion effect compared to non-image based techniques (like laser diffraction), which may be an effective method for powder with more fine particles. Human error may contribute to this inaccuracy when a non-automated analysis method is used. Post-processing SEM images may be time-consuming. The sieving method is an economical way to analyse PSD using a stack of sieves with increasing mesh size from bottom to top [39]. However, fine particles may clog the mesh and be unable to pass through it, which may limit the application of this method to LPBF powder feedstock [39]. For the XCT image analysis method, hundreds or thousands of cross-sectional images of powder samples are stacked together to form 3D images, and these cross-sectional images are analysed to obtain PSD results [56,57,61]. PSD results are influenced by scanning voxel size and field of view, which may easily limit fine particle accuracy [57]. [Table 2.3](#) compares these PSD measurements. Multiple PSD measurements to meet the needs of different sample conditions may be necessary.

Table 2.3 Comparison with different PSD measurements [39,56,57].

Technique	Particle size range	Advantages	Disadvantages
Laser diffraction	0.04-8000 μm	Short analysis time, does not require skilled labour, highly repeatable results.	Errors can result from irregular particles, measurements dependent on instrument design, agglomeration detection is difficult.
Image analysis method	Determined by system resolution	Allows qualitative and quantitative observation of particle shape, flexibility for particle size and shape analysis.	SEM and TEM sample preparation require more effort than optical microscopy. Powder dispersion may be affected by sample preparation (human factor). Sample amount is limited. Data processing is time-consuming.
Sieving method	20-125 μm	Low cost, easy to operate.	Fail to measure fine particles.
XCT	Determined by sample holder and voxel size	Allows qualitative and quantitative observation of particle shape, flexibility for particle size and shape analysis. Sample amount is not limited.	High cost and time-consuming. Resolution is not high as SEM images. Agglomeration detection is difficult.

2.2.2.4 Chemical composition

Powder chemical composition involves surface chemistry and bulk chemistry. Surface oxidation is the main concern regarding surface chemistry as it may cause changes in

powder thermal properties and instability of the melt pool due to the formation of oxides, especially for reactive Ti-6Al-4V powder [49].

Powder bulk chemistry is also one of the most crucial powder characteristics as it has significant effects on final parts properties. It can affect the thermal properties of the powder, such as thermal absorption and conductivity. More importantly, the solidification behaviour would be affected significantly, and as a result, microstructure and mechanical properties are affected [3]. For example, CP Ti [63,64] and Ti-6Al-4V [12,65] powder are typically used for LPBF. Although as-built parts by both materials present martensite structure, after heat treatment, CP Ti without the β -stabiliser element exhibits only α phase while Ti-6Al-4V would show $\alpha+\beta$ phase.

2.2.2.5 Powder flowability

Flowability is one of the critical powder properties widely used in LPBF. It is known that good flowability is essential to create a homogenous powder layer after spreading by a recoater or wiper during the LPBF process [49]. Flowability is decided by inter-particle forces F_i such as Van der Waals attractive forces, gravitational forces F_g , and moisture attached to the powder surface [66], which is related to powder morphology, PSD, and chemical composition. Spherical powders with a smooth surface and large particle size show good flowability [49]. Nickel-based alloy and steel powder usually have better flowability than Ti-6Al-4V alloy, considering the gravitational forces factor [49,55,66]. Powder surface with moisture could disrupt flowability [67].

There are several methods to measure powder flowability [49,66]. The most common and simple method is to use a Hall flowmeter to count the time by 50 g powder passing through a funnel or measure the angle of repose (AOR, angular difference between the slope and base platform). If the AOR values of powder are less than 30 degrees, it usually means powder shows good flowability while poor flowability could be observed if the value is over 40 degrees [68]. However, the AOR method is not dynamic flow measurement and may not present the rheological performance of powders used in LPBF recoater or feeder systems [69]. Freeman FT4 Rheometer can measure powder flowability under torque and axial loading conditions [61,70]. Because flowability measurement is similar to powder feeding during LPBF, the FT4 Rheometer is a much preferred method for powder rheology assessment [49]. Basic flow energy and specific energy measured by the FT4 Rheometer can quantify the flow resistance of powder. The

basic flow energy is the stabilised flow energy that represents the energy needed to cut through the powder sample, and the specific energy gives information about the mechanical interlocking and the cohesive forces [61].

2.2.2.6 Powder reusing (recycling)

It is known that unmelted powder in the vicinity of built parts in LPBF is normally recovered for reuse. This is one of the biggest advantages of LPBF that unmelted powder can be reused. Hann et al. [71] reported that only 3 to 5% of the powder in the dispenser is actually employed to build the part. In addition, the material cost is one of the main costs in the whole process, varying from 5 to 46% of the total cost of making a part based on the price of material feedstock [72]. For example, Lindemann et al. [73] estimated the 316L powder cost accounts for about 12% of the total cost. The estimated price of Ti-6Al-4V powder (~\$363/KG) is ~ four times as 316L powder (~\$88/KG) and AlSi10Mg powder (~\$78/KG), ~ 2.5 times as In718 (~\$145/KG) and In625 (~\$145/KG) powder [74]. Meanwhile, the price of powder used in LPBF is significantly higher than other forms of material, such as ingots, bars, wires, and tubes. This is because other forms of material usually act as precursor materials (feed materials) to produce LPBF powder. The atomisation process and productivity would increase the cost of LPBF powder compared to other forms of material. Hence, reusing powder is important for the powder economy and practical applications, especially for high-cost Ti-6Al-4V powder. Since powder can be reused or recycled, build numbers (or build cycles, or build times) is an important term to describe how many numbers (cycles, times) are carried out and repeated. One build number (cycle, time) can be defined as (1) finishing a build, (2) removing the build plate, (3) sieving unmelted powder, and (4) replacing sieved powder into powder feeder [75]. Among the waste powder, there is still some waste when unmelted powder is collected and recycled. This is because spatter (ejected particles during the LPBF process) originating from powder in the powder bed is formed and removed by the gas flow, and sintered powder with excessive large particles is removed by sieving mesh. Therefore, the powder economy (material utilization) involving waste depends on produced oversized particles (typically over sieving mesh size 63 μm) that are affected by LPBF processing conditions, such as laser processing parameters and gas flow. Ardila et al. [76] reported that In718 material utilization could achieve over 95% (0.6 kg of oversized powder was collected after sieving by employing a total of 25 kg powder as raw powder) after 14 cycles.

In addition to the benefits of powder economy for reused powder, it is also crucial to recognise the changes in powder properties after use and make decisions to use recycled powder properly. Although most of the unmelted powder remains unchanged, powder near built parts in the powder bed may be affected during the interactions between laser and powder, especially considering the spatter effect [77,78]. Particle shape, PSD, and chemical composition, in particular oxygen content, of the virgin powder may change after LPBF processing. There are some reports analysing the related changes in various materials [50,56,76,79–81]. First, some irregular particles, such as satellite particles and agglomerates, may occur in reused powder during LPBF [50,56,76,79,80]. The phenomenon is likely caused by ejected spatter adhering to powder or partially sintering [56]. PSD of reused powder will change when the particle shape changes. There is a general coarsening trend when virgin powder is reused many times due to a reduction in the number of fine particles ($<15\ \mu\text{m}$) and an increase in the number of large particles ($>45\ \mu\text{m}$) [50,76,79,80]. For example, O’Leary et al. [79] reported that there is an increasing trend in the PSD of Ti-6Al-4V after several recycles. 17-4PH powder also shows a coarsening trend in PSD after several builds [56]. The increasing trend of D10, D50, and D90 can be observed, especially from build 5 to build 8. The authors explained that partially sintered powder from small particles like two $30\ \mu\text{m}$ particles may be presented and responsible for this increase [56]. This sintered powder may be caused by laser scanning borders. However, although it is clear for the powder coarsening after reuse, the mechanism behind this phenomenon is still unclear due to the lack of comprehensive investigation into the interactions between laser and powder during LPBF. As for chemical composition, there may be an increase in oxygen level in powder after reuse [50,56,81]. For Ti-6Al-4V, an increasing trend for oxygen can also be observed when powder is reused [75,82–85]. For example, Yáñez et al. [84] reported there is a 19% increase in oxygen content for 12 times reused Ti-6Al-4V powder compared to new powder. Grainger et al. [75] studied the oxygen content of reused powder after 38 build cycles. There is a gradual increase in oxygen content to reach the maximum allowable for ELI specification ($\leq 0.13\ \text{wt.}\%$).

2.2.3 Interactions between laser and powder materials

In LPBF, the powder feedstock is delivered to the powder bed by a recoater or wiper and then selectively melted by the laser [39]. The nature of LPBF involves interactions

between laser and powder materials, which involves complex physical phenomena including recoil pressure, gas flow, Marangoni effect, boiling, and vaporization [86,87]. As a result, spatter is a critical and common by-product and cannot be ignored due to its direct influence on the LPBF process, reused powder, and parts performance [88,89]. Understanding the mechanisms of spatter formation is crucial for LPBF process control as well as the high performance of components. Different types of spatter are typically generated during the interactions between laser and powder in the powder bed. Three typical types of spatter include droplet ejection spatter (including metallic jet), hot spatter, and cold spatter, as demonstrated by Ly et al. [90], as well as Gasper et al. [91] and Leung et al. [92]. The formation mechanisms of each type of spatter are different due to the different physical processes involved.

Droplet ejection spatter is a common phenomenon in LPBF as well as in laser welding and drilling [93] that is closely related to the melt pool behaviour. The mechanism of droplet ejection spatter generation can be explained from knowledge of the established laser welding techniques [90,93]. Melt pool behaviour related to spatter generation is largely affected by recoil pressure and the Marangoni effect [77,78,86]. Liu et al. [77] reported that recoil pressure can be generated and low recoil pressure promotes flattening of the molten pool in LPBF. In contrast, high recoil pressure can create droplet ejection spatter due to the removal of molten material by melt expulsion. Khairallah et al. [86] studied that spatter can be formed when the recoil force exceeds the surface tension of the melt pool during LPBF. The metal liquid moves up the front wall of the depression and spills over onto the powder particles ahead of the laser beam. Then, liquid can be pinched off and deposited as spatter particles in the powder bed. Under recoil pressure and Marangoni flow, the low-viscosity metal liquid is jetted out from the melt pool and stretches during flight, and decomposes into small drops, forming droplet ejection spatter, as reported by Wang et al. [78].

Ly et al. [90] systematically demonstrated the formation mechanism of droplet ejection spatter of Ti-6Al-4V during LPBF and spatter features through ultra-high speed image observation and simulation, which is also evidenced by Leung et al. [92]. Droplet ejection spatter is formed by the ejection of liquid metal away from the melt pool due to the rapid melt pool motion induced by high recoil pressure. It is evident that a protuberance forms at the rim of the depression, which is followed by elongated neck thins out, ejecting a spherical droplet, as shown in [Fig. 2.6\(a\)](#). For the melted liquid at

the rim of the depression to escape as spatter, its kinetic energy (dynamic pressure) must exceed its capillary pressure; the equation is as follows:

$$\rho_L \mu^2 > \frac{\alpha}{R} \quad (1)$$

Where α is the surface tension, ρ_L is the liquid metal mass density, μ is laser scan speed and R is the melt radius of curvature. Spatter can escape in the backward direction as well as the forward direction if the kinetic energy is greater than the surface tension. The particle size of this spatter is typically large (more than 25 μm , can be up to $\sim 100 \mu\text{m}$) as droplets with small size do not easily escape the melt pool. Droplet breakup ejection spatter induced by recoil pressure is typically spherical with speeds of 3–8 m/s.

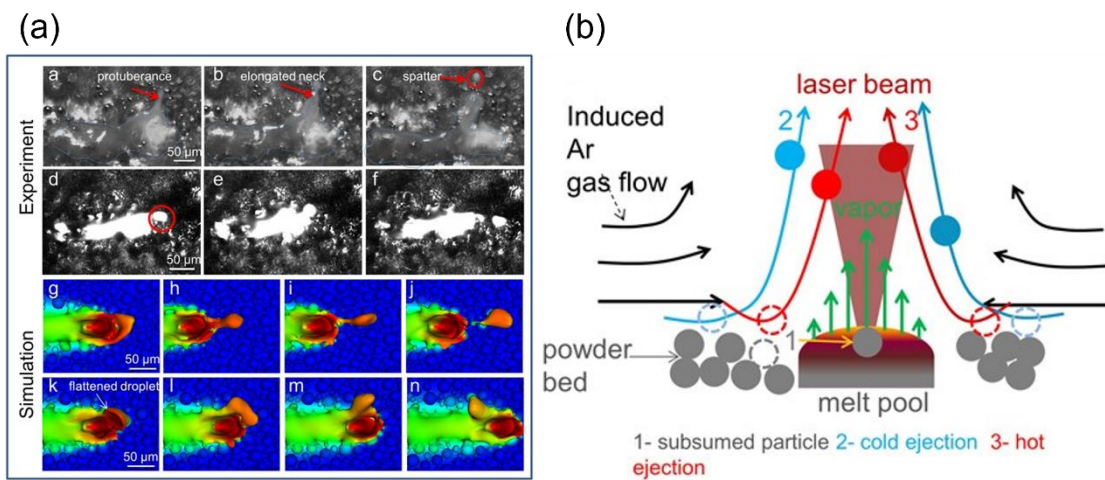


Fig. 2.6 (a) Formation and ejection of droplet ejection spatter, including a protuberance, elongated neck, escapes as a spherical droplet, (b) schematic of particle entrainment (hot and cold spatter) mechanism of the powder bed by an induced argon gas flow with the effect of laser beam [90].

Entrainment-driven spatter (i.e., hot and cold spatter, also called powder spatter) is formed from the powder bed rather than melt pool when a laser is scanned across the powder bed [90], which is a typical feature of the powder bed fusion process. The entrainment-driven spatter mechanism is different from the droplet ejection spatter. The former is a physical process occurring in a powder bed with non-molten metallic powder particles while the latter is the result of a melt pool physical process during LPBF. The powder spatter phenomenon was reported by Liu et al. [77] with the impact of metallic vapor dispersing the non-melted powders around the molten pool. There is no obvious change in the particle size and shape of the powder, which is also confirmed by Wang et al. [78] that non-melted powder particles splash at the front of the molten pool and

cause powder spattering.

The mechanism involved in entrainment-driven spatter has been studied by Ly et al. [90]. The mechanism analysis of this type of spatter can be divided into hot spatter and cold spatter. It is found that laser scanning across a powder bed results in the removal of many particles both upward and rearward. The motion of these particles with high particle velocities (more than 10 m/s) is originated from vapour driven entrainment. The mechanism involves the interaction of powder particles with evaporation-driven Ar gas flow. Gas flow from the vapour jet toward the melt pool can accelerate the entrained particles, and at least three main outcomes can be observed based on the local trajectories (Fig. 2.6(b)): (1) pulled into the melt pool and become subsumed, (2) if the entrained spatter travels toward the vapour jet and intersects with the laser beam (also with vapour plume), this spatter is called hot spatter (with heating of particles) that can undergo very fast acceleration with velocities 6–20 m/s, (3) entrained spatter misses the laser beam and does not experience the heating effect during ejection from powder bed to form cold spatter with velocities ranging from 2–4 m/s. It is noteworthy that hot spatter is the main spatter in all spatter types and accounts for 60%, 25% are cold entrainment ejections, and only 15% are droplet ejection spatter, according to the analysis of 120 videos with power varying from 200 to 300 W and scan speed from 1.5 to 2.0 m/s. Although this statistical analysis through videos may not be very accurate, it can provide a general knowledge that vapour driven entrainment is a more dominant mechanism for spatter formation than that of laser-induced recoil pressure (droplet ejection spatter).

In summary, spatter formation and mechanisms are well studied during the interactions between laser and powder feedstock in LPBF. There are several types of spatter with different characteristics. This spatter information during LPBF may be a good signal to understand particle size evolution during LPBF, which is rarely studied. Meanwhile, the spatter signal may also play an important medium in linking the different powder feedstocks with parts performance when studying the effect of different powder feedstocks on parts performance.

2.2.4 Microstructure of Ti-6Al-4V

Microstructure mainly includes phases, grain structures, grain size, and crystallographic texture. Microstructure plays a key role in the mechanical properties of Ti-6Al-4V parts

by LPBF. The microstructure is mainly affected by powder feedstock, processing conditions, and post heat treatment. Ti is an allotropic element that exhibits two different crystal structures: α -Ti with an HCP structure exists below the β transus temperature (~ 882 °C for Ti) while BCC β -Ti maintains above the β transus temperature [38]. In general, Ti with alloying elements significantly changes the β transus temperature of the allotropic phase and the volume fraction of the α and β phase at room temperature [94]. Alloying elements can either: (1) stabilise the α phase by increasing the β transus temperature, such as Al, O, N, C; (2) stabilise the β phase by decreasing the β transus temperature, such as V, Mo, Nb, Ta, Fe; (3) employ as solid solution straighteners and not influence the β transus temperature, such as Sn, Zr. The β transus temperature is around 975 °C and 995 °C for Ti-6Al-4V (Grade 23, ELI) and Ti-6Al-4V (Grade 5) respectively due to the difference in interstitial elements [38]. These α stabilising elements in multicomponent titanium alloys as an equivalent aluminium content can be expressed by the following equation [38]: $[Al]_{eq.} = [Al] + 0.17 [Zr] + 0.33 [Sn] + 10 [O]$. For these β stabilising elements in multicomponent titanium alloys, an equivalent Mo content is used: $[Mo]_{eq.} = [Mo] + 0.2 [Ta] + 0.28 [Nb] + 0.4 [W] + 0.67 [V] + 1.25 [Cr] + 1.25 [Ni] + 1.7 [Mn] + 1.7 [Co] + 2.5 [Fe]$. The $[Mo]_{eq.}$ can be employed for non-equilibrium microstructure during rapid cooling. The critical $[Mo]_{eq.}$ is ~ 4 wt.%, ~ 10 wt.% for the composition α'/α'' (hexagonal/orthorhombic) martensite boundary, composition α''/β (orthorhombic/metastable β) boundary, respectively.

Ti-6Al-4V typically presents $\alpha+\beta$ phase at room temperature by conventional manufacturing as Al (~ 6 wt.%) is an α stabiliser while V (~ 4 wt.%) is a β stabiliser [38]. However, the as-built state of Ti-6Al-4V ($[Mo]_{eq.}$ less than 4 wt.%) by LPBF mainly presents non-equilibrium martensite α' rather than equilibrium $\alpha+\beta$ phase (see Fig. 2.7) [3,12]. This is because the Ti-6Al-4V parts experience rapid cooling through diffusionless transformation during LPBF rather than $\alpha+\beta$ diffusional transformation. It is noteworthy that for Ti-6Al-4V, the β transus temperature is defined as the temperature at which there is a complete transformation to β phase upon heating from $\alpha+\beta$ phase rather than α phase for titanium, as shown in Fig. 2.7(a).

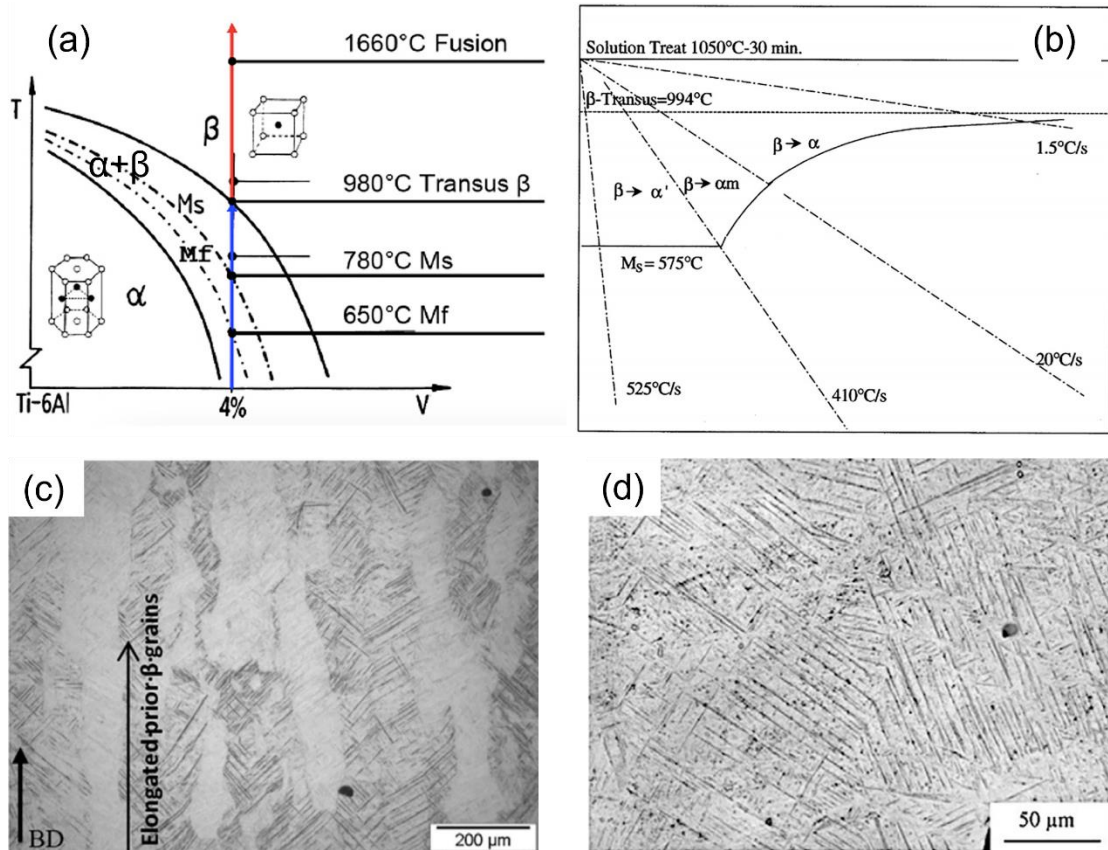


Fig. 2.7 (a) Phase diagram of Ti-6Al-4V [12] (b) phase transformation diagram under different cooling rates [95] (c) prior- β grain structure of Ti-6Al-4V by LPBF [96] (d) typical martensite α' structure of Ti-6Al-4V by LPBF [97].

During melting and solidification in Ti-6Al-4V by LPBF, Ti-6Al-4V experiences $\alpha+\beta \rightarrow \beta \rightarrow \text{liquid} \rightarrow \beta \rightarrow \alpha+\beta/\alpha'$ phase transformation. There is a specific thermal history required for martensite formation. Cooling rates along with build temperatures lower than the martensite start temperature (M_s) is a critical factor for the formation of martensite α' . The M_s temperature may be affected by the initial microstructure and impurity elements, ranging from 575 °C [95] to 800 °C [98]. When the cooling rate exceeds 410 °C/s, complete martensite α' can be produced. There is an incomplete martensite transformation when the cooling rate is between 410 °C/s and 20 °C/s. If the cooling rate is less than 20 °C/s, martensite transformation will not occur. Although a high cooling rate ($\sim 5 \times 10^5$ K/s) [3,99] can be seen in Ti-6Al-4V by LPBF, 100% martensite α' may not be obtained due to the effect of multiple thermal cycles in LPBF. It is found that the α phase can be observed in as-built Ti-6Al-4V through TEM characterisation [100,101].

Yang et al. [102] reported that there are four different martensite structures: primary, secondary, ternary, and quartic α' martensite structures based on the size of martensite α' structure due to the multiple thermal cycles during LPBF. The width of primary α' martensite can be microns level (1~3 μm) while the width of quartic α' martensite may be less than 0.1 μm . The average width of martensite α' structure is usually less than 1 μm . Lattice defects like dislocations and twins are observed in the martensite α' structures [103]. A high density of dislocations can be found through TEM [104] and in situ high energy X-ray diffraction (XRD) [101]. Due to the lattice defects observed in as-built Ti-6Al-4V by LPBF, the lattice parameters (c , a , and c/a ratio) in the HCP structure are also altered, where c is the height of the HCP structure and a is the side length of the basal plane [101,105]. The c is 0.468 nm and a is 0.295 nm in titanium HCP structure with a c/a ratio ~ 1.587 [38]. The c/a ratio is an important value to determine the dislocation slip behaviour [106]. The c , a , and c/a ratios are lower in martensite α' structure in as-built Ti-6Al-4V (c/a ratio ~ 1.5961) by LPBF compared to that of stable α phase in heat treated Ti-6Al-4V (c/a ratio ~ 1.5968 by stress relief, 1.5972 by high temperature annealing) by LPBF [101,105]. It is noteworthy that some retained β can be detected in the as-built Ti-6Al-4V [12].

Columnar prior- β grain structures are usually observed in the as-built Ti-6Al-4V and the length of columnar prior- β grain structures can be up to several mm [3,12]. Columnar prior- β grain structures are caused by the epitaxial solidification across the deposited layers (with partial re-melting of the previously solidified layers), along the build direction (also heat flow direction) which is perpendicular to the bottom of the melt pool [3,107]. The width of columnar prior- β grain structures may be around the hatch distance [100]. The size and morphology of prior- β grains may influence the morphology of martensite α' structures. The columnar to equiaxed transition (CET) is usually observed when the advance of the columnar front is suppressed by equiaxed grains that grow in the constitutionally undercooled liquid ahead of the columnar dendrites [108]. Hence, to achieve CET, constitutional supercooling through introducing solute and/or inoculants and controlling the solidification parameters can be considered [109]. The effect of solute can be usually described by the grain growth restriction factor (Q value). Q is a metric of the growth restriction effect of solute elements on the growth of the solid-liquid interface of the new grains [110]. The Q value equals $mC_0(k-1)$, where m is the slope of the liquidus line, C_0 is the solute concentration

in the bulk alloy, and k is the partition coefficient. It is known that a high Q value is good for CET [111].

During the $\beta \rightarrow \alpha'$ phase transformation of Ti-6Al-4V, this transformation typically obeys the classical Burgers orientation relationship ($(110)_\beta \parallel (0001)_\alpha$ and $[1\bar{1}1]_\beta \parallel [11\bar{2}0]_\alpha$), which is found in conventional manufacturing and LPBF with martensite transformation [38,112,113]. In other words, after phase transformation, the (110) of the β phase is parallel to the basal planes (0001) of the α phase, and the direction of $[1\bar{1}1]$ is parallel to the $[11\bar{2}0]$ direction. One parent β phase can transform to 12 hexagonal variants with different orientations, which may weaken the α' texture (The crystallographic texture can be defined as the distribution of preferred crystallographic orientations in a polycrystalline material, such as Ti-6Al-4V [94].) because of the high number of α' variants in each prior- β grain [114]. There are five misorientation types for α'/α' grain boundaries among all hexagonal variants in the same parent β grain [112,115]. The five misorientation types are $[11\bar{2}0]/60^\circ$ (Type 2), $[\bar{1}.377\bar{1} 2.377 0.359]/60.83^\circ$ (Type 3), $[\bar{1}0 5 5 \bar{3}]/63.26^\circ$ (Type 4), $[1 \bar{2}.38 1.38 0]/90^\circ$ (Type 5), $[0001]/10.53^\circ$ (Type 6). Among all these five types, $[\bar{1}0 5 5 \bar{3}]/63.26^\circ$ (Type 4) is usually dominated in as-built Ti-6Al-4V by LPBF [116–118].

Although α' texture may be weakened through multiple α' variants based on Burgers orientation relationship, the columnar prior- β grains typically exhibit texture with $\langle 001 \rangle_\beta$ along build direction [107,112,113]. This β texture is also observed in Ti-6Al-4V by EBM and DED [12,119]. Strong $\langle 001 \rangle$ fibre texture parallelling to the build direction was observed for various alloys fabricated by powder bed fusion additive manufacturing, such as In718, high-silicon steel (6.9 wt.% Si) [3]. Therefore, it is a common phenomenon to observe this fibre texture in powder bed fusion additive manufacturing. The development of a $\langle 001 \rangle_\beta$ fibre texture along the build direction is related to the low angle of inclination of the solidification front because of the highly elongated shape of the moving melt pool and the raster pattern used for scanning hatching [119]. It is a compromised result of grain growth. Because of this cyclic change in the raster direction, grains preferentially orientated closer to the maximum thermal gradient at the melt pool surface, exhibiting a growth advantage in an individual pass, will be more poorly aligned in the next pass when the beam travel direction reverses or rotates. Therefore, after many layers, the prior- β grains aligned with $\langle 001 \rangle$ direction

parallel to the build direction will dominate the texture (more closely aligned to the maximum temperature gradient when the raster pattern is alternated).

Besides martensite α' structures observed in as-built Ti-6Al-4V by LPBF, some uncommon microstructures can be found in the literature [120–126]. Xu et al. [120,121] achieved ultrafine lamellar ($\alpha+\beta$) microstructures of as-built Ti-6Al-4V via in situ martensite decomposition. Wang et al. [125] found a transition V-rich structure in an HCP structure with a composition close to that of the β phase during the α' to $\alpha+\beta$ phase transformation through in situ martensite decomposition. Few studies reported the orthorhombic martensite α'' (usually observed in high [Mo]_{eq.} (typical over 4 wt.%) with enriched β stabiliser content, such as Ti-6Al-2Sn-4Zr-6Mo by LPBF [127,128]) in as-built Ti-6Al-4V by LPBF [122–124]. The formation of α'' martensite may be due to the rapid cooling from intermediate temperatures (in the $\alpha+\beta$ phase field) during thermal cycles in LPBF. In these intermediate temperatures, element segregation may be formed and β phase is enriched in V [123]. Interestingly, Wang et al. [126] found an oxygen-stabilised face-centered cubic (FCC) Ti phase (~6.6%) in as-built Ti-6Al-4V by LPBF from a phase transformation in martensite α' at elevated temperatures.

In summary, the as-built Ti-6Al-4V with [Mo]_{eq.} less than 4 wt.% by LPBF typically presents columnar prior- β grain boundaries with fine martensite α' structures during multiple thermal cycles with rapid cooling in LPBF. There are four different types of martensite α' structures considering the martensite size. Many lattice defects, including dislocations and twins, can be found in the as-built Ti-6Al-4V. The lattice parameter c/a ratio of the HCP structure is decreased. The phase transformation from β to α' follows the Burgers orientation relationship and 12 possible HCP variants may weaken the α' texture. A $\langle 001 \rangle_{\beta}$ fibre texture along the build direction is typically observed under the multiple thermal cycles in LPBF. Meanwhile, some unusual microstructures can be found in as-built Ti-6Al-4V, including stable $\alpha+\beta$, a transition V-rich structure in an HCP structure, orthorhombic martensite α'' , oxygen-rich FCC phase. Therefore, understanding and manipulating the microstructure in as-built Ti-6Al-4V under different experimental conditions are essential to address the issues from mechanical properties.

2.2.5 Relative density, surface quality, and mechanical properties

Ti-6Al-4V alloy fabricated by LPBF has intrinsic restrictions, including porosity, high surface roughness compared to machined parts, high affinity for oxygen, and high residual stresses [12]. These limitations may damage the mechanical properties of Ti-6Al-4V parts. In theory, a fully dense component can be produced by LPBF. However, pores can be observed in as-built parts if improper processing parameters are employed. Three typical pores (gas pores, lack of fusion (LoF) pores, and keyhole pores) can occur in as-built LPBF parts [3,12,18], as shown in Fig. 2.8. Gas pores are randomly distributed in the as-built parts exhibiting a spherical or elliptic shape (a diameter around 1–100 μm) [12]. Gas pores may be caused by the powder feedstock because it is possible for gases to be entrapped inside powder particles during atomisation [3,12]. There is also a possibility that shielding gas or alloy vapours may be entrapped within the molten pool as another cause [3,12]. LoF pores usually show irregular shapes with possible unmelted powders inside (see Fig. 2.8(a)). These kind of pores are typically caused by insufficient laser energy input that causes poor melting and weak bonding between layers [3,12,18]. The pores induced by LoF could affect the mechanical performances of as-built parts [12,129,130]. Pores induced by keyhole mode are usually caused by overly high energy input [3,18]. The keyhole pores are usually spherical in shape compared to the lack of fusion pores [3,18], as shown in Fig. 2.8(b).

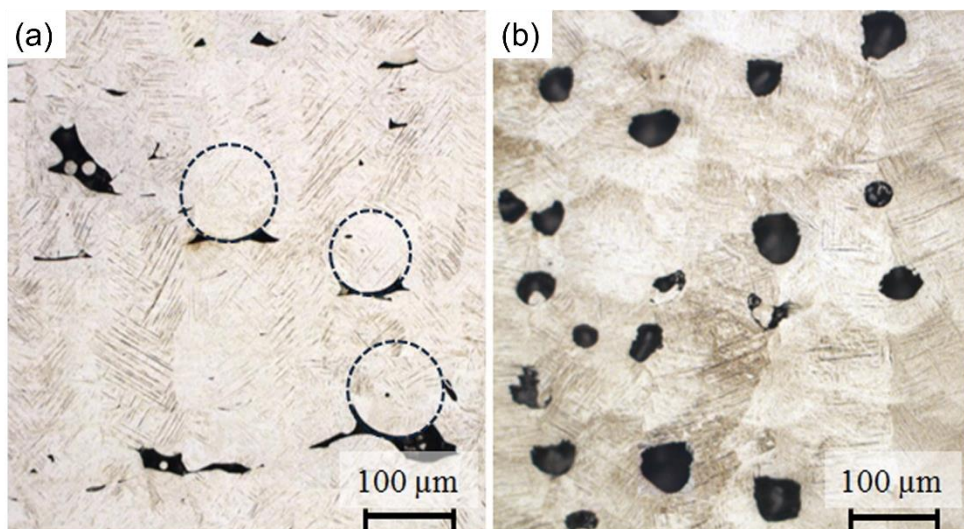


Fig. 2.8 Optical microscopy images of Ti-6Al-4V (a) LoF pores, (b) keyhole pores [131].

Surface roughness is an important performance metric of LPBF components. Powder feedstock, processing parameters, part design, post-processing, and finishing are the major influence factors [3]. Li et al. [132] summarised three main reasons for surface roughness: (1) the adherence of partially melted powders to the side surface, (2) the staircase effect linked to increased layer thickness, and (3) the existence of open pores and incompletely melted regions. Hence, surface roughness is closely related to layer thickness, powder feedstock, and processing parameters when part geometry is fixed for the as-built parts.

The hardness of as-built Ti-6Al-4V is typically higher than equilibrium $\alpha+\beta$ Ti-6Al-4V due to the higher hardness for martensite α' structure (~ 44 HRC) than α phase (~ 30 HRC) [12]. The as-built Ti-6Al-4V by LPBF typically presents high tensile (~ 1200 MPa) and yield strength (~ 1100 MPa) with low ductility ($<10\%$) [12,103]. This may be due to the results of fine martensite α' structure. Ti-6Al-4V by LPBF usually shows higher strength and microhardness but lower ductility compared to CP Ti by LPBF [63,64]. It is noteworthy that anisotropy in mechanical properties in different orientations (typically build in horizontal and vertical directions) can be found [12]. The mechanical anisotropy is related to the microstructural anisotropy in as-built Ti-6Al-4V. The columnar prior- β grains and the presence of α/α' grain boundaries may be the main reasons [12]. Since mechanical properties are closely related to microstructure, any factors like powder feedstock, processing parameters, and heat treatment that affect the microstructure would influence the final mechanical performance.

It is known that dominated martensite α' structures (HCP structures) with minimal β phase are observed in as-built Ti-6Al-4V by LPBF [12,103]. Thus, the deformation mechanisms are mainly from the HCP structures. Dislocation slip and twinning are widely used for deformation mechanisms analysis of Ti-6Al-4V by conventional manufacturing [38]. Fig. 2.9(a) shows various slip planes and slip directions for HCP structure (α titanium and $\alpha+\beta$ titanium). There are three main $\langle\alpha\rangle$ slip systems including $\{0001\}\langle 11\bar{2}0\rangle$ basal $\langle\alpha\rangle$ slip, $\{10\bar{1}0\}\langle 11\bar{2}0\rangle$ prismatic $\langle\alpha\rangle$ slip, $\{10\bar{1}1\}\langle 11\bar{2}0\rangle$ pyramidal $\langle\alpha\rangle$ slip. There are only 4 independent slip systems for these slip directions with $\langle 11\bar{2}0\rangle$. Based on the von Mises criterion, at least five independent slip systems are required to achieve a homogenous plastic deformation. Thus, for activation of dislocation slips, $\{11\bar{2}2\}\langle 11\bar{2}3\rangle$ pyramidal $\langle\alpha + c\rangle$ slip is usually necessary. The

critical resolved shear stress (CRSS) for basal $\langle\alpha\rangle$ slip, prismatic $\langle\alpha\rangle$ slip, pyramidal $\langle\alpha\rangle$ slip, pyramidal $\langle\alpha + c\rangle$ slip are estimated to be 290 MPa, 320 MPa, 430 MPa, and 460 MPa, respectively [101]. Basal $\langle\alpha\rangle$ slip and prismatic $\langle\alpha\rangle$ slip are more easily activated than pyramidal $\langle\alpha\rangle$ slip and pyramidal $\langle\alpha + c\rangle$ slip.

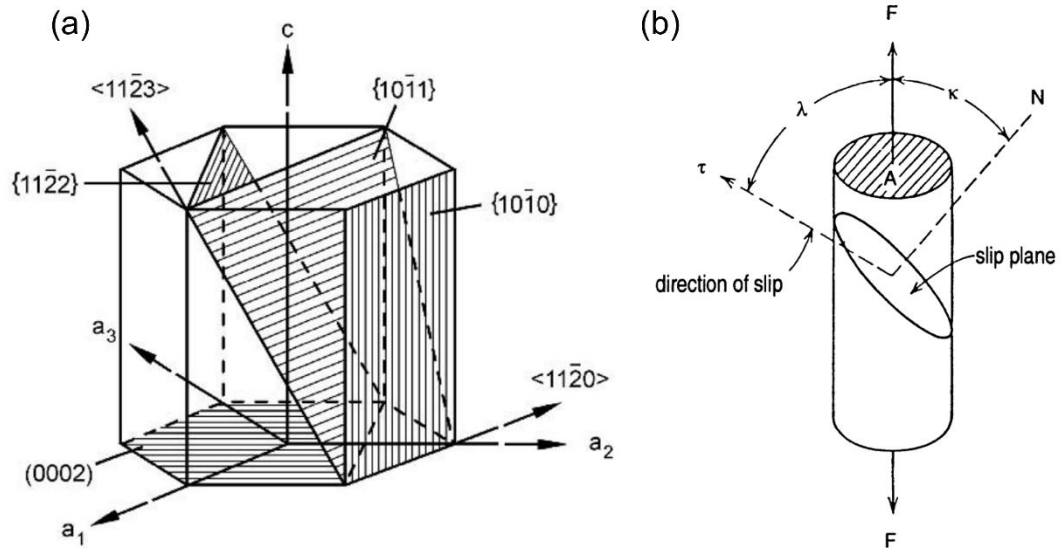


Fig. 2.9 (a) Slip planes and slip directions in the HCP structure, (b) schematic of Schmid factor [38,133].

The start of plastic deformation is usually characterised by yield stress [133]. A dislocation moves when a force has a sufficient component parallel to the slip plane in the slip direction. Therefore, it is the CRSS in the slip system that causes dislocation motion rather than the applied tensile stress. This CRSS (τ) is related to the tensile stress σ by $\tau = \sigma \cos \kappa \cos \lambda = m \sigma$ (this equation is also called Schmid's Law), where κ is the angle between tensile direction and slip plane normal, and λ is the angle between tensile direction and slip direction, as shown in Fig. 2.9(b). The factor $m = \cos \kappa \cos \lambda$ is called the Schmid factor ($0 \sim |m| \sim 0.5$ for tensile deformation). Thus, the activation of dislocation slip is closely related to the Schmid factor (SF). Higher Schmid factor means lower tensile stress is applied to meet the CRSS to achieve dislocation motion and easy to activate the dislocation slip. This Schmid's Law and Schmid factor can also be applied for twinning, where the slip plane is replaced by the twinning plane and the slip direction is replaced by the twinning direction, especially for twin variants analysis [134,135].

Some reports can be found in the literature involving the deformation mechanisms of as-built Ti-6Al-4V about dislocation slip [101,116,136,137]. Basal $\langle\alpha\rangle$ slip and

prismatic $\langle\alpha\rangle$ slip are the main slip systems with low CRSS in Ti-6Al-4V by LPBF [101,136]. Zhang et al. [101] studied the tensile deformation behaviour of as-built Ti-6Al-4V by using in situ high energy XRD. The results indicated that the activation of basal $\langle\alpha\rangle$ slip is easier than prismatic $\langle\alpha\rangle$ slip, which may be related to the c/a ratio in as-built Ti-6Al-4V. This may limit the activation of multiple slip systems of as-built Ti-6Al-4V by LPBF and cause poor ductility. Moridi et al. [137] investigated the deformation and failure mechanisms of as-built Ti-6Al-4V by LPBF. The high aspect ratio α' and α' colonies (i.e., primary α') show good correlation with high prismatic and basal Schmid factors for strain localization. Strain localization causes the void formation within the primary α' . Void growth and coalescence cause the final fracture of the Ti-6Al-4V. Zhao et al. [116] compared the microstructure and mechanical properties of as-built Ti-6Al-4V with the same volumetric energy densities but different power and scanning speed. The Ti-6Al-4V sample with the lowest portion of basal slip system $\{0001\}\langle11\bar{2}0\rangle$ with Schmid factor 0.4–0.5 ($\Sigma\text{SF}(0.4\text{--}0.5)$) presents the poorest ductility compared to other samples with a higher portion of basal slip system.

It is known that basal $\langle\alpha\rangle$ slip and prismatic $\langle\alpha\rangle$ slip are the easiest slip systems in Ti-6Al-4V while it does not accommodate the strain along the c -axis. Therefore, if grains with a c -axis are nearly parallel to the applied stress (called hard grains), $\langle\alpha\rangle$ slip is hard to activate due to very low Schmid factors [134]. Twinning and $\langle\alpha + c\rangle$ slip become important deformation mechanisms for hard grains. Therefore, considering the limited slip systems for HCP structure compared to BCC structure, twinning is also an important deformation mechanism for Ti-6Al-4V. Among deformation twinning types, $\{10\bar{1}2\}\langle10\bar{1}\bar{1}\rangle$ (i.e., $85^\circ\langle11\bar{2}0\rangle$, tension twinning), $\{11\bar{2}1\}\langle11\bar{2}\bar{6}\rangle$ (i.e., $35^\circ\langle10\bar{1}0\rangle$, tension twinning) and $\{11\bar{2}2\}\langle11\bar{2}\bar{3}\rangle$ (i.e., $65^\circ\langle10\bar{1}0\rangle$, compression twinning) are the main twinning modes [38]. Other deformation twinning like $\{10\bar{1}1\}\langle10\bar{1}\bar{2}\rangle$ (i.e., $57^\circ\langle11\bar{2}0\rangle$, compression twinning), $\{11\bar{2}4\}\langle22\bar{4}\bar{3}\rangle$ (i.e., $77^\circ\langle10\bar{1}0\rangle$, compression twinning), $\{11\bar{2}3\}\langle\bar{1}\bar{1}22\rangle$ (i.e., $87^\circ\langle10\bar{1}0\rangle$, tension twinning) may also be observed [118]. However, rare reports can be found for the observation of deformation twinning in as-built Ti-6Al-4V by LPBF [138,139]. The deformation twinning ($\{10\bar{1}1\}\langle10\bar{1}\bar{2}\rangle$) can be observed in as-built Ti-6Al-4V with intrinsic heat treatment strategy by LPBF after compression testing [138,139]. This deformation twinning was identified by in situ high-energy synchrotron X-ray diffraction (HEXRD).

In summary, porosity and surface roughness are important performances for Ti-6Al-4V by LPBF. Achieving fully dense parts and low surface roughness are always desired. The mechanical performance of Ti-6Al-4V by LPBF typically shows high strength but poor ductility due to the observed microstructure, which has been a main concern in recent years. The main deformation mechanism reported in as-built Ti-6Al-4V by LPBF is dislocation slip, which is related to the c/a ratio, slip systems, and Schmid factor. Deformation twinning can be found in literature in as-built Ti-6Al-4V by LPBF with $\alpha+\beta$ microstructure. The performance improvement of as-built Ti-6Al-4V by LPBF through optimisation of powder feedstock, processing conditions, post heat treatment is always desired. The related deformation mechanisms for as-built Ti-6Al-4V by LPBF under different experimental conditions are also essential.

2.3 The role of powder feedstock on performance of Ti-6Al-4V alloy by LPBF

2.3.1 Effect of powder morphology on parts performance

The properties of built parts fabricated by powder with highly spherical shape may also be improved, especially for relative density. There are some reports involving the effects of particle morphology and surface roughness of powder on part properties [61,140,141]. The difference in particle morphology is mainly due to powder manufacturing. Brika et al. [61] compared the performance of Ti-6Al-4V parts by powder produced by GA and PA with a similar PSD, as shown in Fig. 2.10(a, b). Fig. 2.10(c, d) shows that better rheological behaviour and a more efficient particle packing with a highly dense powder bed by more spherical PA powder can be obtained compared to GA powder. As a result, as-built parts by highly spherical PA powder can achieve better relative density (see Fig. 2.10(e)), surface roughness, and mechanical properties than GA powder.

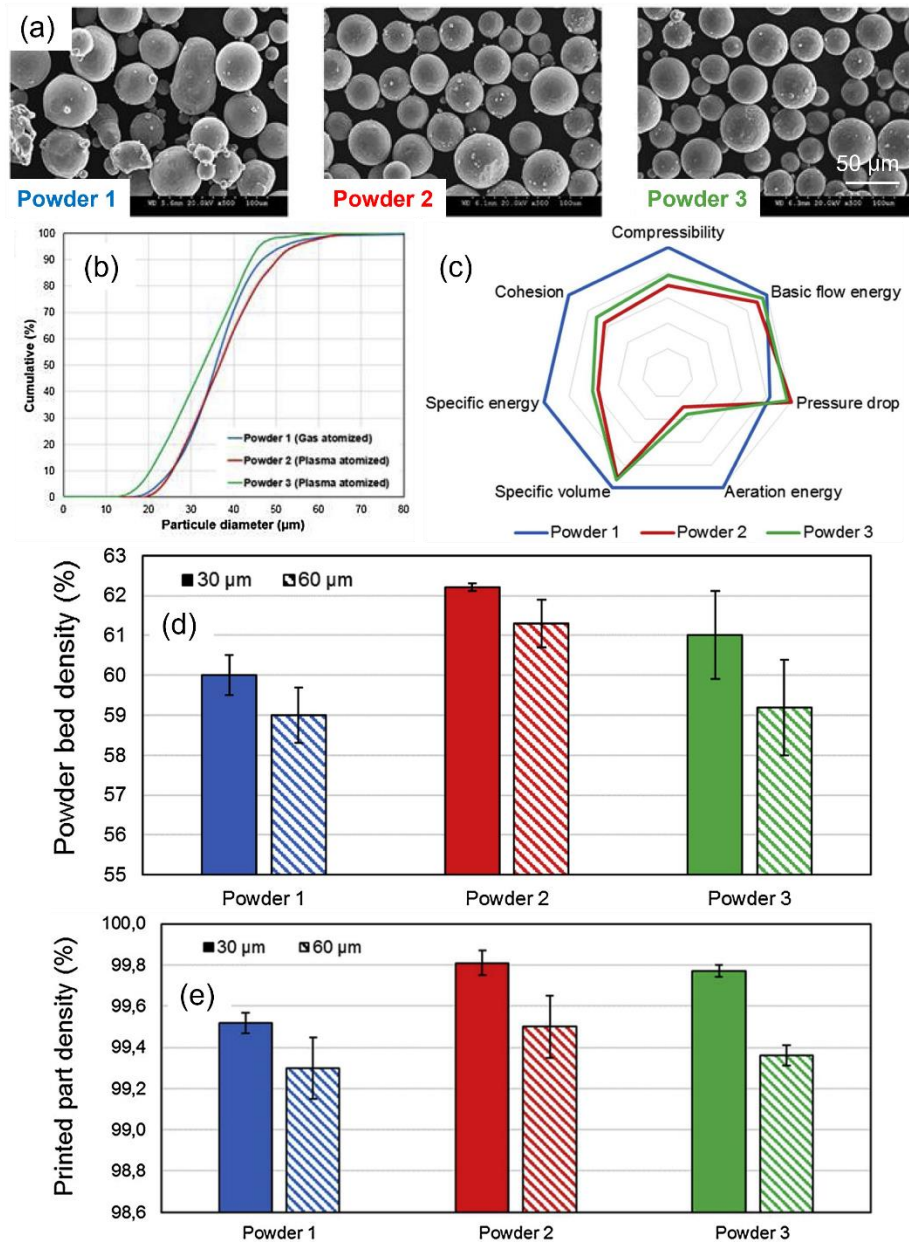


Fig. 2.10 (a) Morphology of Powders 1 (Gas atomised), 2 (Plasma atomised) and 3 (Plasma atomised) by SEM images, (b) cumulative particle size distributions of Powders 1 (20–53 μm), 2 (20–53 μm) and 3 (15–45 μm), (c) the comparison of rheological properties of three powders using Radar diagram, (d) powder bed density and (e) relative density of as-printed parts by three powders with two layer thicknesses (30 μm and 60 μm) [61].

The hydride-dehydride (HDH) process is a cost-efficient method for the fabrication of Ti-6Al-4V powder used as LPBF powder feedstock [9,40,48,142]. Ti-6Al-4V powder fabricated by HDH is at least 30–40% cheaper than GA powder [48,143]. However, the HDH Ti-6Al-4V powder typically shows irregular morphology, which may not be

preferred for LPBF applications. Mehrabi et al. [144] compared powder spreading and flowability with HDH and GA Ti-6Al-4V powder. GA powder shows better spreading behaviour than that HDH powder because of the difference in powder morphology. Jaber et al. [143] studied the effect of Ti-6Al-4V hybrid powders with spherical (PA powder) and irregular shapes (HDH powder) by LPBF. The results indicated that hybrid powders present a decrease in powder flowability and formation of LoF defects with decreased mechanical properties compared to PA powder. Varela et al. [145] reported the performance of HDH Ti-6Al-4V powder by LPBF. There are also some pores in annealed samples while the pores can be reduced and balanced strength-ductility can be achieved by the hot isostatic pressing (HIP) process. The process map of the HDH Ti-6Al-4V powder by LPBF was developed by Wu et al. [146], providing a general guideline for non-spherical powder usage in powder bed fusion AM. The optimised relative density can reach 99.8% after processing parameters optimisation. The results suggest that local packing of powder bed using HDH powder should be noted due to the large local packing variation which may affect the part quality while average packing is reasonable for GA powder. Two porosity formation mechanisms were proposed with the HDH Ti-6Al-4V powder because of the variable local packing and large particle size.

2.3.2 Effect of PSD on parts performance

PSD plays a key role in part properties since PSD can largely affect flowability, powder bed density, and thermal properties [49]. Parts performance, including surface quality, relative density, microstructure, and mechanical properties, is affected by the PSD of powder feedstock [90,147–151]. In this section, the effects of fine and large particles of powder feedstock on parts performance will be presented.

Fine particles have complex effects on powder properties and final parts properties. On the one hand, the addition of fine particles could help to increase the packing density as it may fill in the gaps between large particles. Meanwhile, fine particles are easy to melt completely. As a result, parts properties, such as relative density and surface roughness, may be improved when powder feedstock contains more fine particles. The decrease in surface roughness may be due to powder with more fine particles being more substantially melted, achieving a more stable and smoother melt pool surface, and a diminished balling effect and spatter formation [49,54,150,152]. In general, powders

with fine particles usually use small layer thicknesses that can reduce the stair-step effect and therefore reduce the surface roughness [49]. Gu et al. [147] reported that bimodal distribution Ti-6Al-4V powder with more fine particles (less than 10 μm) presents poor flowability but good relative density compared to uni-modal distribution Ti-6Al-4V powder. Soltani-Tehrani et al. [153] compared the performance of Ti-6Al-4V by LPBF with 15-45 μm (fine) powder feedstock and 15-53 μm (coarse) powder feedstock, as shown in Fig. 2.11(a, b). It is suggested that there are more pores in Ti-6Al-4V parts by coarse 15-53 μm powder feedstock than fine 15-45 μm powder feedstock (see Fig. 2.11(c)). No obvious difference in tensile properties can be found for two powder feedstocks.

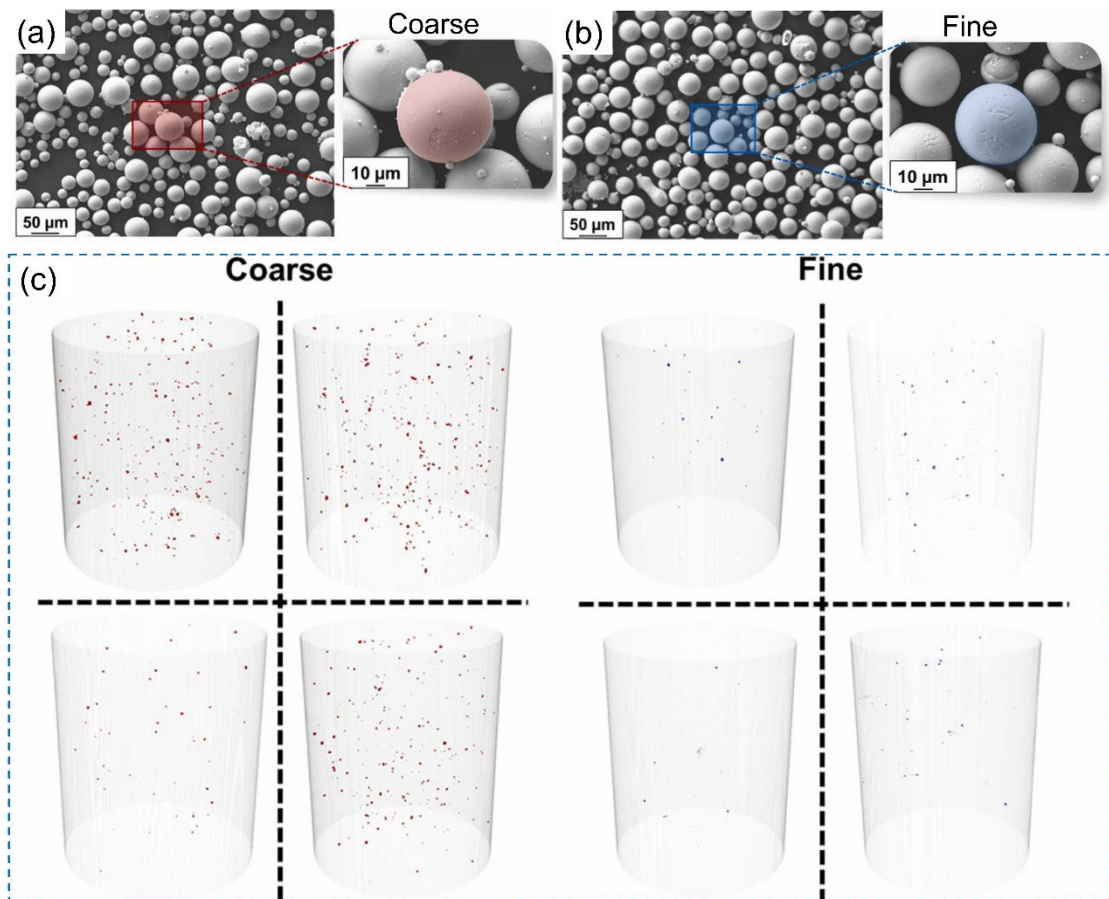


Fig. 2.11 (a) 15-53 μm (coarse) powder feedstock, (b) 15-45 μm (fine) powder feedstock, (c) 3D visualizations of defect population in the parts by coarse and fine powder feedstock using XCT [153].

On the other hand, a certain number of fine particles may largely disrupt the flow behaviour and packing efficiency. This may cause an uneven powder bed during LPBF

[39]. This phenomenon is caused by the formation of agglomerates and/or inter-particle friction. The agglomerates can also decrease powder sphericity. Brika et al. [61] reported the part properties of two PA Ti-6Al-4V powders with PSD corresponding to 15-45 μm and 20-53 μm (see Fig. 2.10). Powder performance and part properties of 20-53 μm powder are slightly better than 15-45 μm , which may mean the negative effect of fine particles for Ti-6Al-4V powder. It is suggested that the reason is due to the high inter-particle friction of 15-45 μm powder with many fine particles. Powder bed density is affected by the cohesion effect. This cohesion effect can induce agglomerates and disrupt the flowability and packing density. The cohesion effect is mainly caused by van der Waals force, which can be expressed by ‘bonding number’ (K) and equation (2) [55]. Hence, if there is a critical value for K, the Ti-6Al-4V with low density (4.42 g/cm^3) should require a larger particle size.

$$K = \frac{F_{c,\max}}{m_i g} = \frac{9\gamma}{4\rho g d^2} \quad (2)$$

Where γ is surface energy density, ρ is the material density, g is gravitational acceleration, and d is the particle size. It is noteworthy that fine particles tend to be evaporated and ejected as spatter during the interactions between laser and powder due to their lower mass [39,54,90].

Regarding large particles, the first concern is layer thickness. Large particles can limit the layer thickness range. If more large particles are employed, high layer thickness should be applied to ensure the powder spreading quality and suitable packing density in the powder bed [39]. However, high layer thickness may not always produce the desired relative density even if laser processing parameters are optimised. Alfaify et al. [149] compared the relative density of three different PSD Ti-6Al-4V powders with layer thickness 60, 80, 100 μm . The results indicate that powder with fewer large particles ($\sim 15\text{-}45 \mu\text{m}$) generally has a higher relative density than powder with larger particles ($\sim 45\text{-}80 \mu\text{m}$, $\sim 50\text{-}105 \mu\text{m}$). However, it is noteworthy that high layer thickness means high energy density to melt fully. High energy density may cause strong spatter during LPBF, influencing part properties [77,78]. Moreover, the surface roughness of parts by large particles increases because spatter may adhere to the top surface of parts [77,78] and a ‘stair-step effect’ by high layer thickness is usually used [39].

In conclusion, the effect of PSD on LPBF parts is still not fully understood, especially

the role of fine particles. The effect of fine particles is largely dependent on the material (density) and processing parameters. In addition, in-process powders (generated powders during LPBF, like spatter) may play a key role in understanding the role of PSD on Ti-6Al-4V parts performance, which is rarely reported. Hence, a comprehensive study of the effect of PSD with a combination of material properties and in-process powders on parts performance is essential.

2.3.3 Effect of chemical composition on parts performance

Although it is usually possible to achieve high strength in Ti-6Al-4V by using LPBF, some drawbacks are still associated with Ti-6Al-4V (such as columnar prior- β grains, poor ductility). Composition modification is an important way to tailor microstructure and mechanical properties. It is not easy to produce new Ti pre-alloy powders due to the high cost of powder production by atomisation. Hence, in-situ alloying applied in LPBF is a common and easy way to modify Ti-6Al-4V composition to achieve desirable microstructure and mechanical properties.

Columnar prior- β grains with needle martensite α' structures are typically observed in Ti-6Al-4V by LPBF [12]. The grain refinement is closely related to the Q value and high Q value is critically important to obtain equiaxed grains in AM alloys [111]. It is known that the Al and V of Q values typically show almost zero. The columnar prior- β grains are mainly due to the low value of grain growth restriction (Q value) in Ti-6Al-4V [154]. There are some reports aiming at breaking the columnar prior- β and refining the prior- β with high Q value additions. Boron (B) acting as α -stabiliser element with a Q value around 65 is usually used to refine grains in additive manufacturing [155,156]. Grain refinement can be observed when Boron addition exceeds 0.5% into Ti-6Al-4V [156]. In addition, needle-like nano/micro TiB particles can be formed due to Ti and B reactions. As a result, the microhardness and wear properties of the Ti-6Al-4V+B can be significantly improved. However, this TiB may affect modified Ti-6Al-4V ductility. Iron (Fe) acting as a β -stabiliser element with a high Q value (around 9-40) is also promising in grain refinement. Simonelli et al. [154] refined prior- β grains and minimised the microstructural anisotropy with different additions of Fe (2, 3, 4 wt.%), as shown in [Fig. 2.12](#). Equiaxed morphology can be found in β grains. After heat treatment, a desirable fully $\alpha+\beta$ lamellae structure in refined prior- β grains is also obtained.

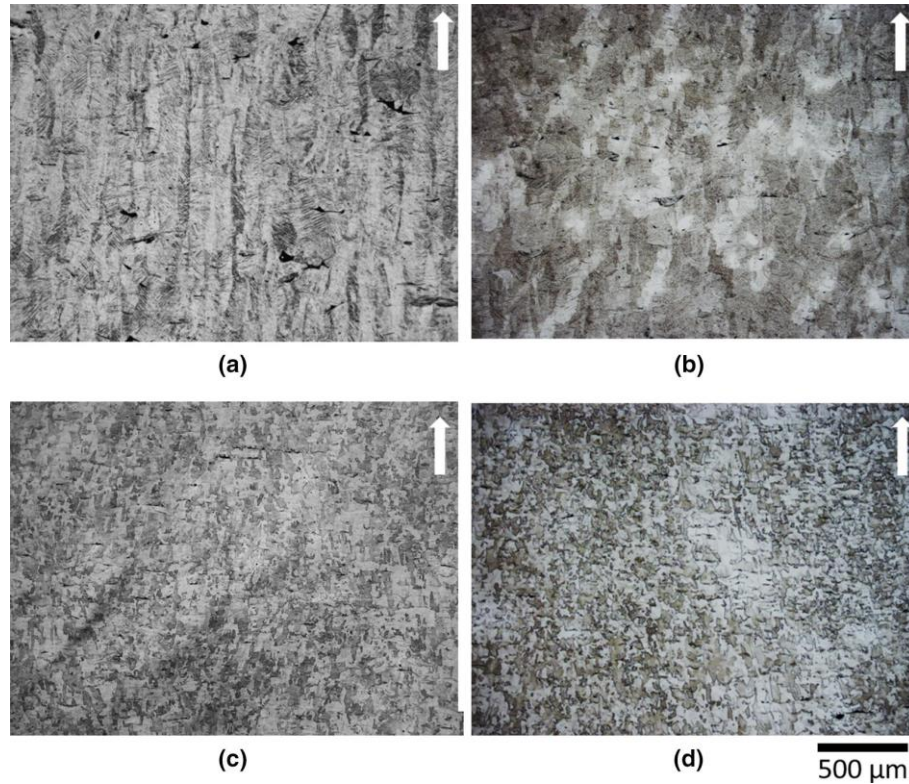


Fig. 2.12 Microstructure of as-built samples with different Fe contents by optical micrographs (a) Ti-6Al-4V, (b) Ti-6Al-4V-2Fe, (c) Ti-6Al-4V-3Fe, and (d) Ti-6Al-4V-4Fe, white arrows show the build direction (i.e., Z direction) [154].

Apart from the refinement of columnar prior- β grains, another significant focus is to tailor the HCP phase and BCC phase content via composition modification of Ti-6Al-4V. Therefore, applying the β -stabiliser element is a common way to tailor the Ti-6Al-4V microstructure. After the addition of 10% Mo into Ti-6Al-4V, a fully β titanium matrix can be obtained rather than the martensite α' structure observed in Ti-6Al-4V by LPBF [157]. As a result, high tensile strength (~ 919 MPa) and excellent ductility ($\sim 20.1\%$) can be achieved. Fe can not only refine the grains but also tune the phase content. Zhang et al. [8] used the common material 316L (with Fe, Cr, Ni, Mo β -stabiliser elements) as an addition to Ti-6Al-4V to modulate the phase. With different 316L additions (2 wt.%, 4.5 wt.%, 6 wt.%), the phase varies from almost martensite α' structure with a small amount of β phase to both martensite α' structure and β phase to full β phase, respectively (see Fig. 2.13). Hence, the phase content can be tuned with proper 316L additions. More importantly, the mechanical properties can be enhanced with increased tensile strength (~ 1300 MPa), improved uniform ductility ($\sim 8.8\%$) and enhanced work-hardening capacity (~ 300 MPa) when 4.5 wt.% 316L addition is

employed. Meanwhile, stress-induced β to α' martensitic transformation (SIMT) can be observed due to the appearance of metastable β . This SIMT contributes to the increased uniform ductility and enhanced work-hardening capacity in Ti-6Al-4V with 4.5 wt.% 316L addition. Besides the different addition content to modify the phase, processing parameters also play an important role in phase content in Ti-6Al-4V with 3 wt.% Fe addition by LPBF [158]. When low energy density is applied, Fe distribution in the microstructure is heterogeneous. As a result, β dominated structure with some martensite α' structures (less than 30%) can be found and simultaneously a high tensile strength (1364 ± 59 MPa) and uniform ductility (11.4 ± 1.9 %) can be obtained. On the contrary, there is a better homogenous mixing of Fe in the Ti-6Al-4V matrix when high energy density is employed. This results in a dominated martensite α' structure with a limited β phase. The microstructure increases strength (1762 ± 50 MPa) but deteriorates ductility (3.1 ± 0.6 %).

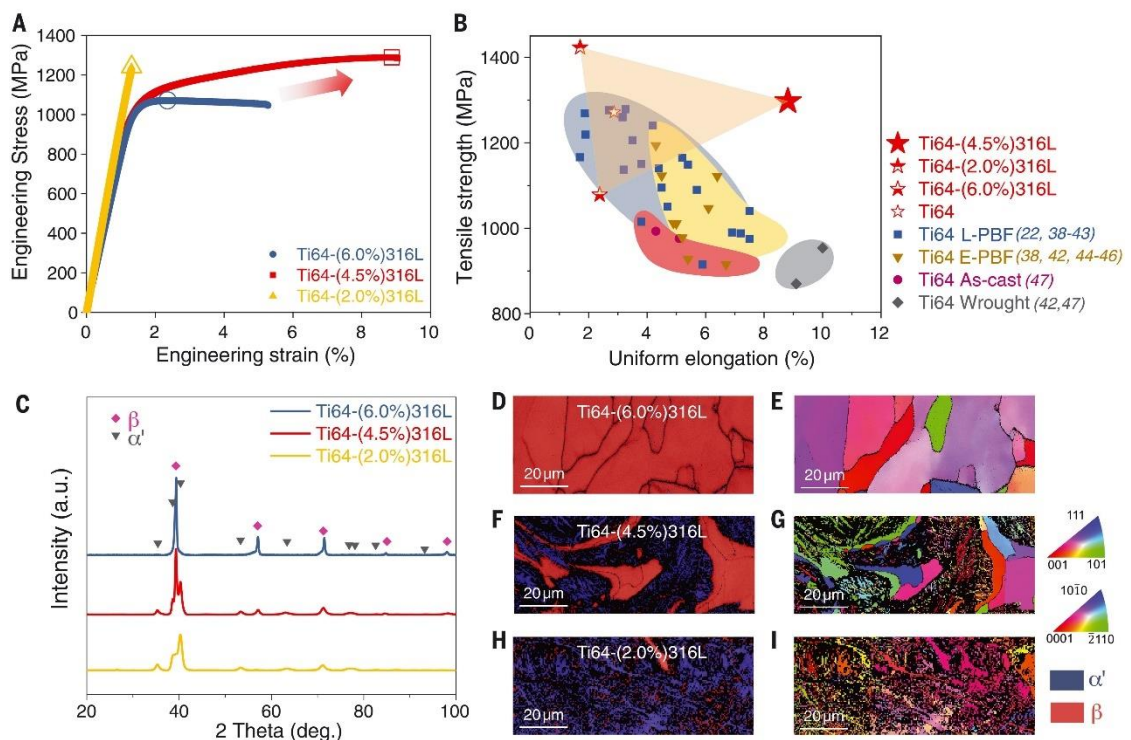


Fig. 2.13 Microstructure and mechanical properties of the as-built Ti-6Al-4V with 316L additions, (A) tensile properties of Ti-6Al-4V-2wt.% 316L, Ti-6Al-4V-4.5wt.% 316L and Ti-6Al-4V-6wt.%316L, (B) mechanical properties comparison between as-built Ti-6Al-4V with 316L additions and Ti-6Al-4V alloy fabricated by different AM methods and conventional technologies, (C) XRD results of modified Ti alloys, (D to I) EBSD phase maps and IPF maps of modified Ti alloys [8].

Ti-6Al-4V has been strengthened through additions inside recently. For example, the microhardness of Ti-6Al-4V by LPBF can be significantly improved from 340 HV to 511 HV after the addition of nano yttria-stabilized zirconia (nYSZ) up to 2.5 wt.% [159]. There is significant improvement in compression strength (1751 MPa) and yield strength (1302 MPa) with 2.5 wt.% nYSZ into Ti-6Al-4V compared to compression strength (1250 MPa) and yield strength (840 MPa) by Ti-6Al-4V. Strengthening of Ti-6Al-4V in LPBF can likewise be obtained via adding Mo₂C particles into Ti-6Al-4V [160]. Remarkable enhancements in microhardness and tensile strength of the Ti-6Al-4V matrix are thought to be related to the laminated α' -Ti/ β -Ti structure, solid solution behaviour of Mo and C, presence of the remaining Mo₂C and precipitated M₂₃C₆ (M was Ti, Al, V, and Mo). Interestingly, to achieve homogenous dispersion of carbon nanotubes (CNTs) in Ti-6Al-4V particles, Liu et al. [161] used fluidized bed chemical vapor deposition (FBCVD) to plant CNTs within Ti-6Al-4V particles, as presented in [Fig. 2.14](#). By activating the catalytic function of the trace Fe impurities in Ti-6Al-4V powder, homogenous CNTs/Ti-6Al-4V composite powder can be obtained [162]. This method can also exhibit a superior strengthening effect through the reinforcement of CNTs/TiC nanoplatelets and nanoparticles.

Some studies focus on functional modification (such as corrosion properties and biomedical application) via composition tailoring of Ti-6Al-4V by LPBF [163–166]. For example, corrosion resistance can be further enhanced through the addition of Pd into Ti-6Al-4V by LPBF [163]. With Cu and Ag added to Ti-6Al-4V by LPBF, implants with good antibacterial properties are likely to be produced. Krakhmalev et al. [164] mixed the Ti-6Al-4V with 1 at.% Cu (1.38 wt%) by LPBF showing promising results based on antibacterial testing. Vilardell et al. [166] fabricated and characterised in-situ alloyed Ti-6Al-4V with 3 at.% Cu addition by LPBF. Three phases including martensite α' , β phase and CuTi₂ intermetallic precipitates can be observed while antibacterial test of in-situ alloyed Ti-6Al-4V-3 at.% Cu is lacking. Macpherson et al. [165] investigated Ti-6Al-4V with 5 wt.% Cu or 0.5 wt.% Ag by LPBF. Ultrafine $\alpha + \beta$ structure with a small amount of Ti₂Cu can be found in Ti-6Al-4V with 5 wt.% Cu, showing increased strength but reduced ductility. For Ti-6Al-4V with 0.5 wt.% Ag, no significant microstructure or phases can be observed, presenting slightly decreased strength while a noticeable increase in ductility. Ti-6Al-4V with 5 wt.% Cu shows moderate

antibacterial properties while little antibacterial properties are exhibited in Ti-6Al-4V with 0.5 wt.% Ag.

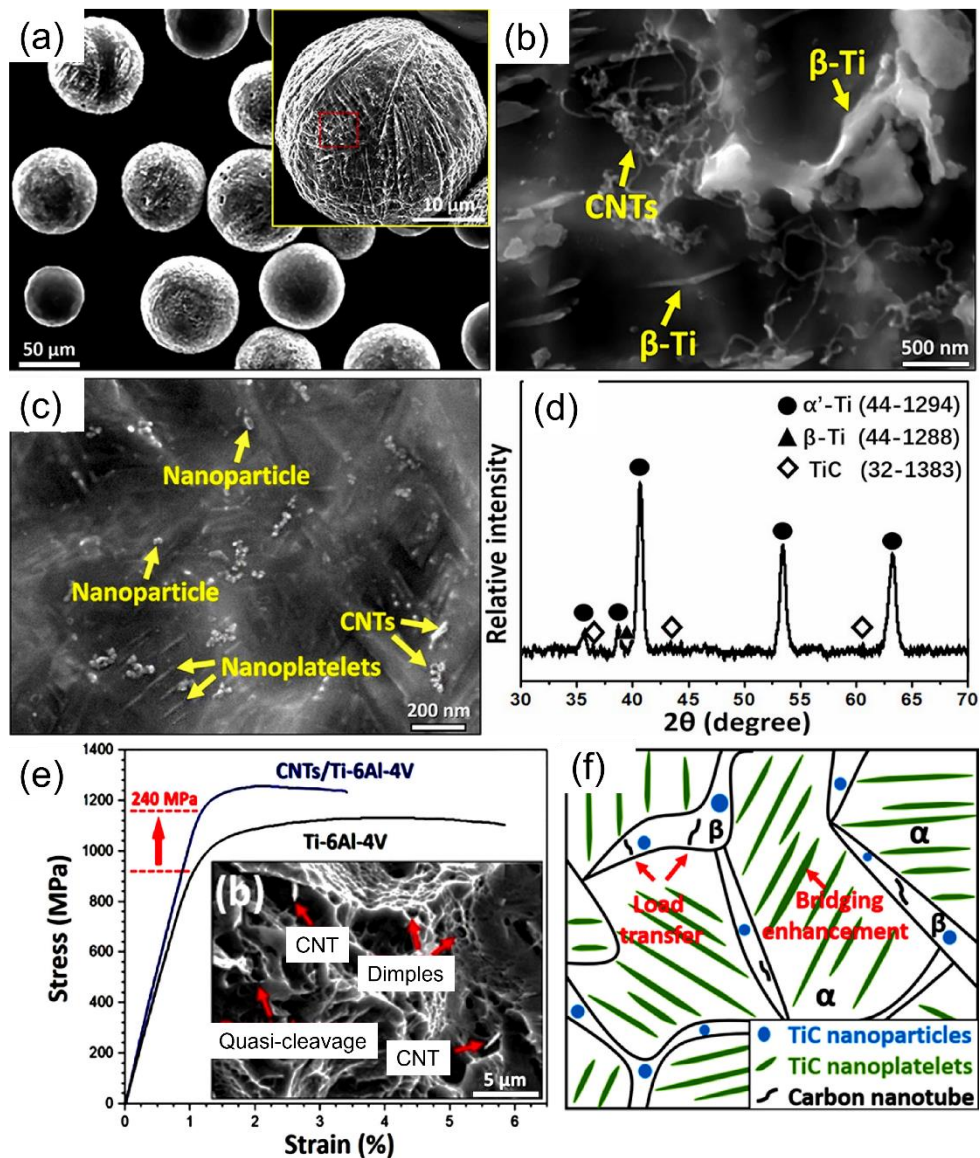


Fig. 2.14 (a) SEM image of Ti-6Al-4V powder with CNTs planted, (b) SEM image in the marked area of (a), (c) SEM image of the as-built sample in high magnification, (d) XRD result of the as-printed sample, (e) mechanical properties of as-built Ti-6Al-4V alloy and composite, (f) schematic diagram of the strengthening mechanisms of the as-built composite [161].

Although in-situ alloying to modify Ti-6Al-4V composition is common, pre-alloy powder with a modified composition of Ti-6Al-4V is crucial to eliminate elemental segregation and satisfy the materials requirement in the AM community. For example, recently, pre-alloy Ti-4Al-4V (the reduction of Al content) by LPBF exhibits balanced

strength-ductility compared to as-built Ti-6Al-4V [167], as presented in Fig. 2.15. Song et al. [168] also studied the influence of Al content on the microstructure and tensile properties of pre-alloyed Ti-4Al-4V, Ti-6Al-4V, Ti-8Al-4V. There is an increase in area fractions of ternary α' laths and strength with increased Al content. Work hardening and uniform elongation values of Ti-4Al-4V and Ti-8Al-4V are both higher than those of Ti-6Al-4V. This can be ascribed to the activation of multiple slip modes in Ti-4Al-4V, and a stronger hetero-deformation induced (HDI) hardening effect in Ti-8Al-4V.

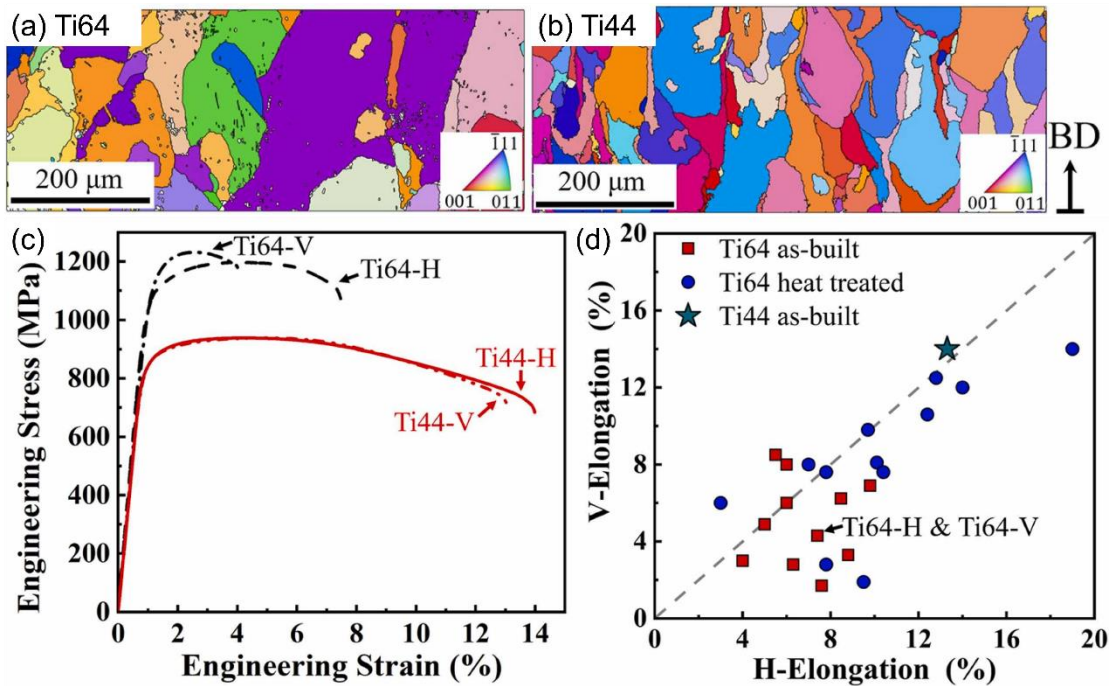


Fig. 2.15 Inverse pole figure (IPF) maps of the reconstructed prior- β grains in (a) Ti-6Al-4V (Ti64), (b) Ti-4Al-4V (Ti44), (c) mechanical properties of the Ti44-H, Ti44-V, Ti64-H and Ti64-V, (d) elongation along H and V directions of as-built Ti44 compared to other literature [167].

In summary, modifying the composition of Ti-6Al-4V in LPBF to tailor microstructure and mechanical properties has become an important topic. Achieving refined prior- β grains and tailoring martensite α' into β phase were significantly studied. The strength can be further enhanced, and improved antibacterial properties for medical applications can be achieved through additions to Ti-6Al-4V. However, tuning the martensite α' structure and achieving balanced strength and ductility through composition modification are few. There are still some gaps in manipulating microstructure and achieving desired mechanical properties.

2.4 The role of heat treatment on performance of Ti-6Al-4V alloy by LPBF

As-built Ti-6Al-4V by LPBF typically exhibits columnar prior- β grain boundaries with martensite α' structure under cyclic heating and cooling. High strength (more than 1200 MPa) but low ductility (<10%) can be therefore observed while the low ductility makes it unsuitable for practical applications. Anisotropy microstructure and anisotropy mechanical properties are common in as-built Ti-6Al-4V. A common method of tuning microstructures and obtaining desired mechanical properties is to employ heat treatment. Exploring heat treatment strategies to enhance microstructure and mechanical performance is crucial for LPBF fabricated Ti-6Al-4V. The primary purpose of the heat treatment is to decompose the non-equilibrium state martensite α' into a stable $\alpha+\beta$ phase and to minimise residual stress [103]. The microstructure largely relies on the heat treatment strategy and the microstructure obtained by heat treatment could affect the final mechanical properties. During heat treatment, heating and cooling stages are considered. For the heating stage, when the hold temperature is over martensite decomposition ($\sim 400^\circ\text{C}$), the martensite α' becomes decomposed into $\alpha+\beta$ phase [120]. If the hold temperature is over the β transus temperature, which means the α phase totally transforms into β phase, as shown in Fig. 2.7(a). For the cooling stage, the phase transformation from β to α (or α') would occur. The cooling rate would play an important role in the microstructure (such as phase and grain size) [106,169]. There are three typical cooling ways, including water quenching (WQ, very fast cooling), air cooling (AC, fast cooling) and furnace cooling (FC, slow cooling). Water quenching would cause the formation of martensite α' if the holding temperature is over M_s . The grain size would be increased when the cooling rate decreases. To reduce oxidation of reactive Ti-6Al-4V, the heat treatment of Ti-6Al-4V should be conducted in a protective argon or vacuum atmosphere. Common heat treatment (including stress relief, annealing, solution treatment and aging, HIP) and novel heat treatment are discussed in this thesis to present the role of heat treatment on microstructure and mechanical properties of Ti-6Al-4V by LPBF.

2.4.1 Stress relief and annealing

In general, as-built Ti-6Al-4V may form residual stress during LPBF. Stress relief heat treatments are usually performed to release the residual stress with temperatures ranging from 450 °C to 730 °C followed by FC or AC [100,103,136]. When high temperatures are applied, residual stress can be relieved more effectively. It is noteworthy that the microstructure size of laths almost maintains or slightly increases because the stress relief temperature is usually located in a low $\alpha+\beta$ field based on the phase diagram. The martensite α' structure can be decomposed into $\alpha+\beta$ for 730 °C heat treatment [136]. Coherent α_2 particles may be precipitated in the Ti-6Al-4V if the stress relief temperature is around 550 °C (especially for a long-time heat treatment). Due to the limitations of microstructure tuning (including grain size and phase fraction) after stress relief, Ti-6Al-4V mechanical properties typically exhibit maintained or decreased strength, and maintained or limited increase in ductility (around 10%) [100,136].

The annealing temperature is usually located in the relatively high $\alpha+\beta$ field based on the phase diagram. The temperature typically ranges from 750 °C to 950 °C ($<\beta$ transus temperature) followed by FC or AC. Non-equilibrium martensite α' structure can be not only decomposed into $\alpha+\beta$ with lamellar structures but also with increased β volume fraction and α width [103,169–171], as shown in Fig. 2.16. When the heat treatment temperature is at or exceeds 900 °C, the lamellar structures show a significant coarsening trend [171]. Globularized grains (equiaxed grains) can be found through the boundary splitting mechanism when the heat treatment temperature is at 900 °C and 950 °C. Due to the increased lamellar size of $\alpha+\beta$ phase in Ti-6Al-4V after annealing, significant balanced strength (~900-1100 MPa) and ductility (~12-20%) of Ti-6Al-4V are achieved compared to as-built Ti-6Al-4V with low ductility. Therefore, annealing is a common method to obtain good enough ductility to meet the Ti-6Al-4V standard with tensile strength over 930 MPa and elongation over 10% [172].

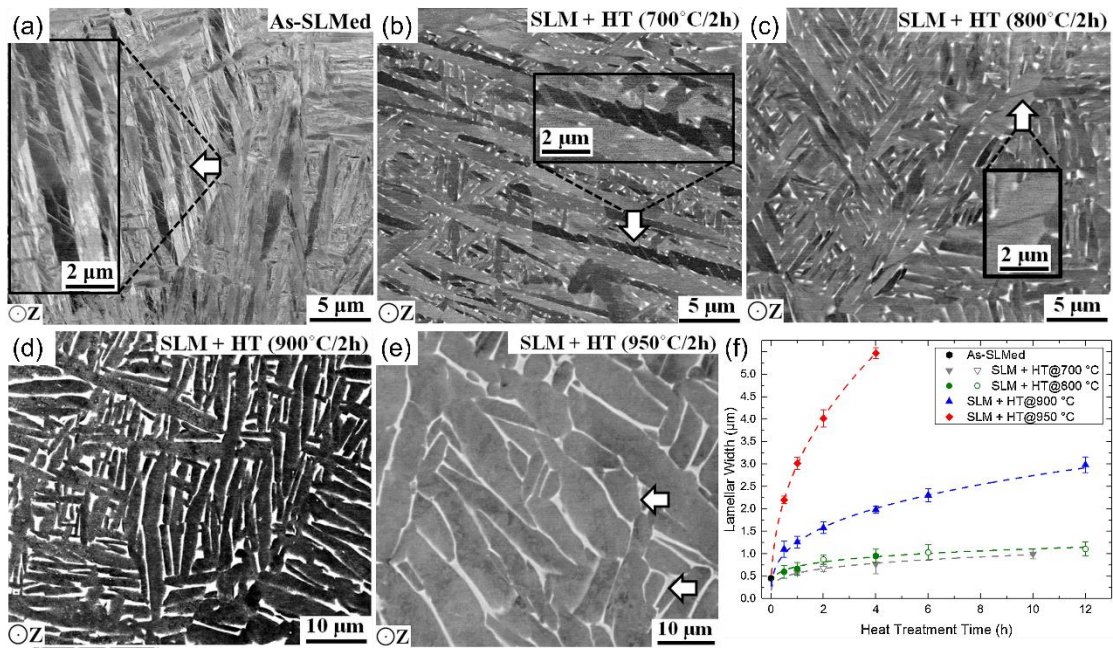


Fig. 2.16 (a) SEM image of as-built Ti-6Al-4V, (b-e) SEM images of heat treated Ti-6Al-4V by 700 °C/2h, 800 °C/2h, 900 °C/2h, 950 °C/2h, respectively, (f) lamellar width of Ti-6Al-4V by different heat treatment temperatures and holding times [171].

When the stress relief and annealing temperature is lower than the β transus temperature, the columnar prior- β grain boundaries will maintain. To break the columnar prior- β grain boundaries and obtain the equiaxed prior- β grain boundaries, heat treatment temperature is typically employed in excess of 1000 °C (β transus temperature less than 1000 °C). As a result, the columnar prior β grains become equiaxed grains [169]. However, due to the quick growth of β grains when temperature above β transus temperature, the grain size of β grains is usually large [112,173]. The mechanical properties of Ti-6Al-4V after annealing above β transus temperature may present low ductility (less than 10%) because of the large size β grains [112,169] rather than balanced strength-ductility achieved by annealing below β transus temperature, which is also observed in near α Ti-6.5Al-2Zr-Mo-V alloy fabricated by LPBF with low ductility by super β transus temperature annealing [25]. It is known that twin structures can often occur in martensite α' except for dislocations [118,171,174,175]. After annealing heat treatment, the twin structures will disappear [171,175].

It is noteworthy that some in-situ experiments on stress relieved and annealed Ti-6Al-4V clarify the phase transformation process and tensile behaviour after heat treatment

[101,105]. This could help understand the effect of heat treatment on crystal structure and tensile properties. For example, Kaschel et al. [105] studied the stress relaxation and phase transformation mechanisms of Ti-6Al-4V by LPBF through in situ high temperature XRD and TEM. Phase transformation from martensite α' to equilibrium $\alpha+\beta$ can be found when the heat treatment temperature is over 400 °C. There is an increasing trend for both lattice parameters a and c when heat treatment temperature increases. Through in situ measurements, the phase transformation is driven by the substitution of Al, V and Ti atoms from the crystal lattice. This is because of concentration changes during heat treatment.

2.4.2 Solution treatment and aging (STA)

STA is normally applied to increase Ti-6Al-4V strength. There are two types of STA (β STA and $\alpha+\beta$ STA) according to the solution temperature. For β STA, the solution temperature is over β transus temperature and as a result, the prior- β grains transform from columnar to equiaxed with large grain size [170,176]. The width of the α lamellae mainly depends on the cooling rate after solution treatment. Fewer α variants leave after the β STA treatment [103]. The β STA probably shows poor ductility (less than 10%) [176] similar to β annealing.

$\alpha+\beta$ STA is an effective way to achieve different microstructures considering the grain size, volume fraction and phase morphology compared to β STA. The solution temperature (over 900 °C) is normally close to the β transus temperature and fast cooling (WQ and AC) is typically employed. As a result, a typical bi-modal microstructure with primary α_p and transformed β_t (with secondary α_s inside) can be achieved in Ti-6Al-4V by LPBF through $\alpha+\beta$ STA treatment [176–179]. For example, Miyazaki et al. [178] studied the effect of solution temperature and time on Ti-6Al-4V microstructure by LPBF, as shown in Fig. 2.17. When the solution temperature increases, an increase in the volume fraction of transformed β_t and a decrease in primary α_p can be observed. In addition, there is a decreasing trend for the aspect ratio of α_p and some equiaxed α_p grains can be found. A reduced number density of α_p , a bigger sized α_p and a more equiaxed α_p can be obtained with increased solution time.

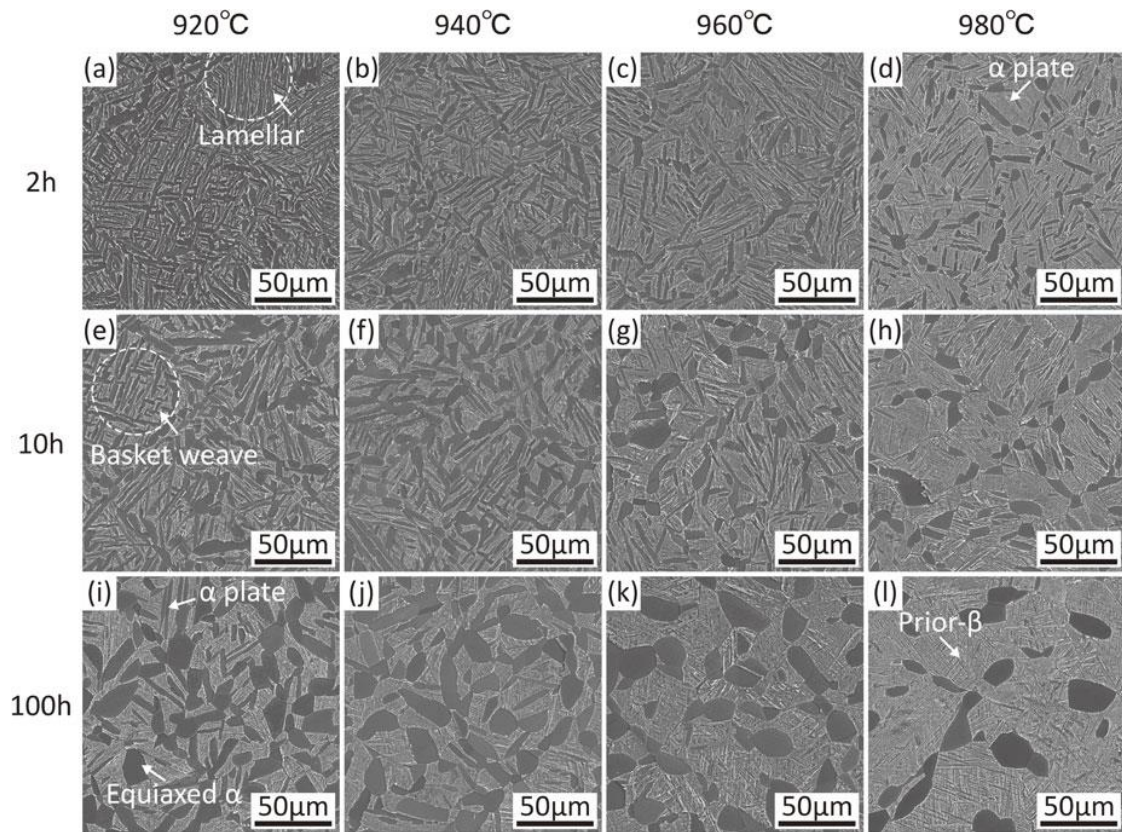


Fig. 2.17 The influence of solution temperature (920 °C, 940 °C, 960 °C, 980 °C) and time (2h, 10h, 100h) on Ti-6Al-4V microstructure [178].

It is noteworthy that plastic deformation before heat treatment is usually required for globularization. LPBF fabricated can achieve the globularization through the boundary splitting process (including thermal grooving, edge spheroidization) due to the high dislocation density generated from the LPBF process [180]. However, the equiaxed α_p dominated microstructure in Ti-6Al-4V seems to be difficult to find in literature with recrystallization process after STA treatment. This may be related to the insufficient dislocation density as the equiaxed α_p dominated microstructure in Ti-6Al-4V is achieved through large plastic deformation by conventional manufacturing [38]. Therefore, achieving fully equiaxed α in Ti-6Al-4V by LPBF is a challenging work.

2.4.3 Hot isostatic pressing (HIP)

It is known that defects such as pores (gas pores, LoF pores, keyhole pores), cracks, and partially melted powders can be observed in LPBF parts [3]. Mechanical properties (in particular fatigue properties) may be affected by these defects. However, defects are difficult to eliminate by stress relief, annealing, STA heat treatments. HIP is a powerful

technique to eliminate internal pores caused by LPBF except for pores connected to the surface [181–184]. Fig. 2.18 shows the role of HIP in the removal of pores caused by keyhole pores and LoF pores in LPBF [183].

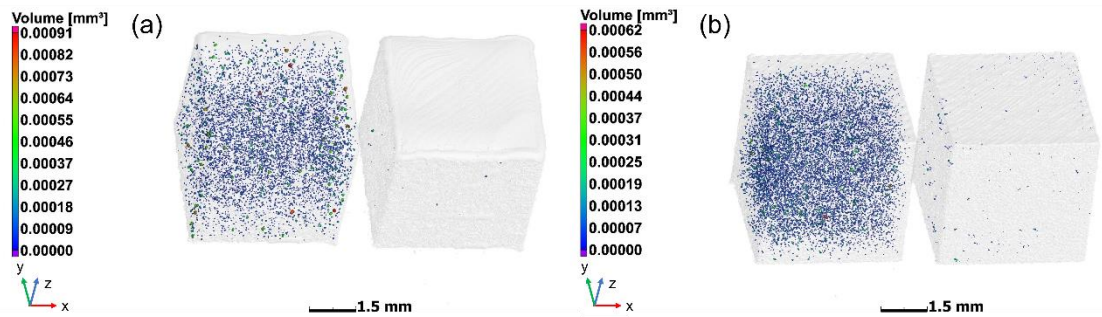


Fig. 2.18 The X-ray tomography results to present the effect of HIP on pores elimination, (a) keyhole pores elimination, (b) LoF pores elimination [183].

HIP for Ti-6Al-4V can also be classified into two types (super β -transus HIP, sub β -transus HIP) based on the HIP temperature. The microstructure observed by HIP is similar to the annealing. For super β -transus HIP, large equiaxed β grains are found [181,185]. Zhang et al. [185] reported that the isotropic mechanical properties could be achieved due to the formation of equiaxed grains by the super β -transus HIP. Sub β -transus HIP is more commonly used for Ti-6Al-4V by LPBF with typical temperature from 850 °C to 950 °C, pressure around 100-150 MPa, holding time around 2-4 h. Likewise, α + β lamellar microstructure is typically obtained and a few equiaxed α grains may be found if the temperature is close to β -transus temperature [184,186]. After sub β -transus HIP, balanced strength and ductility can also be exhibited especially in elongation (up to ~20%) due to both the contribution of α + β lamellar microstructure and pores elimination [181,184,187]. More importantly, fatigue properties can be significantly enhanced after HIP treatment [188–190].

It is noteworthy that HIP can also benefit productivity and processing parameters of LPBF fabricated Ti-6Al-4V [181,182,191]. Plessis et al. [191] built a Ti-6Al-4V shell with powder feedstock inside and then treated by HIP, which saves time and cost for laser scanning the inner area. However, there is a decrease in fatigue strength for this shell structure and further optimisation may be required. Herzog et al. [182] applied high speed processing parameters to fabricate Ti-6Al-4V with LoF pores. The LoF pores can be eliminated through HIP treatment. A combination of LPBF and HIP treatment makes it possible to enlarge the process window. Interestingly, because the low energy

density employed in Ti-6Al-4V can refine the columnar prior- β grains [117], therefore it is possible to achieve refined prior- β grains via combining the LoF (i.e., low energy density) and HIP, studied by Bustillos et al. [181], as presented in Fig. 2.19. Meanwhile, more low aspect ratio α grains (explained by dislocation-induced recrystallization and reduction of surface energy by LoF) can be observed in LoF and HIP samples compared to fully dense samples after HIP with lamellar α . As a result, superior mechanical properties with tensile strength ~ 1000 MPa and elongation $\sim 20\%$ are achieved with the combination of LoF and HIP.

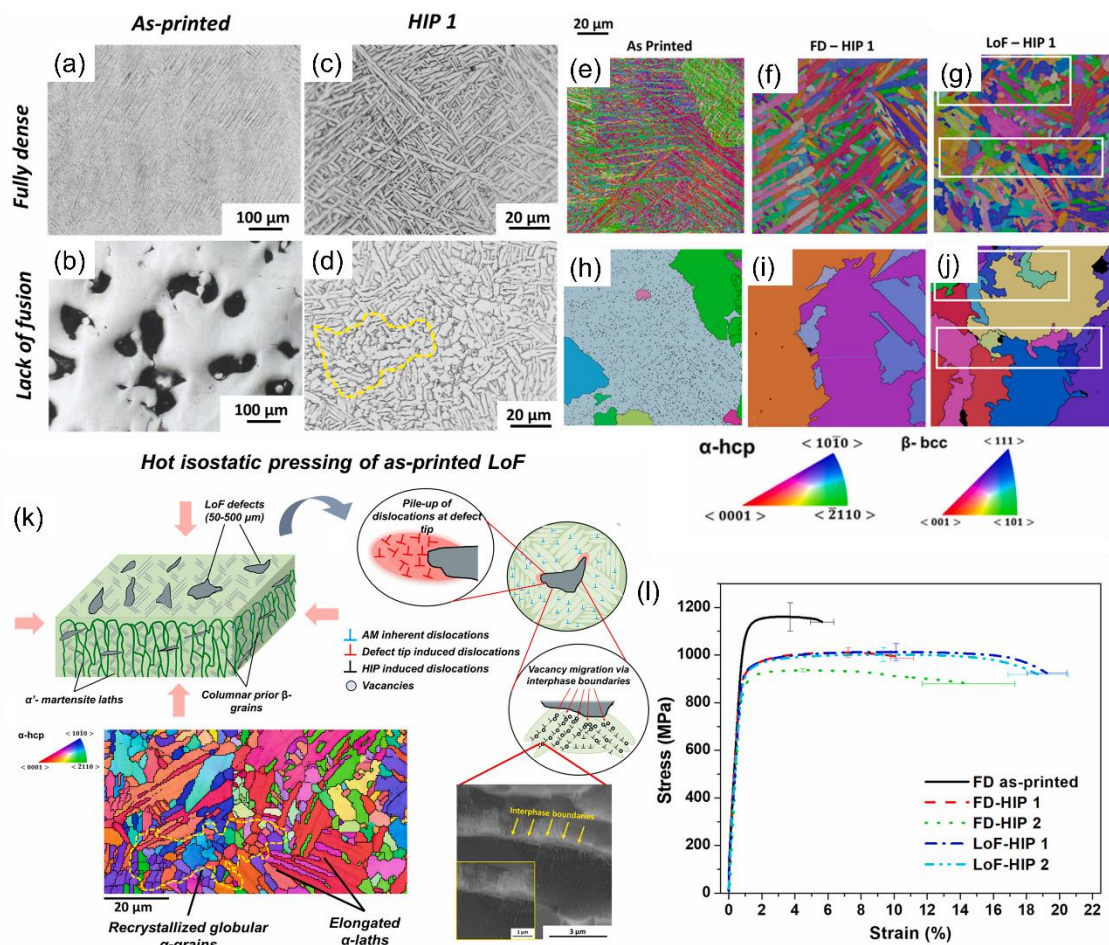


Fig. 2.19 (a-d) Microstructural evolution of as-printed and HIP sample with fully dense (FD) and LoF parameters, (e-g) inverse pole figure maps and (h-j) maps of reconstructed prior- β grains, (k) schematic diagram of the dislocation evolution in a LoF sample during HIP treatment, (l) tensile properties of Ti-6Al-4V in as-printed and HIP [181].

2.4.4 Novel heat treatment

Besides the stress-relief, annealing, STA, and HIP treatments, some novel heat treatments for as-built Ti-6Al-4V have been developed to modify the microstructure and enhance the mechanical properties in recent years. First, in situ heat treatment is a good approach to decompose martensite α' into $\alpha+\beta$ without post heat treatment. This can be achieved through careful laser processing parameters optimisation (especially for focus offset distance) [120,121]. Balanced strength (tensile strength ~ 1100 MPa) and ductility ($\sim 11-12\%$) are observed. The transformation of prior- β grains from columnar to equiaxed is usually observed when heat treatment temperature is over β transus temperature, however, no matter the annealing, STA and HIP (except for the combination of LoF), the prior- β grains are typically large (more than $100\ \mu\text{m}$). A novel heat treatment called rapid heat treatment with a heating rate of up to $10\ \text{°C/s}$ and maintaining the target temperature (over β transus temperature) with a short dwell time of 1 s can be applied to obtain refined prior- β grains [192,193], as shown in Fig. 2.20. This can be attributed to the epitaxial recrystallization of prior- β grains during rapid heat treatment. Balanced strength (tensile strength ~ 940 MPa) and ductility ($\sim 16\%$) can be achieved through this rapid heat treatment strategy.

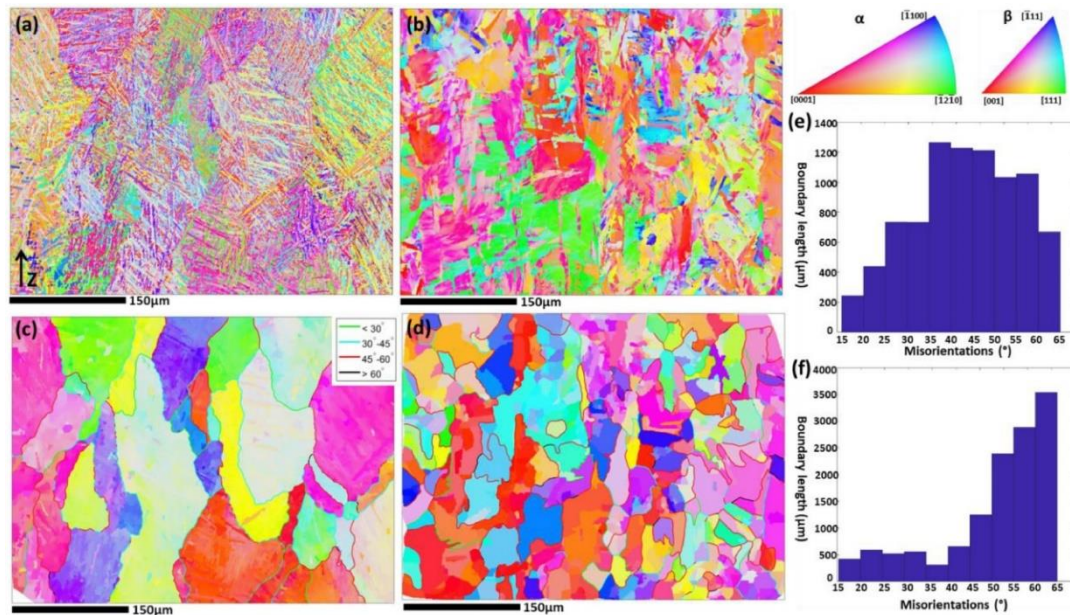


Fig. 2.20 The refinement of prior- β grains through rapid heat treatment, (a, b, e) IPF map, reconstructed prior- β grain map, misorientation boundary of as-built Ti-6Al-4V, (c, d, f) IPF map, reconstructed prior- β grain map, misorientation boundary of Ti-6Al-4V by rapid heat treatment [192].

Sabban et al. [194] reported that when thermal cycling between 975 °C and 875 °C with a heating rate of 2.5 °C/min and cooling rate of 1 °C/min for 24 h is employed, a bimodal microstructure with massive globularized α can be observed. As a result, there is a significant enhancement in the ductility and toughness by thermal cycling heat treatment. In addition, a novel multi-step heat treatment has also been found to globularize lamellar α and form nearly equiaxed α grains [195]. The multi-step heat treatment was carried out from 950 °C (hold time 2 h, FC) to 850 °C (hold time 2 h, FC) to 750 °C (hold time 2h, FC) to 650 °C (hold time 2 h, FC) to room temperature. A superior combination of strength (~tensile strength 950 MPa) and ductility (~22%) can be achieved. Recently, high magnetic field heat treatment was used to LPBF fabricated Ti-6Al-4V [196]. This novel heat treatment can promote the sub-grain boundaries of the α phase and facilitate the globularization α phase. More β phase (~13.4 vol%) can be observed in the high magnetic field heat treatment sample compared to the annealed sample (~6.5 vol%). Enhanced ductility is therefore achieved compared to an annealed sample.

2.4.5 Deformation behaviour of heat treated Ti-6Al-4V

Simonelli et al. [136] studied the fracture modes of stress relieved Ti-6Al-4V. Terrace-like features can be observed on the fracture surface. The results indicate that intergranular α and along the prior- β grain boundaries may be the dominant fracture mode for stress relieved Ti-6Al-4V by LPBF. Zhang et al. [101] employed in situ HEXRD to analyse the tensile deformation behaviour of as-built Ti-6Al-4V, Ti-6Al-4V heat treated at 730 °C (HT-730) and Ti-6Al-4V heat treated at 900 °C (HT-900) (see [Fig. 2.21](#)). The c , a , and c/a ratio of HCP phase increase when heat treatment temperature increases. The ratio of $CRSS_{prism}/CRSS_{basal}$ is estimated to be 1.31 for as-built Ti-6Al-4V and 1.16 for HT-900, based on the EPSC simulation of the macroscopic stress-strain response. It is therefore possible to activate multiple slip modes to improve the work hardening rate and ductility of the HT-900 sample. Dhekne et al. [197] investigated the micro-mechanical deformation behaviour of Ti-6Al-4V by LPBF with heat treatment (first heated at 1025 °C for 20 min and then heated at 880 °C for 1 h) via in situ tensile testing. The results indicate that the primary α phase accommodates lower strain than the transformed β phase and strain accumulation in primary α is mainly observed at the interface areas where the Al content is low.

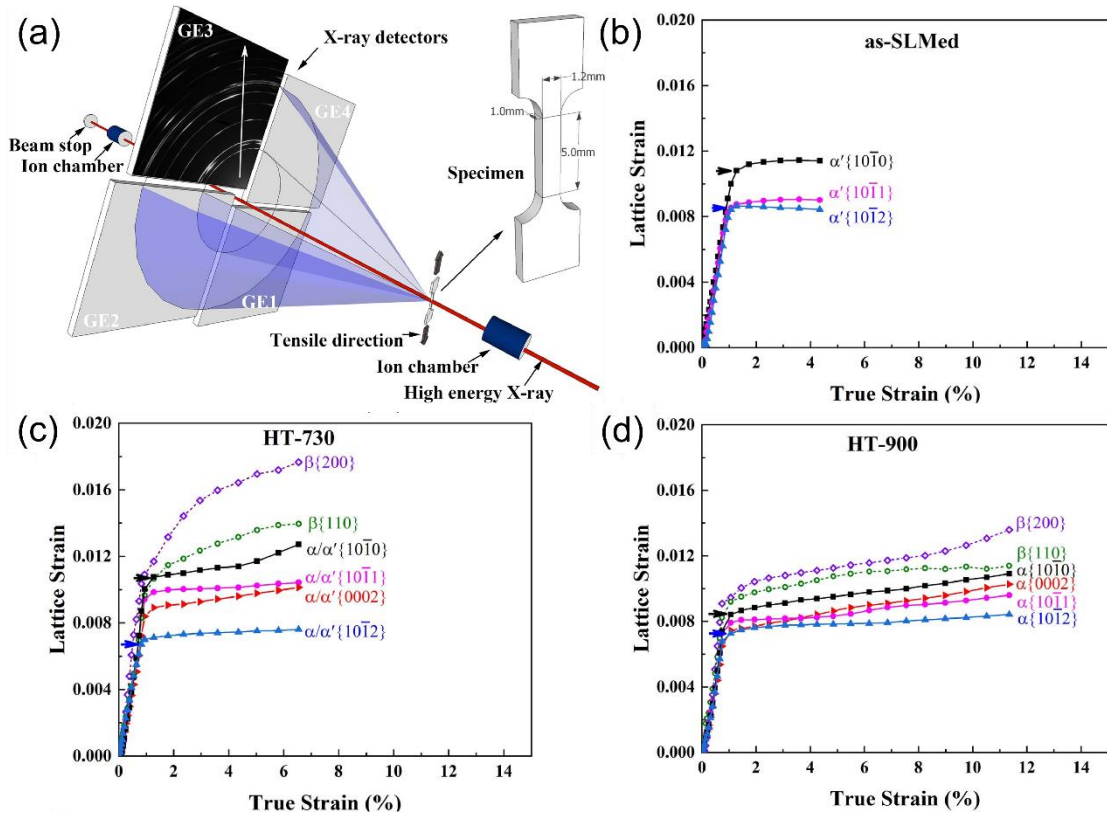


Fig. 2.21 (a) In situ HEXRD experimental setup, evolution of the lattice strains during deformation of (b) as-built Ti-6Al-4V, (c) HT-730, and (d) HT-900 [101].

For the ductility mechanism (i.e., deformation mechanism), besides dislocation slip, deformation twinning is also a crucial mechanism of plastic deformation in titanium and titanium alloys, especially for accommodating plastic strain along the $\langle c \rangle$ axis [38,198], which is also mentioned in section 2.2.5. There are massive research advances in deformation twinning studies thanks to the important role (such as TWIP) on mechanical properties by conventional manufacturing with heat treatment [111,199–201]. For example, Zhao et al. [111] achieved superior mechanical properties (especially at cryogenic temperature) of pure Ti with hierarchical nano-twinned structures by forging along the three principal axes in liquid nitrogen and then relaxation annealing. In addition, the twinning modes formation and confirmation, twinning variants (primary, secondary, tertiary), and their influence factors have been extensively analysed [135,199–203].

Although deformation twinning has been widely studied in Ti and Ti alloys by conventional manufacturing, the study of deformation twinning in titanium and titanium alloys by AM is limited. Bermingham et al. [155] reported the deformation twinning

with tension twinning $\{10\bar{1}2\}\langle 10\bar{1}\bar{1}\rangle$ of heat treated Ti-6Al-4V alloy by wire arc additive manufacturing (WAAM) after compression testing. Cheng et al. [204] observed the tension twinning $\{10\bar{1}2\}\langle 10\bar{1}\bar{1}\rangle$ of Ti-6.5Al-3.5Mo-1.5Zr-0.3Si (known as TC11) alloy by DED after dynamic compression deformation. Wang et al. [205] studied the effect of microstructure on the deformation twinning of Ti-6Al-4V alloy by EBM (with in situ heat treatment) after tensile testing. For LPBF, deformation twinning with tension twinning $\{10\bar{1}2\}\langle 10\bar{1}\bar{1}\rangle$ dominated was observed in CP Ti with low oxygen content after tensile testing by Chen et al. [206]. Barriobero-Vila et al. [139] achieved superior compression strength-ductility of in situ heat treated Ti-6Al-4V alloy with compression twinning $\{10\bar{1}1\}\langle 10\bar{1}2\rangle$ by LPBF after compression testing, confirmed by HEXRD and TEM. From the literature, the deformation twinning analysis by AM was minor compared to conventional manufacturing, in particular for twins' characteristics analysis, influencing factors on deformation twinning behaviour. The deformation twinning with TWIP study may be a critical solution for strength-ductility synergy of Ti-6Al-4V by LPBF.

2.5 Summary of research gaps

In summary, although many studies have been performed about the effects of powder feedstock and heat treatment on Ti-6Al-4V parts performance, there are still some unclear phenomena or issues. Based on the literature review, the critical research gaps can be summarised as follows.

2.5.1 PSD

Although it is clear for powder coarsening after reuse, the mechanism behind the PSD coarsening still needs to be clarified due to the lack of comprehensive investigation into the interactions between laser and powder during LPBF about particle size evolution. Therefore, it is essential to conduct experiments to understand the particle size evolution and PSD coarsening in LPBF, which may be crucial for reused powder usage and management. The role of fine and large particles in different PSD of powder is not fully understood with considerations of materials (different densities of powder would affect the flowability) and in-process powders. Systematic works are rare to understand the effect of different PSD powder feedstocks on parts properties, especially for building a link with different PSD powder feedstocks, in-process powders (such as spatter), and

parts performance. These gaps in PSD are critical for understanding the LPBF process and how PSD role is linked to parts performance.

2.5.2 Chemical composition

Chemical composition plays a vital role in the microstructure and mechanical performance of Ti-6Al-4V by LPBF. Poor ductility (less than 10%) is typically observed in as-built Ti-6Al-4V. Chemical composition tailoring to achieve good ductility (more than 10%) and maintain good enough strength is beneficial for as-built parts (for example, reducing the risk of build failure), but there have been few studies aimed at this target by composition tailoring. Most literature on composition modification of Ti-6Al-4V focuses on the refinement of prior- β grains and strengthening, but unfortunately, the ductility in the as-built state was typically less than 10%. Therefore, achieving and manipulating balanced strength (over 930 MPa for tensile strength) and ductility (over 10%) via chemical composition design are essential.

2.5.3 Heat treatment

Heat treatment is used to obtain desired microstructure and mechanical properties, especially for ductility improvement. Investigating the deformation behaviour of heat treated samples is crucial to understand the role of microstructure on ductility, which may provide good feedback or signal to optimise the microstructure and obtain better mechanical properties. However, research about the deformation behaviour of heat treated Ti-6Al-4V is rare for various heat treatment strategies. A few works reported Ti-6Al-4V dislocation slip behaviour in some heat treatment manners (mentioned in section 2.4.5). Dislocation slip and twinning mode are two main deformation mechanisms in Ti and Ti alloys due to limited dislocation slip systems in the HCP phase of Ti and Ti alloys. Therefore, twinning in Ti-6Al-4V may play a crucial role in deformation and ductility. However, the twinning behaviour study for heat treated Ti-6Al-4V by LPBF after deformation is not well understood. In this regard, it is essential to investigate the twinning behaviour of Ti-6Al-4V under different heat treatments with different microstructures. To achieve superior mechanical performance, further action may be required in twinning optimisation (especially for TWIP).

3 Experimental

3.1 Introduction

Fig. 3.1 illustrates the flowchart of the research used in this thesis. Powder materials, LPBF experiments, and materials characterisation will be introduced in detail. Fig. 3.2 shows the experimental methodology flowchart. Firstly, basic powder properties characterisation is presented, including PSD, morphology, chemical composition, and flowability. A LPBF machine was then used to fabricate samples intended for a variety of purposes. After sample fabrication, sample characterisation is also shown with a variety of characterisation methods. The purpose of this thesis is to assess the effects of powder feedstock and heat treatment on parts performance, as well as mechanisms related to them.

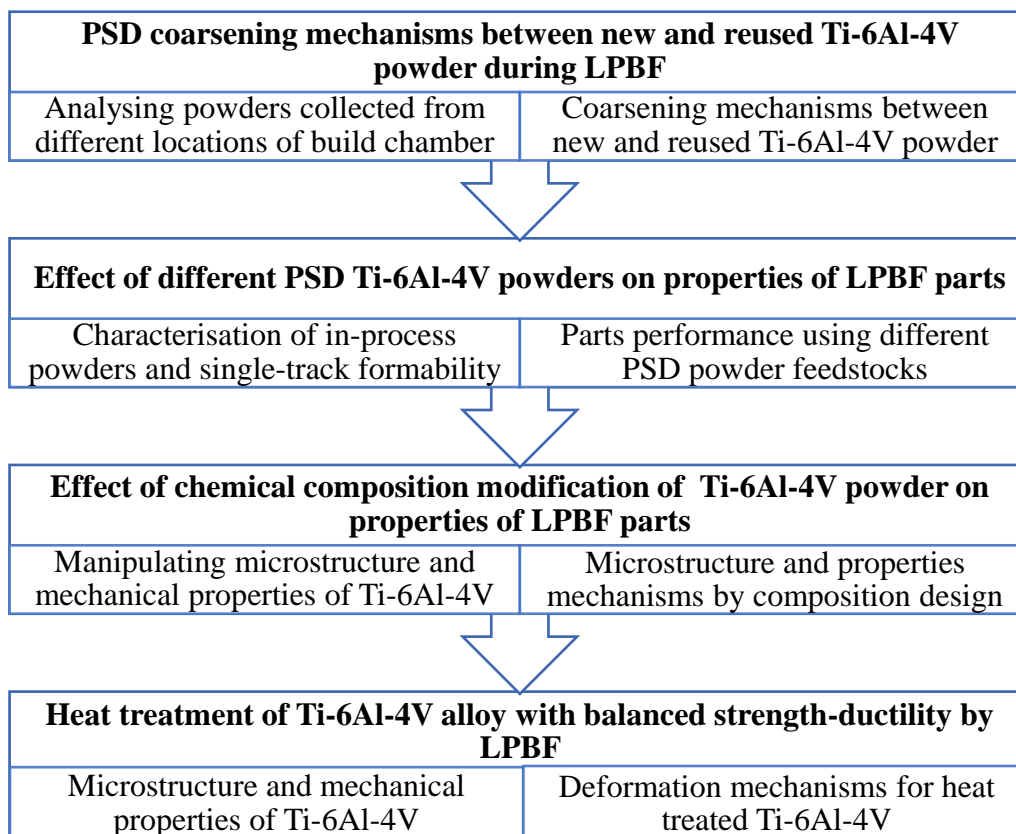


Fig. 3.1 Flowchart of the research including powder feedstock and heat treatment considerations.

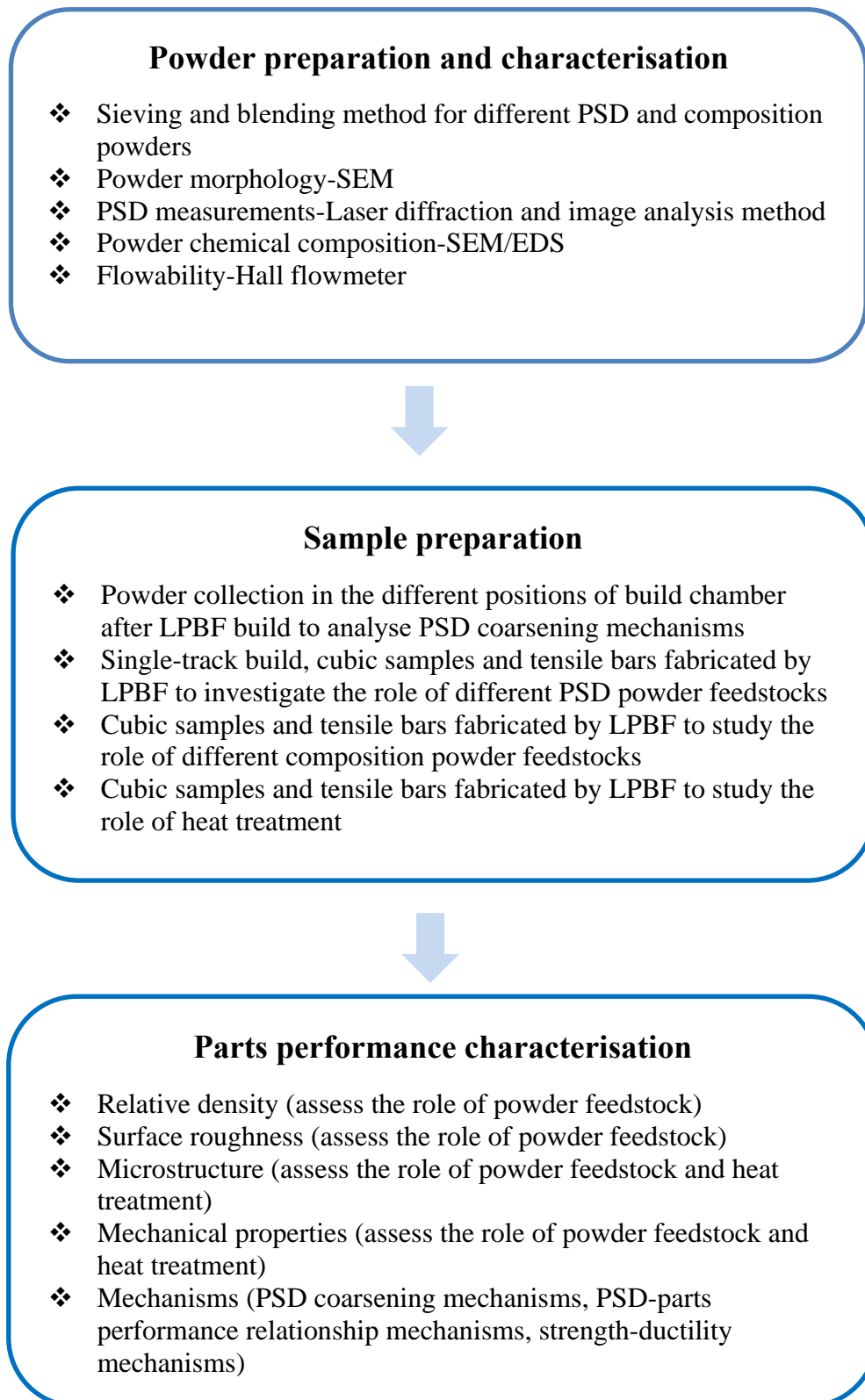


Fig. 3.2 Flowchart of experimental methodology.

3.2 Powder characterisation and preparation

In this thesis, powder feedstock is the main investigation factor for LPBF Ti-6Al-4V experiments. This section will introduce powder characterisation and preparation, including new and reused powders, powder feedstock for different PSDs, and powder feedstock for chemical composition modifications.

3.2.1 Powder characterisation

3.2.1.1 Morphology

SEM is a powerful tool to directly observe the morphology of powder feedstock. For particle shape observation of powder through SEM imaging, virgin and reused powder was dispersed in a carbon tape and directly observed by SEM. In general, good spherical particles can be observed for PA powder in SEM images. The main SEM equipment for powder morphology is a Hitachi TM3030 SEM (Hitachi Ltd., Japan) with a backscatter electron (BSE) mode. Also, the inner pores of particles after virgin Ti-6Al-4V powder cross-section polishing can be visualized by SEM (SEM JEOL 6490LV) with a secondary electron (SE) mode with a large area through low magnification, as shown in Fig. 3.3. Before grinding and polishing, the powder particles of Ti-6Al-4V were carefully mounted by firstly mixing ground resin (fine particles) and powder particles in the bottom of the mounting equipment and then adding normal resin. The mounted sample was carefully ground and polished to reveal the powder cross-section. Ti-6Al-4V powder used in this thesis has no obvious visible inner pores.

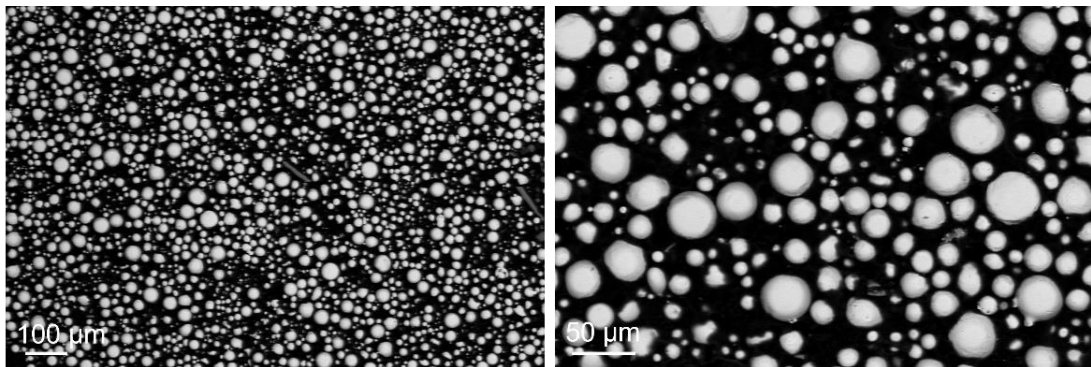


Fig. 3.3 SEM images of cross-sections of virgin Ti-6Al-4V powder feedstock.

3.2.1.2 PSD

There are several methods to measure PSD. Laser diffraction equipment Mastersizer

3000 was employed for PSD measurement using the dry method. It is a fast and repeatable method. Basic measurement conditions like air pressure (0.1-3 bar) and feed rate (20-30%) were also investigated (see Appendix section). However, the laser diffraction method acquires several grams for measurement, which is not suitable for a small amount of powder (less than 1 g). Thus, SEM image method is a good method for calculating PSD for a small amount of powder, such as a spatter collected with a low weight (less than 1 g) in a specific area of the build chamber. A Hitachi TM3030 SEM was used for image analysis of particle size and morphology of Ti-6Al-4V powders. For PSD measurement, powder was also dispersed in a carbon tape and images were directly captured by SEM, which is the same as morphology observation. The spherical projection (area projection) was captured by ImageJ to obtain areas (to convert into equivalent diameter) of particles for PSD measurement. Therefore, rather than viewing cross sections of powder with underestimation of the size, this direct observation can capture and measure the size better. For PSD measurement, images were captured in randomly selected areas at magnifications of 100X, 200X, and 300X as the suitable magnification is key to ensure the image of fine particles with a sufficient resolution and reduce the mis-identified particles during post-processing based on ISO 13322-1 [207]. Open-source software ImageJ was used for particle size analysis based on SEM images [208]. The ImageJ workflow for PSD measurement was shown in the Appendix section. Areas of particles were automatically obtained through the circularity selection setting in ImageJ to calculate the particle diameters. To improve the automated measurement accuracy, a calibration technique was proposed that manual measurement by measuring the diameter of each particle in an SEM image was applied to calibrate the suitable circularity selection by automated measurement. To determine which circularity selection (if spherical particles are mis-identified by ImageJ, the circularity of mis-identified particles will be decreased, circularity selection may help to remove mis-identified particles) is suitable, different levels of circularity were investigated including default circularity (0.0-1.0) and compared to PSD results from manual measurement.

3.2.1.3 Chemical composition

Energy Dispersive X-ray Spectrometry (EDS, accelerating voltage 15 kV, point analysis) was employed to characterise the powder chemical composition during LPBF (Hitachi TM3030). It is suitable for detecting powder oxidation levels. Point analysis of EDS is a common way of powder chemical composition characterisation.

3.2.1.4 Flowability

Hall flowmeter was used to assess flowability based on ASTM standard B213 [209]. The powder amount is 50 g and the funnel hole diameter is 2.5 mm. The flowability for 15-45 μm Ti-6Al-4V powder is around 33.3 s/50g, which suggests good flowability of Ti-6Al-4V powder feedstock.

3.2.2 Powder preparation

First, sieving is an effective method for removing reused powders with over mesh sizes (typically 63 μm mesh for reused powders) and dispersing powder by Retsch AS 200 equipment. For the effect of different PSD powders on the build quality of Ti-6Al-4V alloy by LPBF, standard 15-45 μm powder was sieved by mesh size 38 μm to obtain nominal 15-38 μm and nominal 38-45 μm powder. Apart from sieving for powder preparation, the ultrasonic mixing method (Resodyn acoustic mixers, LabRAM I) is a fast way to mix different powder feedstocks. Powders with different additions were mixed with the acceleration and the mixing time set to 50g (g is gravitational acceleration) for the first 15 s and 20g for the next 75 s and a total of 1.5 mins, respectively [210]. Two repeated times were carried out. The spherical CP Ti (Grade 1, 38-63 μm) and plasma atomised Ti-6Al-4V (Grade 23, 15-45 μm) and were mixed in a size range of 15-63 μm . The nominal Ti-4.5Al-3V (called PT25, $D_{50}=37.7 \mu\text{m}$) was prepared by adding 25 weight percent and 50 weight percent to Ti-6Al-4V to obtain nominal Ti-3Al-2V (half of Ti-6Al-4V, called PT50, $D_{50}=39.8 \mu\text{m}$) powder feedstock. The Ti-6Al-4V with no addition of CP Ti was called PT0 for easy comparison with PT25 and PT50. A SEM (Hitachi TM3030) was used to observe powder feedstocks PT0, CP Ti, PT25, and PT50, as shown in [Fig. 3.4](#).

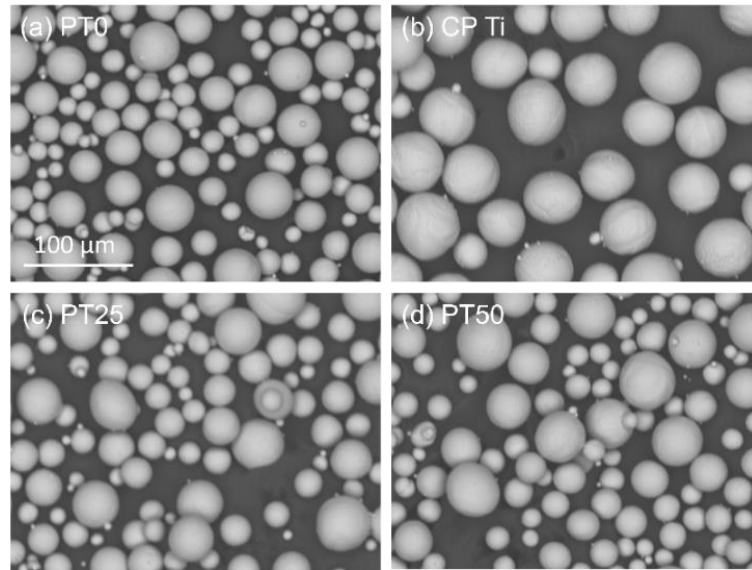


Fig. 3.4 Morphology of powder feedstock observed by SEM (a) PT0, (b) CP Ti, (c) PT25, and (d) PT50.

3.3 Sample fabrication by LPBF

A Renishaw LPBF AM400 machine was used, equipped with an yttrium fibre laser at a wavelength $\lambda = 1070$ nm with a focus diameter around $75 \mu\text{m}$, maximum power of 400 W. The whole build volume is around $250 \times 250 \times 300$ mm, and an inserted reduced build volume (RBV) of around $78 \times 78 \times 55$ mm was also used. This RBV can significantly reduce the amount of powder for LPBF experiments. Due to the missing function of controllable dose volume for powder spreading in the RBV, a powder compacting tool was employed to facilitate the powder spreading efficiency and ensure the built parts with powder covered before laser melting. During machine preparation for printing parts, the powder compacting tool was used to level and compact the powder feedstock in the small powder supplier chamber to improve the dose during powder spreading. RBV is suitable for different PSD and different chemical composition powders' experiments. In the Renishaw AM system, the modulated laser pulse was applied with point distance and exposure time rather than continuously scanning. This means that there is a time delay between each point during the laser jump. The point distance (μm) was defined by the centres of two melt pools (see Fig. 3.5). Exposure time (μs) was the length of time the laser would be on for each point. The scanning speed is roughly determined by point distance and exposure time. More precisely, the delay time between each laser point ($\sim 10 \mu\text{s}$) should also be considered. The main processing parameters for LPBF

single tracks, cubic samples and tensile bars were laser power, point distance, exposure time, hatch distance, and layer thickness.

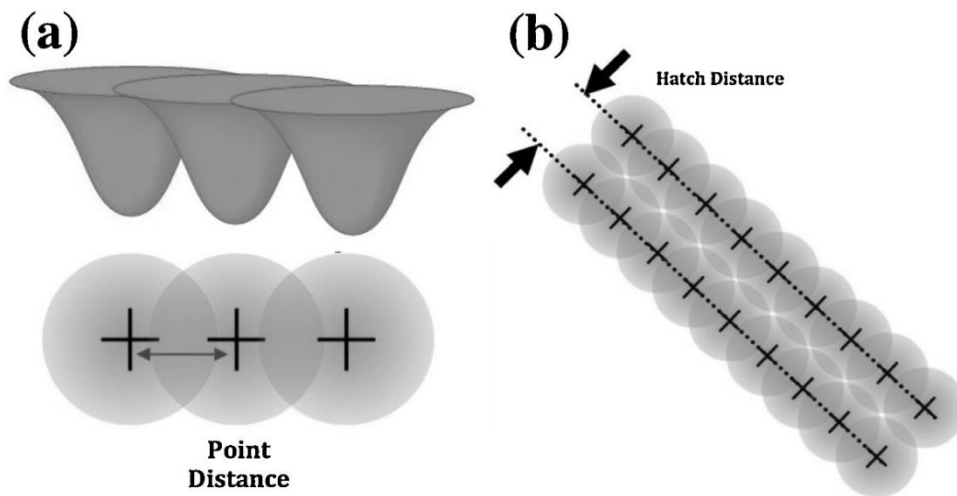


Fig. 3.5 Schematic diagram of modulated laser pulse used in this thesis (a) point distance between two melt pools (b) hatch distance [27].

3.3.1 Sample fabrication for PSD coarsening mechanisms analysis of reused powder

To represent industrial type scenarios, powders were sampled for PSD analysis in their virgin un-used state and after five and twelve LPBF build cycles. To investigate the effect of powder reuse at the end of each build, powders from the build envelope and overflow were collected and sieved using a 63 μm mesh. This was done to segregate reused powder with size over 63 μm . To understand the mechanisms associated with PSD changes, powders were collected and analysed in different locations of the build chamber. This enables the sampling of powders in the build envelope (unaffected powder from powder bed (P-PB), powder near borders of built parts, spatter in the powder bed) and outside of the build envelope (powder from overflow, near gas flow inlet (particles_gas_inlet, P-GI spatter), near gas flow outlet (particles_gas_outlet, P-GO spatter)), all of which are key locations in which particle size change during the LPBF process is expected, as shown in Fig. 3.6(a, c). Powder near the borders of parts was gathered by specially designed structures (called the small holder and large holder with capture volumes of 2x10x18 mm^3 and 20x20x18 mm^3 respectively), as illustrated in Fig. 3.6(b).

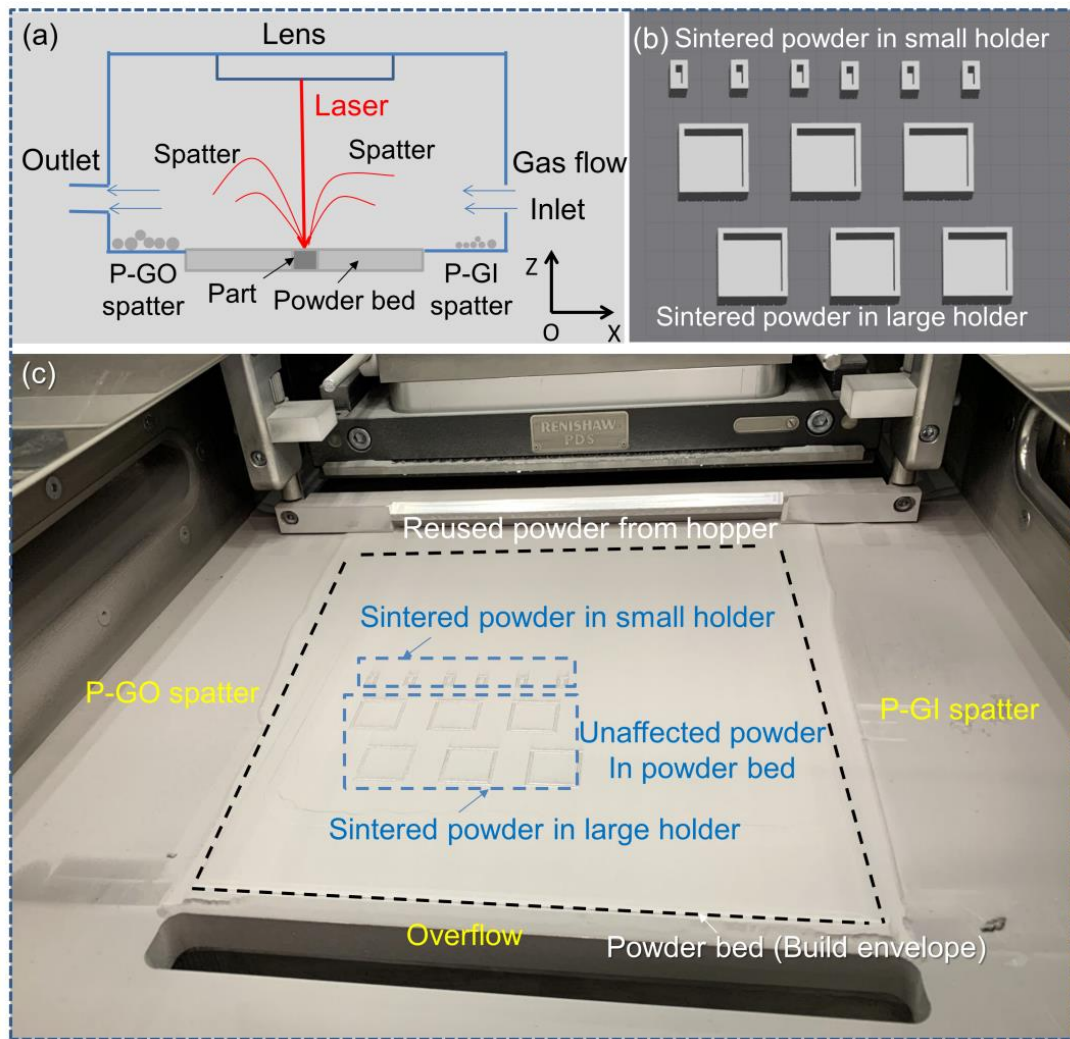


Fig. 3.6 (a) Schematic diagram of powder change under the laser and material interaction during LPBF, (b) designed parts (small holder and large holder) with different geometry for powder analysis around borders of parts, (c) build chamber after completing a build.

The small holder structure with size $2 \times 10 \times 18 \text{ mm}^3$ could collect sufficient sintered powder around laser scanning borders for easy SEM observation due to the thin width (2 mm) of the designed structure with more border area fraction. Powder with sufficient weight (more than 10 g) collected by the large holder structure with size $20 \times 20 \times 18 \text{ mm}^3$ was employed for PSD measurement by laser diffraction to analyse the role of sintered powder. Meanwhile, powder attached to the outer borders of the small holder was collected by carbon tape and observed by SEM. This was to show the role of laser scanning borders on sintered powder and its effect on powder coarsening. The P-GI spatter with a small amount was collected by a carbon tape for SEM observation. The

P-GO spatter was collected by a brush and a small spoon. The powder from the overflow was collected by a small spoon. The powder with spatter in the powder bed was carefully collected around the as-built parts by a small spoon. The most powder in the large hold was first collected by a small spoon and then the rest of the powder could be collected after removing the large holder from the build substrate. The powder in the small holder was carefully collected after removing the small holder from the build substrate. The unaffected powder (away from the as-built parts area) in the powder bed was collected by a small spoon. The spatter travelling over the “unaffected” zone (close to the gas inlet area) may be minimal (less than 0.1g) as most of the spatter was carried into the gas outlet area and the collected powder in the “unaffected” zone was far away from the as-built parts area.

3.3.2 Sample fabrication for the effect of different PSD powder feedstocks on build quality

Single-track experiments with different PSD powder feedstocks were performed on a Renishaw AM400 LPBF machine, equipped with RBV. Each powder runs one single-track build. In each build, single tracks were built on the cuboid part that had been built by LPBF, as shown in [Fig. 3.7](#). The part geometry of each single-track was designed with 0.15x5x0.035 mm to ensure the laser scanning with one single track (i.e., block path strategy in build file preparation software), and only one layer was built. The manufacturer recommends the following default processing parameters for Ti-6Al-4V powder: laser power 200 W, point distance 75 μm , exposure time 50 μs , hatch distance 0.065 mm. Single tracks were processed with laser power (from 100 to 200 W, interval 25 W) and exposure time (from 40 to 90 μs , interval 10 μs). The layer thickness for all builds was 30 μm . After each build, spatter located in the gas outlet area, powder away from the printing area in the powder bed, and powder from overflow were also collected for further analysis (see [Fig. 3.7](#)). After single-track experiments, cubic samples (10x10x5 mm³) and horizontal tensile bars ($\Phi 9$ x 60 mm) by using different PSD powder feedstocks were fabricated using the default processing parameters. These default processing parameters were also employed for composition modification and heat treatment work. To reduce the residual stress of as-built Ti-6Al-4V, a stripe scanning strategy with a stripe width of 5 mm was employed. This is because the shorter scan vectors for the stripe strategy with lower thermal gradients reduce the thermal stresses

compared to the meander strategy with long scan vectors [211,212].

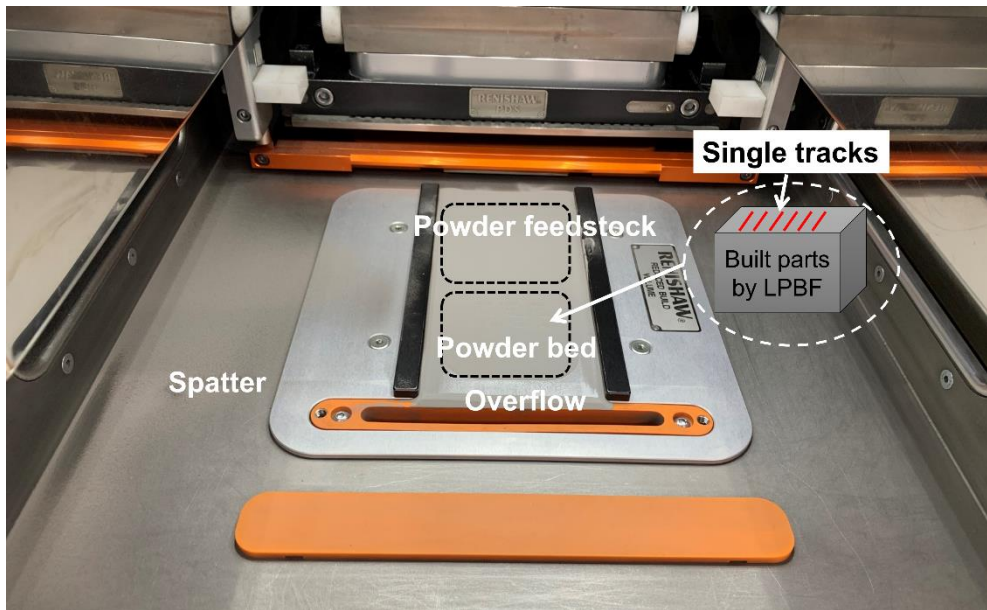


Fig. 3.7 Single-track experiments and in-process powders including spatter, powder from powder bed and overflow in the build chamber.

3.3.3 Sample fabrication for the chemical composition modification of Ti-6Al-4V by CP Ti addition

To fabricate horizontal tensile bars ($\Phi 9 \times 60$ mm) and cubic samples ($10 \times 10 \times 5$ mm³) for each powder feedstock (PT0, PT25, PT50), a Renishaw AM400 LPBF inserted with RBV was used. The same processing parameters were used for all samples. All samples were scanned using a 67° rotation between consecutive layers with a stripe scanning strategy. The employed default processing parameters are recommended by LPBF manufacturer and confirm the good relative density for Ti-6Al-4V by LPBF in Chapter 4.

3.3.4 Sample fabrication conditions for heat treatment experiments

As-built Ti-6Al-4V alloy samples were heat treated in a tube furnace with Ar protection to compare the microstructure and mechanical properties mechanisms of composition modification and heat treatment of Ti-6Al-4V (also expected balanced strength-ductility). Two heat treatment temperatures: stress relief and high temperature annealing were used. For stress relief heat treatment, the temperature was raised from room temperature to 730 °C at 10 °C/min, and then was kept 2 h at 730 °C, then, was cooled

at 7 °C/min in a furnace (called HT730). For high temperature annealing heat treatment, the temperature was raised from room temperature to 900 °C at 10 °C/min, and the temperature was kept at 900 °C for two hours, and then the temperature was cooled to room temperature at 7 °C/min in a furnace (called HT900).

3.4 Sample characterisation

3.4.1 Optical microscopy

Optical microscopy (OM, Nikon ECLIPSE LV100ND) was employed for porosity observation of polishing samples and microstructure observation of etched samples. The porosity (i.e., relative density) of polishing samples captured by OM images was further analysed using open-source software ImageJ, which uses a threshold approach ('MaxEntropy' method) to identify the areas with pores [213,214]. The locations of imaging in polishing samples were randomly selected. The typical prior- β grain boundaries and inside martensite characteristics of Ti-6Al-4V and composition modified Ti alloys by LPBF can be observed by OM.

3.4.2 Alicona G4

The surface roughness of samples of new and reused powder was measured by surface texture equipment Alicona G4. Also, the Alicona G4 was employed to measure the surface roughness of Ti-6Al-4V parts from different PSD powder feedstocks. The vertical resolution and lateral resolution used in the Alicona G4 were 0.5 μm and 4.0 μm , respectively. Although the lateral resolution of 4.0 μm may not be very high with consideration of powder size (15-45 μm), the particles located on top surface and side surface are generally coarser than the powder size due to the attached spatter and sintered powder, evidenced by Chapter 4 and 5. The choice of lateral resolution should consider the scanning area (at least 5x10 mm to cover more particles on the surface of the parts). Newton et al. studied [215] that the differences in area surface roughness (S_a) with lateral resolution 2.0 μm and 4.0 μm are $\sim 0.1 \mu\text{m}$ and $\sim 0.35 \mu\text{m}$ for the top surface and side surface of Ti-6Al-4V by LPBF respectively, which suggests the acceptable of using lateral resolution 4.0 μm for surface roughness measurement and comparison. S_a of scanned topography by Alicona G4 was analysed by Mountainmap software. The surface topography of single tracks by different PSD powder feedstocks can also be assessed by Alicona G4.

3.4.3 X-ray diffraction (XRD)

XRD is a useful technique for identifying polycrystalline materials' crystal structure. The crystal plane spacing d can be determined based on Bragg law (Bragg equation, $n\lambda=2d\sin\theta$). Hence, the phase can be identified through a diffraction pattern with a range of 2θ to obtain the crystal plane spacing d . XRD was typically employed for phase identification. In this thesis, HCP and BCC phase of Ti alloys by LPBF were characterised by XRD (Bruker D8 ADVANCE). In the XRD analysis of polished samples, Cu $K\alpha$ radiation was used with a 2-theta angle range of 30 to 90° and a 0.02° step size. It is also possible to estimate the HCP structure's lattice parameters through XRD (c , a , and c/a ratio). Positions of the two-theta-angle XRD peak were determined using a MATLAB script developed in-house based on the centroid method [216]. The c/a ratio and lattice parameters were estimated based on peak positions in the HCP phase of titanium.

3.4.4 Scanning electron microscope (SEM)

SEM usually enables imaging with high resolution and high depth of field compared to OM. SEM was a powerful tool for surface morphology, microstructure, and elemental distribution differences observation of Ti alloys by LPBF. SE mode and BSE mode are typically employed for different purposes. SE mode was applied for surface morphology and microstructure observation as a secondary electron with low energy was emitted from very near the surface and secondary electron imaging is heavily topography related. BSE mode was suitable for the sample with typical elemental distribution difference because backscatter electrons are caused by the elastic reflection of incident electrons with atoms. Therefore, BSE imaging presents distinct contrasts based on the various atomic numbers. Besides SE and BSE modes used in SEM, EDS can be employed for elemental composition analysis based on the different emissions of Characteristic X-rays by different elements during the interactions between the incident electron beam and the sample surface. The surface morphology of samples on the top surface and side surface by different PSD powder feedstocks was observed by SEM 6490LV. As a fine martensite structure in as-built Ti alloys, high-resolution FEI-SEM 7100F was used for microstructure observation. Meanwhile, the elemental distribution of Ti alloys produced by mixing CP Ti with Ti-6Al-4V alloy and heat treatment of Ti-6Al-4V was determined by EDS incorporated in FEI-SEM 7100F with Aztec software. A SEM (6490LV) with

SE mode was also used to study the fracture mode of tensile bars.

3.4.5 Electron backscatter diffraction (EBSD)

The EBSD technique involves interacting the electron beam and the crystal grains at the surface of a well-polished crystalline material, as shown in Fig. 3.8. EBSD patterns are formed when incident electrons from the beam collide elastically and backscatter from the atomic planes of the crystal grains that follow Bragg's law. A phosphor screen is used to record the EBSD patterns (also known as Kikuchi bands). Kikuchi bands are usually interpreted by a mathematical algorithm known as the Hough transform. Kikuchi bands can be detected in the EBSD pattern using this Hough transform. Then, crystal structure and crystal orientation information can be obtained from the measured bands. EBSD is a crucial technique for crystallographic characterisation.

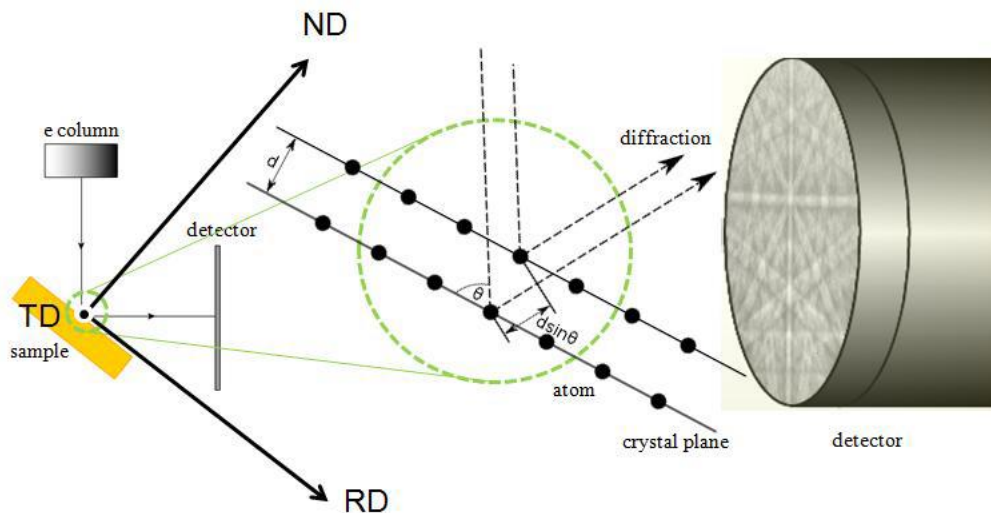


Fig. 3.8 Schematic illustration of the EBSD process and basic principle [94].

In this thesis, a high-resolution FEI-SEM 7100F inserted with Oxford Instruments Aztec HKL Advanced EBSD System (with NordlysMax3) was used for EBSD characterisation. The samples for EBSD characterisation were polished with colloidal silica to get a flat surface. The samples were tilted 70° to obtain a high signal for the EBSD pattern. Due to the fine martensite of as-built Ti-6Al-4V by LPBF, a small step size of $0.25 \mu\text{m}$ was set for the EBSD maps. The selected phases for EBSD analysis were the HCP-Ti phase and the BCC-Ti phase. The collected EBSD data was analysed by AZtecCrystal software. The main information obtained from EBSD was inverse pole figure (IPF) maps, misorientation maps, grain boundary (including low angle grain

boundary, LAGB, 2-10°, and high angle grain boundary, HAGB, >10°) maps, Kernel average misorientation (KAM) maps, band contrast (BC) maps, special grain boundary (identify twins in HCP phase) maps, phase maps, pole figures (PF), All Euler maps. Apart from the cubic samples for composition-related and heat treatment work by EBSD, the fractured tensile bars were also analysed by EBSD to confirm the deformation mechanisms with dislocation slip and twinning.

3.4.6 Microhardness

Microhardness is a crucial mechanical property. To collect microhardness data, a digital microhardness tester (Wilson VH3100) was used to make at least 30 indentations per sample using 500 grams of force and a dwell time of 10 seconds.

3.4.7 Tensile testing

In accordance with ASTM E8/8M-16a [217], tensile bars relating to PSD, chemical composition, and heat treatment are mechanically machined into a dog-bone shape with a gauge diameter of 4 mm and a gauge length of 20 mm. Tensile tests were performed at room temperature using an Instron 5969 at a displacement rate of 0.14 mm/min. Using a video gauge with a high measurement resolution, strain (elongation) was tracked and recorded.

4 PSD coarsening mechanisms of reused Ti-6Al-4V powder by LPBF

4.1 Introduction

Although there are some reports about the study of PSD changes after powder reusing and its effects on parts performance, there is not much systematic work to demonstrate the PSD evolution during LPBF to explain the PSD coarsening. This is discussed in more detail in the literature review chapter. To better understand the PSD evolution and explain the PSD coarsening mechanisms, the characteristics of particle size of various powders collected in the different positions of the build chamber after finishing one build were carried out and the mechanisms of particle size evolution were assessed in this chapter. To investigate the PSD coarsening mechanisms, PSD measurement techniques are critically important. The employment of multiple PSD measurements should meet different sample conditions. Common PSD measurements by laser diffraction and SEM image analysis were used for understanding PSD coarsening mechanisms in LPBF. In this chapter, a high-cost pre-alloyed Ti-6Al-4V powder with a 15-45 μm size range was used as a model powder, given the wide use of this material type and the powder size range typical of industrial applications in LPBF. The effect of particle size evolution on as-built parts performance (including relative density and surface roughness) was also evaluated to further confirm the importance of understanding the mechanisms of particle size evolution.

4.2 Experimental

Plasma atomised pre-alloyed Ti-6Al-4V (Grade 23, ELI) powder with a nominal particle size range of 15-45 μm was used in this chapter as a virgin powder feedstock. To study the particle size evolution, powders were collected for PSD analysis in their virgin state and after five (5 times means that reused powder experienced 5 builds and recycled 5 times) and twelve LPBF build cycles. Powders were collected and analysed in different locations of the build chamber to explore the mechanisms associated with changes in PSD, including powders in the build envelope (P-PB, powder near borders of built parts, spatter in powder bed) and outside of the build envelope (powder from overflow, near gas flow inlet (P-GI spatter), near gas flow outlet (P-GO spatter)). [Fig. 3.6](#) in Chapter 3

presents the various powders in the build chamber. Virgin, reused powders, and various powders were measured by laser diffraction and SEM image analysis. In addition, EDS was used to characterise the level of oxidation of powder during LPBF to understand spatter evolution. The relative density and surface roughness of Build 1 (by virgin powder) and Build 12 (by 12 times reused powder) were measured and compared by optical microscopy and surface texture equipment Alicona G4, respectively. Each sample takes at least two images to assess the relative density.

4.3 Results

4.3.1 Effect of powder reuse on PSD changes

PSD measurement of virgin powder and powder re-used 5 and 12 times was measured by laser diffraction. PSD curves are shown in Fig. 4.1. D10, D50, and D90 measurements from these laser diffraction results are shown in Table 4.1. From the PSD results in Fig. 4.1 and Table 4.1, considering standard deviation (at least measure three powder samples), there is a clear increase in all powder size metrics with re-use. D10, D50, and D90 increase by over 2 μm after 12 times re-use.

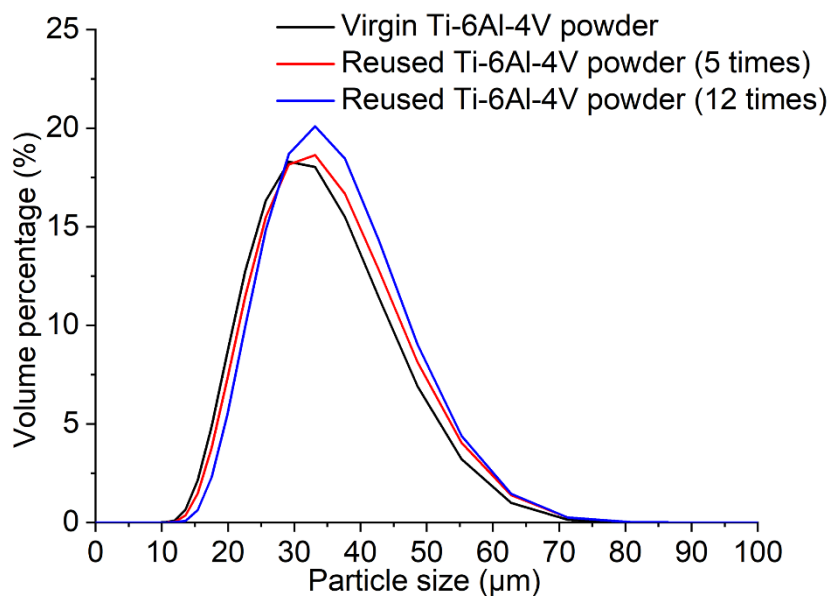


Fig. 4.1 PSD curves of virgin and reused powders using laser diffraction method.

Table 4.1 PSD results of virgin and 5x and 12x reused powder measured by laser diffraction.

	D10 (μm)	D50 (μm)	D90 (μm)
Virgin powder	20.2 ± 0.43	30.4 ± 0.35	45.1 ± 0.19
5x reused powder	21.2 ± 0.28	31.8 ± 0.29	46.9 ± 0.34
12x reused powder	22.4 ± 0.27	32.7 ± 0.09	47.2 ± 0.29

To elucidate the reasoning behind the increase in powder size metrics after re-use, SEM images of virgin and 12x reused powder are shown in Fig. 4.2. Anecdotally, the SEM image in Fig. 4.2(b) appears to show powder coarsening. In particular, the absence of fine particles is apparent. The reduction in the number of fine particles would simply explain the increase in particle size for reused powder.

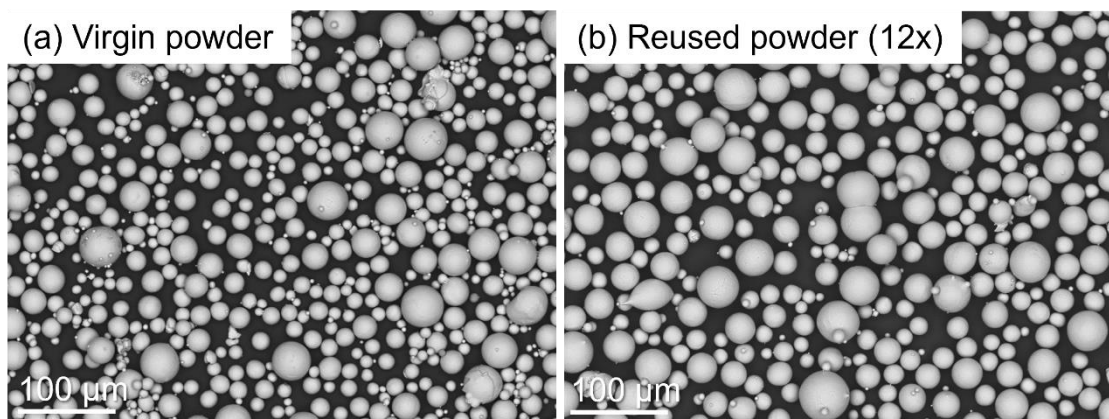


Fig. 4.2 SEM images of (a) virgin powder and (b) reused powder (12x).

In addition, PSD measurement of virgin and reused powder was also carried out through SEM image analysis (four samples used). The results show an optimised image processing method from SEM images, using 0.5-1.0 circularity selection, in ImageJ processing of 300X SEM images, with 2500 particles (see Appendix section). It is worth noting that 12x reused powder also has a coarsening characteristic compared to virgin powder, as shown in Table 4.2.

Table 4.2 PSD results of virgin and reused powder measured by SEM image analysis.

	D10 (μm)	D50 (μm)	D90 (μm)
Virgin powder	13.8	24.3	39.2
12x reused powder	18.4	30.4	41.8

4.3.2 Characteristics of particle size evolution by classification of the build chamber

To determine the origins of powder coarsening, powders in key locations of the build chamber classified outside of the build envelope and in the build envelope were collected. From the outside of the build envelope, powders from the overflow, P-GI spatter, and P-GO spatter were collected and studied after finishing one build. The build chamber after finishing a build can be seen in Fig. 3.6 in Chapter 3. Firstly, overflow powder was analysed. The PSD results of powder from the overflow compared to virgin and P-PB are shown in Fig. 4.3 and Table 4.3. P-PB particle size is generally smaller than virgin powder. It can be seen that the overflow powder shows the highest PSD metrics compared to virgin powder and P-PB.

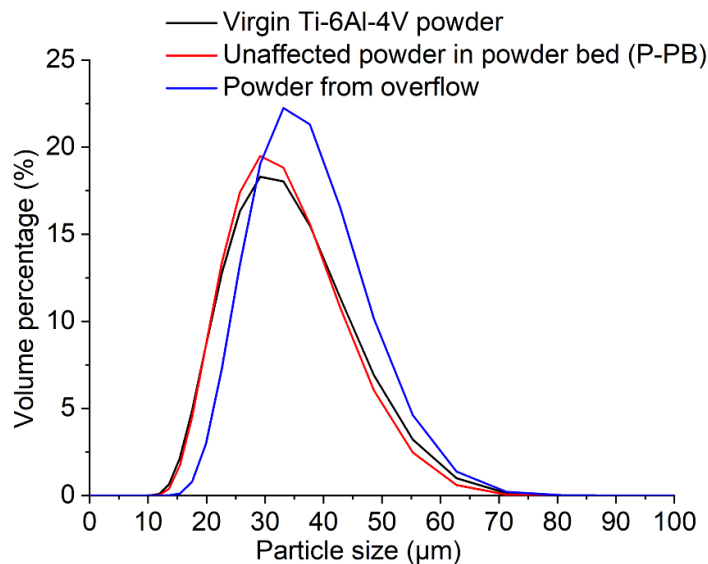


Fig. 4.3 PSD curves of virgin powder, P-PB, and powder from overflow using laser diffraction.

Table 4.3 PSD metrics for virgin powder and P-PB, as well as a powder from overflow, were measured by laser diffraction.

	D10 (μm)	D50 (μm)	D90 (μm)
Virgin powder	20.2 ± 0.43	30.4 ± 0.35	45.1 ± 0.19
P-PB	20.3 ± 0.12	30.0 ± 0.05	43.9 ± 0.09
Powder from overflow	24.4 ± 0.17	34.2 ± 0.22	47.9 ± 0.31

The particle size, by all metrics, is significantly higher for the P-GO spatter than virgin powder and P-PB (see Fig. 4.4), which is consistent with the PSD characteristics of the P-GO spatter in literature [91]. The D10 value increases from 20.2 μm to 26.6 μm compared to virgin powder. The D50 and D90 values increase from 30.4 μm to 45.2 μm and from 45.1 μm to 79.5 μm respectively, as shown in Table 4.4. The PSD curve in Fig. 4.4 for P-GO spatter is skewed heavily to the right, compared to both virgin powder and P-PB. This indicates there are a large number of coarse particles.

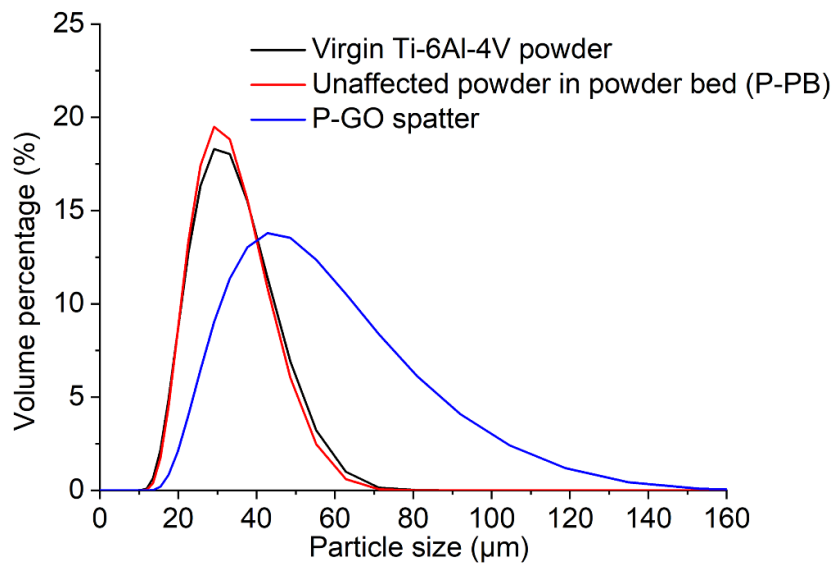


Fig. 4.4 PSD results of virgin powder, P-PB, and P-GO spatter using laser diffraction method.

Table 4.4 PSD metrics for virgin powder, P-PB, and P-GO spatter, measured by laser diffraction.

	D10 (μm)	D50 (μm)	D90 (μm)
Virgin powder	20.2 ± 0.43	30.4 ± 0.35	45.1 ± 0.19
P-PB	20.3 ± 0.12	30.0 ± 0.05	43.9 ± 0.09
P-GO spatter	26.6 ± 0.17	45.2 ± 0.29	79.5 ± 0.57

To interrogate the fine particles of the P-GI spatter, SEM analysis was conducted using optimised parameters (300X at 0.5-1.0 circularity selection), given the total volume was not sufficient for laser diffraction measurement. SEM analysis confirms the substantially reduced particle size metrics compared to the virgin powder, as shown in [Table 4.5](#). The D10 is reduced by approximately half, explained by a significant increase in the number of small particles in this sample.

Table 4.5 PSD of P-GI spatter by SEM images method with 300X, circularity 0.5-1.0, and comparison with virgin powder and reused powder.

	D10 (μm)	D50 (μm)	D90 (μm)
P-GI spatter	7.7	16.6	26.3
Virgin powder	13.8	24.3	39.2
Reused powder (12x)	18.4	30.4	41.8

To further investigate this significant difference in particle size between the P-GO spatter and the P-GI spatter, SEM analysis was conducted. Images and point EDS analysis are shown in [Fig. 4.5](#). The low magnification image in [Fig. 4.5\(a\)](#) shows the much bigger size of the P-GO spatter particles. In particular, there are much fewer loose small particles in the P-GO spatter. Few large particles above 25 μm in diameter are presented in the P-GI spatter ([Fig. 4.5\(b\)](#)). A large particle with apparent contamination was analysed by point EDS with the results in [Fig. 4.5\(e\)](#). Oxygen is detected, which is not observed in other particles.

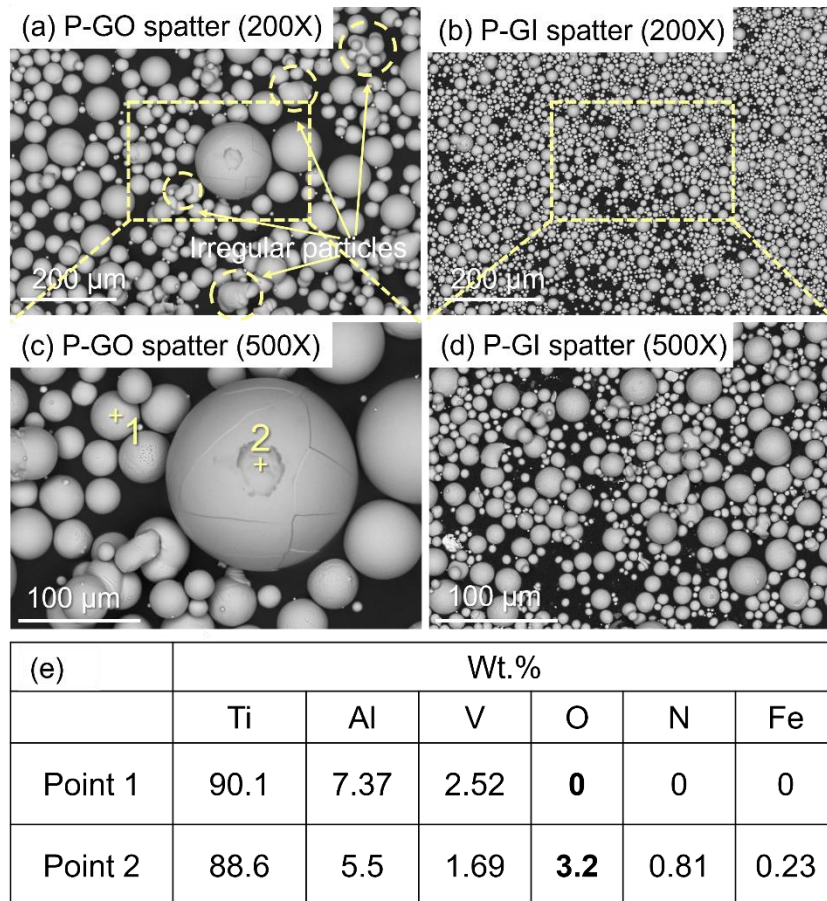


Fig. 4.5 SEM images of P-GO (a, c) and P-GI (b, d) spatter at two different magnifications, EDS point analysis of a particle showing oxygen presence in (e).

Given this clear correlation between chamber position and particle size, the effect of position relative to the build envelope was also of interest. Fig. 4.6 shows images of spatter on as-built cubic parts by default processing parameters and spatter in the powder bed. Fig. 4.6(a) shows that particles on as-built parts are still mostly spherical in morphology. It can be noted that modified powder has been found in the powder bed. This is typical of “spatter” which has been oxidised, given its dark appearance in BSE imaging (see Fig. 4.6(b)). EDS analysis also confirms the presence of oxygen, at higher than 50% on the surface of such particles (see Fig. 4.6(d, e)). In addition, such particles were particularly prone to sintering as shown in Fig. 4.6(b). Within the small holder, some agglomerates, comprising multiple particles sintered together, can be observed in Fig. 4.7. This obvious sintered powder in the small holder is similar to the sintered powder attached to the outer borders of the small holder, which indicates the effect of laser scanning borders on sintered powder formation.

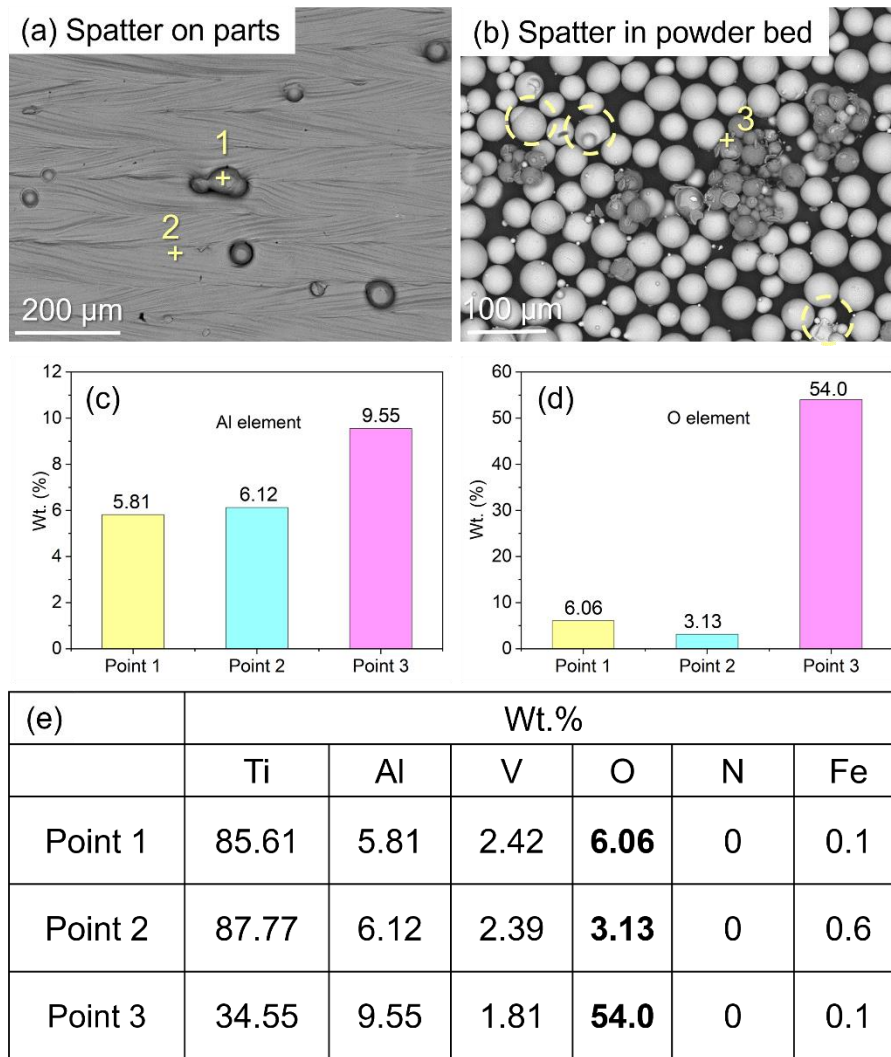


Fig. 4.6 SEM images and EDS analysis of powder morphology and composition change in the build envelope, (a) spatter on parts, (b) spatter in the powder bed, (c) Al elemental content in point 1, point 2, and point 3, (d) O elemental content in point 1, point 2, and point 3, (e) EDS results in different positions.

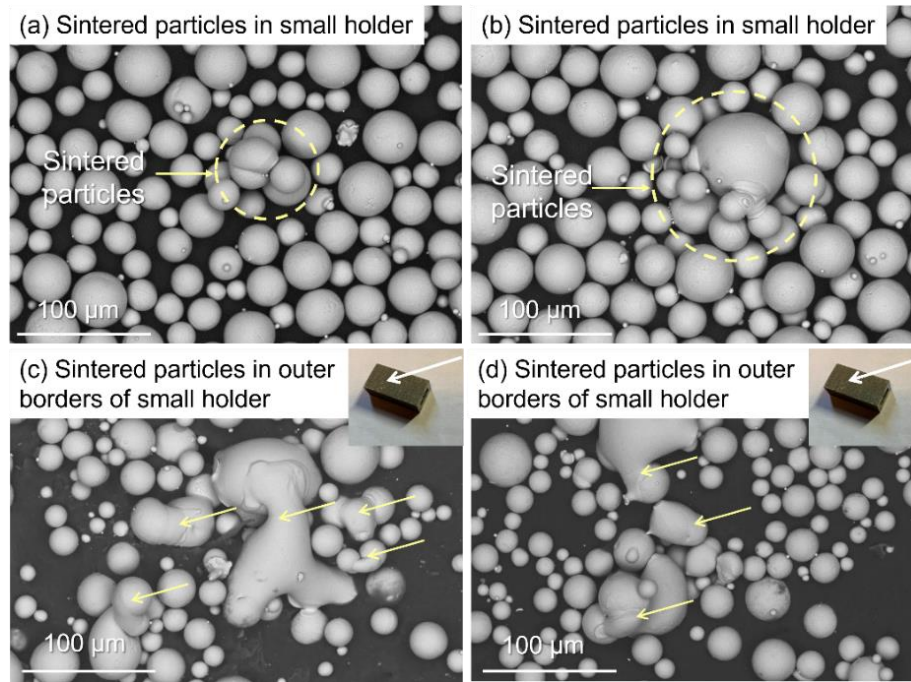


Fig. 4.7 (a) and (b) Sintered powder in small holder, (c) and (d) sintered powder in outer borders of the small holder.

4.3.3 Effect of PSD coarsening on the performance of as-fabricated parts

First, the relative density of Ti-6Al-4V alloy in Build 1 (by virgin powder) and Build 12 (by 12 times reused powder) was characterised after polishing, as shown in Fig. 4.8(a-d). The results suggest that as-built samples by virgin powder (porosity $\sim 0.02\%$) and 12 times reused powder (porosity $\sim 0.04\%$) present good relative density with few pores. However, a larger size pore by 12 times reused powder can be observed compared to that of virgin powder, which agrees with the literature that large size particles may cause a LoF [218].

Fig. 4.8(e, f) show the surface roughness of the Ti-6Al-4V sample on the top surface and side surface in Build 1 and Build 12. The surface roughness of the sample by 12x reused powder ($S_a=19.3\pm 0.33 \mu\text{m}$ on the side surface, $6.67\pm 0.38 \mu\text{m}$ on the top surface) is higher than the surface roughness of the sample in Build 1 ($S_a=16.5\pm 0.50 \mu\text{m}$ on the side surface, $5.86\pm 0.38 \mu\text{m}$ on the top surface). The 3D topography also confirms the better surface quality of as-fabricated parts from virgin powder (see Fig. 4.8(g, h)). This change in surface roughness may also result from PSD coarsening [219].

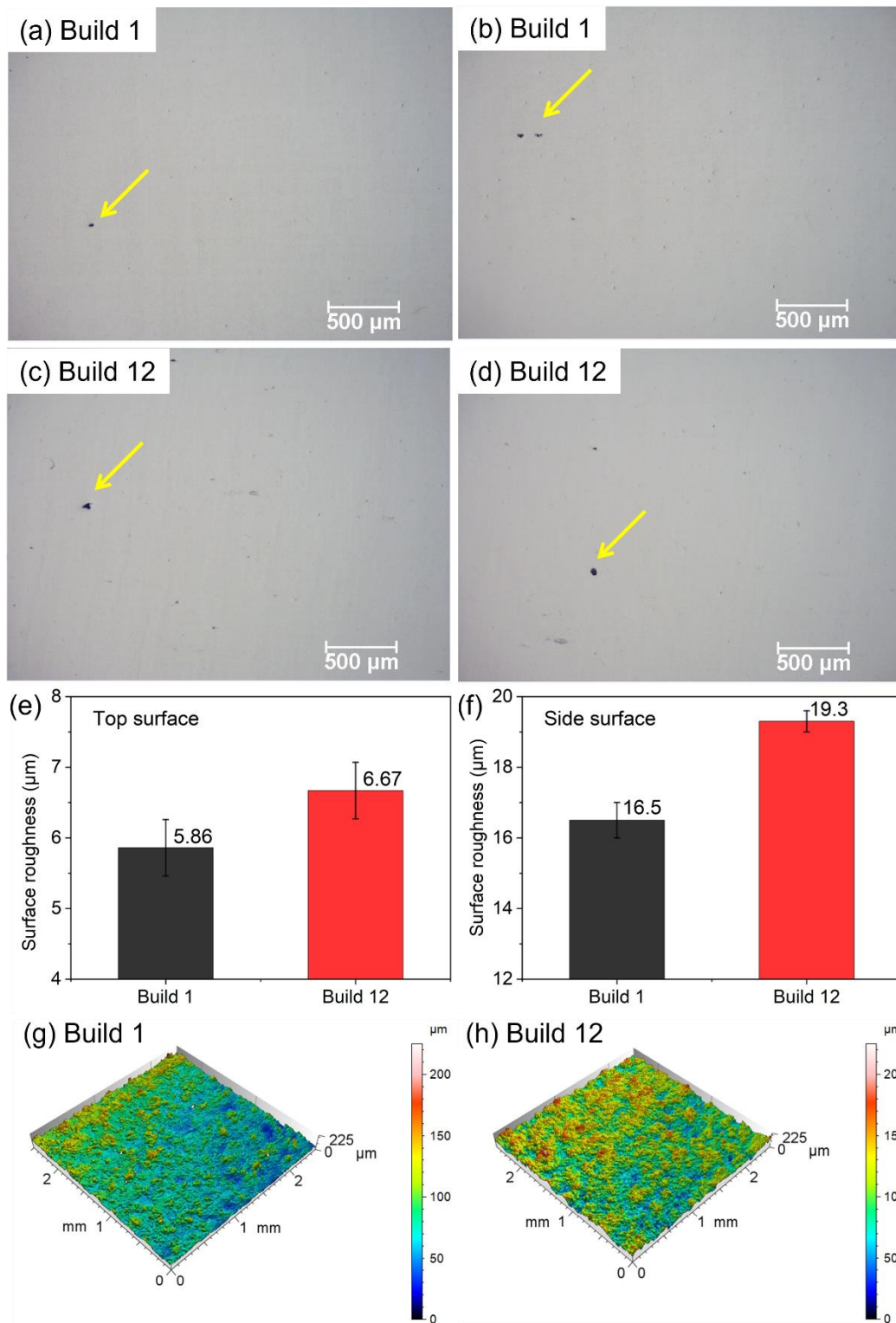


Fig. 4.8 Effect of particle size evolution on as-built parts, porosity (relative density) in (a, b) Build 1 and (c, d) Build 12, surface roughness on the top surface (e) and side surface (f) of Build 1 and Build 12, the surface topography of side surface in (g) Build 1 and (h) Build 12.

4.4 Discussion

4.4.1 Coarsening mechanisms responsible for PSD changes

This study confirms that the re-use of powders during LPBF leads to a progressive increase in particle size. The analysis of the particles sampled inside and outside of the build envelope allows the classification of different plausible contributors to the coarsening of the powder feedstock. These are schematically illustrated in [Fig. 4.9](#).

First, [Fig. 4.9\(a\)](#) shows the role of layer thickness on powder coarsening mechanisms. In this chapter, the layer thickness is 30 μm while the PSD range of Ti-6Al-4V is 15-45 μm , and as a result, more large particles are moved into the overflow during powder spreading, as evidenced by [Fig. 4.3](#) and [Table 4.3](#), which is consistent with prior work [56]. As for mechanisms contributing to coarsening, the particle size in the powder bed is smaller than virgin powder as more large particles are in the overflow after powder spreading. These powders (with more small particles) may be consumed by built parts and formed as spatter that is taken away. As a result, small particles are removed and large particles in the overflow remain (confirmed by laser diffraction in the [Fig. 4.3](#)), which would lead to reused powder coarsening due to the consumptions or removal of fine particles.

[Fig. 4.9\(b\)](#) illustrates the interactions between laser and powder material including various spatters during LPBF. With regards to the particles collected outside of the build envelope to the side of the powder bed, it is proposed that these particles are strongly affected by spatter generation mechanisms during LPBF and gas flow dynamics. Different types of spatter are typically generated during the interactions between laser and powder in the powder bed, as explained in detail by numerous studies [90–92]. Typically, three spatter generation mechanisms are associated with LPBF, namely droplet ejection spatter, hot spatter, and cold spatter. Droplet ejection spatter (more than 25 μm) is formed by the ejection of liquid metal away from the melt pool due to the rapid melt pool motion induced by high recoil pressure [90]. Entrainment-driven spatter (i.e., hot and cold spatter) is formed from the powder bed when a laser is scanned across the powder bed [90]. As the hot spatter and cold spatter originate from the powder bed, their particle size may be expected to have the same size range as that of the powder bed. This spatter may interact with each other under the effect of the vapour plume and

gas flow and finally become located in different areas of the build chamber with abnormal particle size and morphology characteristics. This abnormal particle size may lead to the PSD changes of reused powder.

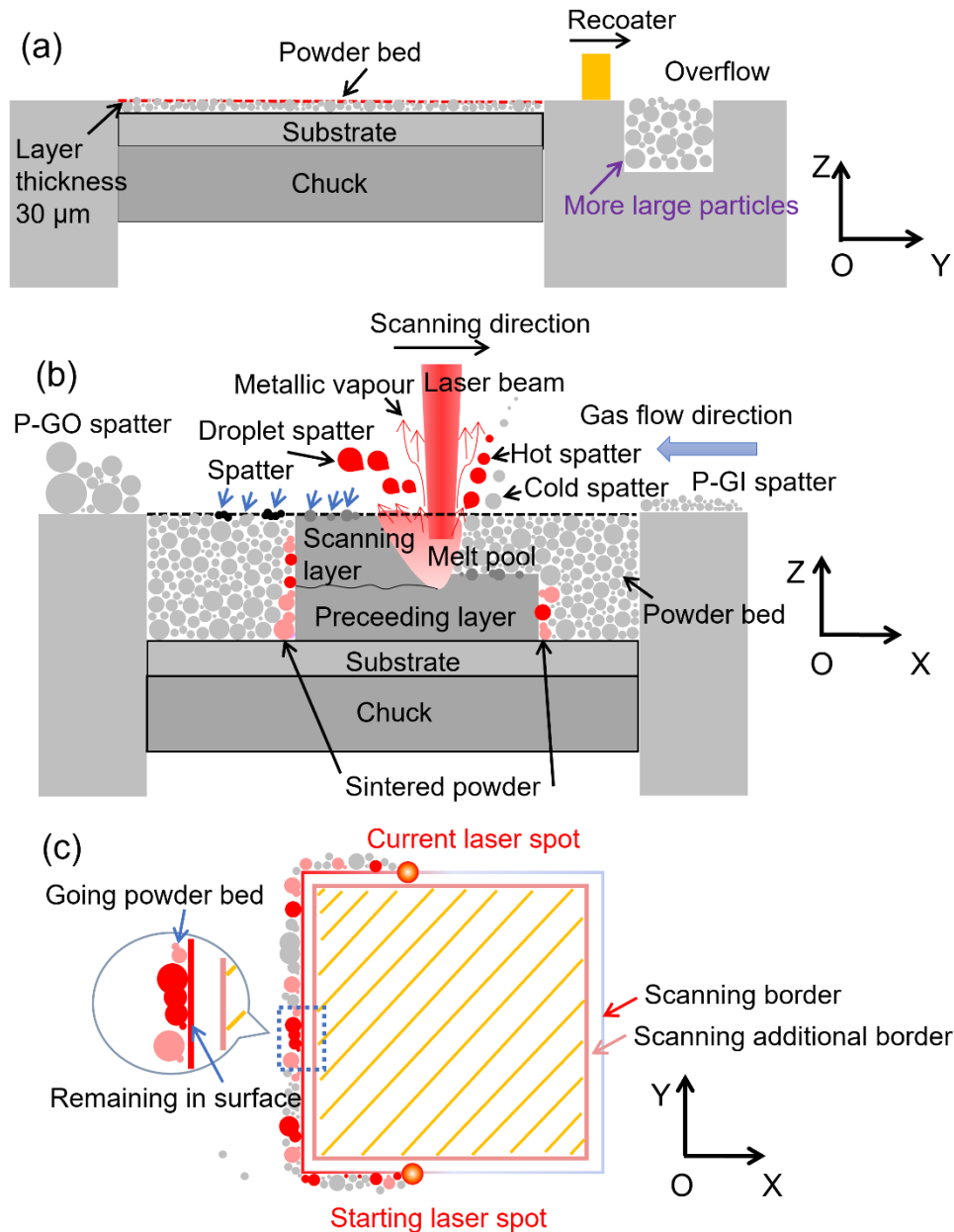


Fig. 4.9 (a) Schematic of the effect of layer thickness on powder coarsening: powder from overflow shows larger particle size than that of powder from the powder bed, (b) schematic of interactions between laser and powder material including various spatters during LPBF: this schematic presents the spatter formation and spatter locations, (c) schematic of the effect of sintered powder by laser scanning borders on powder coarsening.

P-GO spatter which has undergone oxidation is shown in [Fig. 4.5\(c, e\)](#), indicating the existence of droplet ejection spatter (also up to 100 μm particles observed) during LPBF [90,91,220]. In addition, the presence of irregular particles and agglomerates in the P-GO spatter ([Fig. 4.5\(a, c\)](#)) indicates the effect of hot spatter and/or droplet ejection spatter. Meanwhile, cold spatter may also exist due to spherical particles with no obvious sign of oxygen/oxide formation ([Fig. 4.5\(c, e\)](#)). On the other hand, P-GI spatter with a small particle size (less than 30 μm , significantly lower than virgin and reused powder), and no obvious sign of colour change based on BSE images is likely from cold spatter that was ejected at high-speed back to the gas inlet area, being too late to be removed by the gas flow. Therefore, due to the removal of P-GO and P-GI spatter, P-GI spatter has a noticeable effect on powder coarsening while for P-GO spatter it is difficult to directly determine its positive or negative effect on powder coarsening from laser diffraction and SEM results. It should be mentioned that the droplet ejection spatter escapes from the melt pool. The melt pool is formed through the powder in the powder bed melting under heat accumulation by the laser. Therefore, P-GO spatter originates from powder in the powder bed that may have relatively small particle size characteristics (more coarse particles may be driven into the overflow, see [Table 4.3](#)). In addition, small particles with low gravity in the powder bed may more easily form entrainment-driven spatter according to the investigation by Ly et al. [90], which may further suggest that the origin powder in P-GO spatter also has a relatively small particle size compared to reused powder.

After spatter generation and during flight, gas flow is thought to carry most of these particles to the outside of the powder bed [91]. However, some spatter may fall onto the build envelope, which may lead to an increase in the surface roughness of the built parts and a decrease in parts properties [77,78]. In this chapter, a few particles were also observed on the surface of a built part with a slightly elevated oxygen level ([Fig. 4.6](#)). This spatter that adhered to parts is most likely from droplet ejection spatter and hot spatter. It should also be noted that oxygen was detected on the part surface indicating the presence of oxygen in the melt pool and vapour plume, leading to possible oxidation of droplet ejection spatter and hot spatter, which agrees with the investigation by Gasper et al. [91]. Therefore, this provides evidence for the origins of P-GO and P-GI spatter from the perspective of oxide formation. Although there are a few spatter particles adhered to the part and their particle size characteristics cannot be

determined, their origin may be similar to P-GO spatter.

Hence, a similar effect of spatter on the parts and P-GO spatter on powder coarsening can be expected. As for spatter dropping in the powder bed around the as-built parts, it is thought to play a crucial role in the PSD coarsening and parts quality of the following builds. A strong signal of oxygen on the surface of agglomerates (Fig. 4.6(b, d)) suggests that small particles of entrainment-driven spatter pass through the vapour plume at high speed, resulting in collisions which lead to the formation of dark agglomerates with a cracked oxide layer, which is supported by the studies in literature [90,91,221]. In addition, high Al content (~ 9.55 wt.%) is also detected in the oxide layer by EDS (Fig. 4.6(c, e)), which is consistent with literature [222,223] as Al has a greater volatilisation tendency than Ti or V during vaporisation in the high-temperature process and this further supports the role of the vapour plume in entrainment-driven spatter. Dark agglomerates are correlated with powder coarsening. On the other hand, the creation of irregular pre-sintered particles in the powder bed with a coarse particle size (Fig. 4.6(b)) is likely the result of molten droplet spatter or hot spatter adhering to particles in the powder bed, which is in agreement with the explanation of powder coarsening proposed by Tan et al. [49].

Of note is another type of sintered particle (collected by the small holder, Fig. 4.7(a, b)) generated by the laser beam scanning borders of parts (see Fig. 4.9(c)). Such sintered particles attached to parts surfaces are responsible for the increased surface roughness of the part, with those unattached remaining in the powder bed leading to reused powder coarsening. The sintered particles also have a positive effect on powder coarsening due to the reduction of fine particles and the formation of coarse particles, as shown in Fig. 4.7(a, b).

Therefore, P-GI spatter, spatter dropped in the powder bed, and sintered powder have a clear effect on powder coarsening of reused powder. P-GO spatter and powder consumption to build parts may also contribute to powder coarsening due to the particle size characteristic of the powder bed. Three main mechanisms including layer thickness, spatter (droplet ejection spatter, hot spatter, cold spatter), and sintering contribute to the observed PSD changes.

4.4.2 Practical implications of powder management

4.4.2.1 Effect of measurement technique on the PSD

In this chapter, two PSD measurement techniques are employed for PSD coarsening mechanisms analysis. Laser diffraction is a fast and repeatable method to measure spherical particles while it may not be the most effective method to measure powders with fine agglomerates. SEM image analysis can directly measure particle size at higher resolutions, making it a powerful tool for qualitative particle size analysis and quantitative PSD measurement. SEM image analysis can perform PSD measurements with a small amount of powder and therefore can be particularly useful to investigate particles produced during LPBF (such as P-GI spatter, typically less than 0.1 g). It is found that the PSD results by laser diffraction are not consistent with the SEM image method. The particle size measured by the SEM image method is generally smaller than laser diffraction. This difference may be mainly from the principle of the two methods. The diameter of particles by laser diffraction is calculated by measuring the equivalent sphere while fine particles may be agglomerated with a decreased degree of sphericity and increased equivalent particle size during measurement. On the contrary, fine particles may be detected and measured more accurately by the SEM image method.

4.4.2.2 Strategies to minimise PSD changes

Since layer thickness can affect the PSD of P-PB, achieving the PSD of P-PB and overflow close to virgin powder may be effective for maintaining PSD stability. Hence, when the layer thickness can be close to or larger than the D90 of virgin powder (e.g., layer thickness $\geq 40 \mu\text{m}$), the PSD of overflow and P-PB may be consistent with the virgin powder, and as a result, the PSD changes in powder bed caused by powder consumption and spatter formation for powder coarsening of reused powder may be largely decreased.

Different types of spatter are largely dependent on process practicalities [77,78,224]. Spatter formation in LPBF not only makes the powder coarser after reuse but also damages the properties of the final parts and affects the powder economy. Hence, to minimise powder coarsening in LPBF due to spatter formation and related location spatter, it is imperative to consider the effect of laser processing parameters, layer thickness, and gas flow. Laser processing parameters can affect energy input and spatter

formation. For example, Andani et al. [224] studied the effect of energy input on spatter formation during LPBF. Experimental results indicate that the spatter particles can be reduced by decreasing laser power or increasing scan speed. Also, scan speed affects spatter formation more than laser power. Based on evidence of spatter with dark colour (Fig. 4.6(b, e)), high energy input with a high temperature increases element loss of built parts. Therefore, too high energy input may not be suitable for spatter reduction. Gas flow may influence the distribution of spatter in the build chamber [225,226], which would also affect powder coarsening and powder economy. The high intensity of gas flow may take the spatter outside of the powder bed, minimising spatter drops in parts and the powder bed. However, too high an intensity of gas flow may blow away the powder from the powder bed. Meanwhile, the PSD characteristics and weight of the virgin powder will also influence the degree of PSD coarsening. Finally, powder coarsening from sintered powder may be minimised through processing parameters optimisation of scanning borders.

4.5 Conclusions

In this chapter, the PSD coarsening, and underlying mechanisms for this change, for LPBF Ti-6Al-4V powder subjected to increasing numbers of re-use cycles, were systematically investigated. Both laser diffraction and SEM image method confirm virgin powder coarsening after reuse. This is explained by the generation of various forms of spatter and sintered powder during interactions between laser and powder. It may also be closely related to layer thickness. Critically, a link is established between the location of powder with modified particle size and its corresponding origins (droplet ejection spatter, hot, and cold spatter). P-GI spatter, spatter dropped in the powder bed, and sintered powder all increase particle size. P-GO spatter as well as spatter on parts may not be expected to have a strong effect on powder coarsening since these powders generally have a relatively small particle size. Three origins (spatter, sintering, and layer thickness) of powder coarsening are proposed. Therefore, this work has shown that when re-using powder, partitioning of the powder bed can be considered if a repeatable and specific PSD is required in the collected powder batch. Minimising PSD changes via processing parameters, in particular through manipulating layer thickness, sintering, and spatter formation is proposed to further control and maintain powder feedstock quality.

5 The role of PSD on the performance of Ti-6Al-4V alloy by LPBF

5.1 Introduction

Since there is a PSD coarsening trend for reused powder and the coarsening is not significant in 10 or 20 cycles demonstrated in Chapter 4, it is essential to study the effect of large differences in powder PSD on Ti-6Al-4V performance to simulate the large particle size change of powder feedstock after hundreds of cycles. This is one of the reasons to investigate the role of different PSD powder feedstocks. Although studies about the effect of different PSD of Ti-6Al-4V can be found, either those powder feedstocks with different PSD are usually not from the processing of one batch or non-LPBF suitable PSD range (more than 63 μm) is used. In other words, some influence factors when using different powder manufacturing may also play a key role in parts performance rather than the only factor by PSD. This means some unknown factor (such as particle morphology, internal porosity) may affect the results. It is crucial to use different PSD powders from one batch to understand the role of PSD on as-built parts performance. This is another reason to investigate the role of different PSD powder feedstocks. In this chapter, different PSD powder feedstocks are obtained through the sieving of the original 15-45 μm powder feedstock. This could yield a finer and coarser powder than the original powder. The effect of different PSD powders on in-process powders behaviour and single-track formability by LPBF was systematically investigated. For in-process powders behaviour, spatter formation, powder from the powder bed, and powder from overflow were analysed and compared. Single-track formability processed by different processing parameters with morphology, width, and height was evaluated to assess the effect of different PSD powder feedstocks. Meanwhile, surface quality and relative density of as-built parts by three powder feedstocks were also investigated to link in-process powders and single-track formability. Through this investigation, it can be possible to better understand the role of PSD on in-process powders behaviour and final parts performance. It can build a link between PSD, in-process powder behaviour and final parts performance, which may be useful to choose suitable PSD powder feedstock to obtain desired properties.

5.2 Experimental

Plasma atomised pre-alloyed Ti-6Al-4V (Grade 23, ELI) powder with a nominal particle size range of 15-45 μm was employed as raw feedstock (Powder 1). The raw feedstock Powder 1 was 12x reused powder from Chapter 4 with a still size range of 15 to 45 μm despite the coarsening compared to virgin powder. The 12x reused powder (oxygen level below 500 ppm in build chamber) may still follow ELI specifications based on the Renishaw White Paper that reused powder with less than 30 build cycles (oxygen level below 1000 ppm in build chamber) stays within the ELI specifications [75]. Therefore, Powder 1 from 12x reused powder may not have a significant effect on the size range of 15-45 μm and ELI specifications. Powder 2 with nominal particle size range of 15-38 μm was obtained by sieving Powder 1 via 38 μm mesh. The powder was still on 38 μm mesh was named Powder 3 with nominal particle size range 38-45 μm . Single-track formability experiments by different PSD powder feedstocks were performed by a Renishaw AM400 LPBF machine (inserted with RBV). Each powder runs one single-track build. In each build, the single tracks were built on the just finished as-built cuboid part. The processing parameters of single tracks varied in laser power (from 100 to 200 W, interval 25 W) and exposure time (from 40 to 90 μs , interval 10 μs). After each build, in-process powders including spatter located in gas outlet area, powder away from printing area in powder bed, powder from overflow were also collected for further analysis by laser diffraction and SEM.

The single tracks were observed by SEM images and Alicona G4 to evaluate the single-track formability. The relative density of as-built parts was assessed by the Archimedes method and optical microscope images. Surface morphology and surface quality of as-built parts were observed by SEM and Alicona G4, respectively. The microstructure was captured by OM and SEM images. Mechanical properties of Ti-6Al-4V from different PSD powder feedstocks were also compared.

5.3 Results

5.3.1 Powder properties of three powder feedstocks

Fig. 5.1 shows SEM images of three different powder feedstocks (all are below 63 μm for LPBF) obtained by the sieving method with a 38 μm mesh by using the original powder feedstock (Powder 1). Powder 2 with a particle size of 15 to 38 μm is finer than

original Powder 1 with a particle size of 15 to 45 μm , whereas Powder 3 with a particle size of 38 to 45 μm is coarser than Powder 1. To further evaluate the PSD of three powders, PSD curves and PSD results measured by laser diffraction are presented in Fig. 5.1 and Table 5.1. The D50 for Powder 1, Powder 2, and Powder 3 are 33.0 μm , 27.5 μm , 38.6 μm respectively, which is quite consistent with SEM results. For Powder 2, the D90 metric is 38.0 μm while the D10 metric of Powder 3 is 29.4 μm . Table 5.2 shows the flowability and apparent density of three powder feedstocks. All powders can pass through the funnel, which suggests all powder feedstocks have favorable flowability. Powder 3 with more coarse particles exhibits the best flowability (27.1 s/50 g) while Powder 2 with more fine particles has the worst (37.4 s/50 g). For apparent density (also measured by Hall flowmeter), there is no significant difference between these powder feedstocks. The apparent density of Powder 1 (2.56 g/cm³) with the widest particle size range is slightly higher than that of Powder 2 (2.52 g/cm³) and Powder 3 (2.51 g/cm³).

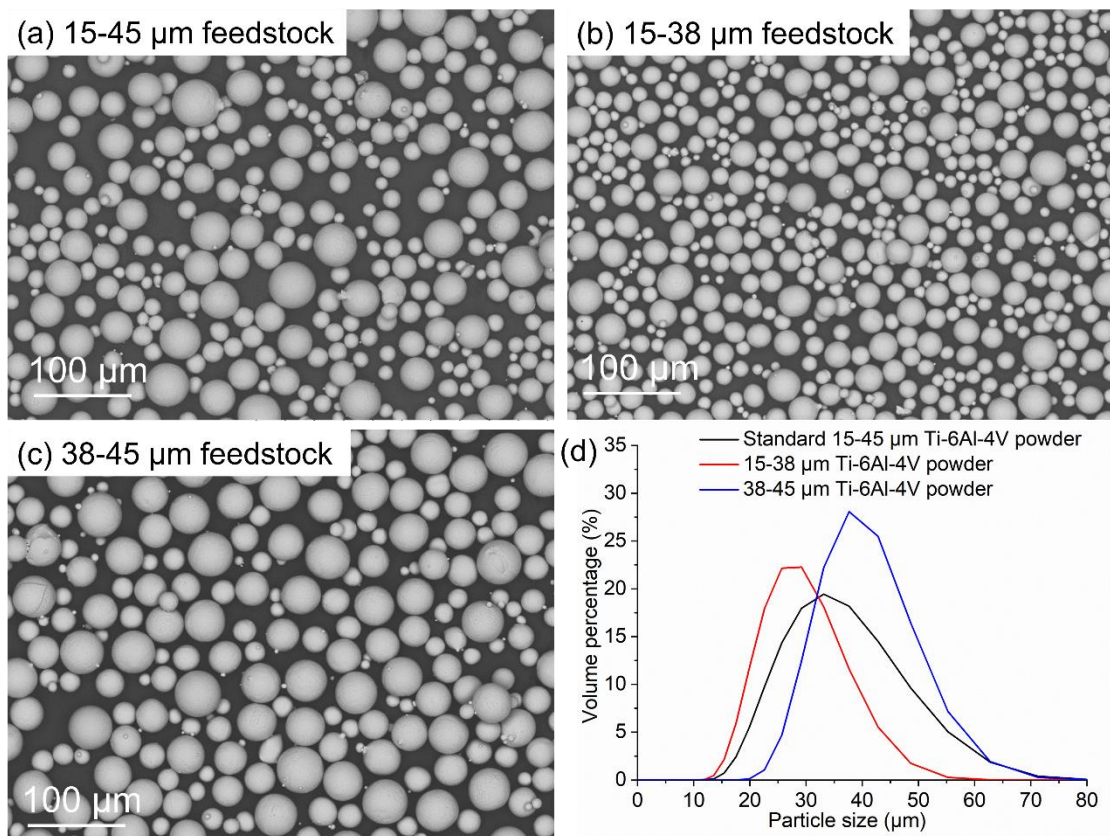


Fig. 5.1 SEM images (a-c) of three powder feedstocks and PSD results (d) measured by laser diffraction.

Table 5.1 PSD results of three powder feedstocks measured by laser diffraction (standard deviation obtained by measuring at least three powder samples).

	D10 (μm)	D50 (μm)	D90 (μm)
15-45 μm Ti-6Al-4V powder	22.2 \pm 0.05	33.0 \pm 0.05	48.4 \pm 0.05
15-38 μm Ti-6Al-4V powder	19.7 \pm 0.33	27.5 \pm 0.19	38.0 \pm 0.09
38-45 μm Ti-6Al-4V powder	29.4 \pm 0.14	38.6 \pm 0.05	50.5 \pm 0.09

Table 5.2 Flowability and apparent density of three powder feedstocks measured by Hall flowmeter.

Hall Flowmeter	Flow rate (s/50 g)	Apparent density (g/cm^3)
15-45 μm Ti-6Al-4V powder	33.3 \pm 0.2	2.56 \pm 0.005
15-38 μm Ti-6Al-4V powder	37.4 \pm 0.4	2.52 \pm 0.006
38-45 μm Ti-6Al-4V powder	27.1 \pm 0.1	2.51 \pm 0.007

5.3.2 In-process powders

Fig. 5.2 shows the comparison of PSD results for three powder feedstocks, powder from the powder bed, and powder from overflow. In each powder feedstock, the PSD results (i.e., D10, D50, D90 metrics) of powder feedstock, powder from the powder bed, and powder from overflow are consistent, which suggests the negligible effect of different PSD powder feedstocks on powder from the powder bed and overflow. In this chapter, the spatter produced by three powder feedstocks was investigated and compared. SEM images (see Fig. 5.3) of three spatters show that all three spatters present extra-large particles (around 100 μm). Except for extra-large particles, the particle size in Powder 2 seems smaller than in Powder 1 while it is larger for Powder 3 than that in Powder 1. This is proved by the PSD results of three spatters, as shown in Fig. 5.4(a) and Table 5.3. The D50 metrics of the three spatters are 40.0 μm , 33.2 μm , and 44.1 μm , respectively. Interestingly, the spatter collected in the gas outlet area was weighed, as shown in Fig. 5.4(b). The three spatters weigh 4.875 g, 3.695 g, and 5.287 g, respectively. This result looks positively related to the particle size of the three powder feedstocks (i.e., fine spatter shows low weight).

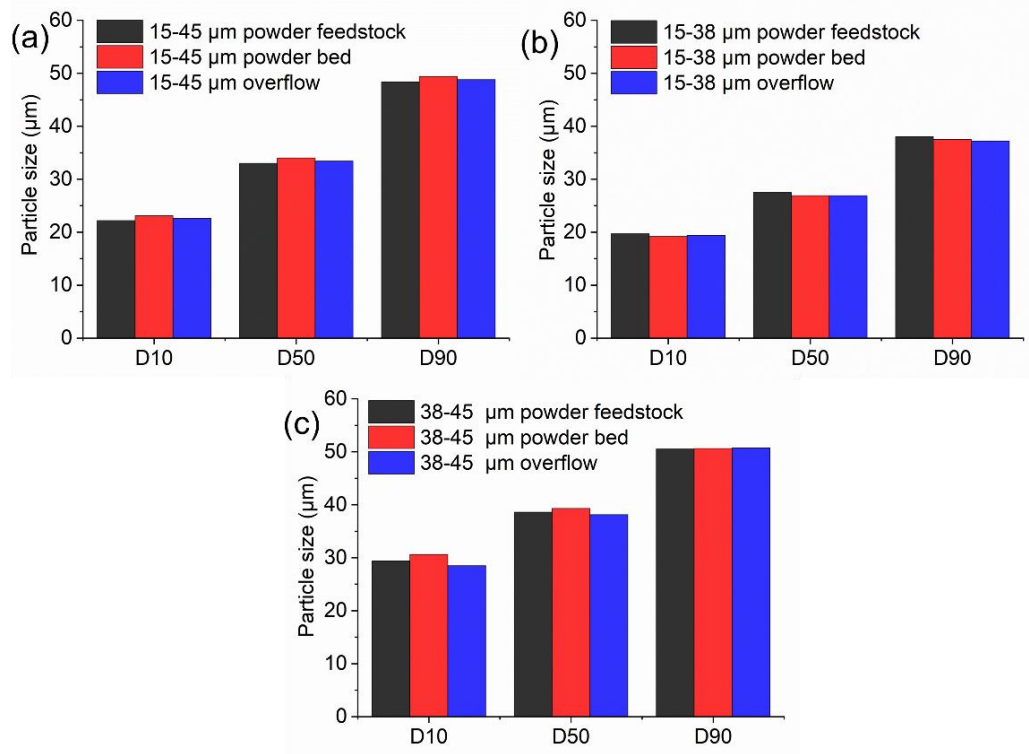


Fig. 5.2 PSD comparison of powder feedstock, powder from the powder bed, and overflow, (a) 15-45 μm powder, (b) 15-38 μm powder, (c) 38-45 μm powder.

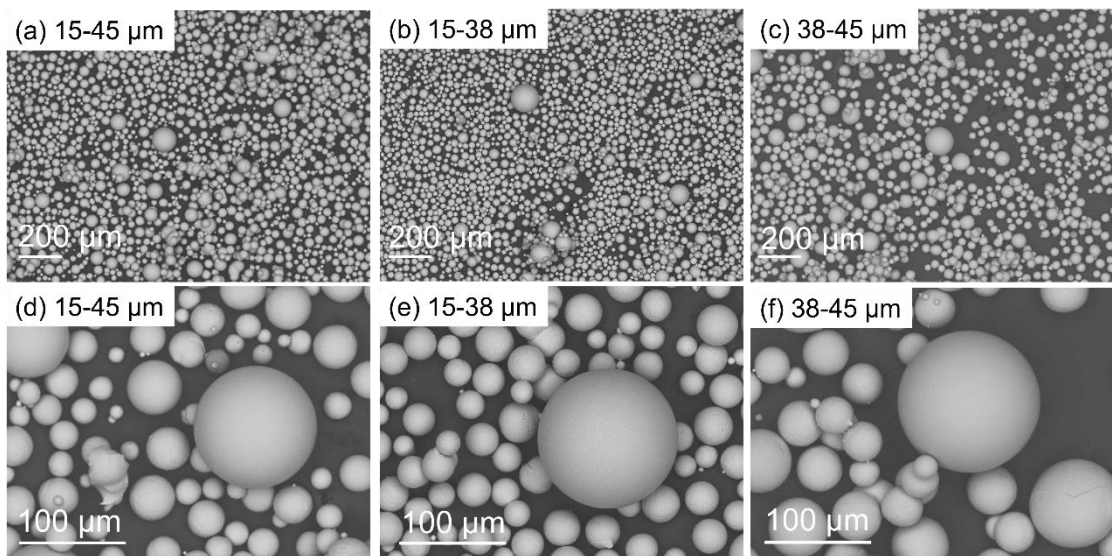


Fig. 5.3 SEM images of three spatters generated by (a) and (d) 15-45 μm powder, (b) and (e) 15-38 μm powder, (c) and (f) 38-45 μm powder.

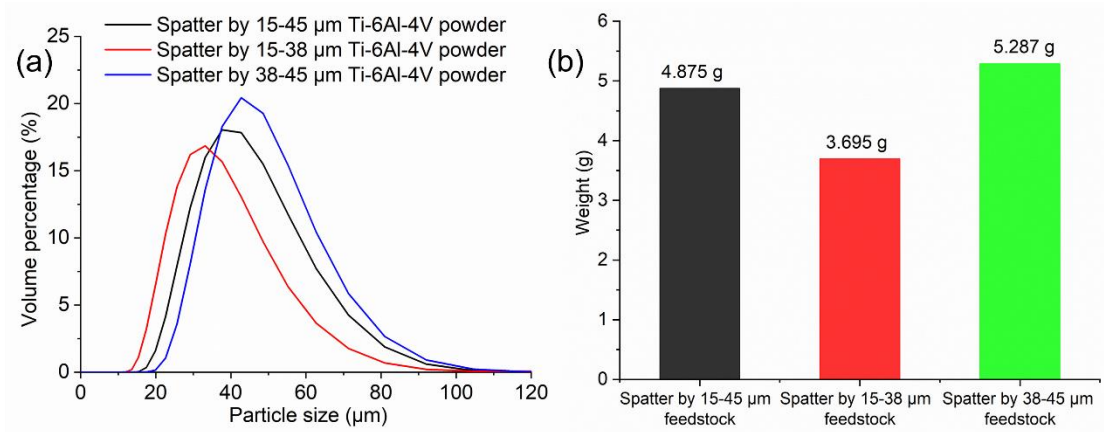


Fig. 5.4 (a) PSD curves of spatter generated by three powder feedstocks, (b) collected spatter weight generated by three powder feedstocks.

Table 5.3 PSD results of spatter using three powder feedstocks.

	D10 (μm)	D50 (μm)	D90 (μm)
Spatter by 15-45 μm Ti-6Al-4V powder	26.6 ± 0.60	40.0 ± 0.55	61.1 ± 0.45
Spatter by 15-38 μm Ti-6Al-4V powder	21.6 ± 0.05	33.2 ± 0.10	53.0 ± 0.10
Spatter by 38-45 μm Ti-6Al-4V powder	30.9 ± 0.05	44.1 ± 0.70	64.7 ± 2.05

5.3.3 Single-track morphology

To clarify the effect of PSD on built parts by LPBF, single tracks with different processing parameters (typical power ranges from 100 W to 200 W, exposure time ranges from 40 μs to 90 μs) were evaluated. Fig. 5.5 shows SEM images of single tracks by three powder feedstocks. In general, all single tracks show a trend from balling (discontinuous) to irregular and continuous when laser power and exposure time increase (high energy density) based on the SEM images as high energy density can fully melt powder during laser scanning. The exposure time looks more dominant than laser power as the continuous track can be observed in high exposure time with low power (like 80 μs , 125 W) while the single track is still irregular in high power with short exposure time (like 50 μs , 200 W). The difference is obviously in low power, such as less than 150 W. Tracks processed at 125 W present obvious differences between three powders, as shown in Fig. 5.5. In general, the track quality by Powder 2 is better for Powder 2 than Powder 1 and Powder 3. For example, when laser power and exposure time are 125W, 40 μs , single-track by Powder 2 is irregular while tracks are obviously

discontinuous by Powder 1 and Powder 3. When the laser power is more than 150 W, obvious differences cannot be observed. It is noteworthy that more spatter particles were found around single tracks are produced by Powder 1 and Powder 3 than Powder 2. This is quite consistent with spatter results around gas outlet collection.

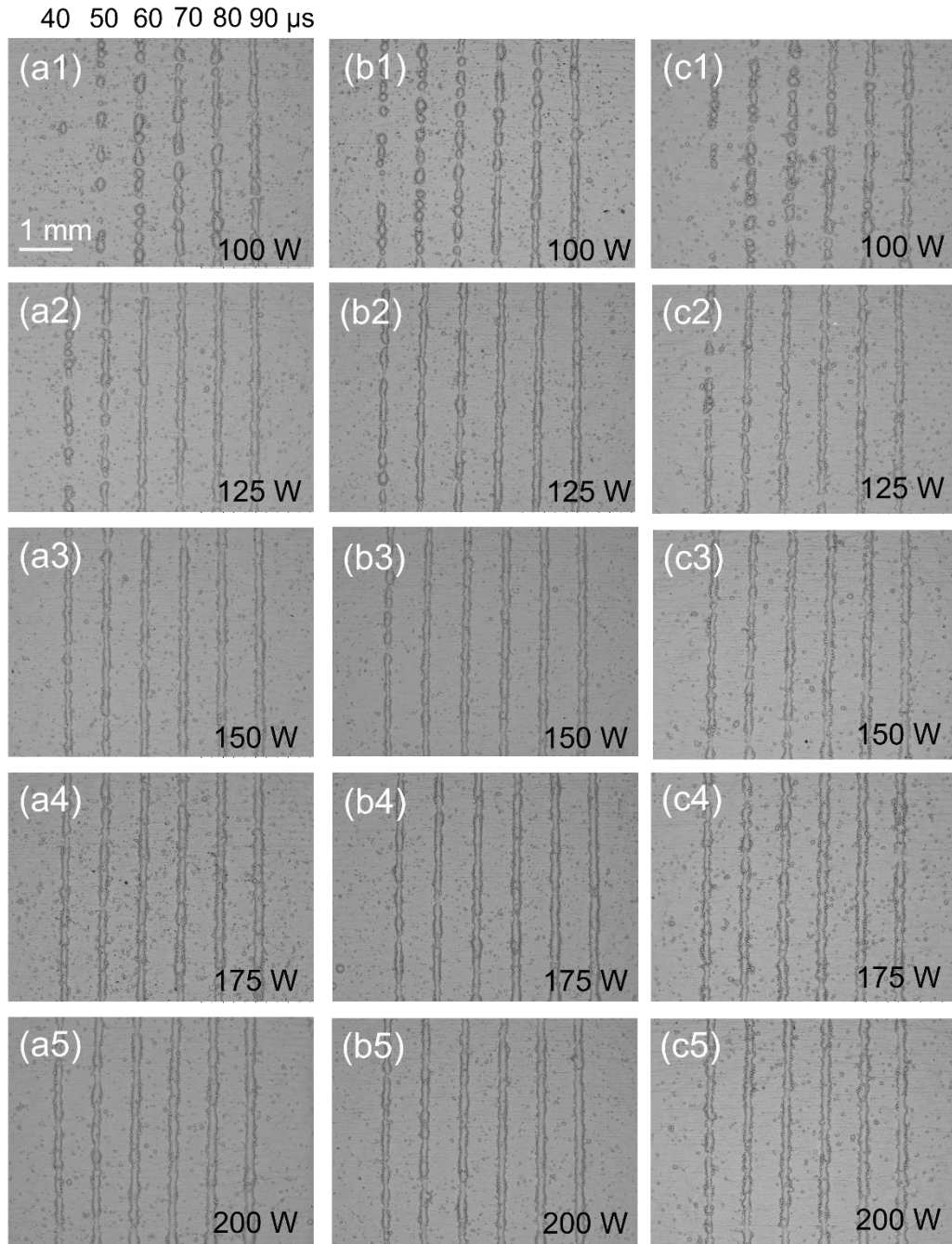


Fig. 5.5 Single-track formability with different processing parameters (power from 100 W to 200 W, and exposure time from 40 μs to 90 μs) by three powder feedstocks, (a1-a5) 15-45 μm powder feedstock, (b1-b5) 15-38 μm powder feedstock, (c1-c5) 38-45 μm powder feedstock.

To further identify the characteristics of single tracks, single tracks can be classified as balling, irregular, and continuous. The average width of irregular and continuous tracks is measured, as shown in Fig. 5.6. The average width and standard deviation of single tracks are calculated with an average of ten positions in each single track by using ImageJ, as shown in Table 5.4. The width of single tracks increases when laser power and exposure time increase for all powder feedstocks. The single tracks by Powder 2 are generally wider than the others. Single tracks by Powder 2 show better formability than that of Powder 1 and Powder 3 based on the SEM images and width of single tracks. It is noteworthy that a stable track with a narrower track (around 100 μm) can be observed by Powder 2, which indicates good suitability for fine structure build. The track width measurement may be affected by the surface roughness of as-built parts by different PSD powder feedstocks. This is because the different surface roughness with more fine or coarse particles may influence the melting stability of single tracks and affect the track width measurement. It is noteworthy that this effect may originate from the different PSD powder feedstocks and will be presented in Discussion section (5.4.2 single-track evolution).

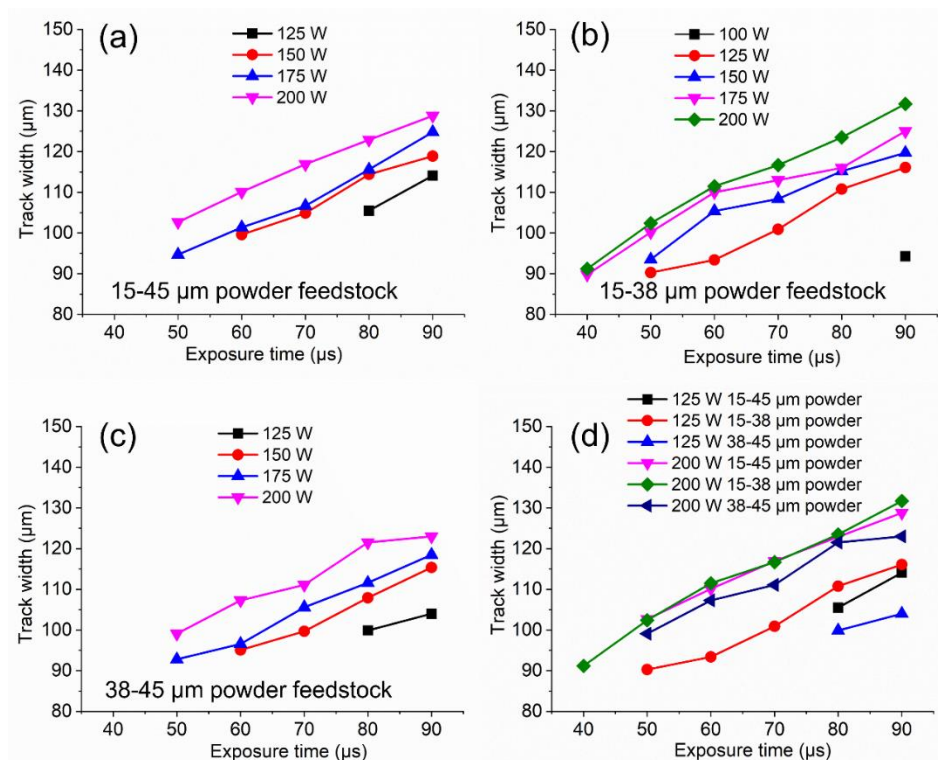


Fig. 5.6 The average width of single tracks fabricated by (a) 15-45 μm powder feedstock, (b) 15-38 μm powder feedstock, (c) 38-45 μm powder feedstock, (d) width comparison by different powder feedstocks.

Table 5.4 The average width and standard deviation of single tracks by different processing parameters in three powder feedstocks, unit: P (power), W; ET (exposure time), μ s; track width, μ m.

Powder	ET/P	100	125	150	175	200
15-45 μ m	40	/	/	/	/	/
15-38 μ m	40	/	/	/	89.8 \pm 16.4	91.1 \pm 20.3
38-45 μ m	40	/	/	/	/	/
15-45 μ m	50	/	/	/	94.7 \pm 20.0	102.7 \pm 16.1
15-38 μ m	50	/	90.3 \pm 16.8	93.5 \pm 17.5	100.2 \pm 17.5	102.4 \pm 17.2
38-45 μ m	50	/	/	/	92.8 \pm 17.5	99.1 \pm 17.0
15-45 μ m	60	/	/	99.6 \pm 16.1	101.4 \pm 12.6	110.3 \pm 13.4
15-38 μ m	60	/	93.4 \pm 18.0	105.4 \pm 11.3	110.0 \pm 14.9	111.5 \pm 14.9
38-45 μ m	60	/	/	95.1 \pm 15.6	99.6 \pm 18.8	107.3 \pm 15.7
15-45 μ m	70	/	/	104.9 \pm 15.7	106.7 \pm 14.9	116.9 \pm 9.0
15-38 μ m	70	/	100.9 \pm 13.6	108.4 \pm 13.1	113.0 \pm 11.8	116.7 \pm 11.3
38-45 μ m	70	/	/	99.7 \pm 16.5	105.6 \pm 11.2	111.1 \pm 13.1
15-45 μ m	80	/	105.5 \pm 17.8	114.4 \pm 13.4	115.6 \pm 10.2	122.9 \pm 13.0
15-38 μ m	80	/	110.8 \pm 10.8	115.2 \pm 9.0	116.0 \pm 10.7	123.5 \pm 9.6
38-45 μ m	80	/	99.9 \pm 17.2	107.9 \pm 16.8	111.6 \pm 13.1	121.5 \pm 12.9
15-45 μ m	90	/	114.1 \pm 13.4	118.9 \pm 13.6	124.8 \pm 10.1	128.8 \pm 13.3
15-38 μ m	90	94.3 \pm 18	116.1 \pm 10.2	119.7 \pm 14.2	125.0 \pm 13.4	131.7 \pm 11.7
38-45 μ m	90	/	104.0 \pm 21.9	115.4 \pm 14.3	118.5 \pm 12.7	123.0 \pm 11.2

The height profile of single tracks is also a key factor as it can affect the quality of the next layer and further affect parts performance. The height profile of single tracks with laser power 125 W and 200 W by three powders was extracted by 3D focus variation microscope, which cannot be analysed by SEM images, as shown in Fig. 5.7. There is a trend from fluctuation to stability for height profile when laser power and exposure time increase, which is consistent with single tracks width. Likewise, Powder 2 seems to have more uniform height tracks (less discontinuous tracks) than that of Powder 1 and 3 in both low (125 W) and high (200 W) laser power. This has been confirmed by roughness profile results (Ra, line surface roughness, the low Ra means more uniform track height) of single tracks by different processing parameters and different PSD powder feedstocks

processed by Alicona G4, as shown in Table 5.5. The low Ra means more uniform track height. Ra values in Powder 2 are generally lower than Powder 1 and Powder 3 under the same processing parameters.

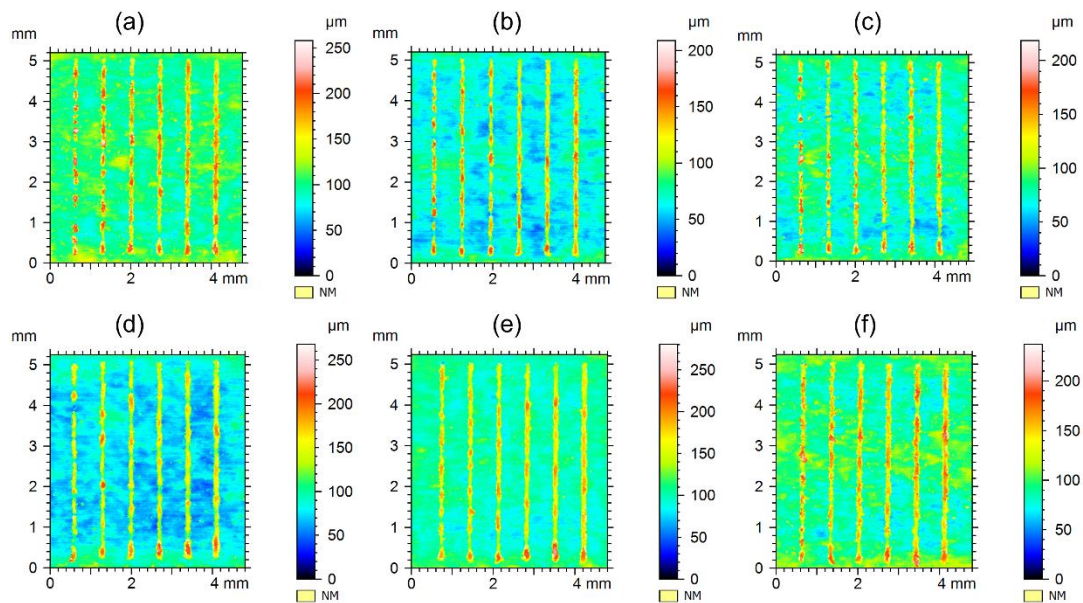


Fig. 5.7 Height profile of single tracks with laser power 125 W (a, b, c) and 200 W (d, e, f) by three powders, (a) and (d) 15-45 μm powder feedstock, (b) and (e) 15-38 μm powder feedstock, (c) and (f) 38-45 μm powder feedstock.

Table 5.5 Ra values of single tracks by different processing parameters (power (P), exposure time (ET)) and different PSD powder feedstocks.

Ra (μm)	P/ET	40 μs	50 μs	60 μs	70 μs	80 μs	90 μs
Powder 1	125 W	32.7	22.3	12.0	9.71	8.36	8.10
Powder 2	125 W	20.2	10.1	13.6	7.57	7.48	7.22
Powder 3	125 W	22.0	15.5	11.0	9.27	9.00	7.99
Powder 1	200 W	15.9	13.7	10.3	9.49	10.1	7.61
Powder 2	200 W	11.5	11.4	10.1	8.46	7.01	5.66
Powder 3	200 W	14.6	11.5	8.97	7.90	7.75	7.05

5.3.4 Surface quality and relative density of the as-built parts

Fig. 5.8 presents the top surface and side surface morphology of the as-built parts with the same default processing parameters using three powder feedstocks. For the top surface, there are some particles on the surface of all parts and an obvious difference in

some particles in all parts is not observed. In this case, the particle size in Powder 2 is the smallest and that in Powder 3 is the largest, which indicates a positive correlation between particle size and powder feedstock. There are massive particles on the side surface for all powder feedstocks (see Fig. 5.8(d-i)). The results are similar to those on the top surface. More fine particles can be found in Powder 2, while more coarse particles are found in Powder 3.

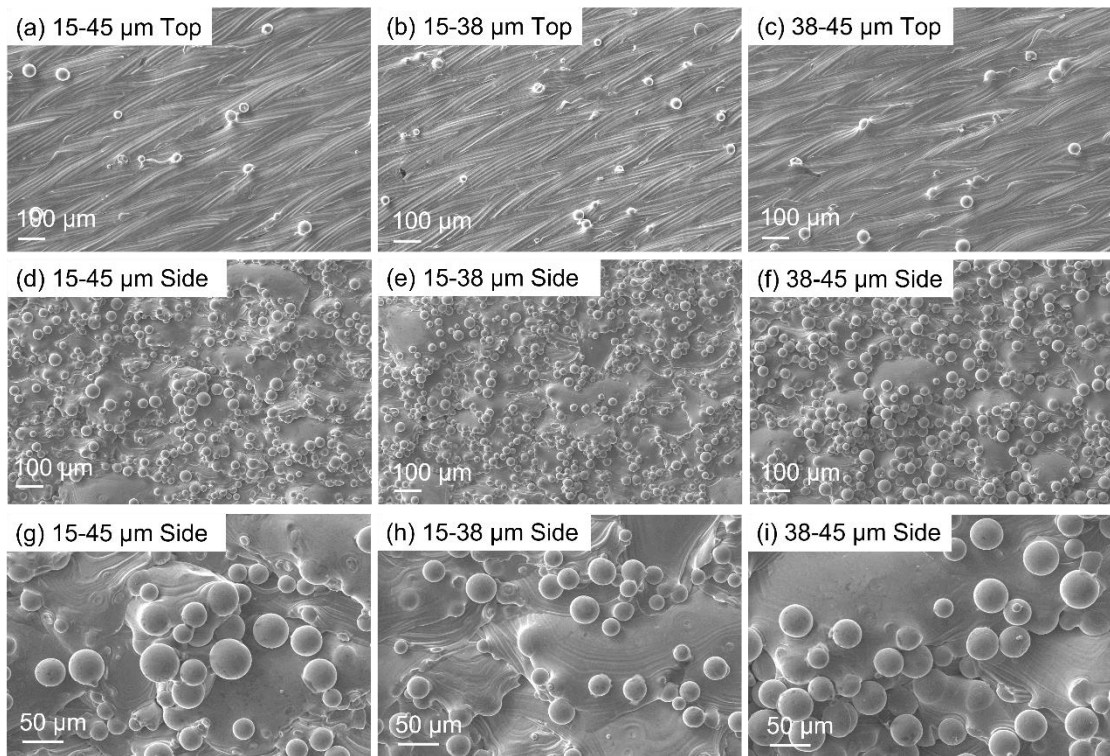


Fig. 5.8 Surface morphology of as-built parts for the (a, b, c) top surface and (d-i) side surface by three powders (a, d, g) 15-45 μm powder feedstock, (b, e, h) 15-38 μm powder feedstock, (c, f, i) 38-45 μm powder feedstock.

Surface roughness results (area surface roughness S_a employed, three measurements for each sample, based on ISO 25178) of the parts for the top surface (with area 2.5 mm x 2.5 mm) are shown in Fig. 5.9. Powder 2 with fine particles presents the lowest surface roughness ($S_a = 4.81 \pm 0.12 \mu\text{m}$) while Powder 1 and 3 are $6.25 \pm 0.10 \mu\text{m}$, and $7.53 \pm 0.21 \mu\text{m}$, respectively. Similar results in the side surface roughness (Powder 1 with $S_a 16.5 \pm 0.08 \mu\text{m}$, Powder 2 with $S_a 15.6 \pm 0.29 \mu\text{m}$, Powder 3 with $S_a 17.8 \pm 0.08 \mu\text{m}$) can also be found (see Fig. 5.10).

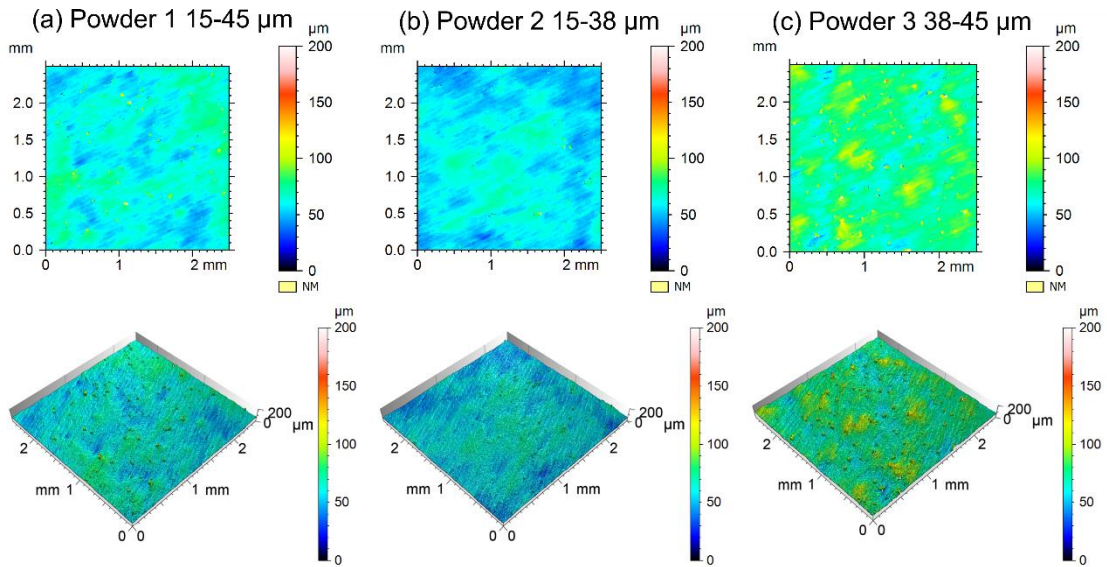


Fig. 5.9 Surface texture and roughness results of the as-built parts for the top surface by three powders, (a) 15-45 μm powder feedstock, (b) 15-38 μm powder feedstock, and (c) 38-45 μm powder feedstock.

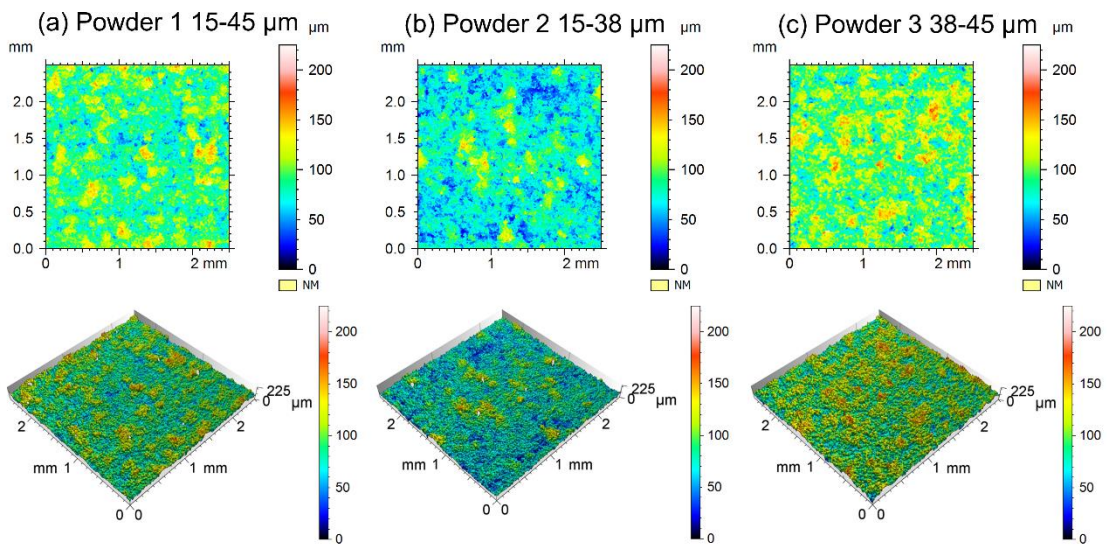


Fig. 5.10 Surface texture and roughness results of the as-built parts for the side surface by three powders, (a) 15-45 μm powder feedstock, (b) 15-38 μm powder feedstock, and (c) 38-45 μm powder feedstock.

The Archimedes relative density (three measurements for each sample) of the as-built parts by Powder 2 is $\sim 99.76 \pm 0.059\%$ which is higher than that of Powder 1 ($\sim 99.65 \pm 0.060\%$) and Powder 3 ($\sim 99.59 \pm 0.057\%$). The standard deviations for all three PSD powder feedstocks are no more than 0.06%. Considering the difference in relative density of three powders and the standard deviation of relative density if using the same

powder feedstock, the relative density by 15-38 μm powder feedstock is higher compared to 15-45 μm powder feedstock and 38-45 μm powder feedstock. Also, the optical microscope images of the polished sample from three powder feedstocks agree with the trend of Archimedes relative density results, as shown in Fig. 5.11.

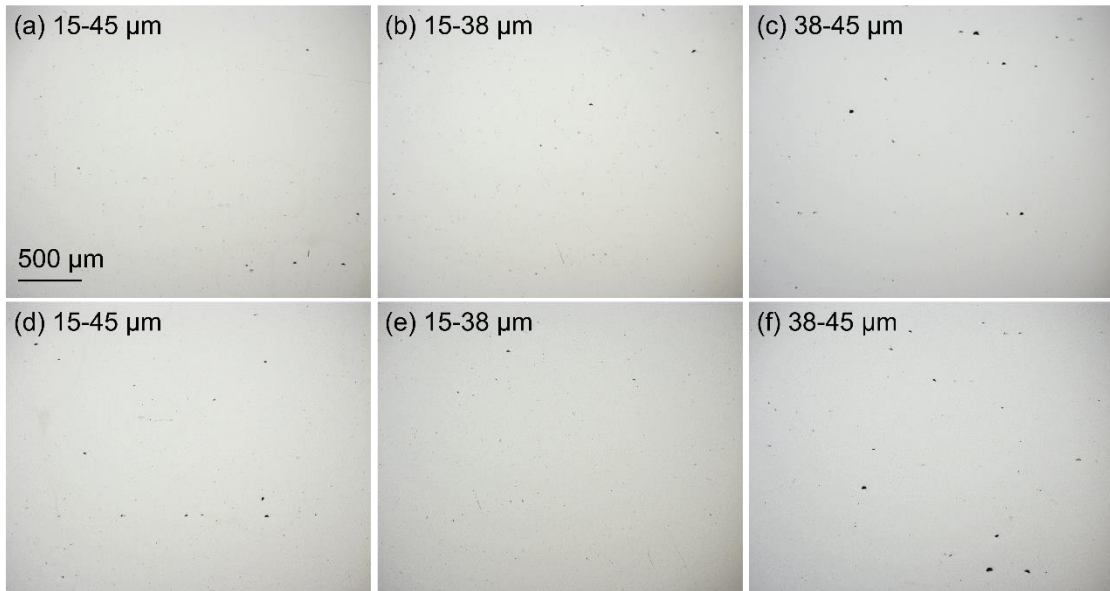


Fig. 5.11 OM images to show pores by (a, d) 15-45 μm powder feedstock, (b, e) 15-38 μm powder feedstock, (c, f) 38-45 μm powder feedstock.

5.3.5 Microstructure and mechanical properties

The microstructure of as-built parts by different PSD feedstocks is also compared, as shown in Fig. 5.12. In optical microscopy images, all samples present typical columnar prior- β grain boundaries with martensite α' inside around ± 45 degrees. In high magnification SEM images, martensite α' structures with various size types can be observed. There is no obvious difference in martensite α' structure by 15-45 μm powder feedstock, 15-38 μm powder feedstock, and 38-45 μm powder feedstock. Hence, no obvious microstructure difference was observed for different PSD powder feedstocks.

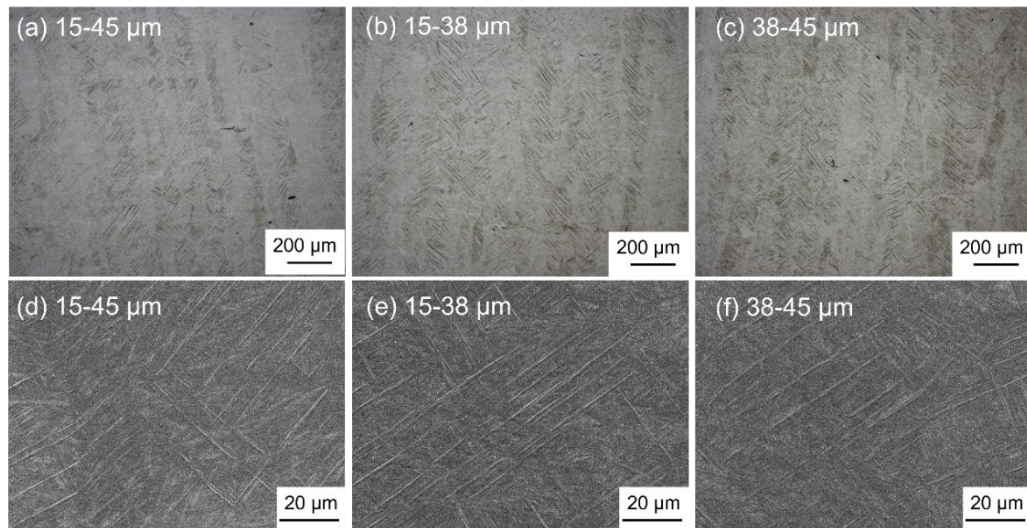


Fig. 5.12 Optical microscopy and SEM images by (a) and (d) 15-45 μm powder feedstock, (b) and (e) 15-38 μm powder feedstock, (c) and (f) 38-45 μm powder feedstock, respectively.

The microhardness results of samples by different PSD powder feedstocks are presented in Fig. 5.13(a). Significant microhardness difference is also not found. Fig. 5.13(b) shows the tensile properties of samples by different PSD powder feedstocks. High tensile strength over 1200 MPa and poor ductility around 5~6% for all samples are presented through tensile testing (two specimens were tested for each powder feedstock). Like microstructure and microhardness, negligible differences in tensile properties can be observed. The fracture surface morphology of tensile samples by different PSD powder feedstocks all shows typical brittle mode with quasi-cleavage and terrace-like features, as shown in Fig. 5.14.

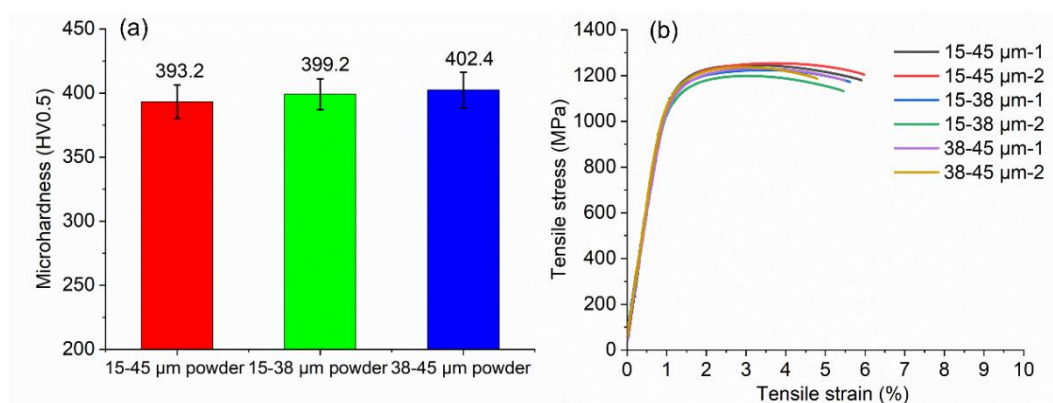


Fig. 5.13 (a) Microhardness results of as-built samples by different PSD powder feedstocks, (b) mechanical properties of tensile bars by 15-45 μm powder feedstock, 15-38 μm powder feedstock, 38-45 μm powder feedstock.

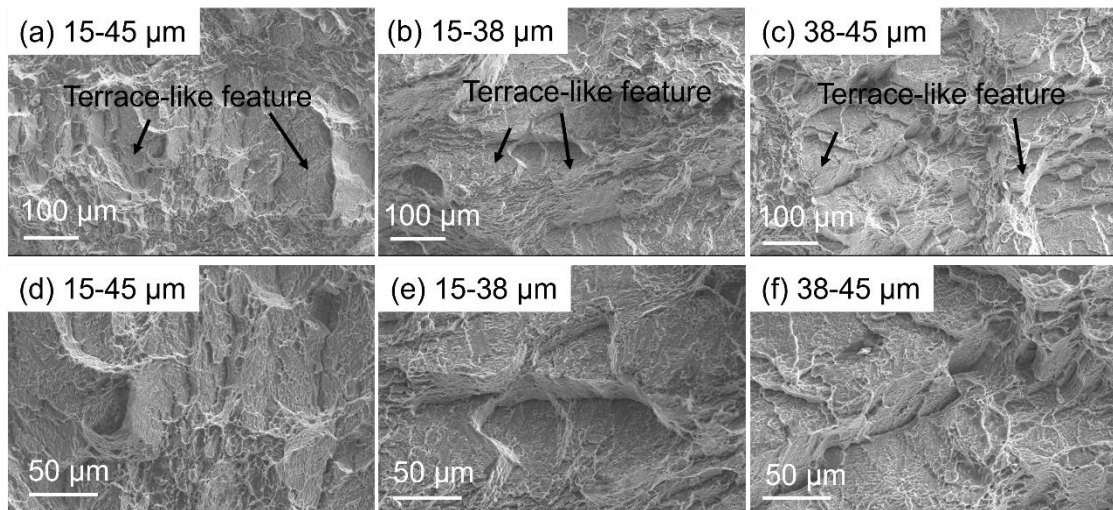


Fig. 5.14 Fractured morphology of tensile bars by (a) and (d) 15-45 μm powder feedstock, (b) and (e) 15-38 μm powder feedstock, (c) and (f) 38-45 μm powder feedstock.

5.4 Discussion

In this chapter, the surface quality, relative density, microstructure, and mechanical properties of as-built parts fabricated by different PSD powder feedstocks were assessed and compared. To understand the interactions between the laser and PSD powder, in-process powders and single-track formability analysis serve as key tools to reveal parts performance differences originating from PSD. It is possible to establish a link between parts performance and in-process powders and single tracks formability, which can further help to understand the role of PSD in the LPBF process and provide a feasible way to predict the performance of the parts through in-process powders and single-track formability.

5.4.1 Relationship between in-process powders and powder feedstocks

5.4.1.1 Spatter

In this chapter, powder feedstock-dependent spatter phenomena are presented. It is known that spatter is generated during the interactions between laser and powder. Three spatter generation mechanisms during LPBF are related to the LPBF process, namely droplet ejection spatter with large particle size (formed by the ejection of liquid metal away from the melt pool due to the rapid melt pool motion induced by high recoil pressure), and entrainment-driven spatter (hot spatter and cold spatter, formed from the

powder bed when a laser is scanned across the powder bed) [90,91]. The spatter collected around the gas outlet (GO spatter) consists of these three types of spatter. The coarse particles (over D90 of powder from powder bed) of GO spatter are most probably from droplet ejection spatter and hot spatter due to observed large size of spherical particles and agglomerated particles (see Fig. 5.3) [90]. The particle size of droplet ejection spatter is related to melt pool dynamics that may be associated with powder from the powder bed and laser processing parameters. Meanwhile, hot spatter is usually agglomerated particles due to the collision of other entrained particles, and it originates from powder from the powder bed. Therefore, the coarse particles of GO spatter may be positively correlated with the particle size of powder feedstock. Similarly, the fine particles of GO spatter should be from cold spatter [90] which is unprocessed particles from the powder bed, which is also proved by a positive correlation with the particle size of powder feedstock. Hence, the PSD of the spatter is quite dependent on the PSD of powder feedstock and that is why the particle size of the spatter by Powder 2 is also the smallest. As for the difference in spatter weight, there are two possible causes. First, based on the particle size characteristic of the three spatters, the spatter by Powder 2 with the smallest particle size may be blown away into the filter by gas flow much easier than that of Powder 1 and Powder 3. As a result, the spatter weight collected around the gas flow outlet will be the lowest by Powder 2. Another possible reason is less spatter generated during the interactions between laser and powder by Powder 2. Therefore, the fine particle size of the spatter by Powder 2 may not have a worse effect on as-built parts performance than that of Powder 1 and 3 based on the spatter behaviour analysis.

5.4.1.2 Powder from powder bed and overflow

In literature [56], when the layer thickness is low (e.g., 20, 30 μm), there is usually segregation of powder feedstock during the recoating process. As a result, powder from the powder bed shows smaller particle size characteristic while powder from overflow presents larger particle size characteristic than that of powder feedstock. However, this phenomenon did not occur in this study for all powder feedstocks, which means no significant effect of powder feedstocks on recoater spreading. The reason is probably caused by the powder condition before spreading. Powder feedstock in a small hopper was compressed by a powder compacting tool before spreading to achieve better spreading while powder feedstock was in loose condition before spreading in other studies. Therefore, powder after compression may have better packing efficiency to

make coarse particles (like more than 30 μm) spread in a powder bed than previous studies, which may be useful to remove the recoater effect on powder segregation.

5.4.2 Single-track evolution

From the morphology of single tracks by three powder feedstocks (see [Fig. 5.5](#)), although there is no huge difference for single tracks by three powder feedstocks at high power and high exposure time (i.e., high energy density), single tracks with better quality (more continuous) for Powder 2 and the worst quality for Powder 3 are observed at low laser power and low exposure time (i.e., low energy density). This is most probably because fine powder can be more easily fully melted while coarse powder may suffer inefficient melt when the laser power is insufficient or the scan speed is fast [227]. These results suggest the possibility of employing low energy density to achieve Ti-6Al-4V dense parts by LPBF.

The difference in the width of single tracks by three different PSD powders depends on the morphology of single tracks. Due to the more uniform and continuous tracks by Powder 2, the width of single tracks by Powder 2 looks larger than the other two powders based on the width measurement of single tracks. Powder 3 with more coarse particles has the lowest width. The surface roughness of LPBF fabricated cuboid parts by different powder feedstocks may also influence the single-track width. As the single tracks were built on LPBF fabricated parts and the surface roughness of the parts was different with low surface roughness by Powder 2 and high surface roughness by Powder 3 (see [Fig. 5.9](#)), there is a good correlation between surface roughness and track width results. This may be due to the higher surface roughness with more coarse particles affecting the stable melting of single tracks and resulting in the decrease of track width. The height profile results are generally consistent with the morphology and width of single tracks. Powder 2 can achieve a more uniform and stable height profile, which suggests the possibility of more uniform and stable melt pool tracks. As-built parts may also contain pores due to fluctuations in the height profile by Powder 1 and 3.

5.4.3 The link between parts performance and in-process powders and single-track formability

During the LPBF process, the surface quality of the as-built part is mainly derived from

the effect of particles attached to the surface (see Fig. 5.8). The particle size most probably plays a key role in surface quality. For top surface roughness, these particles are mainly from two aspects, one may be the spatter dropped on the top surface and spatter size is dependent on powder feedstock. Another may be the balling effect, through single-track analysis, Powder 2 with fine powder presents a better quality of tracks. Hence, spatter and single-track analysis are helpful signals for top surface quality of as-built parts. As for side surface roughness, partial sintering of particles from powder bed can be found (see Fig. 5.8), which suggests the close relationship between PSD of powder feedstock with side surface roughness.

The relative density of as-built parts is easily affected by some factors. The relative density results are compared in the case of different PSD powder feedstocks applied. Through spatter and single tracks analysis, spatter with large particles may be dropped in the powder bed and single tracks may not be stable for Powder 3 and 1, as a result, the as-built part by Powder 2 can obtain higher relative density due to the fine spatter and good single tracks quality, which is also convinced by other studies about the effect of spatter on the relative density [218,228]. Therefore, in-process powders and single tracks analysis are closely related to the surface quality and relative density of the as-built parts.

There is no significant difference in the observed microstructure between all powder feedstocks, which is also found in literature [147]. Although single-track width changes can be observed when using different processing parameters and PSD powder feedstocks, there is no significant change (the difference is less than 4.0 μm) when using the same default processing parameters (used for microstructure and mechanical properties analysis) for the three PSD powder feedstocks. Therefore, the consistent track width may be one of the reasons for this consistent microstructure. Consistent microstructures may be expected due to the similar melting and solidification under high cooling rates during LPBF using the same processing parameters. Due to the similar microstructure (columnar prior- β grain boundaries with martensite α') using different PSD powder feedstocks, the mechanical properties are also consistent. Other strategies from powder feedstock consideration like chemical composition modification are planned to tailor the microstructure and mechanical properties due to the negligible effect of PSD on the microstructure and mechanical properties of Ti-6Al-4V.

5.5 Conclusions

Effects of different PSD Ti-6Al-4V powders on in-process powders and single-track formability by LPBF were systematically investigated. Three powder feedstocks show obvious particle size differences, and all have sufficient flowability. The results indicate that the recoater has almost no effect on powder segregation during powder spreading for all powder feedstocks. There are obvious differences in powder behaviour using different PSD powder feedstocks. Spatter with small particle size and less collected weight is observed in 15-38 μm powder while 38-45 μm powder shows much coarse spatter and more collected weight, which means fewer defects by using fine powder feedstock. Fine 15-38 μm powder presents better single-track formability than standard 15-45 μm powder and coarse 15-38 μm powder. The width of single tracks by fine 15-38 μm powder is slightly larger than the others. Height profile measurement suggests that balling tracks show fluctuation while continuous tracks present good stability. Meanwhile, 15-38 μm powder has more stable tracks compared to 15-45 μm powder and 38-45 μm powder at low power and high power. Enhanced surface quality and better relative density can be achieved by fine 15-38 μm powder, which has a high correlation with the results of in-process powders and single tracks formability. In-process powders and single-track formability might play as good signals to predict the performance of as-built parts by different PSD powder feedstocks. There is no obvious change in microstructure and mechanical properties when using different PSD powder feedstocks, which suggests the limited functions of PSD tool to tailor the microstructure and mechanical properties of Ti-6Al-4V by LPBF. Therefore, next chapters will focus on the microstructure and mechanical properties optimisation of Ti-6Al-4V.

6 Chemical composition modification of Ti-6Al-4V alloy via CP Ti addition by LPBF

6.1 Introduction

In Chapter 5, the effect of different PSD powder feedstocks on the performance of Ti-6Al-4V by LPBF was investigated. An obvious influence on surface roughness and a slight influence on relative density can be found. However, it is found that there are no significant differences in microstructure and mechanical properties when using different PSD powders. It is therefore essential to tailor the microstructure and mechanical properties in other ways to achieve the desired performance.

Ti-6Al-4V alloy fabricated by LPBF generally exhibits columnar prior- β grain boundaries with acicular martensite α' structures. This can be attributed to the high temperature gradient and the high cooling rate experienced during cyclic heating and cooling in LPBF [12,136]. The mechanical properties of as-fabricated Ti-6Al-4V are typically high in tensile (~ 1200 MPa) and yield strength (~ 1100 MPa) but low in ductility ($< 10\%$) [12,136,193,229]. The brittleness of as-built Ti-6Al-4V alloys by LPBF may cause build failure by cracking or delamination of the parts that cannot accommodate thermal stresses created during the process via plastic deformation [3,12]. This distinct microstructure and mechanical performance observed in Ti-6Al-4V by LPBF is also presented in this thesis, as shown in Chapter 5.

Parts made from Ti-6Al-4V by LPBF have a high strength (more than 1200 MPa), which makes a decrease in strength acceptable in exchange for a greater ductility. To achieve a balanced strength-ductility of Ti-6Al-4V, it is therefore reasonable to consider modifying the initial feedstock composition. By introducing CP Ti to Ti-6Al-4V powder feedstock to form new compositions, it is possible to produce compositions with higher ductility. It is also possible to tailor the composition in situ to achieve controllable microstructures that are hard to obtain using pre-alloyed powders.

This chapter combined Ti-6Al-4V (called PT0 for comparison, no CP Ti addition) powder with CP Ti powder to produce two nominal Ti-4.5Al-3V (called PT25, CP Ti addition with 25 wt.%) and Ti-3Al-2V (called PT50, CP Ti addition with 50 wt.%). To provide a reference, the closest alloys to this grade are Ti-4Al-2V (TA17) alloy and Ti-

3Al-2.5V (Grade 9) respectively. An extensive microstructural characterisation (including OM, SEM, XRD, EBSD) was conducted, as well as tensile testing. The mechanical properties of the materials are discussed in detail, with reference to the observed microstructures. Therefore, in this chapter, tunable microstructure and balanced strength-ductility are expected in the as-built state through the chemical composition modification of Ti-6Al-4V powder feedstock. Also, the understanding of strength and ductility mechanisms is crucial.

6.2 Experimental

Plasma atomised Ti-6Al-4V (Grade 23, 15-45 μm , called PT0 in this chapter) and spherical CP Ti (Grade 1, 38-63 μm) were blended to produce nominal Ti-4.5Al-3V (called PT25, CP Ti addition 25 wt.%) and nominal Ti-3Al-2V (half of Ti-6Al-4V, called PT50, CP Ti addition 50 wt.%) respectively. For each powder feedstock (PT0, PT25 and PT50), cubic samples with size 10x10x5 mm³ and tensile bars with $\Phi 9 \times 60$ mm were fabricated using a Renishaw AM400 LPBF inserted RBV with default processing parameters (same as Chapter 4 and 5).

The as-fabricated samples were cut, mounted, grinded and polished for porosity and microstructure analysis by OM and SEM images. Chemical homogeneity of three Ti alloys was obtained by SEM with EDS. Microstructure and crystallographic were further analysed by XRD and EBSD. Microhardness and tensile testing were performed to assess the mechanical properties of three Ti alloys. The fracture morphology of the specimens after tensile testing was observed by SEM. Fractured PT0 and PT50 after tensile testing were also analysed by EBSD to explain the enhanced ductility in PT50.

6.3 Results

6.3.1 Relative density and homogeneity

The relative density of PT0, PT25, and PT50 by LPBF after polishing was observed by optical microscopy images (two images captured for each sample), as presented in [Fig. 6.1](#). The porosity levels of PT0 and PT25 were similar ($\sim 0.02\%$, relative density $\sim 99.98\%$) by ImageJ analysis. There is a slight increase in porosity in the PT50 ($\sim 0.07\%$, relative density $\sim 99.93\%$). This increase in porosity for PT50 may be mainly from the increased particle size in the PT50, which has been confirmed by the results in Chapter

5, namely, powder feedstock with more coarse particles would increase the porosity. In addition, although chemical composition changed in the PT50 when using the same processing parameters, the thermal properties (melting point, thermal conductivity, etc) for CP Ti and Ti-6Al-4V are similar [38] and Sangali et al. [230] presented high relative density in layered CP-Ti/Ti-6Al-4V composites by LPBF using same processing parameters for CP Ti and Ti-6Al-4V. Therefore, the effect of changed chemical composition may have a negligible effect on increased porosity. The relative density of all samples was high (over 99.90%), even when the CP Ti content was as high as 50 wt.%.

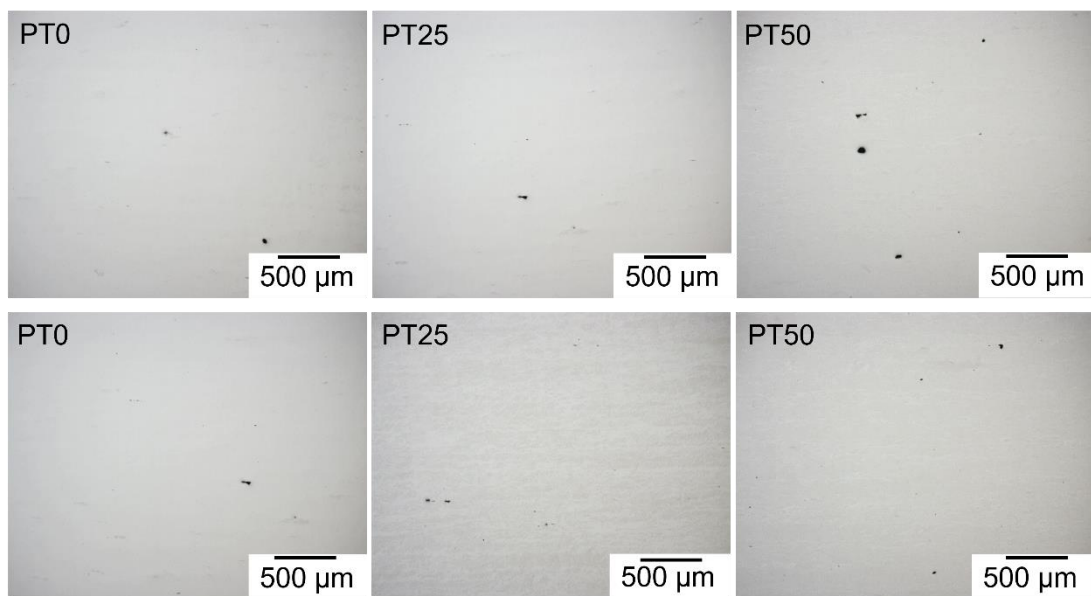


Fig. 6.1 Porosity (relative density) of as-fabricated PT0, PT25, and PT50 captured by optical microscopy images.

All three as-fabricated Ti alloys are presented in Fig. 6.2 to observe the elemental distribution of Ti, Al, and V as elemental segregation may occur when using in-situ alloying for LPBF [231]. BSE images can be used to directly observe the homogeneity of elements. As for PT0, it appears homogeneous without apparent heterogeneities in either BSE or EDS imaging (see Fig. 6.2(a1-a4)) since PT0 is pre-alloyed Ti-6Al-4V. In BSE images, notable areas of dark contrast can be observed in conjunction with CP Ti addition (PT25 and PT50). The elemental distribution of Ti, Al, and V can be seen on the EDS area maps. It is evident that the Al-poor areas in the PT25 and PT50 correspond to the dark areas in the BSE images. The PT25 and PT50 images also show relatively poor V areas corresponding to dark areas in the BSE images. Because of the small

difference between CP Ti and Ti-6Al-4V considering Ti element, these non-uniform areas are most likely Ti rich areas. However, Ti maps do not clearly identify these areas as Ti rich areas. According to the area maps of the EDS for PT0, PT25, and PT50, the average elemental content for the three areas in Fig. 6.2 is shown in Table 6.1. Of particular note is the fact that Al and V content in PT25 (4.9 wt.% and 3.0 wt.%) and PT50 (3.1 wt.% and 1.8 wt.%) are close to those of Ti-4.5Al-3V and Ti-3Al-2V alloys, respectively. In addition, point analysis of EDS for as-fabricated PT0, PT25 and PT50 in microstructure images (see Fig. 6.4(g-i)) is shown in Table 6.2. It corresponds well to the point and area of EDS results for Al and V content.

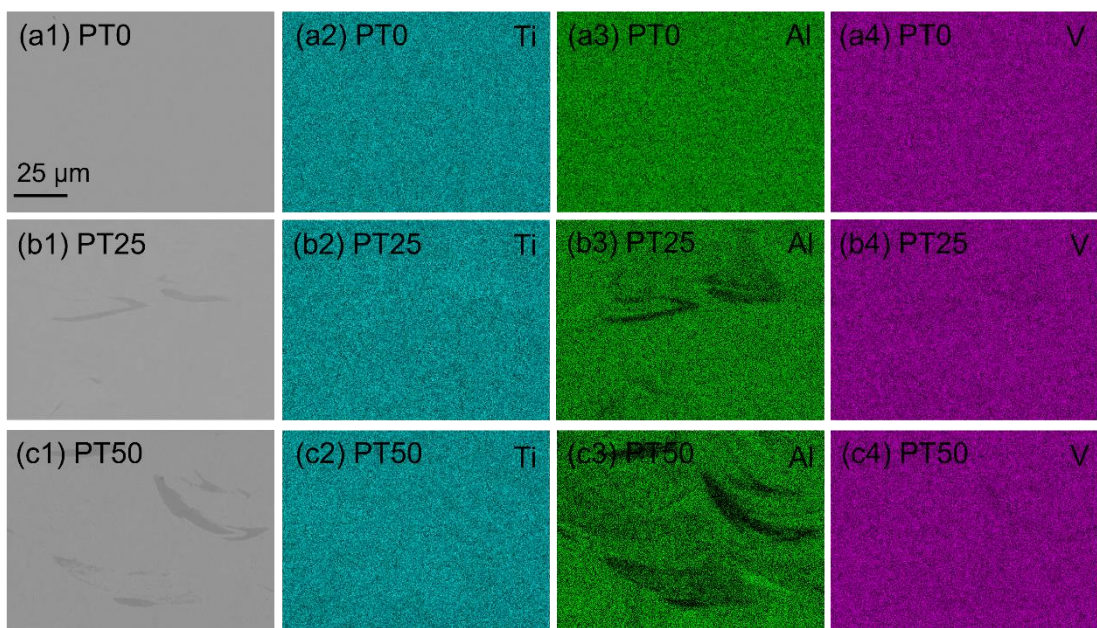


Fig. 6.2 Backscattered electron (BSE) images and EDS area maps of as-fabricated (a1-a4) PT0, (b1-b4) PT25, and (c1-c4) PT50.

Table 6.1 The average elemental content for PT0, PT25 and PT50 from the EDS area maps in Fig. 6.2.

Sample	Ti (wt.%)	Al (wt.%)	V (wt.%)
PT0	Bal.	6.3	3.9
PT25	Bal.	4.9	3.0
PT50	Bal.	3.0	1.8

Table 6.2 The point analysis (in Fig. 6.4(g-i)) of EDS for as-fabricated PT0, PT25 and PT50.

Sample		Ti (wt.%)	Al (wt.%)	V (wt.%)
PT0	1	Bal.	6.2	3.5
	2	Bal.	6.1	3.7
	3	Bal.	6.3	3.7
	4	Bal.	6.2	3.3
	5	Bal.	6.1	3.5
	6	Bal.	6.4	3.4
	average	Bal.	6.2	3.5
PT25	7	Bal.	4.5	2.7
	8	Bal.	5.0	3.2
	9	Bal.	4.6	2.9
	10	Bal.	5.4	3.2
	11	Bal.	5.2	2.9
	12	Bal.	4.4	3.0
	average	Bal.	4.8	2.9
PT50	13	Bal.	3.3	1.8
	14	Bal.	2.8	1.5
	15	Bal.	2.9	1.5
	16	Bal.	3.2	1.5
	17	Bal.	3.3	1.6
	18	Bal.	3.2	1.7
	average	Bal.	3.1	1.6

6.3.2 Microstructure analysis

Fig. 6.3 shows the XRD results for phase identification of as-fabricated PT0, PT25 and PT50. The as-fabricated samples show all peaks to be HCP structures without obvious BCC structures [193]. As can be seen in Fig. 6.3(b) and Table 6.3, there are some slight differences in peak positions among the samples. As the amount of CP Ti is increased, there is a left shift trend. In accordance with the Bragg equation, the interplanar d-spacing value increases with a decrease in the 2-theta degree position (left shift). There

is evidence that the atomic radius of Ti (0.147 nm) is higher than Al (0.143 nm) and V (0.132 nm) [26]. Therefore, PT25 and PT50 have higher d values as Ti content increases and Al and V content decreases (i.e., decreased solid solution effect). The c/a ratio in HCP structure can be calculated by rearranging the Bragg equation [127]:

$$\sin \theta = \frac{\lambda}{2} \sqrt{\frac{4(h^2+hk+k^2)}{3a^2} + \frac{l^2}{c^2}} \quad (1)$$

Where θ is the diffraction angle (2θ related to peak position); λ is the wavelength of the X-ray (1.5406 Å); h, k and l are Miller indices; a and c are the hexagonal lattice parameters. For calculating c, a, and c/a, six main diffraction peaks are considered. According to the XRD results, the c/a ratio decreases with increasing CP Ti addition from 1.5966 for PT0 to 1.5918 for PT50 (see Table 6.3). These c/a ratios for PT0, PT25 and PT50 can be employed for deformation mechanisms analysis and will be presented in the Discussion section.

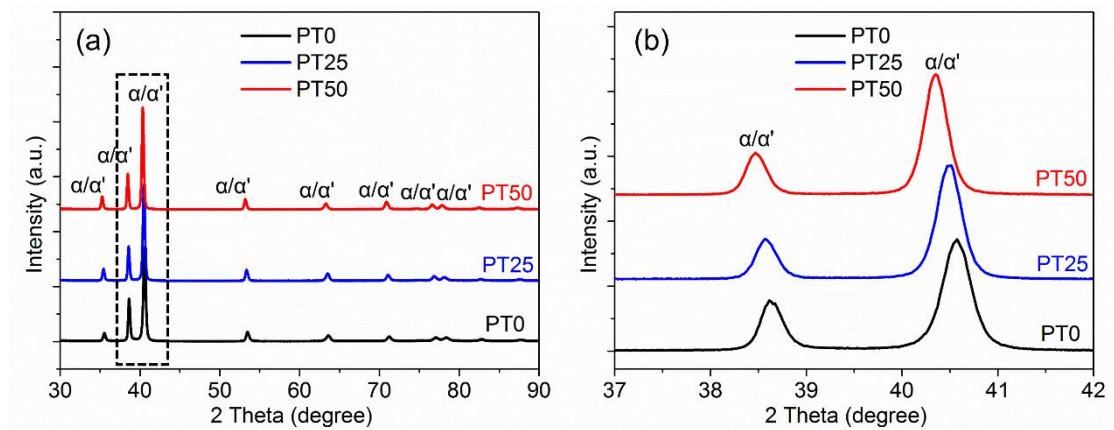


Fig. 6.3 XRD results of as-fabricated PT0, PT25 and PT50.

Table 6.3 XRD data of as-fabricated PT0, PT25, and PT50.

Sample	2θ in (002)	2θ in (101)	c/a
PT0	38.62	40.57	1.5966
PT25	38.59	40.51	1.5934
PT50	38.49	40.35	1.5918
Standard α -Ti HCP [232]	38.45	40.18	1.587

Optical microscopy images of as-fabricated PT0, PT25 and PT50 samples after etching are depicted in Fig. 6.4(a-c). All samples present typical columnar prior- β grain

boundaries with fine martensite α' at an angle of around ± 45 degrees [102], caused by cyclic heating and cooling in LPBF process. The length of prior- β grains might amount to several millimeters and their width ranged from 60 to 80 μm . This distance corresponds to the hatch distance used and is consistent with literature [100]. The martensite α' structure can be further observed by SEM images with high magnification in Fig. 6.4(d-i). A range of acicular martensite α' structures are observed in PT0 (i.e., Ti-6Al-4V) (Fig. 6.4(d, g)). While martensite can form laths of varying thickness, it tends to form a thicker structure. The measured average martensite α' thickness for as-fabricated PT0, PT25 and PT50 are $0.44 \pm 0.18 \mu\text{m}$, $0.61 \pm 0.29 \mu\text{m}$, $0.75 \pm 0.28 \mu\text{m}$, respectively, which further suggests the effect of reduced solid solution element Al and V content on the martensite α' structure [38].

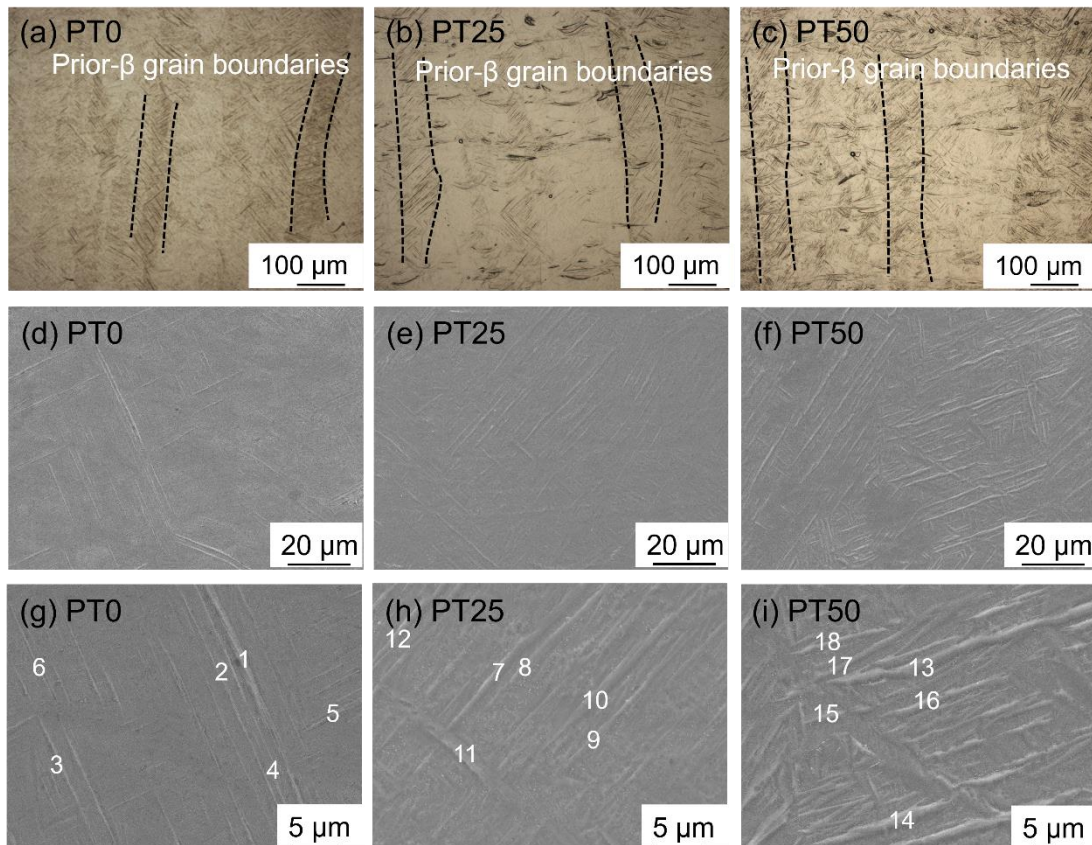


Fig. 6.4 Microstructure of as-fabricated (a, d, g) PT0, (b, e, h) PT25, and (c, f, i) PT50 by OM and SEM. An increasing trend in martensite α' thickness can be observed in SEM images when CP Ti addition increases. Numbers 1-18 in (g-i) are EDS points for elemental composition analysis.

Inverse pole figure (IPF) maps and misorientation distribution of as-fabricated PT0,

PT25, and PT50 are presented in Fig. 6.5. PT50 presents wider martensite α' structures than PT0 (Fig. 6.5(a-c)). This agrees with SEM results. Fig. 6.5(d-f) shows the misorientation distribution results. There is a predominated misorientation angle of $\sim 63.26^\circ$ for all samples, which is consistent with other LPBF and DED Ti-6Al-4V parts with columnar prior- β grains [118,233]. Fig. 6.6 presents the low angle grain boundary (LAGB, $2-10^\circ$, red colour) and high angle grain boundary (HAGB, $>10^\circ$, blue colour) of as-fabricated PT0, PT25, and PT50. LAGBs tend to increase with increasing CP Ti addition (from 5.65% to 9.64% to 11.4%) (see Fig. 6.6(a-c)). A comparison of kernel average misorientation (KAM) maps for all Ti-Al-V alloys is also provided, as shown in Fig. 6.6(d-f). KAM associated with geometrically necessary dislocation (GNDs) are accumulated in strain gradient fields which are caused by geometrical constraints on the crystal lattice. Accordingly, KAM increases with CP Ti addition in a similar manner to LAGB, suggesting more local misorientation for PT25 (average $\sim 0.820^\circ$) and PT50 (average $\sim 0.869^\circ$) compared to PT0 (average $\sim 0.656^\circ$).

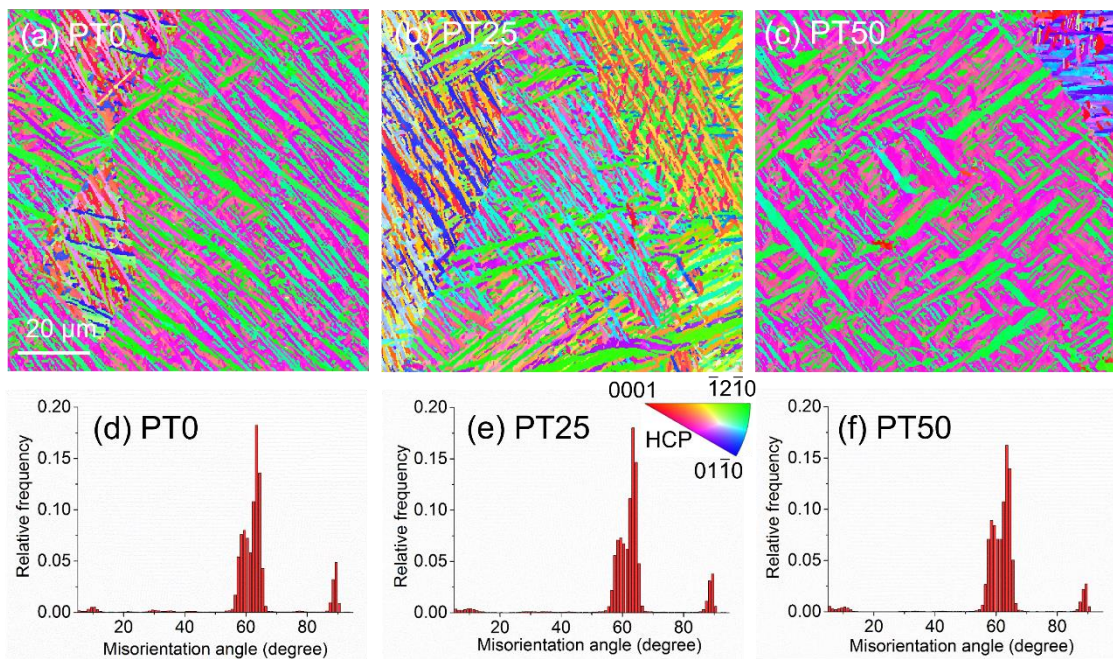


Fig. 6.5 IPF maps and misorientation distribution of as-fabricated (a, d) PT0, (b, e) PT25, and (c, f) PT50.

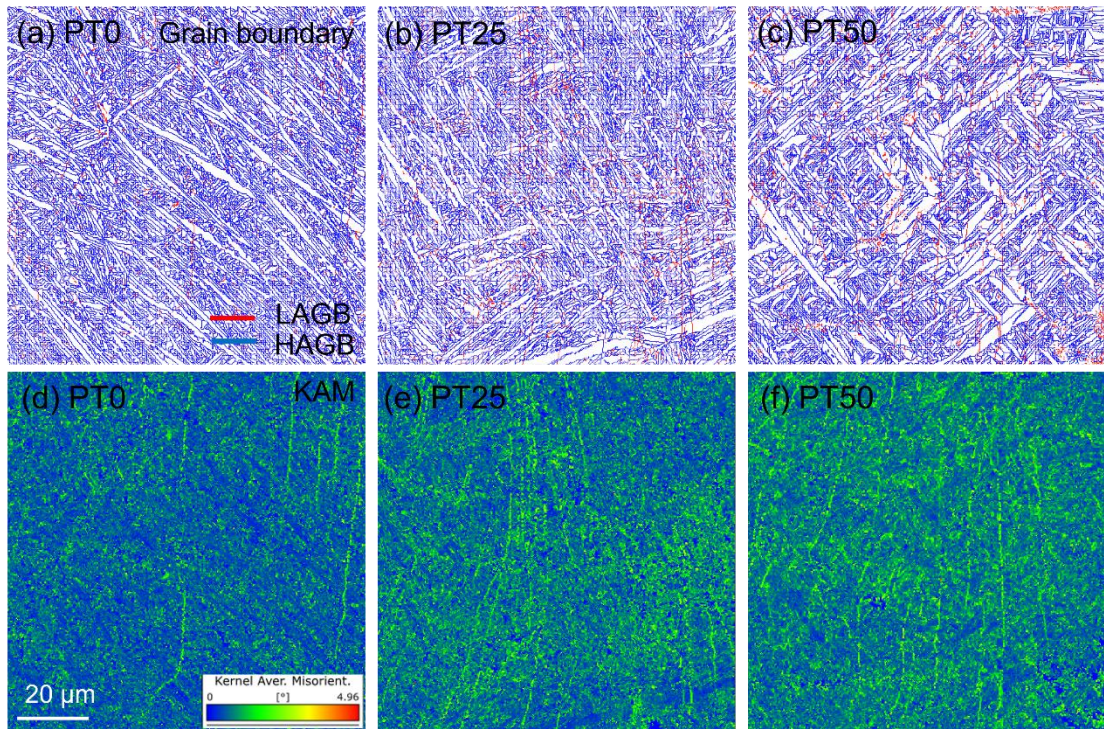


Fig. 6.6 Grain boundary distribution (LAGB, HAGB) and KAM maps of as-fabricated (a, d) PT0, (b, e) PT25, and (c, f) PT50.

6.3.3 Mechanical performance

Before tensile testing, the microhardness of all samples is first performed. PT0, PT25, and PT50 microhardness data (48 indentations for each sample using 500 gf and a dwell time of 10 s) are presented in Fig. 6.7. A decrease in microhardness is evident with CP Ti addition into Ti-6Al-4V, suggesting a reduction in strength. There is a hardness difference of around 38 HV0.5 between PT0 ($\sim 389.1 \pm 8.45$ HV0.5) and PT25 ($\sim 352.6 \pm 11.95$ HV0.5), as well as between PT25 and PT50 ($\sim 312.7 \pm 14.80$ HV0.5).

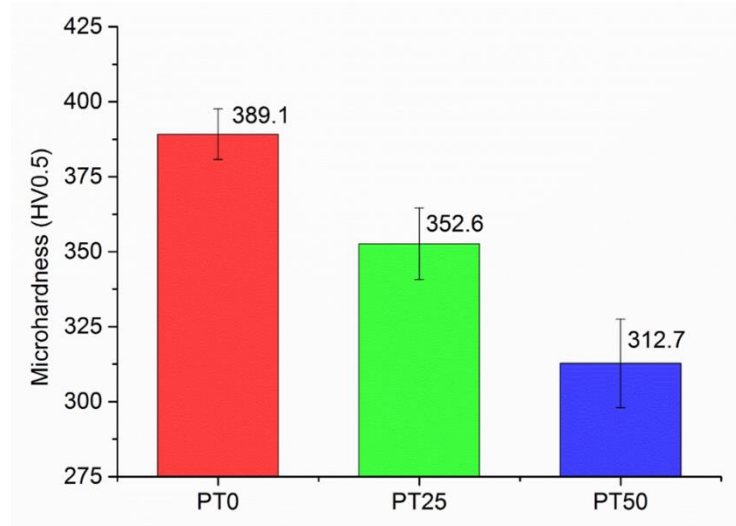


Fig. 6.7 Microhardness results of the as-fabricated PT0, PT25 and PT50 exhibit a reduction in microhardness when CP Ti addition increases, error bars are standard deviation of 48 indentations in each sample.

Tensile testing is employed to assess the mechanical properties of all samples. Fig. 6.8(a) shows tensile properties of all Ti-Al-V samples. Table 6.4 provides the Young's modulus, the tensile strength, the yield strength, and the elongation at break for each Ti alloy (two samples were tested for each Ti alloy). There is a negligible effect of CP Ti addition into Ti-6Al-4V for the Young's modulus in all samples. The mechanical properties of PT0 (Ti-6Al-4V) are in good agreement of LPBF produced Ti-6Al-4V in other literature [12,192,193], with a high strength (tensile strength >1200 MPa) but low ductility (< 10%). The as-fabricated PT0 with low ductility (~4-6%) agrees well with other literature [12,192,193,229,234] in as-fabricated Ti-6Al-4V with elongation around 6% or below 6% by LPBF. Although a dropping trend in strengths can be observed when CP Ti additions increases, the tensile strength (~1000 MPa) and yield strength (~900 MPa) in PT50 are still relatively high. The martensite α' structures observed in the PT50 most likely explains the relatively high strengths. Notably, the tensile properties may also be better than as-cast Ti-6Al-4V alloy [235]. Notably, the elongation of PT50 significantly enhanced by over twice compared to the as-fabricated PT0 (from ~4.3% and ~6.1% for PT0 to ~12.3% and ~13.1% for PT50). The tensile properties of the as-fabricated PT50 also satisfy the annealed wrought Ti-6Al-4V standard [172]. Hence, through Ti-6Al-4V in-situ composition tailoring, balanced strength-ductility of as-fabricated PT50 can be realised. The tensile properties comparison in those as-fabricated and heat treated Ti-6Al-4V from the literature with the present work in PT0, PT25, PT50 is shown in Fig.

6.8(b). The mechanical properties of as-fabricated PT50 are comparable with Ti-6Al-4V after heat treatment found in the literature. That is to say that the elongation ~13% of as-fabricated PT50 typically locates in the range of heat treated Ti-6Al-4V (over 10%).

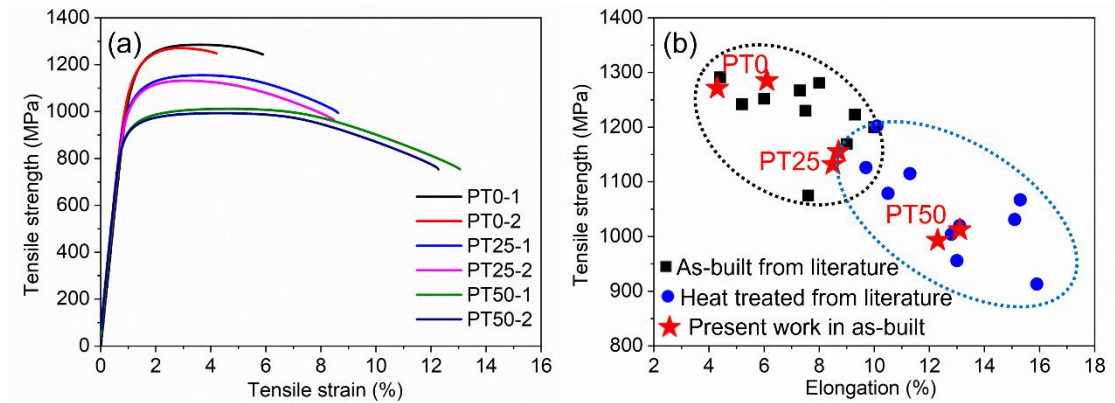


Fig. 6.8 (a) Tensile properties of as-fabricated PT0, PT25, PT50 and (b) comparison with as-fabricated and heat-treated Ti-6Al-4V by LPBF from literature [12,101,229,236–241,102,103,120,136,169,170,192,193] indicating comparable mechanical properties in PT50 with Ti-6Al-4V by heat treatment.

Table 6.4 Young’s modulus, tensile strength, yield strength, elongation at break of as-fabricated PT0, PT25 and PT50.

Sample	Young’s modulus E (GPa)	Tensile strength (MPa)	Yield strength (MPa)	Elongation (%)
PT0-1	115	1285	1128	6.1
PT0-2	116	1271	1118	4.3
PT25-1	119	1155	1009	8.7
PT25-2	112	1132	1011	8.5
PT50-1	118	1012	895	13.1
PT50-2	115	993	890	12.3

To further confirm the ductility and fracture modes of all samples, Fig. 6.9 compares the fracture morphology of all three tensile samples. For as-fabricated PT0 (Ti-6Al-4V), there are typical terrace structures with some small areas of shallow dimples (see Fig. 6.9(a, d)), which is in agreement with the literature [136]. Intergranular α/α' and along the prior- β grain boundaries may be the dominant fracture mode, which suggests the dominance of a brittle fracture mode of as-fabricated Ti-6Al-4V. There is a decrease in

the terrace structure while larger and deeper dimples can be observed in PT25 compared to the as-fabricated PT0, as presented in Fig. 6.9(b, e). These characteristics suggest a mixed brittle-ductile fracture mode observed in PT25. A fracture morphology with significantly deeper and larger dimples (no apparent terrace structure) can be found in the PT50 (Fig. 6.9(c, f)). Hence, a ductile fracture mode dominates in the PT50 and is in good agreement with the good ductility of as-fabricated PT50 in tensile testing (see Fig. 6.8 and Table 6.4) and other heat treatment works [169,236].

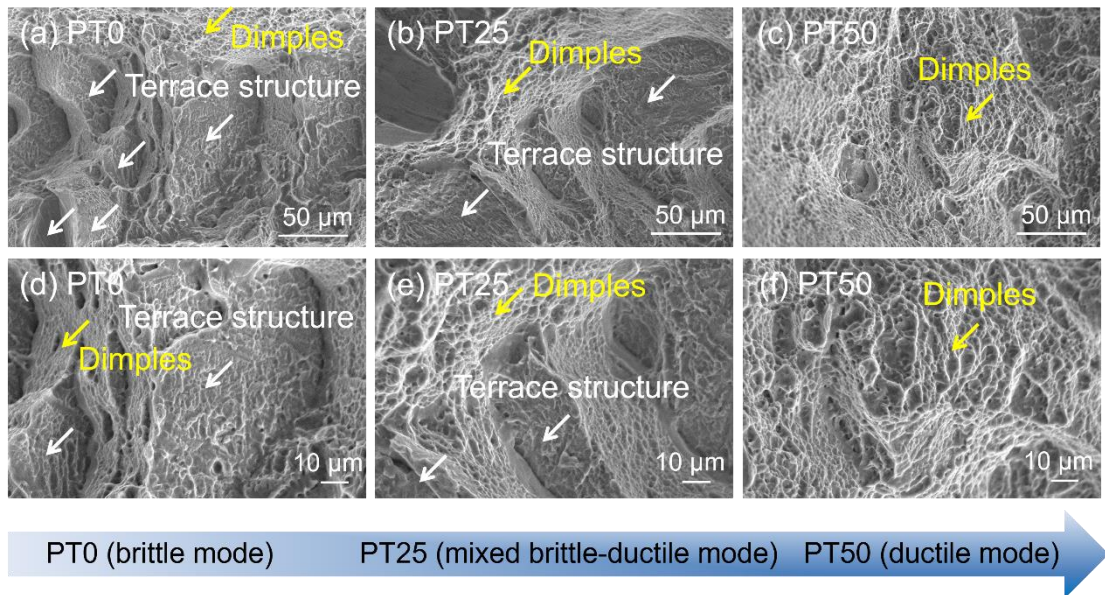


Fig. 6.9 Fracture surface morphologies of as-fabricated (a, d) PT0, (b, e) PT25, and (c, f) PT50, indicating the fracture mode transferred from brittle to mixed brittle-ductile to ductile mode.

6.4 Discussion

This chapter presents experimental results of in-situ alloying through modifying Ti-6Al-4V. Balanced strength and ductility of PT50 is achieved in as-fabricated state via an easy in-situ alloying way without post heat treatment. It is essential to link this in-situ alloying strategy with observed results (such as microstructure and tensile properties). The chemical homogeneity, microstructure, mechanical properties mechanisms will be discussed to understand the role of this in-situ alloying and composition tailoring strategy in this chapter.

6.4.1 Chemical homogeneity

Chemical homogeneity is a crucial and inevitable challenge for in-situ alloying in LPBF despite the advantages of in-situ alloying with cost-saving and time-saving for new alloy development [231]. In-situ alloying using a combination of pre-alloyed and corresponding elemental metal (such as Ti-6Al-4V with CP Ti) was carried out in this chapter, which is different with other literature by all elemental alloying or pre-alloyed with other metals. Differences can be observed in the elemental distribution for PT25 and PT50 compared to other in-situ alloying work. Less fluctuation in elemental concentration from the minor alloying elements across the part is presented in the LPBF parts fabricated from Ti-6Al-4V and CP Ti powder feedstocks in comparison to the in-situ alloying of Ti-6Al-4V using Ti, Al, and V element, reported by Simonelli et al. [242]. This can be explained that at the length scale of tens to hundreds of μm both CP Ti and Ti-6Al-4V powder feedstocks present consistently above 90 wt.% Ti with no area rich in Al (less than 10 wt.%) and V (less than 10 wt.%). Locally rich areas of Al or V may form with high concentration (over 10%) at these length scales by in-situ alloying with Ti, Al, and V elements. The precise contribution of these as a function of number density and size may be hard to assess. Laser melting and cooling process during the LPBF is limited in achieving the necessary melt lifetime or melt size to obtain sufficient homogenization of separate elements in typical powder size ranges (less than $63\ \mu\text{m}$). From microhardness results in Fig. 6.7, although there are fluctuations in different areas even for pre-alloyed Ti-6Al-4V because of the presence of martensite α' and α , these fluctuations are not significant in comparison to the absolute value ranges of almost microhardness values, whereby minimum overlap of hardness ranges is observed (367.8-407.7 HV0.5 for PT0, 327.6-374.8 HV0.5 for PT25, 277.9-341.6 HV0.5 for PT50). This also suggests good metallurgical fusion of Al and V for PT25 and PT50.

Although there is a segregation phenomenon for Al and V, this segregation may not be severe. This is because the non-uniform area is around 1.4% for PT25 and approximately 3.4% for PT50 based on BSE images. This suggests that the whole segregation may be acceptable despite the formation of local segregation. Compositions to be closely representative of pre-alloyed equivalents may be expected, which means the capability of composition tailoring to obtain desired mechanical performance. Because of the expected and good mechanical properties achieved in this chapter, the

low-level segregation may have a minor or limited effect on mechanical properties. Some possible ways can be considered to obtain excellent homogeneity and eliminate segregation. Firstly, a higher energy density to achieve deeper melt pools could improve mixing effect [158]. Brodie et al. [243] demonstrated that segregation could also be eased significantly by remelting scanning strategy. Heat treatment is also a potential method to reduce segregation. A suitable heat treatment should be carried out in the high region of the $\alpha+\beta$ phase field (below the β transus temperature) to facilitate solid state diffusion of the Al and V elements. Further optimised processing parameters can also be considered to achieve a more uniform composition and better strength-ductility in the as-fabricated state.

6.4.2 Composition-dependent microstructure

A summary of the relationship between composition and microstructure for all samples is shown in Fig. 6.10. Two martensitic types (α' and α'') after rapid cooling for Ti alloys are usually observed [38]. It is believed that α' is the main non-equilibrium phase rather than the α'' phase for all three samples. Firstly, α and α' show an HCP structure while α'' is an orthorhombic structure [38,127]. It may be hard to distinguish α and α' by using XRD while it is possible to detect α'' from α and α' . This is confirmed by an $\alpha+\beta$ type titanium (Ti-6Al-2Sn-4Zr-6Mo) by LPBF [127]. Secondly, α'' is usually found in Ti alloys with a higher concentration of β stabilisers (i.e., higher [Mo]eq.). It is thought that the formation of martensite α'' in developed Ti alloys is unlikely due to the decrease in [Mo]eq. for PT25 and PT50 [38]. Low yield strength (around 500-600 MPa) can usually be observed in Ti alloys with α'' martensite dominated structures [127,128]. The yield strengths of the PT0, PT25 and PT50 are around 1122 MPa, 1010 MPa and 893 MPa, respectively. Those are obviously higher than 600 MPa. Finally, there is some literature [244,245] exhibiting martensite α' of Ti-3Al-2.5V (close to PT50) after fast cooling (such as during welding [245]).

Wider martensite α' structures can be found in the PT25 and PT50 than in PT0. This increased width of the martensite α' structure (see Fig. 6.4 and Fig. 6.5) should be from the reduced Al and V solute content in the PT25 and PT50. This phenomenon is well understood in literature [38]. Acicular martensite is generally found in high solute content Ti alloys (Ti-6Al-4V) with a lower martensitic transformation temperature, while lath (also called massive or packet) martensite might be typically observed for

more dilute solute content Ti alloys (e.g., PT25 and PT50) with a higher martensite transformation temperature.

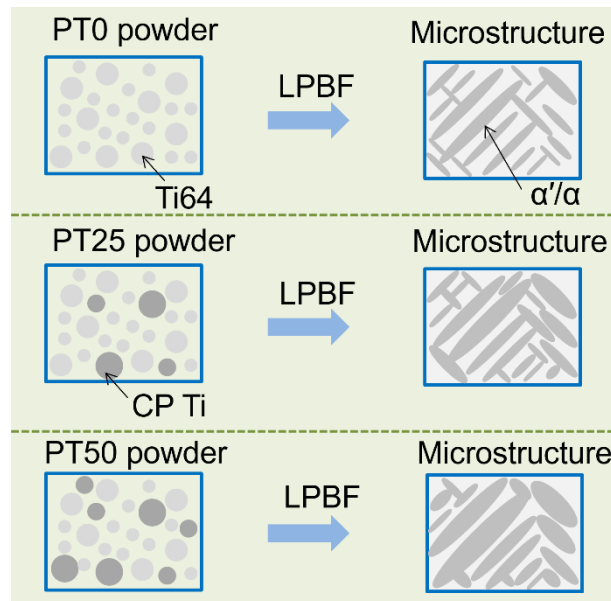


Fig. 6.10 The summary of composition-microstructure relationship by using simply mixed feedstock.

6.4.3 Composition-dependent mechanical properties

6.4.3.1 Mechanisms of ductile behaviour

It is known that the c/a ratio plays an important role in determining the deformation mode of α and $\alpha+\beta$ titanium alloys [106]. High c/a ratio (over 1.630) Ti alloys usually show basal slip and twinning while basal slip, prismatic slip, and pyramidal slip may be activated in low c/a ratio Ti alloys (less than 1.630) [133], suggesting better ductility in low c/a ratio Ti alloys than high c/a ratio Ti alloys based on the dislocation slip mechanism. It is known that a low c/a ratio (~ 1.587) CP Ti by LPBF usually exhibits good ductility (at least around 20%) [232,246,247]. As mentioned before, the c/a ratios in PT0, PT25, and PT50 are 1.5966, 1.5934 and 1.5918, respectively. Basal slip $\{0002\}\langle 11\bar{2}0\rangle$ dominates in the PT0 (Ti-6Al-4V) fabricated by LPBF showing poor ductility in the as-fabricated state [101]. This is because higher c/a ratios with high Al content (such as PT0) increase the basal plane spacing and decrease the prismatic plane spacing [167]. The increase in the prismatic plane spacing (c/a ratio decreases) enhances the prismatic slip rather than basal slip [106]. The decrease in the c/a ratio in PT25 and PT50 may exhibit a lower $CRSS_{prism}/CRSS_{basal}$ ratio compared to PT0. As a result,

multiple slip modes may be activated in the low c/a ratio Ti alloys during tensile deformation, which is confirmed by comparison of Ti-6Al-4V (c/a ratio 1.596) and Ti-4Al-4V (c/a ratio 1.594) [167]. In addition, fractured tensile samples analysed by EBSD (Fig. 6.11) also suggest improved dislocation slips for PT50. More regions with higher local misorientation (average $\sim 1.448^\circ$) based on EBSD KAM maps associated with geometrically necessary dislocations for PT50 after tensile testing can be achieved compared to PT0 (average $\sim 1.022^\circ$), which suggests a high density of dislocations and increased dislocation slip in the PT50. Qiu et al. [248] also demonstrated dominance of dislocation slip by EBSD KAM in a beta titanium alloy by LPBF to obtain good ductility. Meanwhile, the number of LAGBs in PT50 after tensile testing is obviously higher (44.9%) than in PT0 (24.2%), as shown in Fig. 6.11. The LAGB is normally composed of a periodic crystal dislocation arrangement [133]. Hence, extensive dislocation slip events may be expected in PT50, contributing to higher ductility. In addition, it is known that dislocation slip and deformation twinning are the main deformation modes for α and $\alpha+\beta$ titanium [38]. Therefore, investigating the contribution of deformation twinning for Ti alloys by LPBF is also crucial. Through EBSD band contrast (BC) + special boundaries (SB) maps (Fig. 6.11(c, f)), a small amount of $\{10\bar{1}2\}\langle 10\bar{1}\bar{1}\rangle$ (i.e. $85^\circ\langle 11\bar{2}0\rangle$) twins with around 2.64% in as-fabricated Ti-6Al-4V can be observed while as-fabricated nominal Ti-3Al-2V shows $\{10\bar{1}2\}\langle 10\bar{1}\bar{1}\rangle$ twins with around 1.44%. Therefore, both samples present a small contribution of twinning during deformation, and the nominal Ti-3Al-2V (PT50) sample seems to suggest a weaker contribution of twinning. This may suggest the weak contribution to ductility from deformation twinning. This further suggests the increased dislocation slip on improvement of ductility by PT50 compared to PT0. In addition, PT0, PT25 and PT50 mainly present the α/α' Ti-HCP phase in the as-fabricated condition as checked by XRD and microscopy. This may suggest the negligible or minor effect of retained β phase on ductility due to limited content of retained β phase.

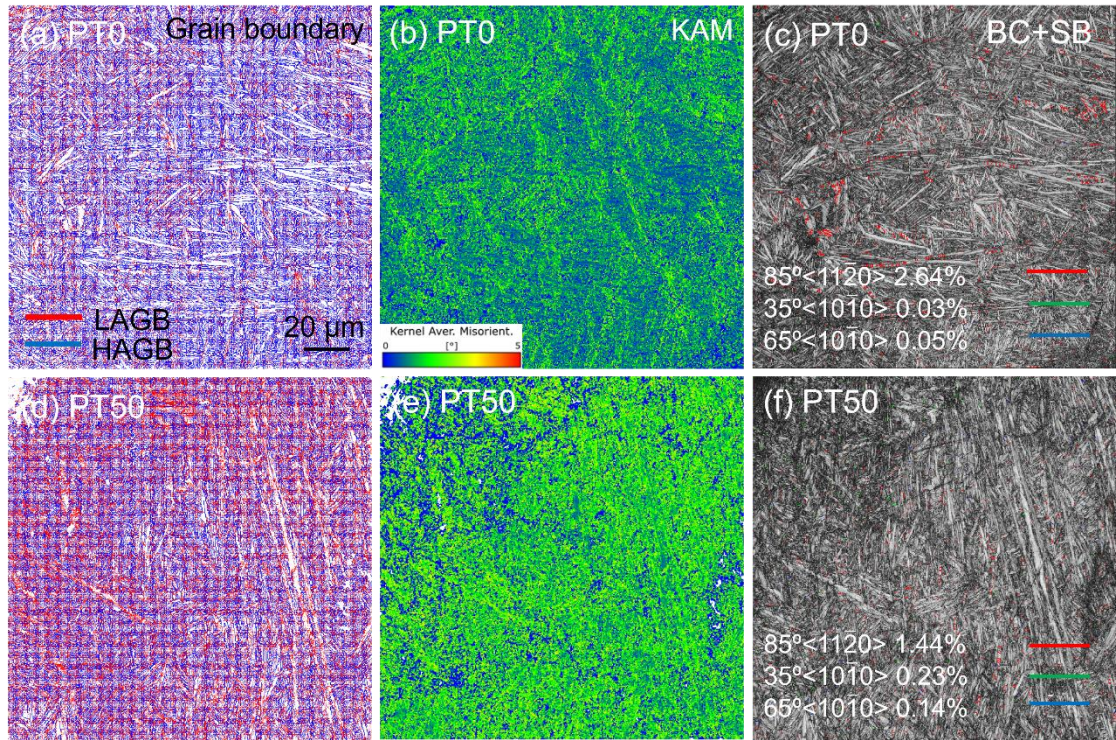


Fig. 6.11 The comparison of grain boundary distribution (a) and (d), and KAM (b) and (e), and band contrast + special boundaries maps in as-fabricated (c) PT0 and (f) PT50 after tensile testing.

Therefore, it is believed that the decreased c/a ratio makes a crucial contribution to the improved ductility of as-fabricated PT25 and PT50. The increased number of LAGBs in as-fabricated PT50 may also play a positive role in ductility. Chen et al. [249] explained that a more stable/uniform deformation and a higher failure tolerance might be obtained with the help of LAGBs, achieving a more balanced strength-ductility at multiple scales.

6.4.3.2 Strength mechanisms

In this chapter, the tensile strength and yield strength of PT25 and PT50 reduced compared to PT0 without CP Ti addition (see Fig. 6.8 and Table 6.4). The strengthening mechanisms in the PT0, PT25 and PT50 can be discussed at least semi-quantitatively. The yield strength (σ_{YS}) of Ti alloys can be assessed by the following equation [167]:

$$\sigma_{YS} = \sigma_0 + \sigma_{SS} + \sigma_{GB} + \sigma_{Dis} \quad (2)$$

To facilitate comparison, one can assume σ_0 as the yield strength of Pure Ti. The term σ_{SS} , the solid solution strengthening, σ_{GB} , grain boundary strengthening and σ_{Dis} dislocation strengthening need some considerations. Assuming ideal mixing, the

strengthening effect of solute elements in solid solutions can be described by [235]:

$$\sigma_{SS} = B_i X_i^{2/3} \quad (3)$$

where B_i is the strengthening coefficient for the solute i and X_i is the atomic concentration of the solute i . The cumulative strengthening effect of solute elements in the Ti-Al-V alloy can therefore be expressed by [250]:

$$\sigma_{ss} = \left(\sum_i B_i^{2/3} X_i \right)^{2/3} \quad (4)$$

It may be expected that PT25 and PT50 with less Al and V content may present lower solid solution strengthening (lower X_i in Al and V content) compared to PT0.

The grain boundary strengthening σ_{GB} is usually evaluated via the Hall-Petch equation:

$$\sigma_{GB} = \frac{k}{\sqrt{d}} \quad (5)$$

Where k is the Hall-Petch coefficient, and d is the martensite α' thickness [103]. Assuming a constant of k equal to $300 \text{ MPa} \cdot \mu\text{m}^{-1/2}$ [251], and the value of martensite α' thickness measured in section 6.3.2, a declined trend of grain boundary strengthening can be estimated when CP Ti addition are added.

The dislocation strengthening (σ_{Dis}) contribution can be expressed by the Bailey-Hirsch formula as follows [252,253]:

$$\sigma_{Dis} = M \alpha_p G b \sqrt{\rho} \quad (6)$$

$$\rho = \frac{12Es}{(1+2\nu^2)Gb} \frac{\varepsilon_{trans}^2}{d^2} \quad (7)$$

where M is the Taylor factor, α_p is a constant coefficient, G is the shear modulus of α' , b is the Burgers vector length, and ρ is the dislocation density. E is the Young's modulus, s is the lath boundary thickness, ν is the Poisson's ratio, and ε_{trans} is the transformation strain from β to α' , d is martensite α' thickness. Therefore, the σ_{Dis} may be mainly related to the martensite α' thickness for composition modified Ti alloys [167]. The σ_{Dis} therefore may also be expected to decline for PT25 and PT50, respectively.

Fig. 6.12 shows the relationships for strength, ductility, hardness, c/a ratio, martensite α' thickness, and inverse square root of martensite α' thickness for PT0, PT25 and PT50. Clear trends are found for all variables which link composition, microstructure, and mechanical properties. It is found that there is an increasing trend for ductility and

martensite α' thickness while a decreasing trend for strength, microhardness, c/a ratio, the inverse square root of martensite α' thickness when CP Ti addition increases. Therefore, tunable, predictable, and desirable mechanical properties may be achieved via the proper addition of CP Ti into Ti-6Al-4V.

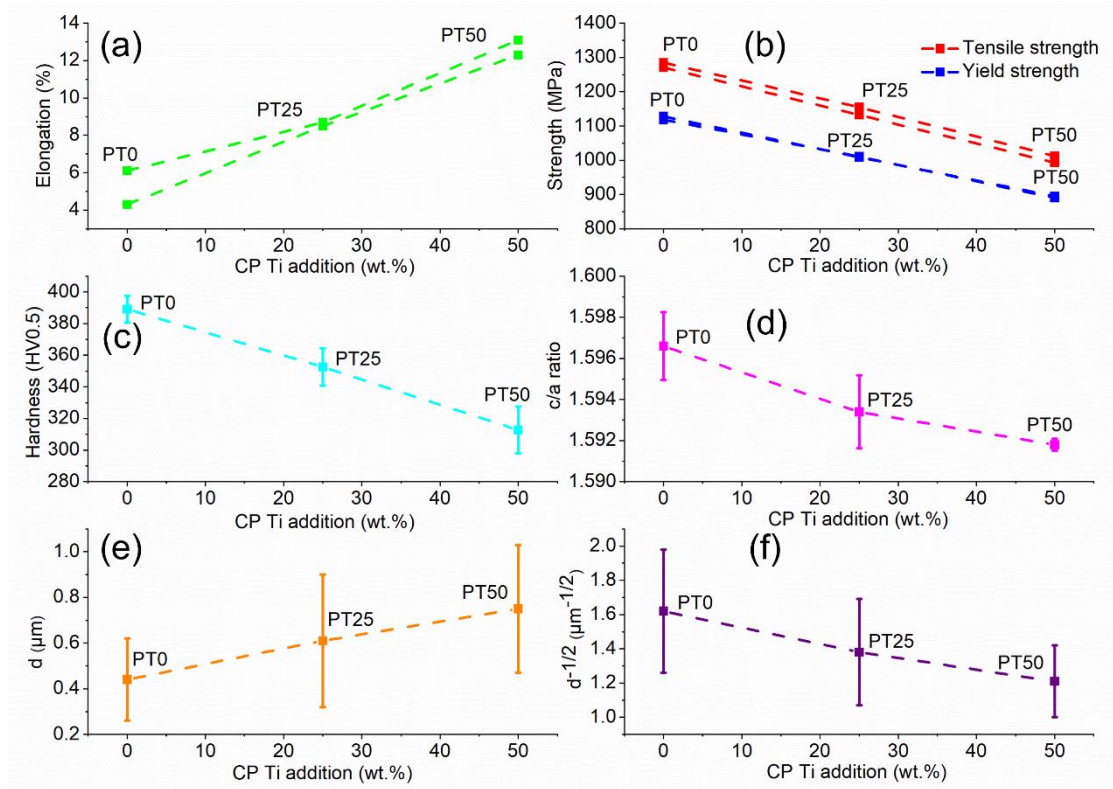


Fig. 6.12 The relationships between (a) ductility, (b) tensile and yield strength, (c) microhardness, (d) c/a ratio, (e) martensite α' thickness, (f) the inverse square root of martensite α' thickness and CP Ti addition.

6.4.4 Materials adaption for Ti alloys by LPBF

In this chapter, Ti-Al-V based alloys with nominal Ti-4.5Al-3V (close to ~TA17, Ti-4Al-2V) and Ti-3Al-2V (close to ~Grade 9, Ti-3Al-2.5V) through the addition of CP Ti into Ti-6Al-4V were successfully fabricated by LPBF. The tensile strength of ~1003 MPa of PT50 (nominal Ti-3Al-2V) is higher than Ti-3Al-2.5V by conventional manufacturing (~600-850 MPa) [98,254,255]. The main increase in strength of Ti-3Al-2V by LPBF could be from the fine martensite structure, which makes it possible to obtain comparable mechanical properties of Ti-6Al-4V by casting [235]. In-situ alloying with desired composition Ti-6(1-x)Al-4(1-x)V (x is the CP Ti content) via mixing with different CP Ti content into Ti-6Al-4V by LPBF can be expected and achieved. This

method demonstrates the facilely tunable microstructure and therefore mechanical properties. This work enhances the low ductility of as-fabricated Ti-6Al-4V through a facile and accessible way, which may be more practical and economical compared to heat treatment method. The addition of CP Ti inside Ti-6Al-4V, also has the potential to expand the applications, including for biocompatibility purposes due to the reduction of Al and V, while exhibiting better strength compared to CP Ti.

To conclude, achieving microstructure and mechanical properties tuning to satisfy desired requirements in the as-fabricated state is feasible via material adaption for Ti-6Al-4V by in-situ alloying with CP Ti addition. Besides, CP Ti can also act as a composition modifier for other Ti alloys to achieve desired microstructure and properties. For instance, as-fabricated near α Ti alloy Ti-6.5Al-2Zr-1Mo-1V (TA15) by LPBF also presents high strength but low ductility [25,256], and this in-situ composition tailoring method may also be possible to achieve the balance of strength-ductility of as-fabricated parts. More importantly, non-equilibrium structures in Ti alloys by LPBF can be formed based on [Mo]_{eq} by rapid cooling rates, varying from martensite α' , martensite α'' to metastable β (may include ω phase) and stable β . The non-equilibrium structure of as-fabricated Ti alloys by LPBF may also be tuned with proper CP Ti addition [38]. For example, high solute content Ti alloys (such as Ti-6Al-2Sn-4Zr-6Mo) with martensite α'' and low yield strength fabricated by LPBF [127] may be transformed to a martensite α' structure through CP Ti addition. Metastable or stable β Ti alloys with proper CP Ti addition by LPBF may also activate the transformation-induced plasticity (TRIP) and/or TWIP effect to obtain better strength and ductility. Therefore, the in-situ CP Ti addition mixing with Ti alloys is an effective method to tailor the microstructure and mechanical properties for the LPBF community. Other alloy systems may also benefit from this strategy (for example, pure Fe with steels, pure Ni with Ni superalloys).

6.4.5 Comparison with PSD work

Compared to previous Chapter 5 with the limited effect of different PSD powder feedstocks on microstructure and mechanical properties of Ti-6Al-4V, this chapter exhibits a facile way to modify the chemical composition of Ti-6Al-4V powder feedstock through CP Ti addition and therefore achieve tunable microstructure and mechanical properties of Ti-6Al-4V. Thus, different roles of PSD and chemical composition in Ti-6Al-4V powder feedstock on parts performance can be concluded.

PSD mainly affects surface quality and porosity while chemical composition mainly influences microstructure and mechanical properties, which may provide a whole solution for desired performance by choosing proper powder feedstock.

6.5 Conclusions

In this chapter, a facile in-situ composition tailoring (composition design) strategy is applied for Ti-6Al-4V alloy by LPBF to figure out the low ductility issue and maintaining good strength (~1000 MPa) because of the formation of the martensitic α' structure. The main results can be summarised as follows:

1. By employing in-situ composition tailoring of Ti-6Al-4V (PT0) alloy through CP Ti addition, developed Ti-Al-V alloys with nominal Ti-4.5Al-3V (PT25) and Ti-3Al-2V (PT50) can be achieved. Good relative density of PT25 (over 99.90%) and PT50 (over 99.90%) can be obtained using the same processing parameters as PT0.
2. There are some non-uniform areas in PT25 and PT50. There is an increase in the martensite α' thickness when CP Ti addition increases. A trend from acicular to lath transformation for martensite α' structure with increasing CP Ti addition can be observed.
3. There is a decreasing trend in the strength and microhardness and an increase trend in ductility when CP Ti addition increases. Balanced strength-ductility for as-fabricated PT50 can be obtained with tensile strength ~1000 MPa, yield strength ~900 MPa, and elongation ~13%, which satisfies the wrought Ti-6Al-4V standard. The mechanical properties can therefore be easily manipulated by proper CP Ti addition into Ti-6Al-4V.
4. It is believed that the decrease in the c/a ratio contributes to the increase in dislocation slip and hence improves ductility for PT25 and PT50. The LAGB and KAM results by EBSD further indicate the dislocation slip and ductility improvement of the modified Ti-Al-V alloy. The increased number of LAGBs for PT50 may also benefit this enhanced ductility. The reduced strength is mainly caused by the decrease in grain boundary strengthening and solid solution strengthening.

This composition design strategy by facile blending with Ti-6Al-4V and CP Ti can

acquire a good balance of strength and ductility. This strategy may also be industrially interested in a fast, simple, and economical way to fabricate Ti alloy parts with balanced strength-ductility. This strategy may be possible to implement in other Ti alloys, steels, and Ni-based superalloys to get a desired microstructure and better balanced and tailored strength-ductility or other desired properties. This may be a practical and economical strategy for materials adaption and development in LPBF.

7 Heat treatment of Ti-6Al-4V alloy by LPBF with stress relief and annealing

7.1 Introduction

In Chapter 6, balanced strength and ductility can be obtained via composition tailoring of Ti-6Al-4V and strength-ductility mechanisms are also analysed. It is found that the decrease in grain boundary strengthening, and solid solution strengthening are mainly responsible for the decrease in strength and the increase in dislocation slip is the main reason for the increase in ductility. It is known that heat treatment is a common way to obtain balanced strength and ductility with decreased strength and enhanced ductility for as-built Ti-6Al-4V. Even though both methods (composition tailoring and heat treatment) achieve balanced strength-ductility, their strength-ductility mechanisms may differ. For the strength mechanism, strength may mainly relate to grain boundary strengthening and solid solution strengthening which is determined by grain size and composition. As for the ductility mechanism (i.e., deformation mechanism), besides dislocation slip, deformation twinning is also a crucial mechanism of plastic deformation in titanium and titanium alloys, especially for accommodating plastic strain along the $\langle c \rangle$ axis [38,198]. Deformation twins (common type $85^\circ\langle 11\bar{2}0 \rangle$ (tension twinning), $35^\circ\langle 10\bar{1}0 \rangle$ (tension twinning), $65^\circ\langle 10\bar{1}0 \rangle$ (compression twinning)) are widely observed in CP Ti and Ti alloys by conventional manufacturing [38,134,199]. As discussed in the literature section, rare studies were reported about deformation twins of Ti-6Al-4V by AM, especially by LPBF. In this chapter, it is interesting to explore the microstructure and mechanical properties and related mechanisms of heat treated Ti-6Al-4V.

Therefore, besides the basic microstructure and mechanical properties analysis, investigating the deformation behaviour (especially for deformation twinning) and strength mechanisms are interesting and significant. Study of deformation twinning behaviour of heat treated Ti-6Al-4V is the main aim in this chapter. This study on strength-ductility mechanisms especially the findings of deformation twinning may provide new insight to achieve superior strength and ductility of Ti alloys by LPBF via composition design and/or optimised heat treatment strategy. Two typical heat treatment temperatures (stress relief at 730 °C with 2 h, called HT730 and annealing at 900 °C

with 2 h, called HT900) for as-built Ti-6Al-4V by LPBF are employed and compared for this chapter. There are two main reasons to choose the two temperatures. Stress relief at 730 °C is typically employed to release the residual stress and decompose martensite α' into $\alpha+\beta$ but with slight increase for α size [136,257]. Annealing at 900 °C can release the residual stress and significantly increase the α size [169,171]. Another reason is that Zhang et al. [101] studied the dislocation slip behaviour of Ti-6Al-4V with as-built, heat treatment at 730 °C and 900 °C without deformation twinning study. Hence, the effect of residual stress and grain size based on the choice of two temperatures on deformation behaviour (including dislocation slip and deformation twinning) can be investigated.

7.2 Experimental

Plasma atomised Ti-6Al-4V (Grade 23, ELI, 15-45 μm) powder feedstock was used in this chapter. Ti-6Al-4V ELI is chosen because the low interstitial elements may make the Ti-6Al-4V more ductile (oxygen embrittles this alloy) and therefore the Ti-6Al-4V may be more resistant to cracks potentially deriving from thermal stresses [12,258–260]. Besides, the choice of Ti-6Al-4V ELI may be critical for the observation of deformation twinning as the low oxygen level (less than 0.13 wt.%) in Ti-6Al-4V ELI may facilitate the deformation twinning formation [38,261,262]. The cubic samples and tensile bars were fabricated by a Renishaw AM400 LPBF machine inserted with RBV (oxygen level below 500 ppm in the build chamber) using default processing parameters. Ti-6Al-4V alloy cubic samples and tensile bars were heat treated in a tube furnace with Ar protection. Two heat treatment temperatures with stress-relief (730 °C with 2 h by FC, called HT730) and annealing (900 °C with 2 h by FC, called HT900) were used.

The as-built Ti-6Al-4V, HT730, HT900 cubic samples were cut, ground, and polished for further microstructural analysis by OM, SEM, XRD. Microhardness (48 indentations for each sample using 500 gf and a dwell time of 10 s) and tensile properties (based on ASTM E8/8M) were also performed. EBSD (a step size of 0.25 μm) were employed for cubic samples and fractured tensile samples of as-built, HT730 and HT900 to analyse crystallographic and deformation twinning behaviour. Subsets were extracted from All Euler maps (φ_1 0-180°, Φ 0-180°, φ_2 0-60°) to further analyse the twin variants and Schmid factor of two heat treated (HT730 and HT900) samples based on the angle between the c-axis of parent grains and tensile direction. All six possible Schmid factors of twin variants of one parent grain can be calculated based on the orientation of the

parent grain and tensile direction [263]. All six possible orientations of twin variants can thus be determined by the orientation (employing Euler values) of parent grain. The Schmid factor of twin variants was calculated using an in-house developed Excel code.

7.3 Results

7.3.1 Microstructure and elemental distribution

Fig. 7.1 shows the XRD results of as-built, HT730 and HT900. XRD peaks of the HCP titanium phase are observed in all three samples. The HCP phase may contain martensite α' and/or α since both structures have similar lattice parameters. From enlarged Fig. 7.1(b) with 2θ from 34° to 44° , after heat treatment, the peak positions of HCP phase slightly move left and full width at half maximum (FWHM) decreases. According to the Bragg equation, the interplanar d-spacing value of the HCP phase increases when the peak position angle decreases (left shift). This phenomenon can be explained by the elemental diffusion after heat treatment. Considering the rapid cooling for as-built Ti-6Al-4V in LPBF, the martensite α' dominates in the as-built sample. After stress relief (HT730) and annealing (HT900), martensite α' transforms into $\alpha+\beta$. It is known that martensite α' is a supersaturated solid solution with homogenous distribution of Al and V. The V element is mainly enrich in the β phase after heat treatment [26,174], which is also confirmed by the following elemental distribution results. Therefore, it means that the V content in the equilibrium α phase is lower than that in α' martensite. High solute content can cause greater distortion of the crystal structure, resulting in the broadening of the XRD diffraction peaks in the as-built Ti-6Al-4V [264,265]. Therefore, peak broadening can be found in the as-built Ti-6Al-4V compared to HT730 and HT900. The atomic radius of titanium (0.147 nm) is higher than vanadium (0.132 nm) [26]. The lattice parameter of the α phase is higher than that of α' martensite, which is the reason why the XRD peaks shift left. In addition, the lattice parameter and c/a ratio were also calculated based on the same method in Chapter 6. A c/a ratio of the HCP can be calculated by rearranging the Bragg equation [127]:

$$\sin \theta = \frac{\lambda}{2} \sqrt{\frac{4(h^2+hk+k^2)}{3a^2} + \frac{l^2}{c^2}} \quad (1)$$

Where θ is the diffraction angle (2θ related to peak position); λ is the X-ray wavelength (1.5406 Å); h, k and l are Miller indices; a and c are the hexagonal lattice parameters. It

is important to note that c , a , and c/a are calculated by using six main diffraction peaks (crystal planes). The peak position, c/a ratio of as-built, HT730 and HT900 are summarised in Table 7.1. Meanwhile, HT730 and HT900 present a small peak of β phase and the volume fraction of β phase is slightly higher for HT900 than HT730.

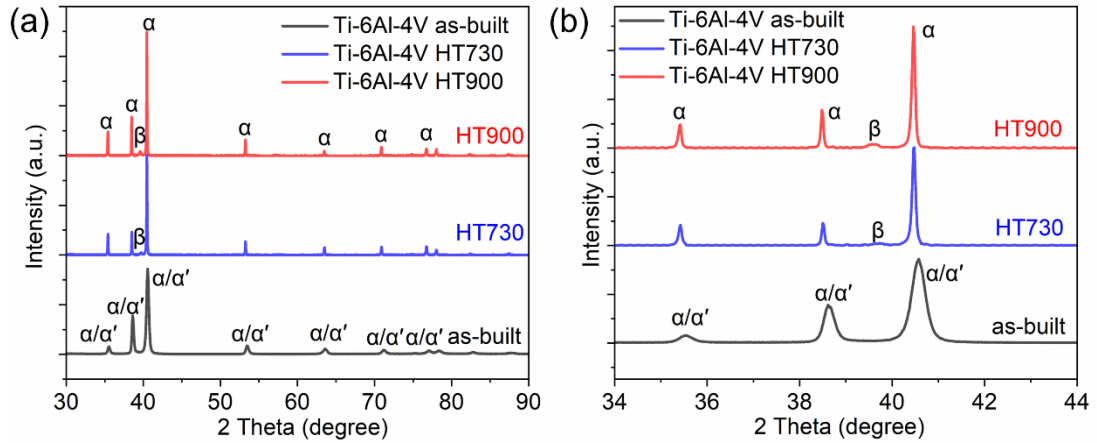


Fig. 7.1 XRD results (a) 2θ from 30° to 90° and (b) 2θ from 34° to 44° (show the main peaks) of as-built Ti-6Al-4V, HT730, and HT900.

Table 7.1 XRD data (peak position, c/a ratio) of as-built Ti-6Al-4V, HT730, and HT900.

Sample	2θ in (002)	2θ in (101)	c/a
As-built	38.62	40.57	1.5966
HT730	38.56	40.52	1.5972
HT900	38.54	40.51	1.5978

The microstructure of as-built, HT730 and HT900 is presented in Fig. 7.2. All samples show typical columnar prior- β grain boundaries, which confirms heat treatment below β transus temperature cannot break columnar prior- β grain boundaries. For as-built Ti-6Al-4V, the columnar prior- β grain boundaries consist of fine martensite α' that is mostly distributed at an angle of around ± 45 degrees [102]. For HT730 and HT900, it is mainly the α phase inside the prior- β grain boundaries.

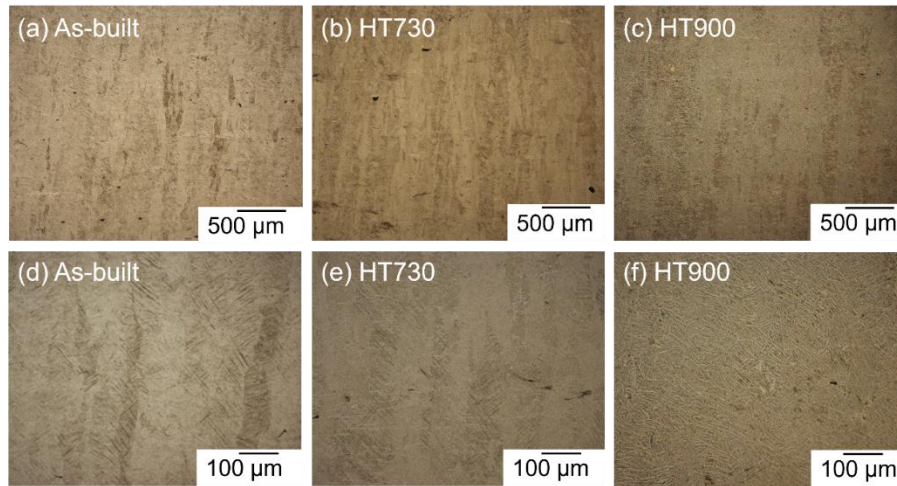


Fig. 7.2 Optical microscopy images of etched microstructure for (a) and (d) as-built Ti-6Al-4V, (b) and (e) HT730, and (c) and (f) HT900.

Fig. 7.3 presents the microstructure from SEM images with different magnifications. For as-built Ti-6Al-4V, typical acicular martensite α' structures with several types can be observed. The width of acicular α structures is slightly increased for HT730 compared to as-built Ti-6Al-4V while a dramatic increase in the width of α is shown in HT900. A small amount of globular α can be observed in HT900 while the lath α phase with a high length-width ratio dominates. Meanwhile, β phase is found in HT730 and HT900, especially in HT900, which agrees well with XRD results. This kind of microstructure is consistent or similar to other literature in as-built [102] and heat treatment states [103].

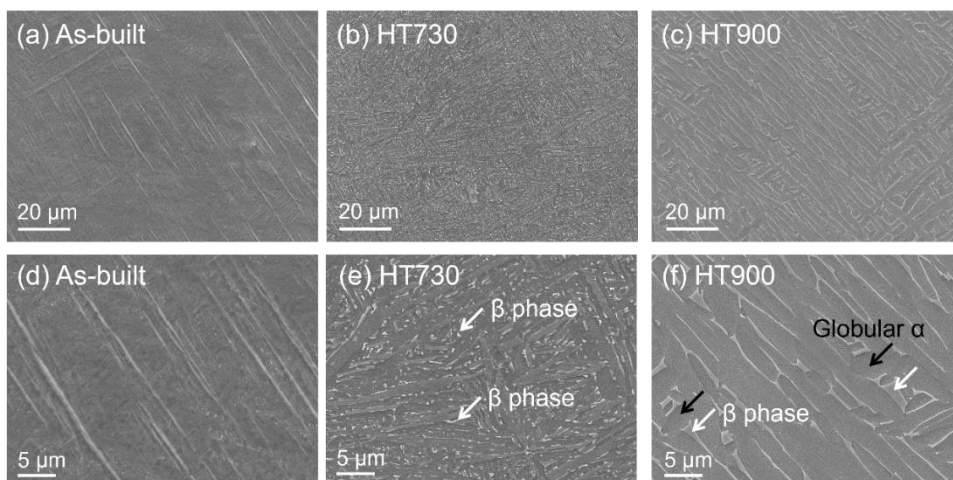


Fig. 7.3 SEM images of etched microstructure for (a) and (d) as-built Ti-6Al-4V, (b) and (e) HT730, and (c) and (f) HT900. β phase can be observed in HT730 and HT900, and a small amount of globular α can be found in HT900.

Elemental distribution of Ti, Al, and V in as-built Ti-6Al-4V, HT730, and HT900 samples is shown in Fig. 7.4. Based on BSE imaging and EDS maps, as-built Ti-6Al-4V is homogeneous. The BSE and EDS results of HT730 are similar to that of as-built Ti-6Al-4V. Although the HT730 sample has a small amount of β phase, it does not show up on BSE and EDS maps. The obvious β phase can be observed in the BSE of HT900 with white colour. These β phase enriched areas present low Al and high V content while the α phase has high Al and low V, which further explains the peak shift in XRD results. This elemental diffusion is explained by the fact that Al is α stabiliser element while V is β stabiliser element [38].

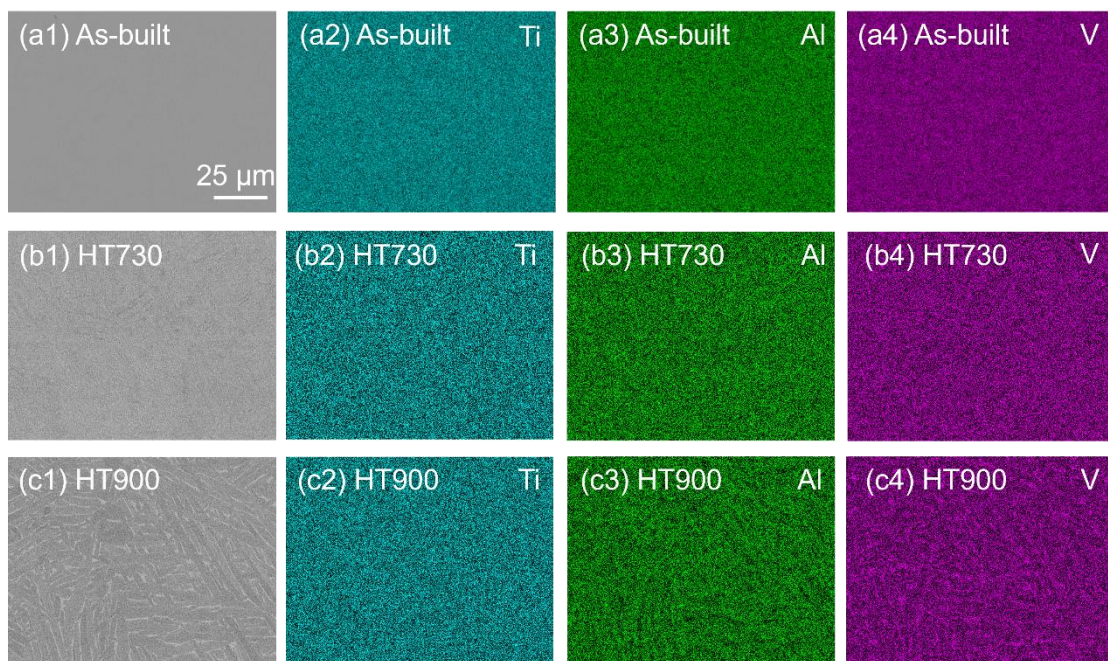


Fig. 7.4 BSE images and EDS area maps of (a1-a4) as-built Ti-6Al-4V, (b1-b4) HT730, and (c1-c4) HT900.

7.3.2 Mechanical properties

First, Table 7.2 shows the microhardness results of as-built Ti-6Al-4V, HT730 and HT900. There is a decreasing trend in hardness for heat treated Ti-6Al-4V because of the decomposition of martensite α' into $\alpha+\beta$, from as-built ~ 389.1 HV0.5 to HT730 ~ 366.9 HV0.5 to HT900 ~ 335.4 HV0.5.

Table 7.2 Microhardness results of as-built Ti-6Al-4V, HT730 and HT900, errors are standard deviation of 48 indentations in each sample.

Sample	As-built	HT730	HT900
Microhardness (HV0.5)	389.1±8.45	366.9±9.84	335.4±10.68

Fig. 7.5 shows the tensile properties of three samples with engineering stress-strain curves. The results of Young's modulus, tensile strength, yield strength and elongation are also summarised in Table 7.3. The Young's modulus is almost the same for as-built Ti-6Al-4V, HT730 and HT900, which indicates the ignorable effect of heat treatment on the bonds within the HCP structure. As-built Ti-6Al-4V shows high strength (tensile strength more than 1200 MPa) but low ductility (less than 10%), in agreement with other LPBF fabricated Ti-6Al-4V [12,192,193]. The elongation of as-built Ti-6Al-4V by LPBF is around 6% or below 6%, which is similar to as-built Ti-6Al-4V in some literature in as-built Ti-6Al-4V by LPBF [12,192,193,229,234]. When as-built Ti-6Al-4V is heat treated at 730 °C and 900 °C, the tensile strength and yield strength decrease while elongation shows an increased trend, which means well balanced strength-ductility can be obtained with proper heat treatment. This phenomenon is also similar to other literature on Ti-6Al-4V by heat treatment [12,103].

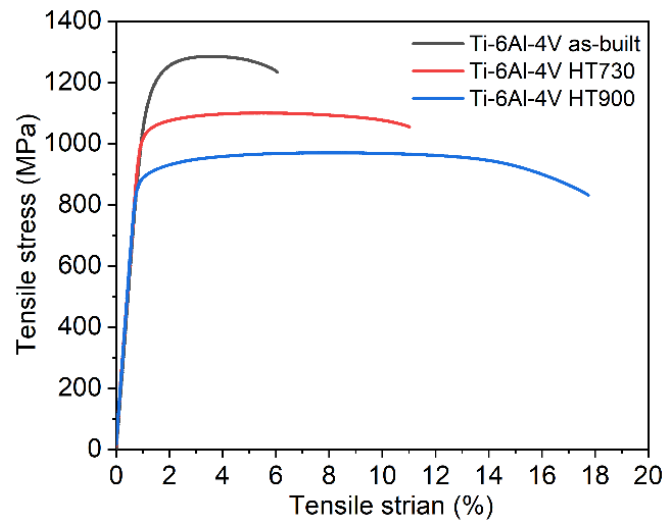


Fig. 7.5 Tensile properties of three samples (as-built Ti-6Al-4V, HT730 and HT900).

Table 7.3 Mechanical properties of as-built Ti-6Al-4V, HT730 and HT900 (errors are standard deviation, two samples are used for each alloy).

Sample	Young's modulus E (GPa)	Tensile strength (MPa)	Yield strength (MPa)	Elongation (%)
As-built	116±1	1278±7	1122±6	5.2±0.9
HT730	116±1	1091±10	1018±10	11.8±0.8
HT900	117±1	976±6	884±4	15.8±1.9

The fractured morphology of as-built Ti-6Al-4V, HT730 and HT900 after tensile testing is also observed and compared, as presented in Fig. 7.6. Fig. 7.6(a, d) shows that as-built Ti-6Al-4V exhibits typical terrace structures with shallow dimples that are similar to those reported in the literature by Simonelli et al. [136]. Intergranular α/α' and along the prior- β grain boundaries may be the dominant fracture mode. A terrace structure with limited dimples indicates that LPBF as-built Ti-6Al-4V is prone to brittle fractures. For stress relief HT730, the terrace structure is also observed but largely reduced. More obvious dimples are observed, compared to as-built Ti-6Al-4V are presented, as shown in Fig. 7.6(b, e). These characteristics may suggest a preferred ductile fracture mode for HT730. The fracture surface of HT900 shows deeper and larger dimples, but no obvious terrace structure (Fig. 7.6(c, f)). This indicates a dominant ductile fracture mode and is in accordance with the good ductility of HT900 (see Fig. 7.5 and Table 7.3).

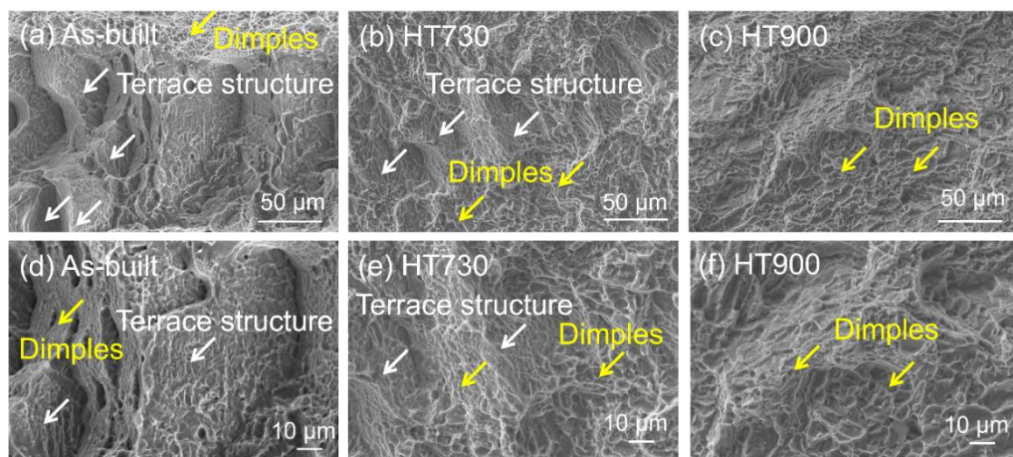


Fig. 7.6 Fracture surface morphology of (a, d) as-built Ti-6Al-4V, (b, e) HT730, and (c, f) HT900, showing obvious ductile mode in HT900 compared to brittle mode in as-built Ti-6Al-4V.

7.3.3 EBSD analysis before and after tensile testing

7.3.3.1 The deformation twinning formation

To further analyse crystallographic characteristics and deformation behaviour after tensile testing, EBSD was employed for all three samples before and after tensile testing (XOZ plane of all samples was used for EBSD analysis, tensile direction was along the X direction). First, Fig. 7.7 shows the phase maps of as-built Ti-6Al-4V, HT730, and HT900 before and after tensile testing. The HCP phase (martensite α' or α) is dominant phase for all samples and a small amount ($\sim 3\text{-}5\%$) of BCC phase (β phase) can be observed for HT900, which is generally consistent with other heat treatment works [101,174]. These results are consistent with XRD results (see Fig. 7.1). The β phase fraction for all before and after tensile testing samples are shown in Fig. 7.7. Due to the fine size of the β phase in as-built Ti-6Al-4V, the EBSD with a small step size ($0.25\ \mu\text{m}$) may not detect all β phase, but this may not have a significant influence in β phase fraction because of the small amount of β phase in as-built Ti-6Al-4V by LPBF based on XRD result and literature [101,174]. There is no huge difference in phase maps for all samples after tensile testing.

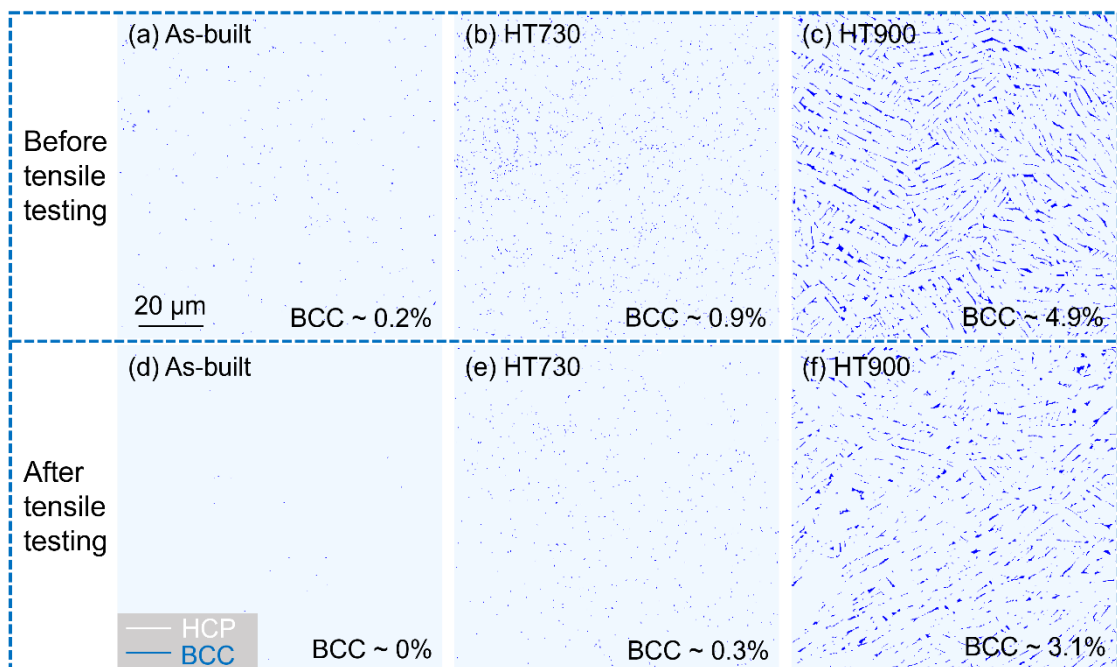


Fig. 7.7 Phase maps of as-built Ti-6Al-4V, HT730, and HT900 before (a-c) and (d-f) after tensile testing.

Fig. 7.8 shows misorientation distribution of all three samples before and after tensile testing to analyse the grain boundary misorientation (typically observe the appearance of special misorientation angle). Before tensile testing, typical distinct α/α variant boundaries for all three samples are consistent. Misorientation distribution of all samples shows a most common boundary $[\bar{1}055\bar{3}]/63.26^\circ$, which is consistent with other Ti-6Al-4V work by LPBF and DED [118,233]. After tensile testing, obvious differences can be found in misorientation results. The volume fraction of misorientation around $[\bar{1}055\bar{3}]/63.26^\circ$ shows a decreasing trend while the volume fraction of misorientation around less than 10° increases after stress relief (HT730) and further annealing (HT900). It is noteworthy that there is an obvious peak with a misorientation angle around 85° for HT900 after tensile testing. This result suggests significant special boundaries may be formed. The misorientation axis inserted in misorientation maps confirms the axis around $\langle 11\bar{2}0 \rangle$. This suggests the formation of significant deformation twins with $85^\circ \langle 11\bar{2}0 \rangle$ in HT900 as misorientation maps are widely used to identify deformation twins in CP Ti and Ti-6Al-4V [203,266–268]. In other words, deformation twinning may occur because 85° is a typical misorientation angle for tension twinning with $85^\circ \langle 11\bar{2}0 \rangle$ (angle/rotation axis) in α titanium [111,134,135,205].

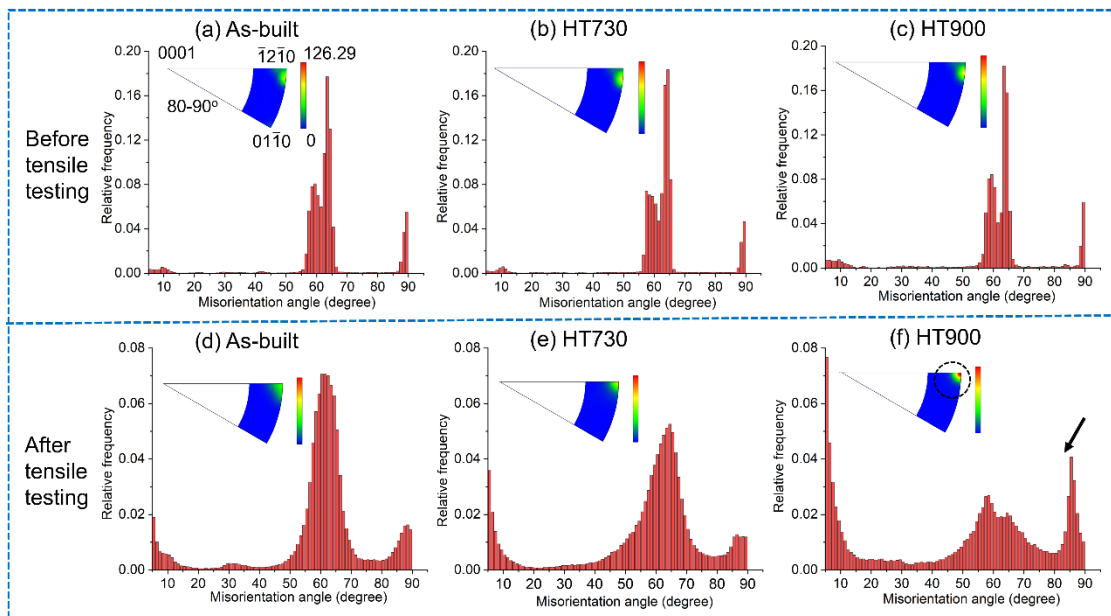


Fig. 7.8 Misorientation distribution of as-built Ti-6Al-4V, HT730, and HT900 before (a-c) and after (d-f) tensile testing. The misorientation axis with 80° - 90° is inserted in misorientation maps.

Band contrast plus special boundary maps for all three samples before and after tensile testing are shown in Fig. 7.9. Three common deformation twinning modes with special boundaries, $85^\circ\langle 11\bar{2}0\rangle$ (tension twinning), $35^\circ\langle 10\bar{1}0\rangle$ (tension twinning), $65^\circ\langle 10\bar{1}0\rangle$ (compression twinning), are included. For three samples before tensile testing, the volume fraction of all possible twinning is negligible (less than 0.5%). A small amount ($\sim 2.64\%$) of twins with $85^\circ\langle 11\bar{2}0\rangle$ can be observed for as-built Ti-6Al-4V after tensile testing. There is a slight increase in HT730 ($\sim 4.15\%$) compared to the as-built Ti-6Al-4V. A significant increase for HT900 ($\sim 16.0\%$) is presented in Fig. 7.9(f). For other types of twinning, only a very small amount ($\sim 0.36\%$) of twins with $65^\circ\langle 10\bar{1}0\rangle$ is observed for HT900 after tensile testing. This small number of twins with $65^\circ\langle 10\bar{1}0\rangle$ is consistent with the small peak around 65° in misorientation results in HT900 after tensile testing (see Fig. 7.8(f)). Therefore, misorientation maps have a good match with special boundary results. This further confirms the formation of tension twinning $85^\circ\langle 11\bar{2}0\rangle$ based on the band contrast plus special boundary maps [201,206,267].

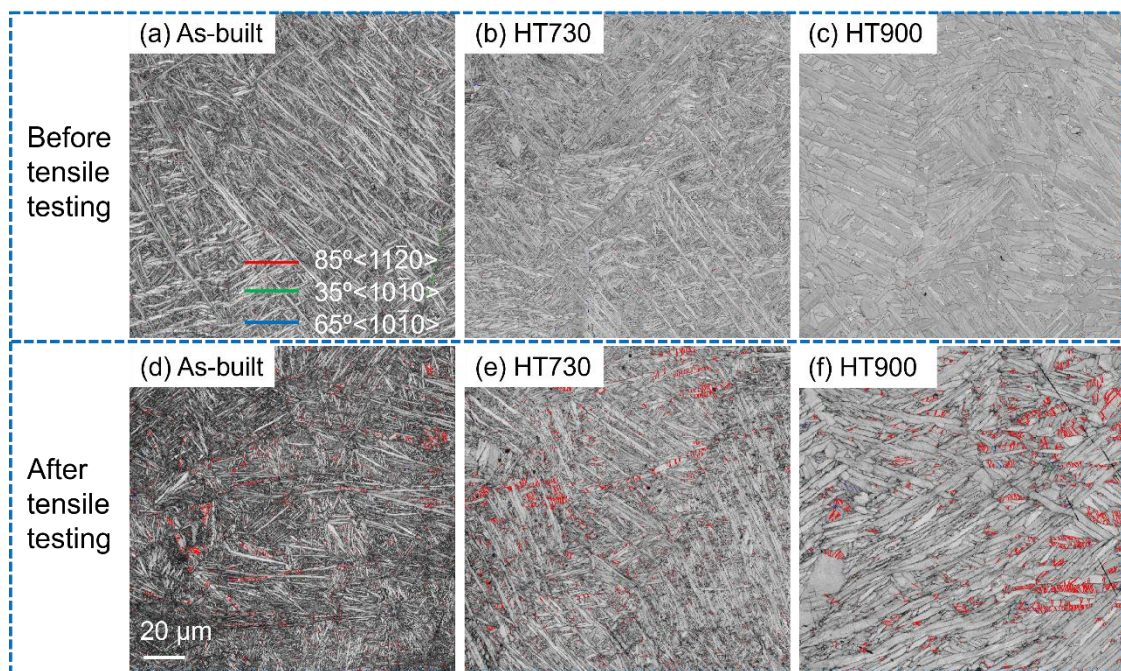


Fig. 7.9 Band contrast + special boundary maps for all three samples (a-c) before and (d-f) after tensile testing. Twins $85^\circ\langle 11\bar{2}0\rangle$ (tension twinning), $35^\circ\langle 10\bar{1}0\rangle$ (tension twinning), $65^\circ\langle 10\bar{1}0\rangle$ (compression twinning) are marked with red, green, blue, respectively.

LAGB ($2-10^\circ$) and HAGB ($>10^\circ$) of as-built Ti-6Al-4V, HT730, and HT900 are also compared, as shown in Fig. 7.10. Before tensile testing, the LAGB fraction is around

6.13% for as-built Ti-6Al-4V. A decrease in LAGB fraction can be obtained for HT730 (~2.68%) due to stress relief. However, this LAGB fraction increased after higher temperature heat treatment for HT900 (~7.04%) compared to HT730. This increase for HT900 may be related to the transformation strain (β to α) [195]. The globularization via boundary splitting, thermal grooves, cylinderization during heat treatment is expected to facilitate by the LAGB in a similar role as the pre-existing nano-twins or sub-structures [195], which is confirmed by the formation of globular α in SEM image (see Fig. 7.3(f)).

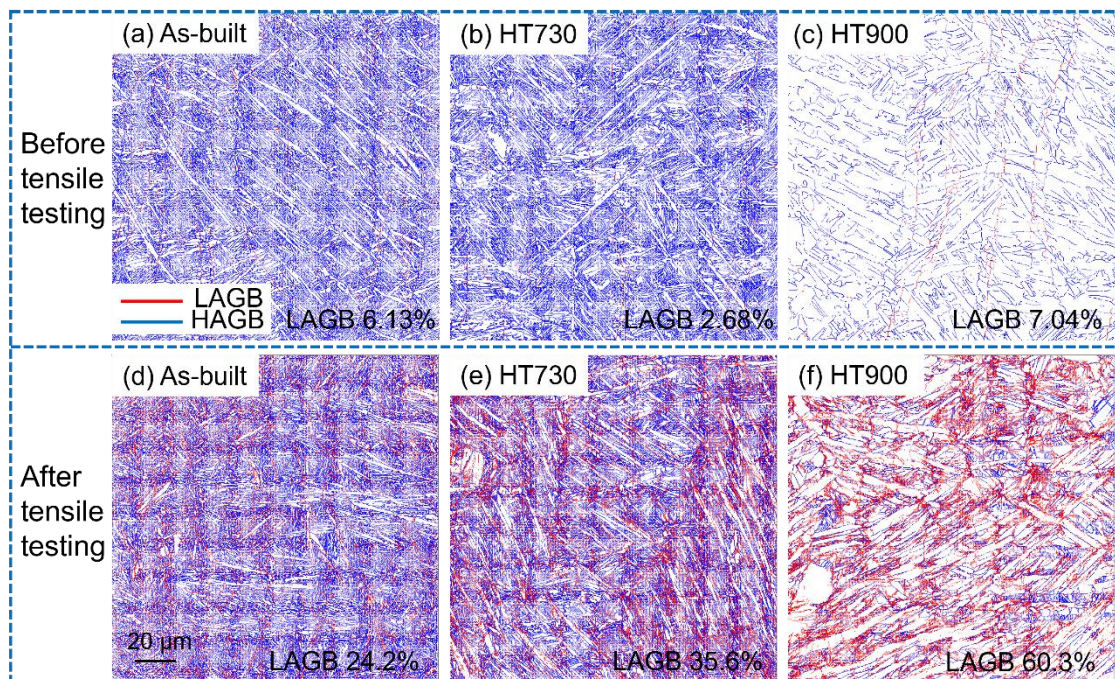


Fig. 7.10 Grain boundary maps of as-built Ti-6Al-4V, HT730, and HT900 before and after tensile testing, LAGB ($2-10^\circ$) marked with red colour, HAGB ($>10^\circ$) marked with blue colour.

Fig. 7.11 presents the inverse pole figure (IPF) + special boundary maps for all three samples before and after tensile testing. It is clear that the α width in HT730 is slightly higher than martensite α' in as-built Ti-6Al-4V and a significant increase in α width in HT900 can be observed. This is consistent with SEM images (see Fig. 7.3). Obvious twins inside large grain size of α can be found in HT900 (Fig. 7.11(f)).

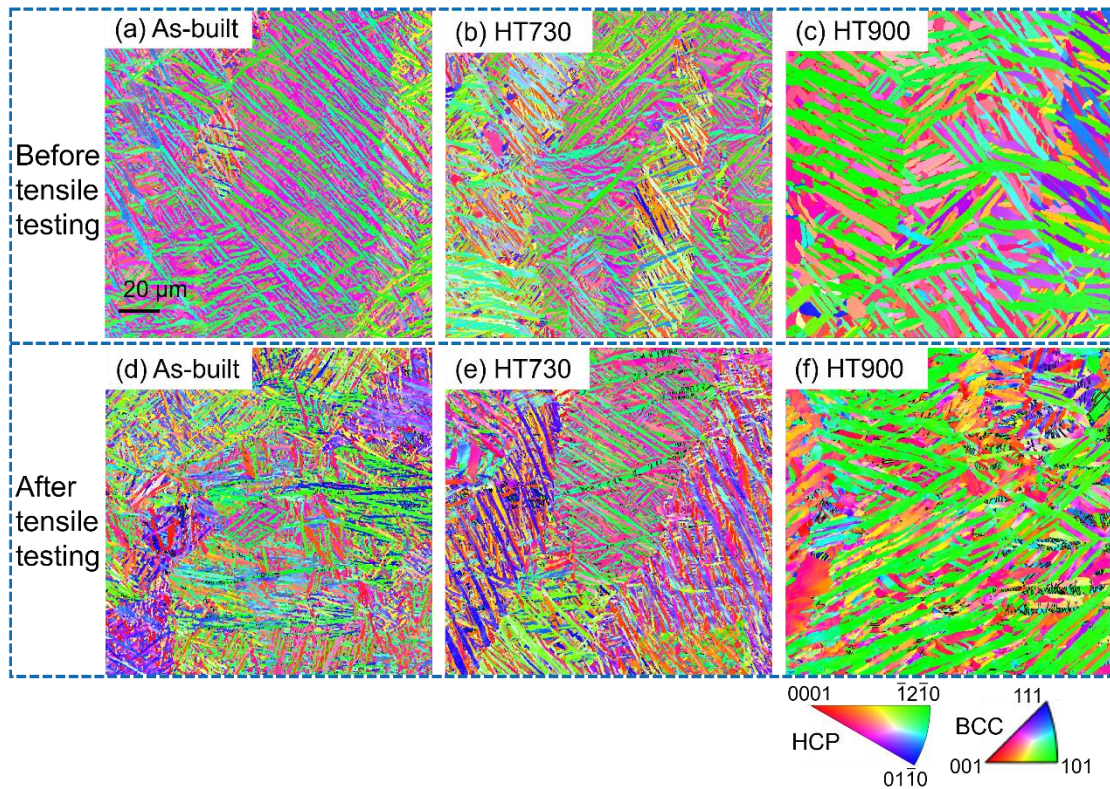


Fig. 7.11 Inverse pole figure (IPF//Z0) + special boundaries maps of as-built Ti-6Al-4V, HT730, and HT900 before (a-c) and (d-f) after tensile testing.

Fig. 7.12 shows the pole figures (PF) of as-built Ti-6Al-4V, HT730, and HT900 before and after tensile testing. Before tensile testing, the maximum texture value (to identify the crystal orientation) is around 10.21 for as-built Ti-6Al-4V. After stress relief (HT730), the texture slightly increases to 13.92. A significant increase of texture for HT900 of 21.68 compared to as-built Ti-6Al-4V is observed. There is no obvious texture difference for as-built Ti-6Al-4V and HT730 after tensile testing compared to before tensile testing. Interestingly, a notable decrease (from 21.68 to 12.14) in HT900 texture after tensile testing can be achieved, which suggests the significant role of massive twins on weakening of texture.

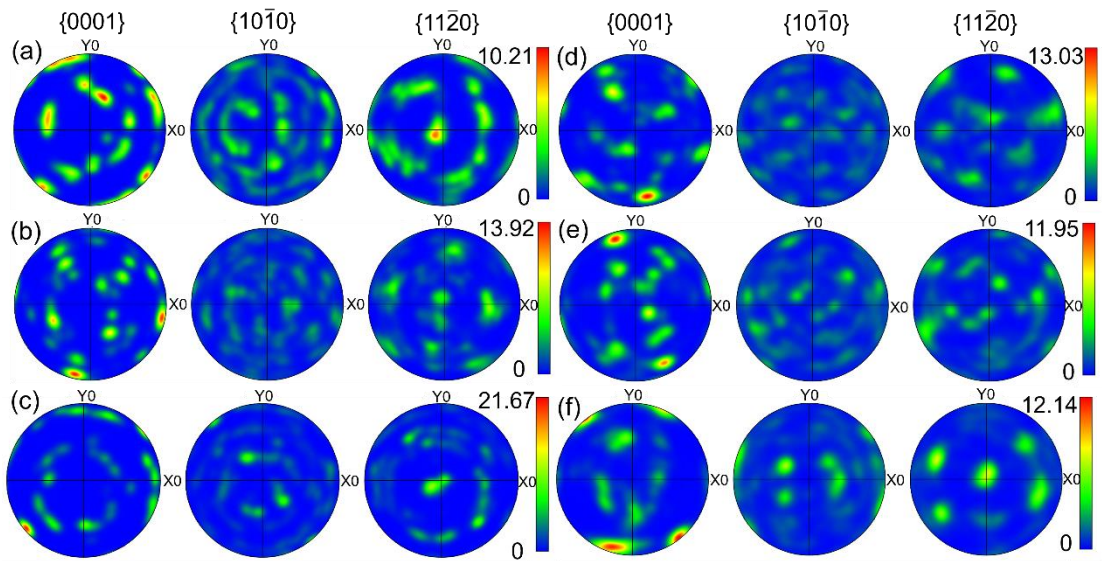


Fig. 7.12 Pole figure (PF) maps of as-built Ti-6Al-4V (a, d), HT730 (b, e), and HT900 (c, f) before (a-c) and after (d-f) tensile testing.

Fig. 7.13 presents the KAM maps for as-built Ti-6Al-4V, HT730, and HT900 before and after tensile testing. KAM decreases when heat treatment temperature increases before tensile testing. After tensile testing, an increase for all three samples can be found. This suggests the dislocation slip forms after tensile testing for each sample.

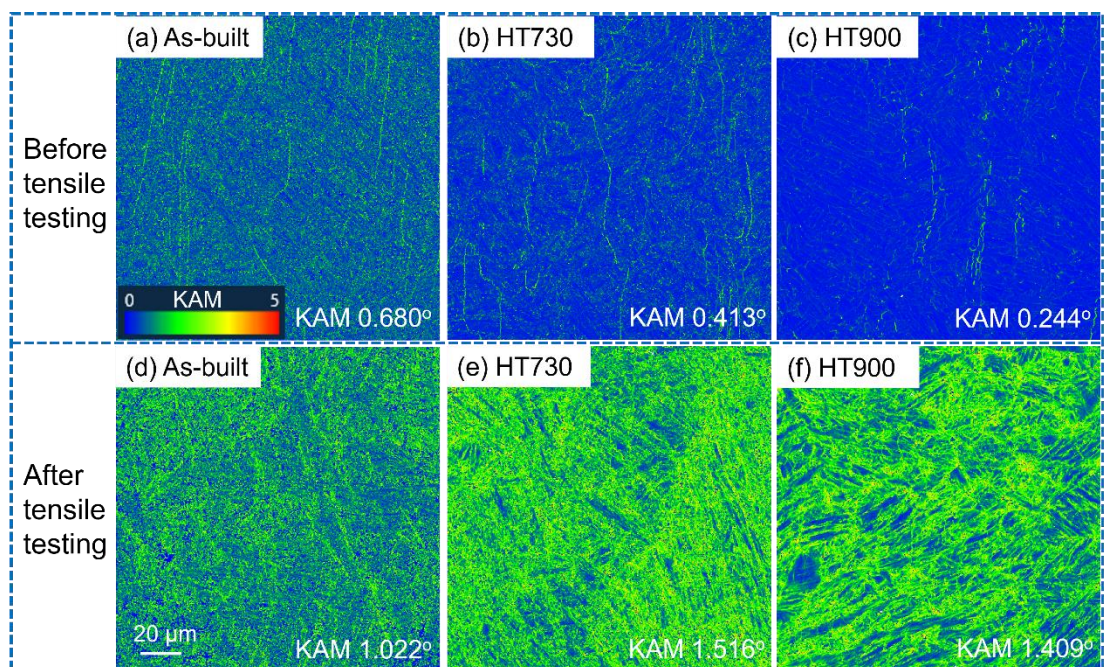


Fig. 7.13 KAM maps of (a, d) as-built Ti-6Al-4V, (b, e) HT730, and (c, f) HT900 (a-c) before and (d-f) after tensile testing.

7.3.3.2 The deformation twinning behaviour

To further confirm and analyse the observed deformation twins (in particular for twin variants and Schmid factor (SF) analysis) for HT730 and HT900, IPF//X0 (i.e., tensile direction) and all Euler maps with twins and subsets are employed as IPF images cannot clearly distinguish crystal orientations with similar axis [263], as illustrated in Fig. 7.14.

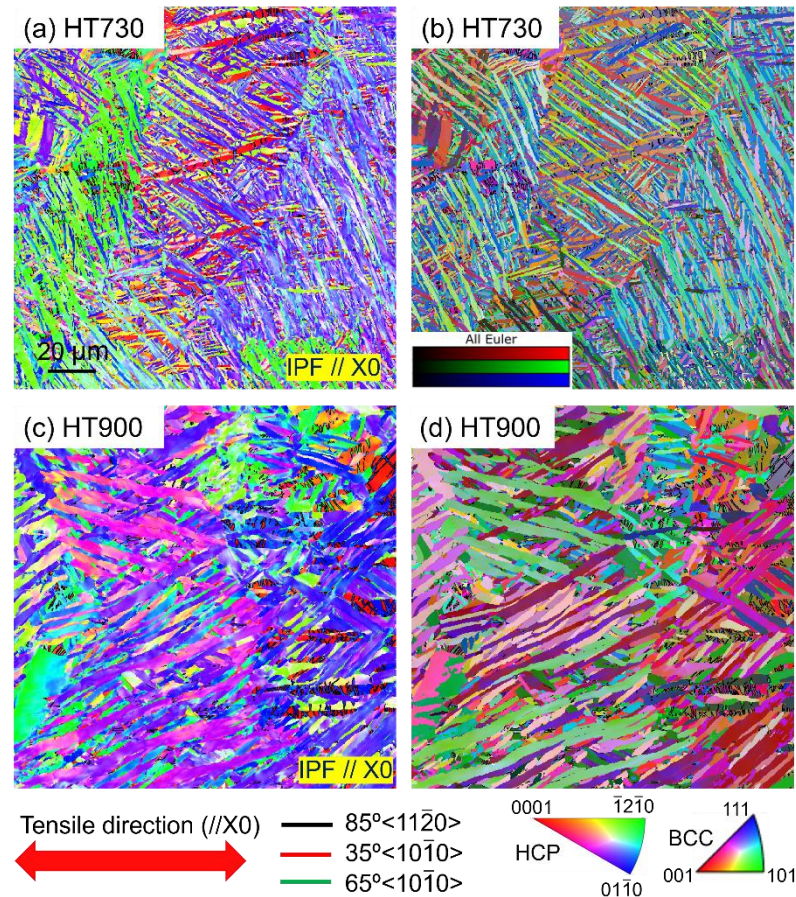


Fig. 7.14 IPF maps (//X0) of (a) HT730 and (c) HT900, and All Euler maps of (b) HT730 and (d) HT900 after tensile testing.

Parent grains with deformation twins are classified into two types for analysis based on the angles of the c-axis of parent grains with tensile direction (i.e., $\sim 0^\circ$, $\sim 45^\circ$). First, Fig. 7.15 depicts the three subsets (subset 1 to subset 3) of HT730 with the c-axis of parent grains along with tensile direction (i.e., $\sim 0^\circ$). Among all three subsets, point-to-point analysis of misorientation with twins and parent grains clearly indicates the 85° rotation between twin and parent grain, which confirms the tension twinning $85^\circ \langle 11\bar{2}0 \rangle$ (that means parent grains rotate 85° along axis $\langle 11\bar{2}0 \rangle$ to form twins).

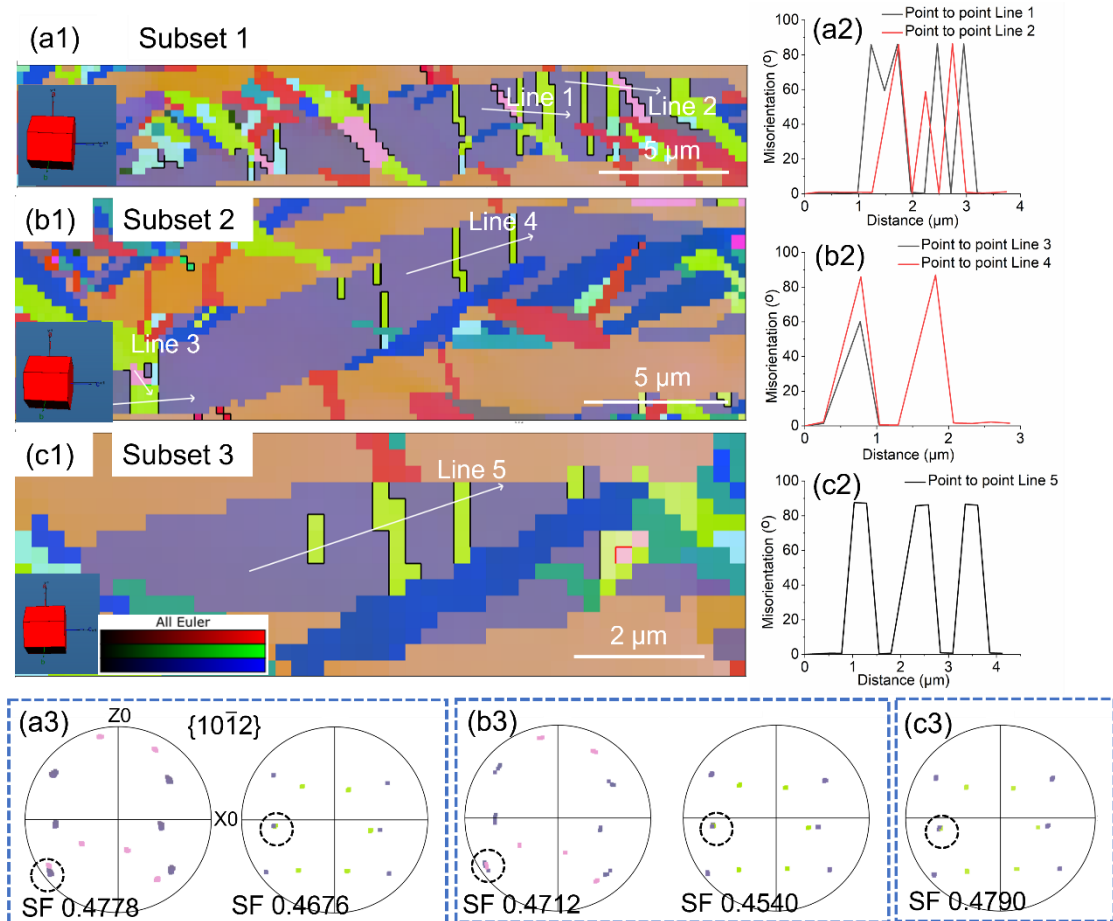


Fig. 7.15 Twin variants and Schmid factor analysis with c-axis of parent grains nearly paralleling to tensile direction in HT730, subset 1 to subset 3 (a1, b1, c1) All Euler maps, (a2, b2, c2) point-to-point misorientation maps with twins and parent grains, (a3, b3, c3) discrete pole figures of each twin and parent grain for twinning plane $\{10\bar{1}2\}$.

In subset 1 (Fig. 7.15), the c-axis of parent grain is nearly parallel to X0-axis (i.e., tensile direction). Twin and twin interaction with a boundary misorientation angle around 60° can be observed, which is consistent with literature in pure titanium [267,269]. Discrete pole figures of each twin and parent grain for twinning plane $\{10\bar{1}2\}$ are also presented. There are two coincident points for twins and parent grain. The Schmid factors of all six possible twin variants are also presented, as shown in Table 7.4. All possible twin variants and observed twin variants have high Schmid factors (> 0.45). However, only two twin variants are observed based on the discrete pole figures analysis (see Fig. 7.15). Similar results are obtained for subset 2 and subset 3 with the c-axis of parent grains

nearly paralleling to tensile direction presenting no more than two twin variants, as shown in [Fig. 7.15](#).

Table 7.4 Schmid factors of all six possible twin variants (Schmid factor bold for observed twin variants) in HT730 (C0 means c-axis of parent grains nearly along tensile direction, C45 means c-axis of parent grains offsetting tensile direction ~ 45°).

Type	Subset	V1	V2	V3	V4	V5	V6
C0	Subset 1	0.4924	0.4918	0.4912	0.4828	0.4778	0.4676
	Subset 2	0.4871	0.4871	0.4836	0.4736	0.4712	0.4540
	Subset 3	0.4963	0.4962	0.4937	0.4910	0.4818	0.4790
C45	Subset 4	0.2197	0.1929	0.1407	0.0821	0.0661	0.0193
	Subset 5	0.2103	0.1765	0.1623	0.1094	0.0712	0.0155
	Subset 6	0.1659	0.1564	0.1546	0.0798	0.0728	0.0076

[Fig. 7.16\(a\)](#) shows that twins can also be found in the parent grain of subset 4 with c-axis offsetting tensile direction around 45°. All six possible Schmid factors for twin variants are low (less than 0.25, see [Table 7.4](#)). Two twin variants appear with Schmid factor around 0.2197 and 0.1929 (the largest and second largest Schmid factors in all six possible variants), which is consistent with Schmid factor law. This is also found in another two subsets (subset 5 and subset 6) with c-axis offsetting tensile direction around 45° presenting twin variants with the largest or second largest Schmid factor (see [Fig. 7.16\(b, c\)](#) and [Table 7.4](#)).

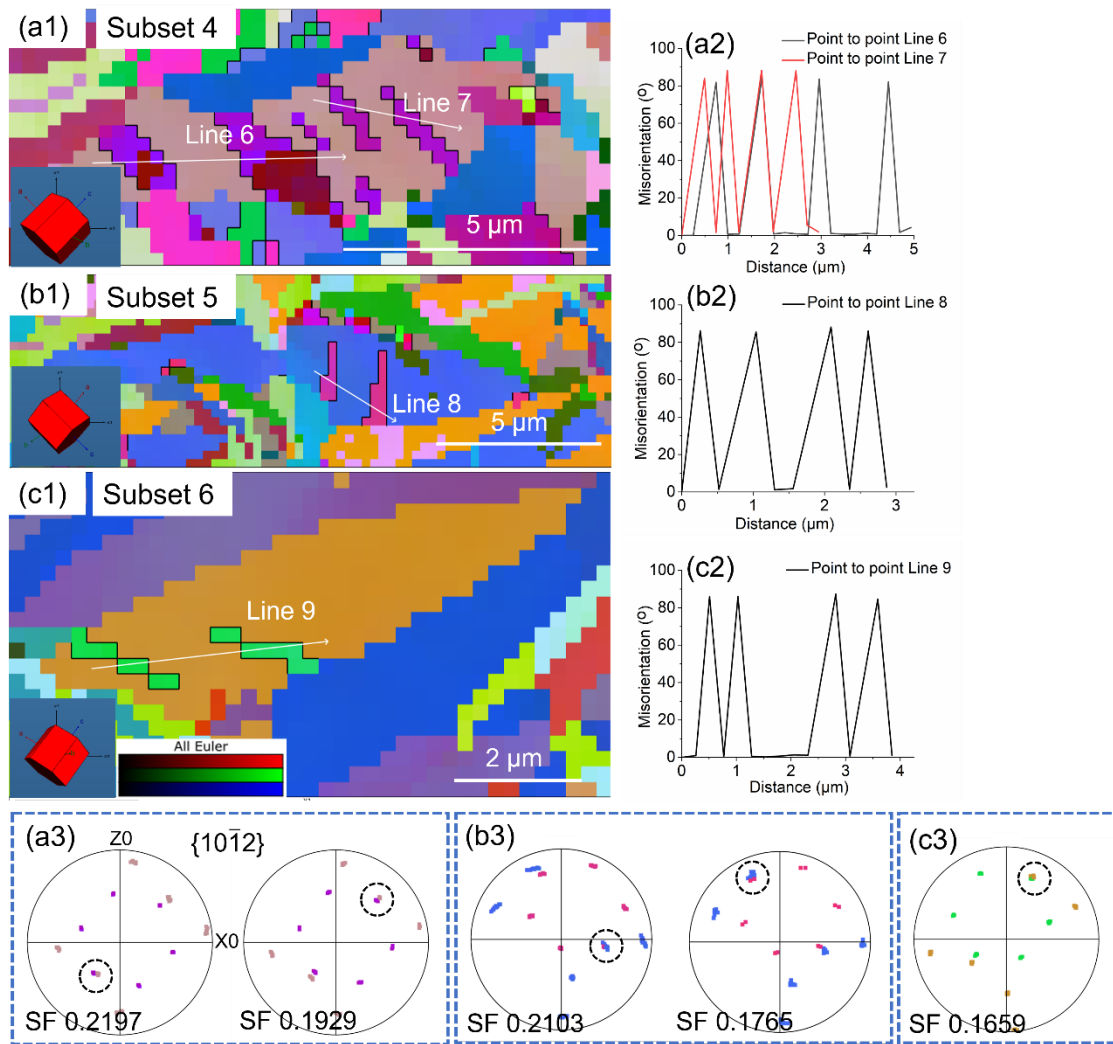


Fig. 7.16 Twin variants and Schmid factor analysis with c-axis of parent grains offsetting tensile direction around 45° in HT730, subset 4 to subset 6 (a1, b1, c1) All Euler maps, (a2, b2, c2) point-to-point misorientation maps with twins and parent grains, (a3, b3, c3) discrete pole figures of each twin and parent grain for twinning plane $\{10\bar{1}2\}$.

All Euler maps of HT900 after tensile testing are shown in Fig. 7.14(d). Fig. 7.17 shows three subsets (subset 7 to subset 9) of parent grains with a c-axis nearly along with the tensile direction from HT900. Likewise, point-to-point analysis of misorientation between twins and parent grains clearly exhibits the 85° rotation between twins and parent grains. Significant twin and twin intersections with boundary misorientation angles around 60° can be observed in subset 7 to subset 9 (Fig. 7.17) which is more significant compared to that of HT730 (Fig. 7.15). This phenomenon suggests multiple growth twin variants and grain refinement [270–272]. In subset 7 (see Fig. 7.17(a)), the

c-axis of the parent grain nearly paralleling to tensile direction presents six twin variants with high Schmid factors (over 0.45), which means all six possible twin variants observed in one parent grain. Five twin variants can be seen in the parent grain nearly paralleling to tensile direction in subset 8 (Fig. 7.17(b)) with high Schmid factors (over 0.45). Four twin variants can be also found in subset 9 with high Schmid factors (over 0.45), as shown in Fig. 7.17(c).

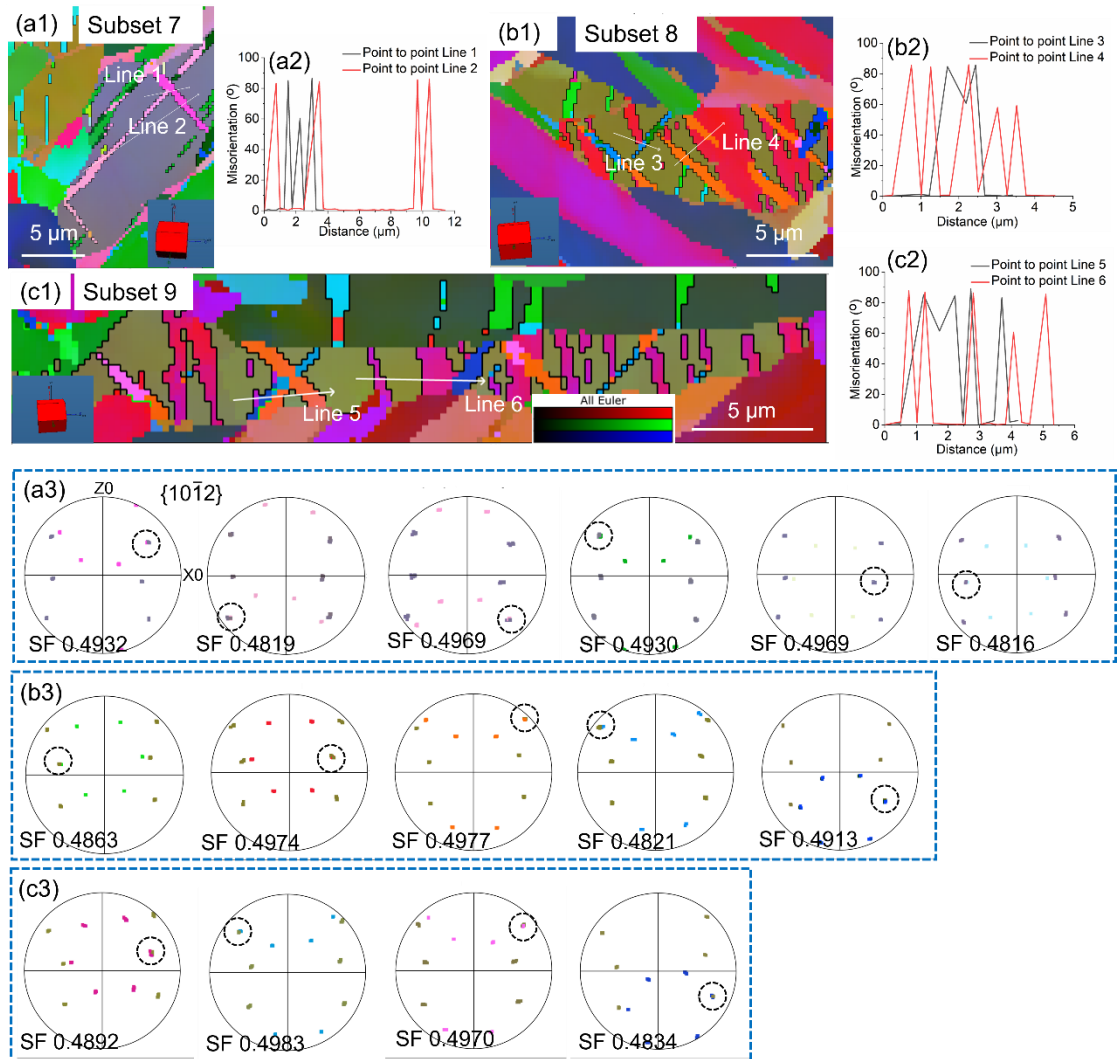


Fig. 7.17 Twin variants and Schmid factor analysis with c-axis of parent grains nearly paralleling to tensile direction in HT900, subset 7 to subset 9 (a1, b1, c1) All Euler maps, (a2, b2, c2) point-to-point misorientation maps with twins and parent grains, (a3, b3, c3) discrete pole figures of each twin and parent grain for twinning plane $\{10\bar{1}2\}$.

Table 7.5 Schmid factors of all six possible twin variants (Schmid factor bold for observed twin variants) in HT900 (C0 means c-axis of parent grains nearly along tensile direction, C45 means c-axis of parent grains offsetting tensile direction ~ 45°).

Type	Subset	V1	V2	V3	V4	V5	V6
C0	Subset 7	0.4969	0.4969	0.4932	0.4930	0.4819	0.4816
	Subset 8	0.4977	0.4974	0.4958	0.4913	0.4863	0.4821
	Subset 9	0.4983	0.4974	0.4970	0.4904	0.4892	0.4834
C45	Subset 10	0.2472	0.1736	0.1178	0.0999	0.0931	0.0375
	Subset 11	0.2191	0.1903	0.1491	0.0920	0.0649	0.0210
	Subset 12	0.1688	0.1555	0.1548	0.0775	0.0546	0.0095

All six possible Schmid factors of twin variants are also less than 0.25 when parent grains with c-axis offset tensile direction around 45°. There are four twin variants can be also identified in subset 10 (Fig. 18(a)). Four twin variants show four Schmid factors with 0.1178, 0.0999, 0.0931, 0.0375, respectively. Only twin variants with the largest and second largest Schmid factor are not observed (see Table 7.5). Twin variants with low Schmid factor are also reported by others [263,267]. Two other parent grains in subset 11 and 12 with the c-axis offsetting tensile direction around 45° are shown in Fig. 7. 18(b, c). Twin intersections are also found in subset 11. Two twin variants with the second largest and third largest Schmid factors are observed in subset 11.

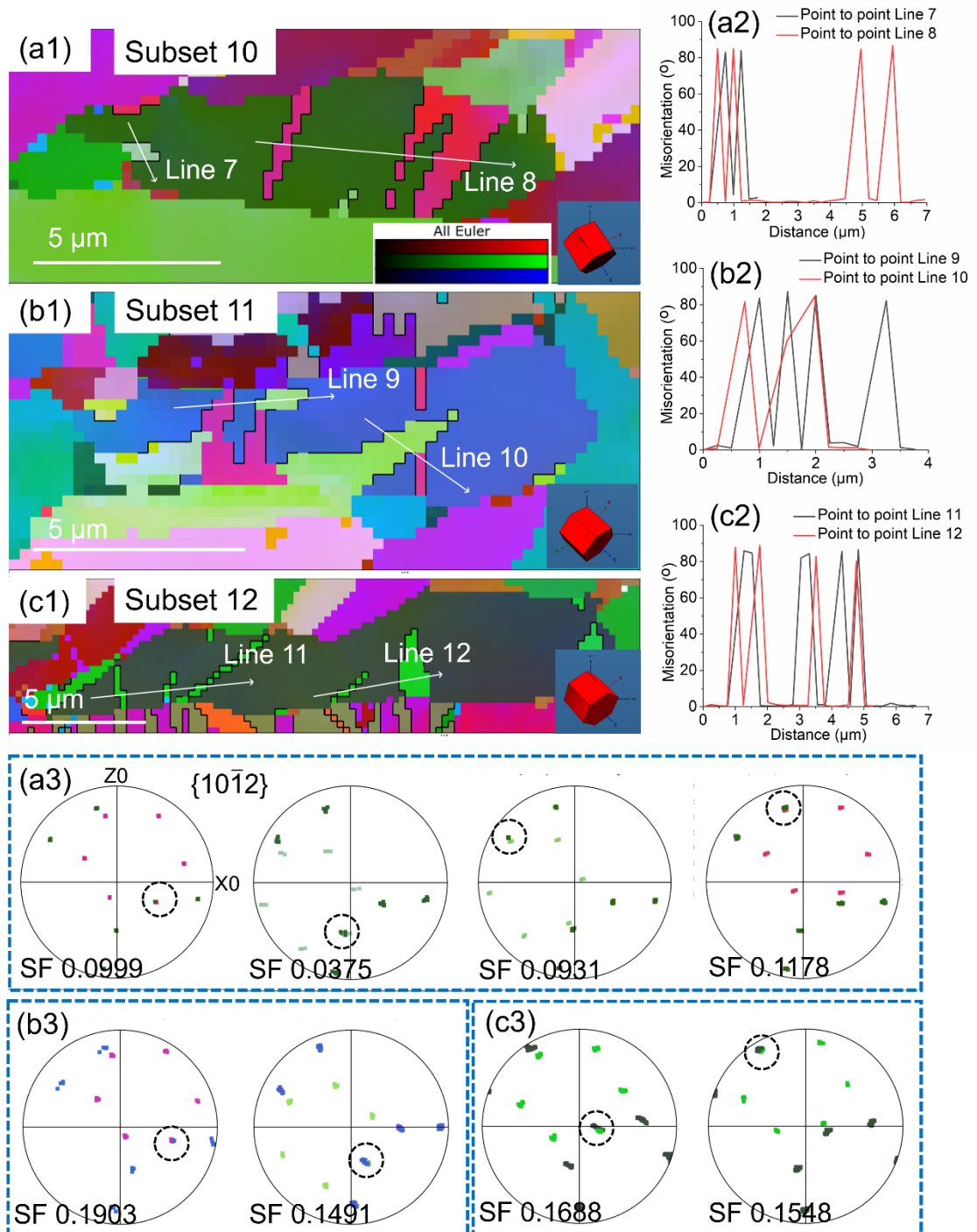


Fig. 7.18 Twin variants and Schmid factor analysis with c-axis of parent grains offsetting tensile direction around 45° in HT900, subset 10 to subset 12 (a1, b1, c1) All Euler maps, (a2, b2, c2) point-to-point misorientation maps with twins and parent grains, (a3, b3, c3) discrete pole figures of each twin and parent grain for twinning plane $\{10\bar{1}2\}$.

Fig. 7.19 shows the Schmid factor maps of HT730 and HT900 after deformation by EBSD in common slip systems including $\{0001\}\langle 11\bar{2}0\rangle$ basal $\langle\alpha\rangle$ slip, $\{10\bar{1}0\}\langle 11\bar{2}0\rangle$ prismatic $\langle\alpha\rangle$ slip, $\{10\bar{1}1\}\langle 11\bar{2}0\rangle$ pyramidal $\langle\alpha\rangle$ slip, $\{11\bar{2}2\}\langle 11\bar{2}3\rangle$ pyramidal $\langle\alpha + c\rangle$ slip and $\{10\bar{1}2\}\langle 10\bar{1}\bar{1}\rangle$ twinning deformation. There is no significant difference of all Schmid factor maps between HT730 and HT900 considering parent grains with twinning. It is noteworthy that parent grains with twinning along tensile direction usually presents high Schmid factors in $\{10\bar{1}2\}\langle 10\bar{1}\bar{1}\rangle$ in HT730 and HT900 which is generally consistent with the Schmid factor in twin variants in Figs. 7.15-18. This is most probably because twins are formed in a twinning plane and direction within parent grains. Parent grains (c-axis along the tensile direction, called hard grains) show low Schmid factor in basal $\langle\alpha\rangle$ slip, prismatic $\langle\alpha\rangle$ slip, pyramidal $\langle\alpha\rangle$ slip and large Schmid factor in pyramidal $\langle\alpha + c\rangle$ slip, which suggests the activation of $\langle\alpha + c\rangle$ slip and/or deformation twinning (confirmed by IPF maps ($//X0$) plus special boundary results). For grains with high Schmid factor in $\langle\alpha\rangle$ slip and $\langle\alpha + c\rangle$ slip, it is usually difficult to form deformation twinning and may activate dislocation slip. Interestingly, those parent grains (c-axis offset tensile direction around 45°) with deformation twins present high Schmid factors in all $\langle\alpha\rangle$ slip and $\langle\alpha + c\rangle$ slip, which may suggest the possible simultaneity of dislocation slip and twinning.

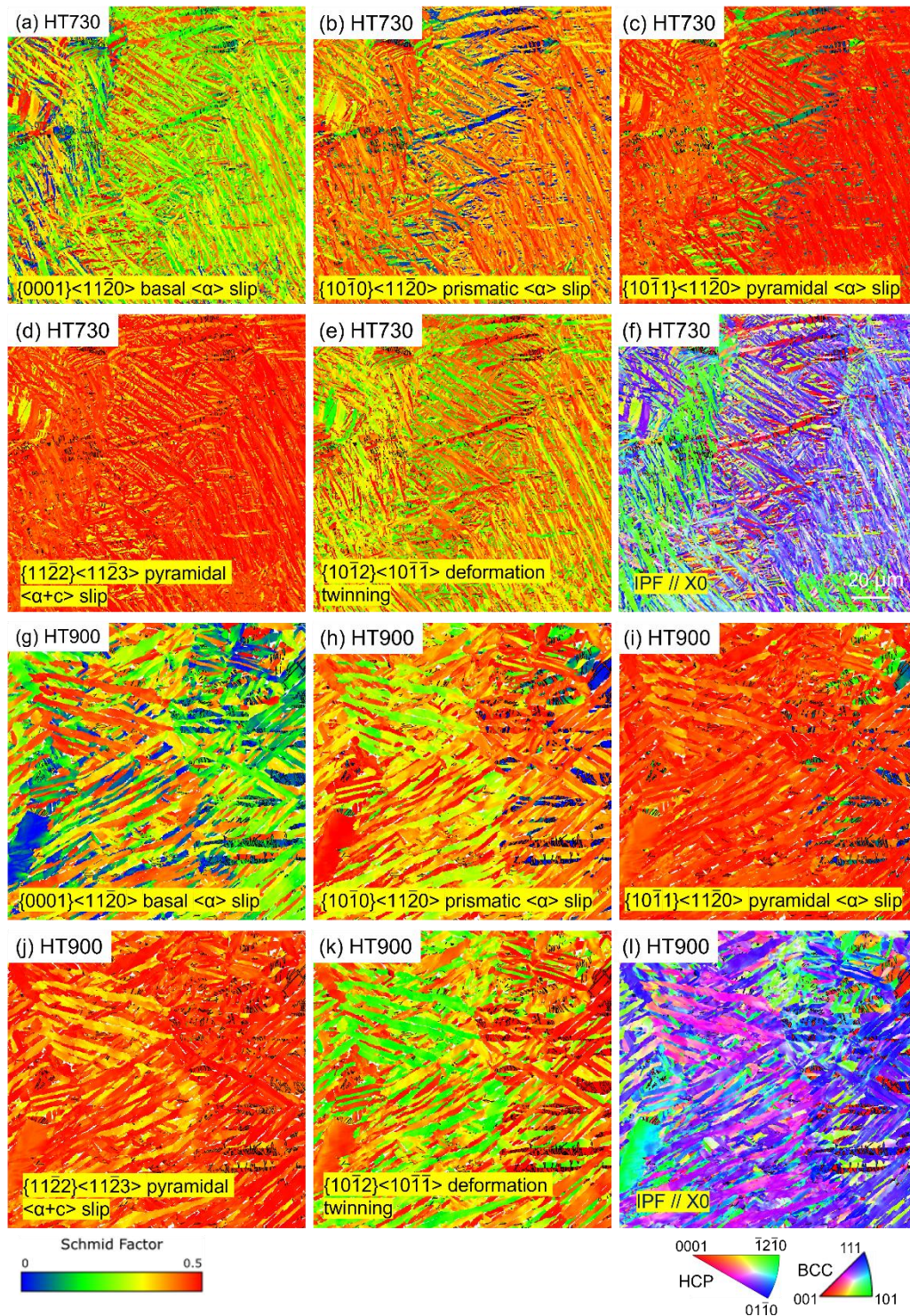


Fig. 7.19 Schmid factor maps of (a-d) HT730 and (g-j) HT900 after deformation in $\{0001\}\langle 11\bar{2}0 \rangle$ basal $\langle \alpha \rangle$ slip, $\{10\bar{1}0\}\langle 11\bar{2}0 \rangle$ prismatic $\langle \alpha \rangle$ slip, $\{10\bar{1}1\}\langle 11\bar{2}0 \rangle$ pyramidal $\langle \alpha \rangle$ slip, $\{11\bar{2}2\}\langle 11\bar{2}3 \rangle$ pyramidal $\langle \alpha + c \rangle$ slip, $\{10\bar{1}2\}\langle 10\bar{1}\bar{1} \rangle$ twinning deformation of (e) HT730 and (k) HT900, IPF//X0 of (f) HT730 and (l) HT900, showing the complementary relationship between dislocation slip and deformation twinning.

7.4 Discussion

Barriobero-Vila et al. [139] reported compression twinning $\{10\bar{1}1\}\langle 10\bar{1}\bar{2}\rangle$ in Ti-6Al-4V alloy by LPBF through in situ heat treatment after compression testing, confirmed by HEXRD and TEM without detailed twins' analysis, which suggests the thin width of deformation twins (less than 0.1 μm) and therefore is difficult to identify for EBSD analysis. In this chapter, deformation twins can be observed through the EBSD analysis of Ti-6Al-4V by LPBF with stress relief and high temperature annealing after tensile testing. Twin variants and Schmid factor analysis are investigated, which is not found in the literature for Ti-6Al-4V by LPBF after tensile testing. Several critical points for the observation of massive deformation twins for Ti-6Al-4V after tensile testing can be summarised in this thesis: (1) Ti-6Al-4V ELI powder feedstock used with low oxygen level [38,261,262], (2) low oxygen level (less than 500 ppm) in the build chamber [260], (3) large grain size by high temperature annealing [205,268,269,273], (4) small step size (0.25 μm) used to identify twins although the large grain size in the heat treated Ti-6Al-4V does not require small step size [193,195,203,268]. The observed deformation twins may play a crucial role in ductility. Therefore, deformation mechanisms and deformation twinning behaviour will be discussed to understand ductility mechanisms and influence factors on twinning behaviour. This may provide new insight to optimise the mechanical properties of Ti-6Al-4V considering deformation mechanisms and deformation twinning.

7.4.1 Deformation mechanisms

First, it is known that dislocation slip is one of the most important deformation mechanisms for Ti-6Al-4V alloy [38,101]. In this heat treatment chapter, dislocation slip may play a crucial role in plastic deformation. First, based on the c/a ratio results, there are slight increases in the c/a ratio in HT730 and HT900 in this chapter compared to as-built Ti-6Al-4V that are consistent with Zhang et al. [101] using the same heat treatment temperature in Ti-6Al-4V alloy by LPBF. It was reported that the ratio of $\text{CRSS}_{\text{prism}}/\text{CRSS}_{\text{basal}}$ is estimated to be 1.31 and 1.16 for the martensite α' phase in the as-built and α phase HT900 specimens, respectively. Multiple slip systems are more likely to be activated in HT900, which enhances the dislocation slip and improves ductility. As for the role of β phase on deformation, β phase cannot be detected in as-built Ti-6Al-4V based on XRD, however, a very small amount of β phase can be found

from EBSD results. Zafari et al. [274] reported that the fine size β phase may cause considerable stress concentrations at the α'/β interface during tensile testing and thus decrease ductility. For HT730, fine size β phase content increases and Zhang et al. [101] thought that stress concentration at the α'/β interface may be larger than as-built Ti-6Al-4V based on the in-situ tensile testing experiments. β phase grew and became coarser in HT900 and thus stress concentration at the α'/β interface may be eliminated, which may benefit ductility.

From KAM maps (see Fig. 7.13), the KAM difference between after tensile testing and before tensile testing for as-built, HT730 and HT900 is 0.342° , 1.103° , 1.165° , respectively. This suggests enhanced dislocation slip in HT730 and HT900 compared to the as-built Ti-6Al-4V because KAM is related to the strain accumulation after tensile deformation. The enhanced dislocation slip confirmed by KAM was also reported by Qiu et al. [248] in β titanium alloy by LPBF. It is noteworthy that there is no obvious difference in the KAM values for HT730 and HT900. Hence, there may be another ductility mechanism contributing to HT900 ductility. Fig. 7.20 shows the KAM maps plus the special boundary for as-built Ti-6Al-4V, HT730 and HT900 after tensile testing. It can be found that most grains with deformation twins present low KAM (blue colour), especially for HT900. Hence, deformation twinning may play an important role in strain accommodation for HT900 during tensile testing. The findings about the deformation twinning for Ti-6Al-4V by LPBF may provide new insight into the deformation mechanisms and mechanical properties optimisation approach of Ti-6Al-4V.

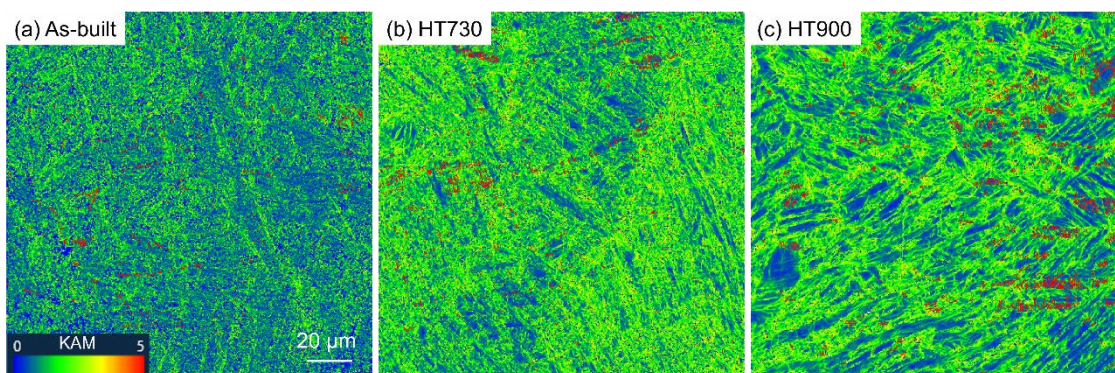


Fig. 7.20 KAM maps plus the special boundary (i.e., deformation twins, marked with red colour) for (a) as-built Ti-6Al-4V, (b) HT730 and (c) HT900 after tensile testing.

7.4.2 Twinning behaviour

In this chapter, deformation twins can be observed in HT730 and HT900 after tensile testing, especially for HT900. The twinning fraction for as-built, HT730 and HT900 are 2.64%, 4.15% and 16.0%, respectively. Two factors including residual stress (pre-strain) and grain size can be considered for twinning fraction in this chapter based on literature in Ti and Ti alloys by conventional manufacturing [273]. For as-built Ti-6Al-4V and HT730, the grain size is almost the same (slight difference) while stress relieved HT730 has low residual stress compared to as-built Ti-6Al-4V (see Fig. 7.13). Hence, the reduction of residual stress for HT730 obtains a limited increase in twinning fraction compared to as-built Ti-6Al-4V with residual stress. This may be due to the dislocation stored in the as-built Ti-6Al-4V is not suitable to form embryonic twins during deformation and more studies are expected to clarify the related mechanisms of pre-strain on deformation twinning [273]. For increased heat treatment temperature, grain size is significantly increased for HT900 compared to HT730 (see Fig. 7.3 and Fig. 7.11). Therefore, grain size may make a significant contribution to deformation twinning. The effect of grain size on deformation twinning can also be found in the literature [205,268,269,273]. It is more likely that deformation twins will be found in polycrystalline samples with larger grains. For example, Huang et al. [268] investigated the effect of grain size on the deformation twinning of CP Ti fabricated by conventional manufacturing. The deformation twin fraction can be increased when the grain size increases. Studies are being conducted to clarify the reason for the grain size effect on twinning, however, it has not yet been determined [273]. There is a view that twins originate from defects (such as slip dislocations). Accordingly, the large grains contain more twins since they have large grain boundary areas and large grain volumes and, therefore, are more likely to nucleate. Besides the grain size, the chemical composition of the α phase in HT730 and HT900 should be also considered. The EDS of HT730 and HT900 for the α phase is presented in Table 7.6. It is known that Al content influences the deformation twinning of Ti alloys. Fitzner et al. [275] studied the effect of aluminium on twinning in binary Ti-Al alloy. The results indicated that there is a turning point at around 4 wt.% aluminium in twinning activity and the twinning activity would suffer a dramatic loss with further increase in aluminium content. There are several factors affecting this phenomenon, including the decrease of stacking fault energy (SFE) caused by aluminium or its solute solution strengthening effect. From the aspect of Al

content, HT730 shows slightly lower Al than that of HT900 due to the Al element diffusing into α phase with high temperature heat treatment [38]. There may be a slight increase in twinning activity for HT730 than HT900 based on the Al content. For the V content, it is also higher for HT730 than HT900 due to the V element diffusing into β phase with high temperature heat treatment [38]. The Al rich in α phase and V poor in α phase for high temperature HT900 are consistent with other high temperature heat treatment works [173,276]. Deformation twins can be found in all Ti-6Al, Ti-6Al-2V, and Ti-6Al-4V by Wire + Arc Additive Manufacturing (WAAM) after impact testing [277]. However, no further information reveals the effect of V content on deformation twinning activity and impact testing with high strain rate is also different from quasi static testing. It is known that there is around 1% β phase in HT730 and around 5% β phase in HT900. The β phase may be a benefit to accommodate the strain in α phase and reduce the strain concentration during the deformation [101] and β phase have a positive effect on dislocation slip due to more slip systems. Therefore, the β phase may be a negative factor for twinning activity. Although there is around 5% β phase in HT900, twinning activity can be still observed. This suggests there is a noticeable effect of grain size on deformation twinning formation.

Table 7.6 Elemental content by EDS results of HT730 and HT900 for α phase.

α phase	Ti	Al (wt. %)	V (wt. %)
HT730	Bal.	6.36±0.06	3.66±0.72
HT900	Bal.	7.16±0.17	1.83±0.25

The difference in twin variants for HT730 and HT900 is also found. In general, there are more growth twin variants for HT900 than HT730, especially for the c-axis of parent grains along with the tensile direction. The formation of more twin variants and more twin-twin interactions may also be attributed to the large grain size in HT900, which was also demonstrated by Wang et al. [269]. The appearance of twin variants with low Schmid factor in HT900 may be the result of twins accommodating heterogeneous deformation among neighbouring grains [263,267]. These results suggest that tuning deformation twinning via manipulating grain size of Ti-6Al-4V (such as further increase the heat treatment temperature) to promote TWIP and enhance ductility can be considered.

7.4.3 Comparison with composition modified Ti alloys

7.4.3.1 Chemical homogeneity and microstructure

In Chapter 6, balanced strength and ductility of as-built parts were achieved via chemical composition modification of Ti-6Al-4V. Therefore, herein the difference in chemical homogeneity, microstructure, and strength and ductility mechanisms for two ways (composition modification and heat treatment) to achieve balanced strength and ductility are compared and discussed. For the chemical composition modification method, Al and V poor areas can be observed in PT25 and PT50. This is due to the mechanical mixing method. The pre-alloying method may avoid the non-uniform area. However, for heat-treated HT730 and HT900, due to the diffusion of α -stabiliser Al and β -stabiliser V after heat treatment, Al is enriched in α phase and V is enriched in β phase. This kind of elemental distribution due to α -stabiliser element and β -stabiliser element would exist after heat treatment. There is also a difference in microstructure between chemical composition modification and heat treatment method. For chemical composition modification, PT25 and PT50 present a non-equilibrium state α/α' structure without an obvious β phase while HT730 and HT900 show equilibrium state α structure and β phase. In addition, there is a decreasing trend in the c/a ratio for PT25 and PT50 by chemical composition modification while slight increase in the c/a ratio can be found for HT730 and HT900 by heat treatment.

7.4.3.2 Strength and ductility mechanisms

In this thesis, balanced strength and ductility were achieved for both chemical composition modification and heat treatment methods. However, the strength and ductility mechanisms are different. First, for the strength mechanism, based on the discussion in Chapter 6, yield strength is mainly dependent on solid solution strengthening and grain boundary strengthening. It is known that reduced strength is observed for both methods compared to as-built Ti-6Al-4V. For PT25 and PT50 obtained by dilution of Ti-6Al-4V via CP Ti addition, the solid solution strengthening for PT25 and PT50 is reduced compared to Ti-6Al-4V. For heat treatment, there is no significant difference in elemental Al and V content. Hence, the solid solution strengthening for HT730 and HT900 may be comparable with as-built Ti-6Al-4V. The grain boundary strengthening is related to the α/α' width based on Hall-Petch equation. There is a gradual increase in α/α' width when CP Ti addition increases for PT25 and

PT50 while slight increase in α/α' width for HT730 but a huge increase in α/α' width for HT730 compared to as-built Ti-6Al-4V. Therefore, there is a mild decrease in grain boundary strengthening in PT25 and PT50. However, slight decrease grain boundary strengthening for HT730 and a significant decrease for grain boundary strengthening in HT900 can be observed. As for the ductility mechanism for the two methods, significant differences can also be found. For chemical composition modification method, dislocation slip dominated ductility mechanism and no obvious deformation twinning are observed for PT25 and PT50. Both dislocation slip and deformation twinning are found in HT730 and HT900, especially for HT900.

Therefore, this chapter provides new insight about the deformation mechanisms of Ti-6Al-4V by LPBF. The observation of massive deformation twins in heat treated Ti-6Al-4V may open a new way considering how to manipulate the deformation twins to improve the mechanical properties (especially for ductility) of Ti-6Al-4V. Related factors such as powder feedstock, processing parameters, post heat treatment affecting the deformation twinning behaviour of Ti-6Al-4V may be future studies. For example, besides grain size optimisation by heat treatment, it is also interesting to investigate the effect of grain morphology (equiaxed, lamellar, bimodal) on deformation twinning behaviour.

7.5 Conclusions

In summary, a systematic investigation of microstructural and mechanical properties in heat treated Ti-6Al-4V by LPBF was performed. The aim of this chapter was to study the deformation twinning behaviour of two heat treated Ti-6Al-4V by LPBF. The deformation twins in stress relief (HT730) and annealing (HT900) Ti-6Al-4V after tensile deformation were observed. The deformation twinning behaviour was analysed with EBSD for the heat treated Ti-6Al-4V. Massive deformation twins can be observed in annealing Ti-6Al-4V after tensile deformation. The deformation twins in annealed Ti-6Al-4V after tensile deformation may have a positive effect on texture randomization. Grains with a c-axis along with tensile direction for both two heat treatment samples prefer to form deformation twins due to the difficulty for dislocation slip with low Schmid factor in $\langle\alpha\rangle$ slip. There are more growth twins, significant twin-twin intersections, and more twin variants observed in annealing sample after deformation than the stress relief sample. Some grains with c-axis offsetting with tensile direction

can also find deformation twins for two heat treatment samples. High Schmid factor twin variants among all possible variants may form in the offset parent grains in HT730 while low Schmid factor twin variants appear in the offset parent grains in the HT900 sample. It is believed that the deformation twins coordinate plastic deformation with dislocation slip to increase ductility in heat treated Ti-6Al-4V. This work gives new insight into the deformation twinning behaviour in LPBF, which may provide a view of research via twinning optimisation to achieve better strength-ductility in CP Ti, Ti-6Al-4V and other Ti alloys. This is different from previous literature mainly focused on the contribution of dislocation slip to ductility. The starting point of the deformation twinning study in this chapter may be beneficial to further understand the deformation mechanisms of Ti-6Al-4V.

8 Conclusions

8.1 General conclusions

In this thesis, a systematic study of Ti-6Al-4V performance by LPBF with powder feedstock and heat treatment considerations was conducted. The investigated performance mainly includes surface quality, relative density, microstructure and mechanical properties, and those performance can affect the practical applications. Therefore, this thesis investigates the relationship between powder feedstock, heat treatment, and Ti-6Al-4V performance. Moreover, the related mechanisms involved in powder feedstock and heat treatment have been performed. This may be beneficial for further powder feedstock and heat treatment optimisation to obtain better performance of Ti-6Al-4V. Surface quality and relative density have a close relationship with PSD. In contrast, chemical composition modification, and heat treatment can manipulate Ti-6Al-4V microstructure and mechanical properties. The conclusions can be divided into three sections including PSD findings, chemical composition findings, and heat treatment findings.

8.1.1 PSD findings

Reused powder usually exhibits a coarsening trend for PSD, which is confirmed by both laser diffraction and SEM image methods. Underlying mechanisms for PSD coarsening of reused powder were systematically investigated via various types of powders collection in different positions of the build chamber after LPBF build. Through the analysis of various types of powders (such as spatter and sintered powder) during interactions between laser and powder, PSD coarsening mechanisms can be attributed to three main factors: (i) layer thickness; (ii) spatter; (iii) sintered powder. Low layer thickness (such as 30 μm) will cause large particles moving into overflow and leaving more fine particles in powder bed. This may be one of the reasons for PSD coarsening. Spatter including P-GI spatter, P-GO spatter, and spatter dropped in the powder bed may also increase the particle size of reused powder based on spatter evolution during LPBF. Meanwhile, a link is established between spatter with modified particle size in different positions and its corresponding origins (droplet ejection spatter, hot, and cold spatter). Large pores and increased surface quality are observed in parts built by reused powder compared to virgin powder. It is suggested that build chamber partitioning can be

considered if a repeatable and specific PSD is required in the collected powder for recycling. To further control and maintain powder feedstock quality, optimisation of processing parameters, including layer thickness, sintering, and spatter formation, is proposed.

Then, different PSD Ti-6Al-4V powder feedstocks are obtained by the sieving method. Effects of different PSD powder feedstocks on in-process powders, single-track formability, and parts performance by LPBF were systematically investigated. Obvious differences cannot be found in powder from overflow while spatter presents significant differences when using different PSD Ti-6Al-4V powder feedstocks. In 15-38 μm powder feedstock, fine spatter and less collected weight are observed whereas 38-45 μm powder presents coarser spatter and more collected weight. Fine 15-38 μm powder feedstock exhibits better single-track formability compared to standard 15-45 μm powder and coarse 38-45 μm powder based on single-track morphology, single-track width, and single-track height profile measurement. By using 15-38 μm powder feedstock, improved surface quality and better relative density can be obtained. This has a high correlation with the results of in-process powders and single-track formability, which suggests that in-process powders and single-track formability may act as effective signals to predict the performance of as-built parts by different PSD powder feedstocks. It is noteworthy that significant differences in microstructure and mechanical performance cannot be observed when applying different PSD powder feedstocks.

8.1.2 Chemical composition findings

Chemical composition modification applied to Ti-6Al-4V is a powerful approach to modify microstructure and mechanical properties. In this thesis, a facile method to tune the Ti-6Al-4V composition is presented through CP Ti addition into Ti-6Al-4V. This facile in-situ composition tailoring strategy can modify the microstructure and achieve balanced strength-ductility of Ti alloy in the as-built state to address the low ductility issue in Ti-6Al-4V. Developed Ti-Al-V alloys with nominal Ti-4.5Al-3V (PT25) and nominal Ti-3Al-2V (PT50) can be obtained through different CP Ti additions into Ti-6Al-4V (PT0). PT25 and PT50 present a high relative density (over 99.90%) using the same processing parameters as Ti-6Al-4V. For microstructure, an increase in martensite α' thickness and a decrease in c/a ratio can be found when CP Ti addition increases. There is a decreasing trend in strength and an increasing trend in ductility when CP Ti

addition increases. Balanced strength-ductility (tensile strength ~ 1000 MPa, yield strength ~ 900 MPa, and elongation $\sim 13\%$) for as-built PT50 can be achieved, which satisfies the wrought Ti-6Al-4V standard. Mechanical properties can therefore be facilely manipulated by proper CP Ti addition into Ti-6Al-4V. The reduced strength in modified alloys is mainly due to the decrease in grain boundary strengthening and solid solution strengthening. The critical enhanced ductility is believed to be from the increase in dislocation slip with multiple slip systems based on the c/a ratio analysis. This strategy may be possible to employ in other Ti alloys, steels, and Ni-based superalloys to obtain a desired microstructure and better strength-ductility or other desired properties (such as crack-free). This practical and economical strategy may benefit materials adaption and development in LPBF.

8.1.3 Heat treatment findings

In this thesis, the microstructural and mechanical properties of heat treated Ti-6Al-4V by LPBF were studied. After heat treatment, martensite α' decomposes into $\alpha+\beta$ and balanced strength and ductility can be achieved. While balanced strength-ductility can be observed in Ti-6Al-4V by heat treatment, this thesis shows deformation mechanisms such as deformation twinning, which is not significantly observed in composition modified Ti-6Al-4V. EBSD confirmed and analysed deformation twinning behaviour for heat treated Ti-6Al-4V after tensile testing. Massive deformation twins can be observed in HT900 after tensile deformation. This improves texture randomization. For both two heat treatment (HT730 and HT900) samples, grains with c -axis nearly along with tensile direction prefer to form deformation twins as it is difficult for the activation of dislocation slip with low Schmid factor in $\langle\alpha\rangle$ slip. More growth twins, significant twin-twin intersections, and more twin variants are observed in HT900 after deformation than in HT730. Two heat treatment samples show deformation twins in some grains with c -axis offsetting from the tensile direction. Low Schmid factor twin variants occur in the offset grains (c -axis around 45° with tensile direction) in the HT900 sample, however, high Schmid factor twin variants among all possible variants form in HT730. The differences in deformation twinning behaviour can be mainly explained by the large grain size in HT900. It is suggested that the deformation twins coordinate plastic deformation with dislocation slip to improve ductility in heat treated Ti-6Al-4V. This heat treatment work gives new insight into deformation twinning behaviour in

LPBF, which may provide a novel twinning optimisation solution to achieve better strength-ductility in CP Ti, Ti-6Al-4V and other Ti alloys.

8.2 Benefits of the study to academia

Several benefits to academia can be summarised in this thesis. First, the study of PSD coarsening mechanisms benefits the understanding of particle size evolution during LPBF. Deeper understanding of the effect of spatter on PSD coarsening is obtained. Spatter acts as a bridge to link the different PSD powder feedstocks with surface quality and relative density. The impact of spatter on LPBF processes is therefore well understood through PSD-related studies.

In this thesis, the concept of in-situ alloying through pure metals and corresponding alloys may be useful in the adaption and development of materials in the LPBF field. It can be expanded to other Ti alloys, Ni-based alloys, steels to address common issues (such as cracking) and promote performance. It may not be perfect for alloy final composition in some cases. However, it may provide a solution to explore various alloys through this intermediate in-situ alloying first to verify feasibility before producing pre-alloy powder.

The observed deformation twins in heat treated Ti-6Al-4V in this thesis may open an exciting way to understand and improve Ti-6Al-4V ductility by LPBF. In previous literature, dislocation slip was mainly focused on plastic deformation in LPBF. However, twinning is also critical for HCP materials with limited dislocation slip systems. Therefore, more and more attention may be paid, and more research will be studied on the deformation twinning of Ti-6Al-4V and Ti alloys by LPBF after the observation of massive deformation twins in annealed Ti-6Al-4V.

8.3 Benefits of the study to the industry

Some benefits to the industry based on this thesis can be found. For example, PSD coarsening mechanisms may help the industry to maintain reused powder properties and increase recycling times and save costs. This means managing powder feedstocks may be beneficial. Fine PSD powder feedstock can reduce surface roughness and increase surface quality. This would be helpful for industry if high surface quality is required.

In this thesis, a facile way to address the poor ductility of Ti-6Al-4V without post-processing. Both materials are commercially available and easily accessible. This may also be interesting for the industry. Because post-processing for Ti-6Al-4V is usually costly and sometimes unavailable. Meanwhile, the increased ductility in modified Ti-6Al-4V may reduce build failure rates during LPBF. Therefore, it may be an effective solution for industry to obtain balanced strength-ductility Ti alloy without heat treatment.

8.4 Future work

Despite systematic work to investigate the performance of Ti-6Al-4V by LPBF with powder feedstock and heat treatment considerations, there are still some works that can be done in future. These works can expand the understanding of powder feedstock and heat treatment. This may enable us to achieve the superior performance of Ti-6Al-4V. In this chapter, future recommendations on three aspects of PSD, chemical composition, and heat treatment are proposed.

This thesis investigates PSD coarsening mechanisms by analysing interactions between laser, powder feedstock, recoater, and gas flow. It does not build a relationship between PSD coarsening degree and processing parameters, gas flow. It needs to be further investigated to determine the effect of processing parameters and gas flow. This may help to strictly control the PSD and oxygen level of reused powder, especially spatter control during LPBF. This kind of work would be industrially interesting. However, massive LPBF experiments need to be carried out to establish the relationships involving PSD of reused powder, processing parameters and gas flow, spatter formation. Since fine PSD powder feedstock (such as 15-38 μm) presents better single-track formability, especially at low power, therefore, this fine PSD powder feedstock may be a suitable candidate for fine lattice structures. Future work can be considered to study the effect of different PSD powder feedstocks on the performance of lattice parts by LPBF. Different PSD powder feedstocks may affect size resolution and relative density, especially compression mechanical properties.

In this thesis, balanced strength and ductility can be achieved by mixing Ti-6Al-4V with CP Ti. Some points can be considered for future work. First, segregation is common for in-situ alloying. This coarse particle size in CP Ti may affect the chemical homogeneity of modified Ti alloys. This suggests that employing CP Ti powder with PSD around

several μm (to obtain satellite powder feedstock into Ti-6Al-4V) may improve the chemical homogeneity. This is one of the solutions to enhance the chemical homogeneity. Another solution is processing parameters optimisation. For example, a scanning strategy with remelting each layer may reduce segregation. High energy density (high power or low scan speed) to enhance melting during LPBF may also be an effective way to improve chemical homogeneity for in-situ alloying. Therefore, PSD and processing parameters optimisation is recommended for future work to minimise segregation. Second, the ductility in modified Ti-6Al-4V (PT50) is around 13% which is lower than HT900 with around 16%. Further improving the ductility in the PT50 through processing parameters optimisation is possible and this can also be a future work. This is because processing parameters optimisation is already applied in Ti-6Al-4V to boost ductility. Additionally, by increasing the CP Ti addition (for example, 60% or 70%, ensuring sufficient strength), ductility can be increased based on the microstructure and mechanical properties analysis. Therefore, to improve the performance of modified Ti-6Al-4V, several ways, including powder optimisation, processing parameters optimisation, can be recommended for future work. Besides, as presented in the discussion section of Chapter 6, the CP Ti addition can likewise be employed in other Ti alloys to modify the microstructure and mechanical properties. For example, high solute content Ti-6Al-2Sn-4Zr-6Mo presents martensite α'' and low yield strength, which may be modified with CP Ti addition to tune the microstructure into α'/α'' or fully α' and thus tailor the mechanical performance.

In this thesis, deformation twins are observed in heat treated Ti-6Al-4V (especially in HT900), which benefits the deformation process and increases ductility. This is a starting point for deformation twinning studies for heat treated Ti-6Al-4V by LPBF. There are still many gaps in considering deformation twinning behaviour in different experimental conditions. In addition, there are gaps in making full use of deformation twinning to enhance the strength and ductility of Ti-6Al-4V. Therefore, several works can be recommended for future work. For example, what is the effect of microstructures (such as lamellar, bi-modal, equiaxed) on the deformation twinning behaviour of Ti-6Al-4V? To better understand deformation twinning behaviour and its relationship with microstructure and mechanical properties, it is recommended that future work be conducted on the above question. Besides, another interesting future work is to study the deformation twinning behaviour and the interactions between dislocation slip and

deformation twinning through in-situ EBSD and in-situ TEM tensile testing. This may gain a deeper understanding of deformation twinning formation and movement as well as the role of deformation twinning on ductility enhancement. After that, optimisation in powder feedstock, processing parameters and post-processing can be considered to achieve better performance of Ti-6Al-4V.

Appendix-PSD measurements

1.1 Air pressure and feed rate calibration by laser diffraction

To understand the effect of non-laser parameters on PSD and identify the correct initial parameters for experimentation, air pressure (disperse the powder with compressed air), and powder feed rate (influence the dispersion of powder during measurement) were varied. Fig. A1 shows the effect of air pressures (from 0.1 to 3 bar) and feed rates on PSD results of reused powder measured by laser diffraction. PSD results were consistent under different air pressure (from 0.1 to 3 bar) and feed rate (from 20% to 30%). These results indicate that there is negligible effect of air pressure and feed rate at above ranges on PSD.

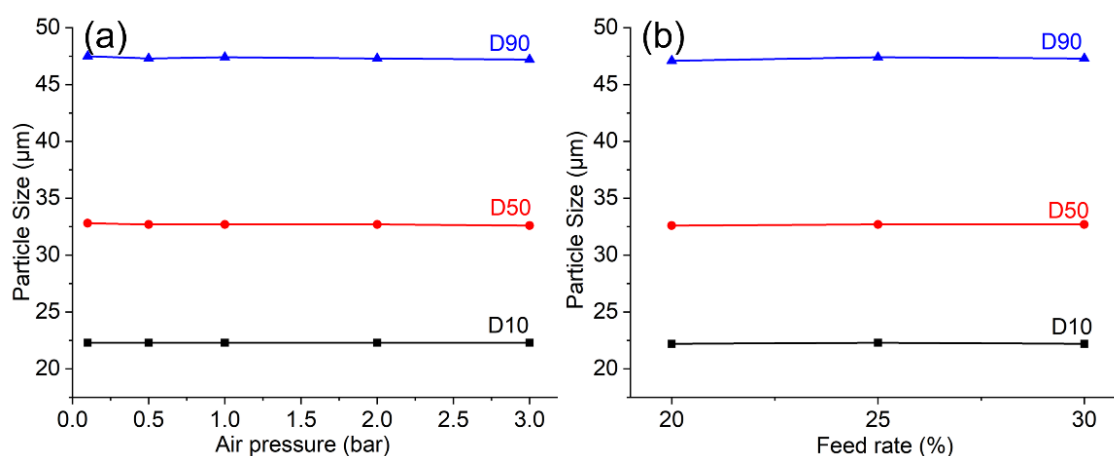


Fig. A1 PSD results of reused powder under different air pressure (a) and feed rate (b).

1.2 PSD of virgin and reused powder measured by SEM image analysis

To clarify the coarsening in powder size, a comprehensive SEM image analysis study of 12x reused powder was also performed to meet different sample conditions (such as spatter with a small amount, less than 1g). Fig. A2 shows the ImageJ workflow of PSD measurement by SEM image analysis. SEM image was loaded into ImageJ with a scale bar setting through the command “Analyze→Set Scale” (see Fig. A2(a)). Then, processed image with selected and identified particles can be obtained through the command “Image→Type and Image→Adjust→Threshold” by by converting the 8-bit

image and thresholding (see Fig. A2(b)). After that, setting through the command “Analyze→Analyze Particles and Set Measurements” was employed (see Fig. A2(c)). Finally, Area results can be achieved through the command “Analyze→Measure” (see Fig. A2(d)). The equivalent diameter can be obtained through the area results. Table A1 shows the PSD results of virgin powder using different SEM magnifications of 100X, 200X, 300X, and different numbers of total particles measured for each.

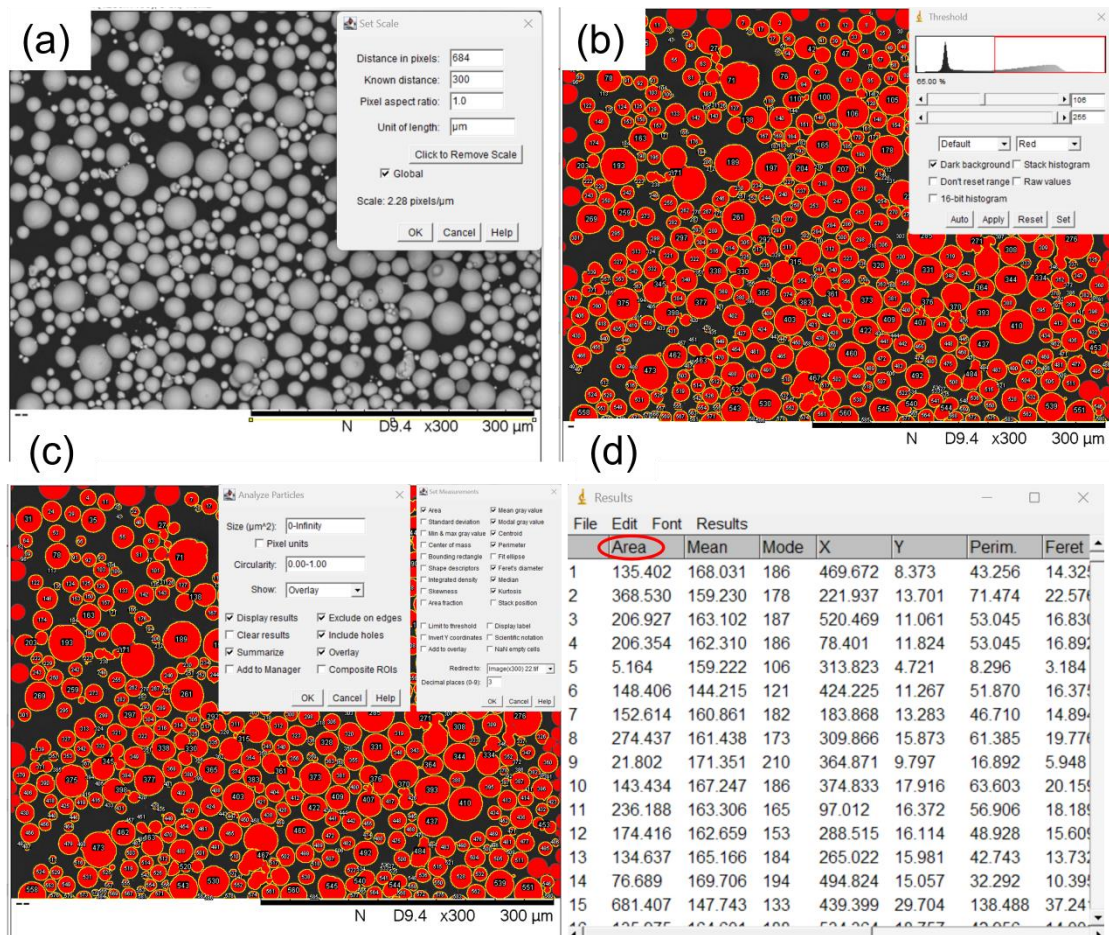


Fig. A2 The ImageJ workflow of PSD measurement by SEM image analysis.

Table A1 PSD results of virgin powder by SEM images method with magnification 100X, 200X, 300X.

Magnification	Number of particles	D10 (μm)	D50 (μm)	D90 (μm)
100X	2,500	17.2	35.3	70.0
	5,000	17.5	35.8	71.7
	10,000	17.1	35.2	69.2
200X	2,500	14.1	26.1	42.5
	5,000	14.8	28.9	46.3
	10,000	14.8	28.3	46.6
300X	2,500	14.5	27.2	41.8
	5,000	14.5	27.2	42.5
	10,000	14.5	26.6	42.1

It can be seen that image analysis at different SEM magnifications yielded different PSD results. The disparity between results is particularly stark at 100X magnification. Particle sizes by all metrics at 100X were significantly larger than those at 200X and 300X. For example, the D90 at 100X yielded an average of 70 μm compared to 45 μm for 200X magnification. This large difference implies a change in the measuring mechanism. To analyse this further, images used for automated image analysis, scaled to the same location at the same scale, are shown in [Fig. A3](#).

In [Fig. A3](#) it can be seen that some particles are mis-identified. In [Fig. A3\(a\)](#), a group of particles is identified as one particle, explained by the poor resolution at this magnification, meaning the blurring of particles together in the image. This results in a significantly increased D90 value. In [Fig. A3\(b\)](#), the outlines clearly identify all particles. However where there is a slight overlap, or where particles come close to each other, there is sometimes a mis-identification of particles. This results in two particles being recognised as one. This explains why the PSD metrics are significantly lower than in the 100X case and only slightly higher than in the 300X case. In the 300X magnification image in [Fig. A3\(c\)](#), almost all particles are correctly measured, however, there is still some inevitable mis-identification where particles overlap.

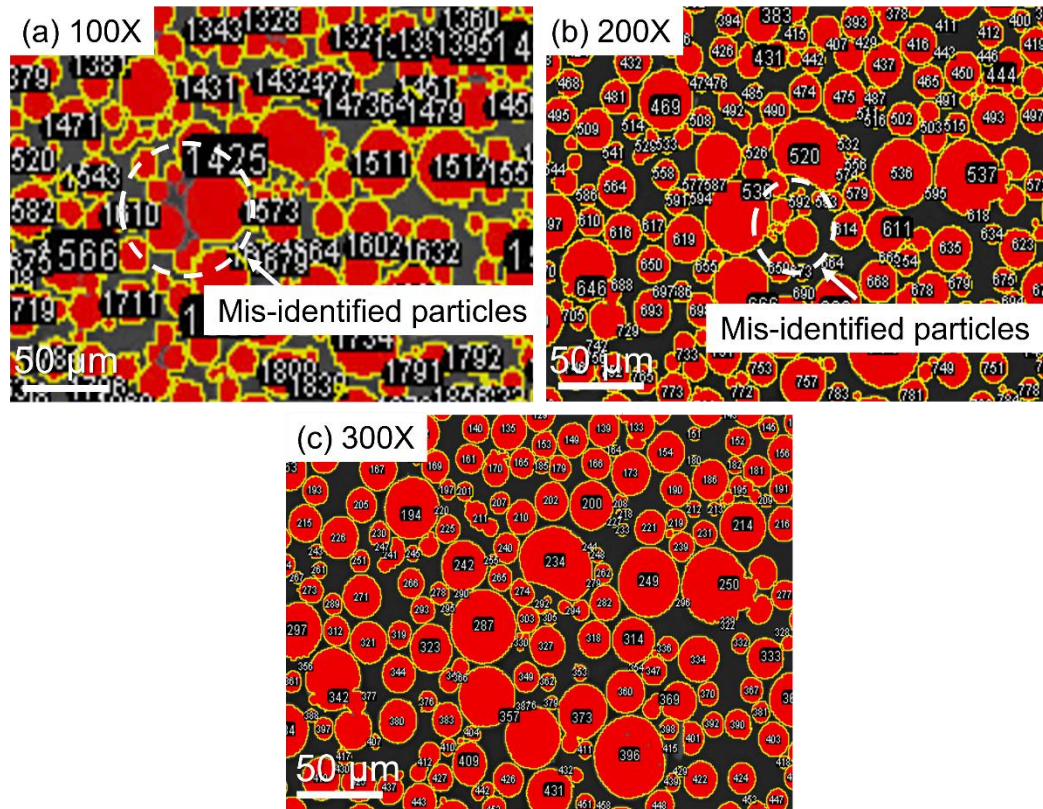


Fig. A3 SEM images of particles after automated ImageJ processing under different magnifications of (a) 100X, (b) 200X, and (c) 300X. Mis-identified particles are highlighted.

In [Table A1](#), the impact of increasing the total number of particles analysed on PSD metrics can be seen. At all magnifications, there was no significant change in powder size metrics for the increasing numbers of total particles measured. This indicates that 2500 particles may be sufficient for accurate analysis. Given the presence of touching particles which adversely affects the automated measurement of SEM images of particles, the factor of circularity was considered to effectively reduce particle mis-identification. The results are shown in [Table A2](#). To demonstrate the differences in image processing strategy between default constrained circularity, an example analysed image and an image of manually measured particles can be seen in [Fig. A4](#).

Table A2 PSD results under different circularity selections compared to SEM images with ImageJ processing by measuring each particle manually.

	Magnification	D10 (μm)	D50 (μm)	D90 (μm)
Manual	300X	13.3	22.8	36.1
Default circularity 0.0-1.0	300X	15.0	26.4	40.6
Circularity 0.2-1.0	300X	14.9	25.7	39.1
Circularity 0.4-1.0	300X	14.4	23.7	35.9
Circularity 0.5-1.0	300X	14.0	23.0	35.8
Circularity 0.6-1.0	300X	13.7	22.1	34.7
Circularity 0.8-1.0	300X	13.7	22.0	34.5

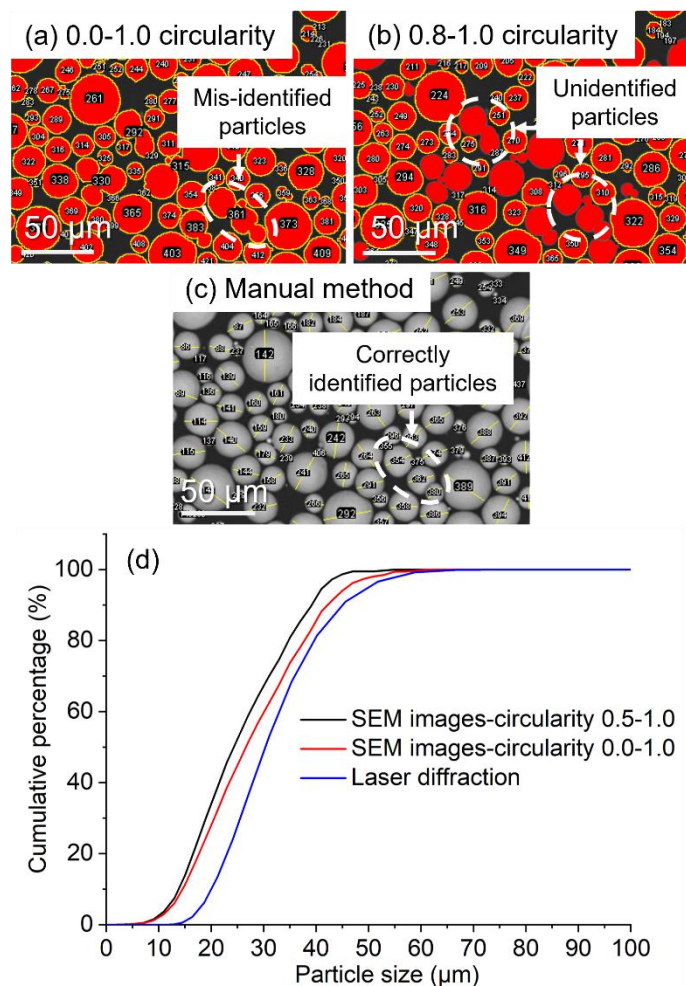


Fig. A4 SEM images with ImageJ processing under different circularity selections (a, b) and compared with manual measurement from SEM image (c) analysis performed at 300X magnification, (d) the comparison of PSD with laser diffraction.

It can be seen that for the D50 metrics the 0.5-1.0 circularity restriction is close to that produced by the manual measurement method – 23.0 μm compared to 22.8 μm respectively, and the 0.4-1.0 yielded the closest value for the D90 metric – 35.9 μm compared to 36.1 μm for the manual method. For the D10 metric, the most restrictive circularity filters of 0.6-1.0 and 0.8-1.0 yielded the value closest to that of the manual measurement – 13.7 μm in both cases compared to 13.3 μm respectively. It should be noted that these discrepancies are small and on the order of fractions of 1 μm therefore accuracy can generally be considered good.

[Fig. A4](#) shows the effect of the extremes of circularity selection on the correct identification of particles. With the widest circularity filter in [Fig. A4\(a\)](#) of 0.0-1.0, misidentification of particles is common, where some particles overlap. In [Fig. A4\(b\)](#), where particles not meeting the strict circularity filter are rejected, several particles are not included in the selection, which would otherwise have been wrongly included in the measurement. Therefore the rejection of these particles is thought to have improved the accuracy of the measurement, given these rejected particles are not of a particular size range which could have skewed the results. Given the close range of the 0.5-1.0 circularity filter measurements to manual measurements across all metrics, this parameter was chosen for further analysis.

The results of automated image analysis at 300X and with the default and optimised circularity methods compared to laser diffraction are shown in [Table A3](#) and [Fig. A4\(d\)](#). There is a significant difference between laser diffraction and image analysis method. This difference is particularly large in the case of the D10, which is notably higher for the laser diffraction method. Laser diffraction is closest to image analysis data for D90 metric. Moving to 12x reused Ti-6Al-4V powder, the same SEM imaging method is applied for PSD measurement. PSD results by SEM images (including default circularity and optimised circularity) and laser diffraction method are also compared, as shown in [Table A4](#).

Table A3 Comparison of virgin powder PSD results by SEM images (including default circularity and optimised circularity) and laser diffraction method.

	Number of particles	D10 (μm)	D50 (μm)	D90 (μm)
Circularity 0.5-1.0	10,000	13.8	24.3	39.2
Circularity 0.0-1.0	10,000	14.5	26.6	42.1
Laser diffraction	-	20.2	30.4	45.1

Table A4 Comparison 12x reused powder PSD results by SEM imaging and laser diffraction method.

	Number of particles	D10 (μm)	D50 (μm)	D90 (μm)
Circularity 0.5-1.0	10,000	18.4	30.4	41.8
Circularity 0.0-1.0	10,000	19.0	31.7	43.5
Laser diffraction	-	22.4	32.7	47.2

References

- [1] ISO/ASTM 52900:2021(en), Additive manufacturing — General principles — Fundamentals and vocabulary, (2021).
- [2] J.P. Kruth, G. Levy, F. Klocke, T.H.C. Childs, Consolidation phenomena in laser and powder-bed based layered manufacturing, *CIRP Ann. - Manuf. Technol.* 56 (2007) 730–759. <https://doi.org/10.1016/j.cirp.2007.10.004>.
- [3] T. DebRoy, H.L. Wei, J.S. Zuback, T. Mukherjee, J.W. Elmer, J.O. Milewski, A.M. Beese, A. Wilson-Heid, A. De, W. Zhang, Additive manufacturing of metallic components – Process, structure and properties, *Prog. Mater. Sci.* 92 (2018) 112–224. <https://doi.org/10.1016/j.pmatsci.2017.10.001>.
- [4] A. Lee, A.R. Hudson, D.J. Shiwardski, J.W. Tashman, T.J. Hinton, S. Yerneni, J.M. Bliley, P.G. Campbell, A.W. Feinberg, 3D bioprinting of collagen to rebuild components of the human heart, *Science*. 365 (2019) 482–487. <https://doi.org/10.1126/science.aav9051>.
- [5] M.A. Skylar-Scott, J. Mueller, C.W. Visser, J.A. Lewis, Voxeled soft matter via multimaterial multinozzle 3D printing, *Nature*. 575 (2019) 330–335. <https://doi.org/10.1038/s41586-019-1736-8>.
- [6] J.H. Martin, B.D. Yahata, J.M. Hundley, J.A. Mayer, T.A. Schaedler, T.M. Pollock, 3D printing of high-strength aluminium alloys, *Nat. Publ. Gr.* 549 (2017) 365–369. <https://doi.org/10.1038/nature23894>.
- [7] D. Zhang, D. Qiu, M.A. Gibson, Y. Zheng, H.L. Fraser, D.H. StJohn, M.A. Easton, Additive manufacturing of ultrafine-grained high-strength titanium alloys, *Nature*. 576 (2019) 91–95. <https://doi.org/10.1038/s41586-019-1783-1>.
- [8] T. Zhang, Z. Huang, T. Yang, H. Kong, J. Luan, A. Wang, D. Wang, W. Kuo, Y. Wang, C.T. Liu, In situ design of advanced titanium alloy with concentration modulations by additive manufacturing, *Science*. 374 (2021) 478–482. <https://doi.org/10.1126/science.abj3770>.
- [9] W.J. Sames, F.A. List, S. Pannala, R.R. Dehoff, S.S. Babu, The metallurgy and processing science of metal additive manufacturing, *Int. Mater. Rev.* 61 (2016)

315–360. <https://doi.org/10.1080/09506608.2015.1116649>.

- [10] D. Gu, X. Shi, R. Poprawe, D.L. Bourell, R. Setchi, J. Zhu, Material-structure-performance integrated laser-metal additive manufacturing, *Science*. 372 (2021) 1–15. <https://doi.org/10.1126/science.abg1487>.
- [11] S. Sanchez, P. Smith, Z. Xu, G. Gaspard, C.J. Hyde, W.W. Wits, I.A. Ashcroft, H. Chen, A.T. Clare, Powder Bed Fusion of nickel-based superalloys: A review, *Int. J. Mach. Tools Manuf.* 165 (2021) 1–77. <https://doi.org/10.1016/j.ijmachtools.2021.103729>.
- [12] S. Liu, Y.C. Shin, Additive manufacturing of Ti6Al4V alloy: A review, *Mater. Des.* 164 (2019) 1–23. <https://doi.org/10.1016/j.matdes.2018.107552>.
- [13] A.Y.M. Alfaify, The Effect of Changing Particle Size Distribution and Layer Thickness on the Density of Parts Manufactured Using the Laser Powder Bed Fusion Process, PhD Thesis. (2019).
- [14] <https://www.carpenteradditive.com/metal-powders> [Accessed on 27 December 2023].
- [15] D. Svetlizky, M. Das, B. Zheng, A.L. Vyatskikh, S. Bose, A. Bandyopadhyay, J.M. Schoenung, E.J. Lavernia, N. Eliaz, Directed energy deposition (DED) additive manufacturing: Physical characteristics, defects, challenges and applications, *Mater. Today*. 49 (2021) 271–295. <https://doi.org/10.1016/j.mattod.2021.03.020>.
- [16] <https://www.renishaw.com/en/additive-manufacturing-products--17475> [Accessed on 18 May 2023].
- [17] N. Uçak, A. Çiçek, K. Aslantas, Machinability of 3D printed metallic materials fabricated by selective laser melting and electron beam melting: A review, *J. Manuf. Process.* 80 (2022) 414–457. <https://doi.org/10.1016/j.jmapro.2022.06.023>.
- [18] H. Shipley, D. McDonnell, M. Culleton, R. Coull, R. Lupoi, G. O'Donnell, D. Trimble, Optimisation of process parameters to address fundamental challenges during selective laser melting of Ti-6Al-4V: A review, *Int. J. Mach. Tools Manuf.* 128 (2018) 1–20. <https://doi.org/10.1016/j.ijmachtools.2018.01.003>.

- [19] <https://www.eos.info/en/additive-manufacturing/3d-printing-metal/eos-metal-systems> [Accessed on 18 May 2023].
- [20] <https://www.ge.com/additive/additive-manufacturing/machines/m2series5> [Accessed on 18 May 2023].
- [21] <https://www.xa-blt.com/en> [Accessed on 21 December 2023].
- [22] P. Bajaj, A. Hariharan, A. Kini, P. Kürnsteiner, D. Raabe, E.A. Jäggle, Steels in additive manufacturing: A review of their microstructure and properties, *Mater. Sci. Eng. A.* 772 (2020) 1–25. <https://doi.org/10.1016/j.msea.2019.138633>.
- [23] N.T. Aboulkhair, M. Simonelli, L. Parry, I. Ashcroft, C. Tuck, R. Hague, 3D printing of Aluminium alloys: Additive Manufacturing of Aluminium alloys using selective laser melting, *Prog. Mater. Sci.* 106 (2019) 1–45. <https://doi.org/10.1016/j.pmatsci.2019.100578>.
- [24] X. Tang, X. Chen, F. Sun, P. Liu, H. Zhou, S. Fu, The current state of CuCrZr and CuCrNb alloys manufactured by additive manufacturing: A review, *Mater. Des.* 224 (2022) 1–31. <https://doi.org/10.1016/j.matdes.2022.111419>.
- [25] S. Li, X. Lan, Z. Wang, S. Mei, Microstructure and mechanical properties of Ti-6.5Al-2Zr-Mo-V alloy processed by Laser Powder Bed Fusion and subsequent heat treatments, *Addit. Manuf.* 48 (2021) 1–13. <https://doi.org/10.1016/j.addma.2021.102382>.
- [26] J. Jiang, Z. Ren, Z. Ma, T. Zhang, P. Zhang, D.Z. Zhang, Z. Mao, Mechanical properties and microstructural evolution of TA15 Ti alloy processed by selective laser melting before and after annealing, *Mater. Sci. Eng. A.* 772 (2020) 1–11. <https://doi.org/10.1016/j.msea.2019.138742>.
- [27] C. Qiu, Q. Liu, Multi-scale microstructural development and mechanical properties of a selectively laser melted beta titanium alloy, *Addit. Manuf.* 30 (2019) 1–13. <https://doi.org/10.1016/j.addma.2019.100893>.
- [28] Q. Liu, C. Qiu, Variant selection of α precipitation in a beta titanium alloy during selective laser melting and its influence on mechanical properties, *Mater. Sci. Eng. A.* 784 (2020) 1–9. <https://doi.org/10.1016/j.msea.2020.139336>.

- [29] H. Asgari, M. Mohammadi, Microstructure and mechanical properties of stainless steel CX manufactured by Direct Metal Laser Sintering, *Mater. Sci. Eng. A.* 709 (2018) 82–89. <https://doi.org/10.1016/j.msea.2017.10.045>.
- [30] X. Yan, C. Chen, C. Chang, D. Dong, R. Zhao, R. Jenkins, J. Wang, Z. Ren, M. Liu, H. Liao, R. Lupoi, S. Yin, Study of the microstructure and mechanical performance of C-X stainless steel processed by selective laser melting (SLM), *Mater. Sci. Eng. A.* 781 (2020) 1–10. <https://doi.org/10.1016/j.msea.2020.139227>.
- [31] X. Wu, C. Cai, L. Yang, W. Liu, W. Li, M. Li, J. Liu, K. Zhou, Y. Shi, Enhanced mechanical properties of Ti-6Al-2Zr-1Mo-1V with ultrafine crystallites and nano-scale twins fabricated by selective laser melting, *Mater. Sci. Eng. A.* 738 (2018) 10–14. <https://doi.org/10.1016/j.msea.2018.09.087>.
- [32] Q. Jia, P. Rometsch, P. Kürnsteiner, Q. Chao, A. Huang, M. Weyland, L. Bourgeois, X. Wu, Selective laser melting of a high strength Al-Mn-Sc alloy: Alloy design and strengthening mechanisms, *Acta Mater.* 171 (2019) 108–118. <https://doi.org/10.1016/j.actamat.2019.04.014>.
- [33] R. Seede, D. Shoukr, B. Zhang, A. Whitt, S. Gibbons, P. Flater, A. Elwany, R. Arroyave, I. Karaman, An ultra-high strength martensitic steel fabricated using selective laser melting additive manufacturing: Densification, microstructure, and mechanical properties, *Acta Mater.* 186 (2020) 199–214. <https://doi.org/10.1016/j.actamat.2019.12.037>.
- [34] C. Qiu, N.J.E. Adkins, M.M. Attallah, Selective laser melting of Invar 36: Microstructure and properties, *Acta Mater.* 103 (2016) 382–395. <https://doi.org/10.1016/j.actamat.2015.10.020>.
- [35] M. Garibaldi, I. Ashcroft, M. Simonelli, R. Hague, Metallurgy of high-silicon steel parts produced using Selective Laser Melting, *Acta Mater.* 110 (2016) 207–216. <https://doi.org/10.1016/j.actamat.2016.03.037>.
- [36] P. Barriobero-Vila, J. Gussone, A. Stark, N. Schell, J. Haubrich, G. Requena, Peritectic titanium alloys for 3D printing, *Nat. Commun.* 9 (2018) 1–9. <https://doi.org/10.1038/s41467-018-05819-9>.

- [37] ASTM B348/B348M-21, Standard Specification for Titanium and Titanium Alloy Bars and Billets, (2021).
- [38] G. Lütjering, J. C. Williams, Titanium, 2007.
- [39] A.T. Sutton, C.S. Kriewall, M.C. Leu, J.W. Newkirk, Powder characterisation techniques and effects of powder characteristics on part properties in powder-bed fusion processes, *Virtual Phys. Prototyp.* 12 (2017) 3–29. <https://doi.org/10.1080/17452759.2016.1250605>.
- [40] J. Dawes, R. Bowerman, R. Trepleton, Introduction to the additive manufacturing powder metallurgy supply chain, *Johnson Matthey Technol. Rev.* 59 (2015) 243–256. <https://doi.org/10.1595/205651315X688686>.
- [41] G. Chen, S.Y. Zhao, P. Tan, J. Wang, C.S. Xiang, H.P. Tang, A comparative study of Ti-6Al-4V powders for additive manufacturing by gas atomization, plasma rotating electrode process and plasma atomization, *Powder Technol.* 333 (2018) 38–46. <https://doi.org/10.1016/j.powtec.2018.04.013>.
- [42] H. Eskandari Sabzi, Powder bed fusion additive layer manufacturing of titanium alloys, *Mater. Sci. Technol.* 35 (2019) 875–890. <https://doi.org/10.1080/02670836.2019.1602974>.
- [43] N.K. Y Seki, S Okamoto, H Takigawa, Effect of atomization variables on powder characteristics in the high-pressured water atomization process, *Met. Powder Rep.* 45 (1990) 38–40. [https://doi.org/10.1016/S0026-0657\(10\)80014-1](https://doi.org/10.1016/S0026-0657(10)80014-1).
- [44] A.J. Pinkerton, L. Li, Direct additive laser manufacturing using gas- and water-atomised H13 tool steel powders, *Int. J. Adv. Manuf. Technol.* 25 (2005) 471–479. <https://doi.org/10.1007/s00170-003-1844-2>.
- [45] I.E. Anderson, R.S. Figliola, H. Morton, Flow mechanisms in high pressure gas atomization, *Mater. Sci. Eng. A.* 148 (1991) 101–114.
- [46] G. Cattano, Feasibility studies on Laser Powder Bed Fusion of powders mixtures based on Aluminium alloys or High Entropy Alloys, PhD Thesis. (2019).
- [47] J.J. Dunkley, Metal Powder Atomisation Methods for Modern Manufacturing, *Johnson Matthey Technol. Rev.* 63 (2019) 226–232.

<https://doi.org/10.1595/205651319x15583434137356>.

- [48] P. Sun, Z.Z. Fang, Y. Zhang, Y. Xia, Review of the Methods for Production of Spherical Ti and Ti Alloy Powder, *JOM*. 69 (2017) 1853–1860. <https://doi.org/10.1007/s11837-017-2513-5>.
- [49] J.H. Tan, W.L.E. Wong, K.W. Dalgarno, An overview of powder granulometry on feedstock and part performance in the selective laser melting process, *Addit. Manuf.* 18 (2017) 228–255. <https://doi.org/10.1016/j.addma.2017.10.011>.
- [50] M.J. Heiden, L.A. Deibler, J.M. Rodelas, J.R. Koepke, D.J. Tung, D.J. Saiz, B.H. Jared, Evolution of 316L stainless steel feedstock due to laser powder bed fusion process, *Addit. Manuf.* 25 (2019) 84–103. <https://doi.org/10.1016/j.addma.2018.10.019>.
- [51] E.O. Olakanmi, Effect of mixing time on the bed density, and microstructure of selective laser sintered (SLS) aluminium powders, *Mater. Res.* 15 (2012) 167–176. <https://doi.org/10.1590/S1516-14392012005000031>.
- [52] P.W. Cleary, M.L. Sawley, DEM modelling of industrial granular flows: 3D case studies and the effect of particle shape on hopper discharge, *Appl. Math. Model.* 26 (2002) 89–111. [https://doi.org/10.1016/S0307-904X\(01\)00050-6](https://doi.org/10.1016/S0307-904X(01)00050-6).
- [53] R.J. Hebert, Viewpoint: metallurgical aspects of powder bed metal additive manufacturing, *J. Mater. Sci.* 51 (2016) 1165–1175. <https://doi.org/10.1007/s10853-015-9479-x>.
- [54] B. Liu, R. Wildman, C. Tuck, I. Ashcroft, R. Hague, Investigation the effect of particle size distribution on processing parameters optimisation in selective laser melting process, 22nd Annu. Int. Solid Free. Fabr. Symp. - An Addit. Manuf. Conf. SFF 2011. (2011) 227–238.
- [55] H. Chen, Q. Wei, Y. Zhang, F. Chen, Y. Shi, W. Yan, Powder-spreading mechanisms in powder-bed-based additive manufacturing: Experiments and computational modeling, *Acta Mater.* 179 (2019) 158–171. <https://doi.org/10.1016/j.actamat.2019.08.030>.
- [56] J.A. Slotwinski, E.J. Garboczi, P.E. Stutzman, C.F. Ferraris, S.S. Watson, M.A. Peltz, Characterization of metal powders used for additive manufacturing, *J. Res.*

Natl. Inst. Stand. Technol. 119 (2014) 460–493.
<https://doi.org/10.6028/jres.119.018>.

- [57] P. Sperling, A. Beerlink, B. Willie, G. Stephan, Standard method for microCT-based additive manufacturing quality control 4: Metal powder analysis, *MethodsX*. 5 (2018) 1336–1345. <https://doi.org/10.1016/j.mex.2018.10.021>.
- [58] V.A. Hackley, L.S. Lum, V. Gintautas, C.F. Ferraris, *Particle Size Analysis by Laser Diffraction Spectrometry: Application to Cementitious Powders*, (2004).
- [59] S. Ma, Q. Tang, X. Han, Q. Feng, J. Song, R. Setchi, Y. Liu, Y. Liu, A. Goulas, D.S. Engstrøm, Y.Y. Tse, N. Zhen, Manufacturability, Mechanical Properties, Mass-Transport Properties and Biocompatibility of Triply Periodic Minimal Surface (TPMS) Porous Scaffolds Fabricated by Selective Laser Melting, *Mater. Des.* 195 (2020) 1–15. <https://doi.org/10.1016/j.matdes.2020.109034>.
- [60] M.S. Knieps, W.J. Reynolds, J. Dejaune, A.T. Clare, A. Evirgen, In-situ alloying in powder bed fusion: The role of powder morphology, *Mater. Sci. Eng. A*. 807 (2021) 1–12. <https://doi.org/10.1016/j.msea.2021.140849>.
- [61] S.E. Brika, M. Letenneur, C.A. Dion, V. Brailovski, Influence of particle morphology and size distribution on the powder flowability and laser powder bed fusion manufacturability of Ti-6Al-4V alloy, *Addit. Manuf.* 31 (2020) 1–16. <https://doi.org/10.1016/j.addma.2019.100929>.
- [62] C. Scheu, W.D. Kaplan, Introduction to Scanning Electron Microscopy, *In-Situ Electron Microsc. Appl. Physics, Chem. Mater. Sci.* (2012) 1–37. <https://doi.org/10.1002/9783527652167.ch1>.
- [63] K. Chen, D.J. Huang, H. Li, N. Jia, W. Chong, Avoiding abnormal grain growth when annealing selective laser melted pure titanium by promoting nucleation, *Scr. Mater.* 209 (2022) 1–7. <https://doi.org/10.1016/j.scriptamat.2021.114377>.
- [64] C.S. Wang, C.L. Li, Y.T. Zuo, J.K. Hong, S.W. Choi, G.D. Zhang, Q. Mei, C.H. Park, J.T. Yeom, Tailoring bimodal structure for high strength and ductility in pure titanium manufactured via laser powder bed fusion, *J. Alloys Compd.* 901 (2022) 1–15. <https://doi.org/10.1016/j.jallcom.2021.163590>.
- [65] A.T. Clare, R.S. Mishra, M. Merklein, H. Tan, I. Todd, L. Chechik, J. Li, M.

- Bambach, Alloy design and adaptation for additive manufacture, *J. Mater. Process. Technol.* 299 (2022) 1–35. <https://doi.org/10.1016/j.jmatprotec.2021.117358>.
- [66] A.B. Spierings, M.V.T.B.K. Wegener, Powder flowability characterisation methodology for powder-bed- based metal additive manufacturing, *Prog. Addit. Manuf.* 1 (2016) 9–20. <https://doi.org/10.1007/s40964-015-0001-4>.
- [67] S. Vock, B. Klöden, A. Kirchner, T. Weißgärber, B. Kieback, Powders for powder bed fusion: a review, *Prog. Addit. Manuf.* 4 (2019) 383–397. <https://doi.org/10.1007/s40964-019-00078-6>.
- [68] D. Geldart, E.C. Abdullah, A. Hassanpour, L.C. Nwoke, I. Wouters, Characterization of powder flowability using measurement of angle of repose, *China Particuology.* 4 (2006) 104–107. [https://doi.org/10.1016/s1672-2515\(07\)60247-4](https://doi.org/10.1016/s1672-2515(07)60247-4).
- [69] M. Krantz, H. Zhang, J. Zhu, Characterization of powder flow: Static and dynamic testing, *Powder Technol.* 194 (2009) 239–245. <https://doi.org/10.1016/j.powtec.2009.05.001>.
- [70] R. Freeman, Measuring the flow properties of consolidated, conditioned and aerated powders - A comparative study using a powder rheometer and a rotational shear cell, *Powder Technol.* 174 (2007) 25–33. <https://doi.org/10.1016/j.powtec.2006.10.016>.
- [71] B.A. Hann, Powder Reuse and Its Effects on Laser Based Powder Fusion Additive Manufactured Alloy 718, *SAE Int. J. Aerosp.* 9 (2016) 209–213. <https://doi.org/10.4271/2016-01-2071>.
- [72] M. Barclift, S. Joshi, T. Simpson, C. Dickman, Cost modeling and depreciation for reused powder feedstocks in powder bed fusion additive manufacturing, *Solid Free. Fabr. 2016 Proc. 27th Annu. Int. Solid Free. Fabr. Symp. - An Addit. Manuf. Conf. SFF 2016.* (2016) 2007–2028.
- [73] C. Lindemann, U. Jahnke, M. Moi, R. Koch, Analyzing product lifecycle costs for a better understanding of cost drivers in additive manufacturing, *23rd Annu. Int. Solid Free. Fabr. Symp. - An Addit. Manuf. Conf. SFF 2012.* (2012) 177–

188.

- [74] Wohlers Report-3D Printing and Additive Manufacturing Global State of the Industry, (2023).
- [75] L. Grainger, Investigating the effects of multiple re-use of Ti6Al4V powder in additive manufacturing (AM), White Pap. Renishaw. (2016) 1–10. <https://www.renishaw.com/en/how-much-can-you-recycle-metal-additive-manufacturing-powder--38882>.
- [76] L.C. Ardila, F. Garciandia, J.B. González-díaz, P. Álvarez, A. Echeverria, Effect of IN718 recycled powder reuse on properties of parts manufactured by means of Selective Laser Melting, *Phys. Procedia.* 56 (2014) 99–107. <https://doi.org/10.1016/j.phpro.2014.08.152>.
- [77] Y. Liu, Y. Yang, S. Mai, D. Wang, C. Song, Investigation into spatter behavior during selective laser melting of AISI 316L stainless steel powder, *Mater. Des.* 87 (2015) 797–806. <https://doi.org/10.1016/j.matdes.2015.08.086>.
- [78] D. Wang, S. Wu, F. Fu, S. Mai, Y. Yang, Y. Liu, C. Song, Mechanisms and characteristics of spatter generation in SLM processing and its effect on the properties, *Mater. Des.* 117 (2017) 121–130. <https://doi.org/10.1016/j.matdes.2016.12.060>.
- [79] R. O’Leary, R. Setchi, P. Prickett, G. Hankins, N. Jones, An Investigation into the Recycling of Ti-6Al-4V Powder Used Within SLM to Improve Sustainability, *SDM’2015 2nd Int. Conf. Sustain. Des. Manuf.* (2015) 14–17.
- [80] L. Cordova, M. Campos, T. Tinga, Revealing the Effects of Powder Reuse for Selective Laser Melting by Powder Characterization, *JOM.* 71 (2019) 1062–1072. <https://doi.org/10.1007/s11837-018-3305-2>.
- [81] A.T. Sutton, C.S. Kriewall, S. Karnati, M.C. Leu, J.W. Newkirk, Characterization of AISI 304L stainless steel powder recycled in the laser powder-bed fusion process, *Addit. Manuf.* 32 (2020) 1–14. <https://doi.org/10.1016/j.addma.2019.100981>.
- [82] L. Denti, A. Sola, S. Defanti, C. Sciancalepore, F. Bondioli, Effect of powder recycling in laser-based powder bed fusion of Ti-6Al-4V, *Manuf. Technol.* 19

- (2019) 190–196. <https://doi.org/10.21062/ujep/268.2019/a/1213-2489/mt/19/2/190>.
- [83] P.E. Carrion, A. Soltani-Tehrani, N. Phan, N. Shamsaei, Powder Recycling Effects on the Tensile and Fatigue Behavior of Additively Manufactured Ti-6Al-4V Parts, *JOM*. 71 (2019) 963–973. <https://doi.org/10.1007/s11837-018-3248-7>.
- [84] A. Yáñez, M.P. Fiorucci, O. Martel, A. Cuadrado, The Influence of Dimensions and Powder Recycling on the Roughness and Mechanical Properties of Ti-6Al-4V Parts Fabricated by Laser Powder Bed Fusion, *Materials (Basel)*. 15 (2022) 1–15. <https://doi.org/10.3390/ma15165787>.
- [85] A. Soltani-Tehrani, J.P. Isaac, H. V. Tippur, D.F. Silva, S. Shao, N. Shamsaei, Ti-6Al-4V powder reuse in laser powder bed fusion (L-PBF): The effect on porosity, microstructure, and mechanical behavior, *Int. J. Fatigue*. 167 (2023) 1–16. <https://doi.org/10.1016/j.ijfatigue.2022.107343>.
- [86] S.A. Khairallah, A.T. Anderson, A. Rubenchik, W.E. King, Laser powder-bed fusion additive manufacturing: Physics of complex melt flow and formation mechanisms of pores, spatter, and denudation zones, *Acta Mater*. 108 (2016) 36–45. <https://doi.org/10.1016/j.actamat.2016.02.014>.
- [87] S. Pal, I. Drstvensek, Physical Behaviors of Materials in Selective Laser Melting Process, *DAAAM Int. Sci. B.* (2018) 239–256. <https://doi.org/10.2507/daaam.scibook.2018.21>.
- [88] A. Bin Anwar, Q.C. Pham, Spattering in selective laser melting: A review of spatter formation, effects and countermeasures, *Proc. Int. Conf. Prog. Addit. Manuf.* (2018) 541–546. <https://doi.org/10.25341/D4D30J>.
- [89] Z. Li, H. Li, J. Yin, Y. Li, Z. Nie, X. Li, D. You, K. Guan, W. Duan, L. Cao, D. Wang, L. Ke, Y. Liu, P. Zhao, L. Wang, K. Zhu, Z. Zhang, L. Gao, L. Hao, A Review of Spatter in Laser Powder Bed Fusion Additive Manufacturing: In Situ Detection, Generation, Effects, and Countermeasures, *Micromachines*. 13 (2022) 1–41. <https://doi.org/10.3390/mi13081366>.
- [90] S. Ly, A.M. Rubenchik, S.A. Khairallah, G. Guss, M.J. Matthews, Metal vapor micro-jet controls material redistribution in laser powder bed fusion additive

- manufacturing, *Sci. Rep.* 7 (2017) 1–12. <https://doi.org/10.1038/s41598-017-04237-z>.
- [91] A.N.D. Gasper, B. Szost, X. Wang, D. Johns, S. Sharma, A.T. Clare, I.A. Ashcroft, Spatter and oxide formation in laser powder bed fusion of Inconel 718, *Addit. Manuf.* 24 (2018) 446–456. <https://doi.org/10.1016/j.addma.2018.09.032>.
- [92] C.L.A. Leung, S. Marussi, R.C. Atwood, M. Towrie, P.J. Withers, P.D. Lee, In situ X-ray imaging of defect and molten pool dynamics in laser additive manufacturing, *Nat. Commun.* 9 (2018) 1–9. <https://doi.org/10.1038/s41467-018-03734-7>.
- [93] H. Nakamura, Y. Kawahito, K. Nishimoto, S. Katayama, Elucidation of melt flows and spatter formation mechanisms during high power laser welding of pure titanium, *J. Laser Appl.* 27 (2015) 1–10. <https://doi.org/10.2351/1.4922383>.
- [94] M. Simonelli, Microstructure evolution and mechanical properties of selective laser melted Ti-6Al-4V, PhD Thesis. (2014).
- [95] T. Ahmed, H.J. Rack, Phase transformations during cooling in $\alpha + \beta$ titanium alloys, *Mater. Sci. Eng. A.* 243 (1998) 206–211. [https://doi.org/10.1016/s0921-5093\(97\)00802-2](https://doi.org/10.1016/s0921-5093(97)00802-2).
- [96] M. Strantza, R. Vafadari, D. De Baere, B. Vrancken, W. Van Paepegem, I. Vandendael, H. Terryn, P. Guillaume, D. Van Hemelrijck, Fatigue of Ti6Al4V structural health monitoring systems produced by selective laser melting, *Materials (Basel)*. 9 (2016) 1–15. <https://doi.org/10.3390/ma9020106>.
- [97] Y.L. Hao, S.J. Li, R. Yang, Biomedical titanium alloys and their additive manufacturing, *Rare Met.* 35 (2016) 661–671. <https://doi.org/10.1007/s12598-016-0793-5>.
- [98] R. Boyer, G. Welsch, E.W. Collings, *Materials properties handbook : titanium alloys*, (1994).
- [99] I.A. Roberts, C.J. Wang, R. Esterlein, M. Stanford, D.J. Mynors, A three-dimensional finite element analysis of the temperature field during laser melting of metal powders in additive layer manufacturing, *Int. J. Mach. Tools Manuf.* 49 (2009) 916–923. <https://doi.org/10.1016/j.ijmachtools.2009.07.004>.

- [100] P. Kumar, O. Prakash, U. Ramamurty, Micro-and meso-structures and their influence on mechanical properties of selectively laser melted Ti-6Al-4V, *Acta Mater.* 154 (2018) 246–260. <https://doi.org/10.1016/j.actamat.2018.05.044>.
- [101] D. Zhang, L. Wang, H. Zhang, A. Maldar, G. Zhu, W. Chen, J.S. Park, J. Wang, X. Zeng, Effect of heat treatment on the tensile behavior of selective laser melted Ti-6Al-4V by in situ X-ray characterization, *Acta Mater.* 189 (2020) 93–104. <https://doi.org/10.1016/j.actamat.2020.03.003>.
- [102] J. Yang, H. Yu, J. Yin, M. Gao, Z. Wang, X. Zeng, Formation and control of martensite in Ti-6Al-4V alloy produced by selective laser melting, *Mater. Des.* 108 (2016) 308–318. <https://doi.org/10.1016/j.matdes.2016.06.117>.
- [103] S. Cao, Y. Zou, C.V.S. Lim, X. Wu, Review of laser powder bed fusion (LPBF) fabricated Ti-6Al-4V: process, post-process treatment, microstructure, and property, *Light Adv. Manuf.* 2 (2021) 1–20. <https://doi.org/10.37188/lam.2021.020>.
- [104] T. Voisin, N.P. Calta, S.A. Khairallah, J.B. Forien, L. Balogh, R.W. Cunningham, A.D. Rollett, Y.M. Wang, Defects-dictated tensile properties of selective laser melted Ti-6Al-4V, *Mater. Des.* 158 (2018) 113–126. <https://doi.org/10.1016/j.matdes.2018.08.004>.
- [105] F.R. Kaschel, R.K. Vijayaraghavan, A. Shmeliov, E.K. McCarthy, M. Canavan, P.J. McNally, D.P. Dowling, V. Nicolosi, M. Celikin, Mechanism of stress relaxation and phase transformation in additively manufactured Ti-6Al-4V via in situ high temperature XRD and TEM analyses, *Acta Mater.* 188 (2020) 720–732. <https://doi.org/10.1016/j.actamat.2020.02.056>.
- [106] C. Leyens, M. Peters, *Titanium and Titanium Alloys*, 2003.
- [107] M. Simonelli, Y.Y. Tse, C. Tuck, On the texture formation of selective laser melted Ti-6Al-4V, *Metall. Mater. Trans. A.* 45 (2014) 2863–2872. <https://doi.org/10.1007/s11661-014-2218-0>.
- [108] A. Badillo, C. Beckermann, Phase-field simulation of the columnar-to-equiaxed transition in alloy solidification, *Acta Mater.* 54 (2006) 2015–2026. <https://doi.org/10.1016/j.actamat.2005.12.025>.

- [109] D. Zhang, A. Prasad, M.J. Bermingham, C.J. Todaro, M.J. Benoit, M.N. Patel, D. Qiu, D.H. Stjohn, M.A. Qian, M.A. Easton, Grain Refinement of Alloys in Fusion-Based Additive Manufacturing Processes, *Metall. Mater. Trans. A.* 51 (2020) 4341–4359. <https://doi.org/10.1007/s11661-020-05880-4>.
- [110] A.M. Mitrašinović, F.C. Robles Hernández, Determination of the growth restriction factor and grain size for aluminum alloys by a quasi-binary equivalent method, *Mater. Sci. Eng. A.* 540 (2012) 63–69. <https://doi.org/10.1016/j.msea.2012.01.072>.
- [111] S. Zhao, R. Zhang, Q. Yu, J. Ell, R.O. Ritchie, A.M. Minor, Cryoforged nanotwinned titanium with ultrahigh strength and ductility, *Science.* 376 (2022) 1363–1368. <https://doi.org/10.1126/science.abo5247>.
- [112] G.M. Ter Haar, T.H. Becker, The influence of microstructural texture and prior beta grain recrystallisation on the deformation behaviour of laser powder bed fusion produced Ti–6Al–4V, *Mater. Sci. Eng. A.* 814 (2021) 1–16. <https://doi.org/10.1016/j.msea.2021.141185>.
- [113] M.W. Wu, K. Ni, H.W. Yen, J.K. Chen, P. Wang, Y.J. Tseng, M.K. Tsai, S.H. Wang, P.H. Lai, M.H. Ku, Revealing the intensified preferred orientation and factors dominating the anisotropic mechanical properties of laser powder bed fusion Ti-6Al-4V alloy after heat treatment, *J. Alloys Compd.* 949 (2023) 1–21. <https://doi.org/10.1016/j.jallcom.2023.169494>.
- [114] J. Yang, H. Yu, Z. Wang, X. Zeng, Effect of crystallographic orientation on mechanical anisotropy of selective laser melted Ti-6Al-4V alloy, *Mater. Charact.* 127 (2017) 137–145. <https://doi.org/10.1016/j.matchar.2017.01.014>.
- [115] S.C. Wang, M. Aindow, M.J. Starink, Effect of self-accommodation on α/α boundary populations in pure titanium, *Acta Mater.* 51 (2003) 2485–2503. [https://doi.org/10.1016/S1359-6454\(03\)00035-1](https://doi.org/10.1016/S1359-6454(03)00035-1).
- [116] R. Zhao, C. Chen, W. Wang, T. Cao, S. Shuai, S. Xu, T. Hu, H. Liao, J. Wang, Z. Ren, On the role of volumetric energy density in the microstructure and mechanical properties of laser powder bed fusion Ti-6Al-4V alloy, *Addit. Manuf.* 51 (2022) 1–12. <https://doi.org/10.1016/j.addma.2022.102605>.

- [117] C.M. Cepeda-Jiménez, F. Potenza, E. Magalini, V. Luchin, A. Molinari, M.T. Pérez-Prado, Effect of energy density on the microstructure and texture evolution of Ti-6Al-4V manufactured by laser powder bed fusion, *Mater. Charact.* 163 (2020) 1–9. <https://doi.org/10.1016/j.matchar.2020.110238>.
- [118] H. Wang, Q. Chao, L. Yang, M. Cabral, Z.Z. Song, B.Y. Wang, S. Primig, W. Xu, Z.B. Chen, S.P. Ringer, X.Z. Liao, Introducing transformation twins in titanium alloys: an evolution of α -variants during additive manufacturing, *Mater. Res. Lett.* 9 (2021) 119–126. <https://doi.org/10.1080/21663831.2020.1850536>.
- [119] A.A. Antonysamy, J. Meyer, P.B. Prangnell, Effect of build geometry on the β -grain structure and texture in additive manufacture of Ti6Al4V by selective electron beam melting, *Mater. Charact.* 84 (2013) 153–168. <https://doi.org/10.1016/j.matchar.2013.07.012>.
- [120] W. Xu, M. Brandt, S. Sun, J. Elambasseril, Q. Liu, K. Latham, K. Xia, M. Qian, Additive manufacturing of strong and ductile Ti-6Al-4V by selective laser melting via in situ martensite decomposition, *Acta Mater.* 85 (2015) 74–84. <https://doi.org/10.1016/j.actamat.2014.11.028>.
- [121] W. Xu, E.W. Lui, A. Pateras, M. Qian, M. Brandt, In situ tailoring microstructure in additively manufactured Ti-6Al-4V for superior mechanical performance, *Acta Mater.* 125 (2017) 390–400. <https://doi.org/10.1016/j.actamat.2016.12.027>.
- [122] L.E. Murr, S.A. Quinones, S.M. Gaytan, M.I. Lopez, A. Rodela, E.Y. Martinez, D.H. Hernandez, E. Martinez, F. Medina, R.B. Wicker, Microstructure and mechanical behavior of Ti-6Al-4V produced by rapid-layer manufacturing, for biomedical applications, *J. Mech. Behav. Biomed. Mater.* 2 (2009) 20–32. <https://doi.org/10.1016/j.jmbbm.2008.05.004>.
- [123] N. Kazantseva, P. Krakhmalev, M. Thuvander, I. Yadroitsev, N. Vinogradova, I. Ezhov, Martensitic transformations in Ti-6Al-4V (ELI) alloy manufactured by 3D Printing, *Mater. Charact.* 146 (2018) 101–112. <https://doi.org/10.1016/j.matchar.2018.09.042>.
- [124] Z. Xie, Y. Dai, X. Ou, S. Ni, M. Song, Effects of selective laser melting build orientations on the microstructure and tensile performance of Ti-6Al-4V alloy, *Mater. Sci. Eng. A.* 776 (2020) 1–7. <https://doi.org/10.1016/j.msea.2020.139001>.

- [125] H. Wang, Q. Chao, H.S. Chen, Z.B. Chen, S. Primig, W. Xu, S.P. Ringer, X.Z. Liao, Formation of a transition V-rich structure during the α' to $\alpha + \beta$ phase transformation process in additively manufactured Ti-6Al-4V, *Acta Mater.* 235 (2022) 1–12. <https://doi.org/10.1016/j.actamat.2022.118104>.
- [126] H. Wang, Q. Chao, X.Y. Cui, Z.B. Chen, A.J. Breen, M. Cabral, N. Haghdad, Q.W. Huang, R.M. Niu, H.S. Chen, B. Lim, S. Primig, M. Brandt, W. Xu, S.P. Ringer, X.Z. Liao, Introducing C phase in additively manufactured Ti-6Al-4V: A new oxygen-stabilized face-centred cubic solid solution with improved mechanical properties, *Mater. Today.* 61 (2022) 11–21. <https://doi.org/10.1016/j.mattod.2022.10.026>.
- [127] A. Carrozza, A. Aversa, P. Fino, M. Lombardi, A study on the microstructure and mechanical properties of the Ti-6Al-2Sn-4Zr-6Mo alloy produced via Laser Powder Bed Fusion, *J. Alloys Compd.* 870 (2021) 1–11. <https://doi.org/10.1016/j.jallcom.2021.159329>.
- [128] A. Carrozza, A. Aversa, P. Fino, M. Lombardi, Towards customized heat treatments and mechanical properties in the LPBF-processed Ti-6Al-2Sn-4Zr-6Mo alloy, *Mater. Des.* 215 (2022) 1–10. <https://doi.org/10.1016/j.matdes.2022.110512>.
- [129] F.R. Kaschel, M. Celikin, D.P. Dowling, Effects of laser power on geometry, microstructure and mechanical properties of printed Ti-6Al-4V parts, *J. Mater. Process. Tech.* 278 (2020) 1–12. <https://doi.org/10.1016/j.jmatprotec.2019.116539>.
- [130] T. Montalbano, B.N. Briggs, J.L. Waterman, S. Nimer, C. Peitsch, J. Sopcisak, D. Trigg, S. Storck, Uncovering the coupled impact of defect morphology and microstructure on the tensile behavior of Ti-6Al-4V fabricated via laser powder bed fusion, *J. Mater. Process. Technol.* 294 (2021) 1–8. <https://doi.org/10.1016/j.jmatprotec.2021.117113>.
- [131] G. Kasperovich, J. Haubrich, J. Gussone, G. Requena, Correlation between porosity and processing parameters in TiAl6V4 produced by selective laser melting, *Mater. Des.* 105 (2016) 160–170. <https://doi.org/10.1016/j.matdes.2016.05.070>.

- [132] P. Li, D.H. Warner, A. Fatemi, N. Phan, Critical assessment of the fatigue performance of additively manufactured Ti-6Al-4V and perspective for future research, *Int. J. Fatigue*. 85 (2016) 130–143. <https://doi.org/10.1016/j.ijfatigue.2015.12.003>.
- [133] G. Gottstein, *Physical Foundations of Materials Science*, 2004.
- [134] L. Wang, Y. Yang, P. Eisenlohr, T.R. Bieler, M.A. Crimp, D.E. Mason, Twin nucleation by slip transfer across grain boundaries in commercial purity titanium, *Metall. Mater. Trans. A*. 41 (2010) 421–430. <https://doi.org/10.1007/s11661-009-0097-6>.
- [135] H. Qin, J.J. Jonas, Variant selection during secondary and tertiary twinning in pure titanium, *Acta Mater.* 75 (2014) 198–211. <https://doi.org/10.1016/j.actamat.2014.04.065>.
- [136] M. Simonelli, Y.Y. Tse, C. Tuck, Effect of the build orientation on the mechanical properties and fracture modes of SLM Ti-6Al-4V, *Mater. Sci. Eng. A*. 616 (2014) 1–11. <https://doi.org/10.1016/j.msea.2014.07.086>.
- [137] A. Moridi, A.G. Demir, L. Caprio, A.J. Hart, B. Previtali, B.M. Colosimo, Deformation and failure mechanisms of Ti–6Al–4V as built by selective laser melting, *Mater. Sci. Eng. A*. 768 (2019) 1–9. <https://doi.org/10.1016/j.msea.2019.138456>.
- [138] J.M. Vallejos, P. Barriobero-Vila, J. Gussone, J. Haubrich, K. Kelm, A. Stark, N. Schell, G. Requena, In Situ High-Energy Synchrotron X-Ray Diffraction Reveals the Role of Texture on the Activation of Slip and Twinning during Deformation of Laser Powder Bed Fusion Ti–6Al–4V, *Adv. Eng. Mater.* 23 (2021) 10–14. <https://doi.org/10.1002/adem.202001556>.
- [139] P. Barriobero-Vila, J.M. Vallejos, J. Gussone, J. Haubrich, K. Kelm, A. Stark, N. Schell, G. Requena, Interface-Mediated Twinning-Induced Plasticity in a Fine Hexagonal Microstructure Generated by Additive Manufacturing, *Adv. Mater.* 33 (2021) 1–8. <https://doi.org/10.1002/adma.202105096>.
- [140] H. Attar, K.G. Prashanth, L.C. Zhang, M. Calin, I. V. Okulov, S. Scudino, C. Yang, J. Eckert, Effect of powder particle shape on the properties of in situ Ti-

- TiB composite materials produced by selective laser melting, *J. Mater. Sci. Technol.* 31 (2015) 1001–1005. <https://doi.org/10.1016/j.jmst.2015.08.007>.
- [141] K. Riener, N. Albrecht, S. Ziegelmeier, R. Ramakrishnan, L. Haferkamp, A.B. Spierings, G.J. Leichtfried, Influence of particle size distribution and morphology on the properties of the powder feedstock as well as of AlSi10Mg parts produced by laser powder bed fusion (LPBF), *Addit. Manuf.* 34 (2020) 1–11. <https://doi.org/10.1016/j.addma.2020.101286>.
- [142] O. Ivasishin, V. Moxson, Low-cost titanium hydride powder metallurgy, *Titan. Powder Metall.* (2015) 117–148. <https://doi.org/10.1016/B978-0-12-800054-0/00008-3>.
- [143] H. Jaber, T. Kovacs, K. János, Investigating the impact of a selective laser melting process on Ti6Al4V alloy hybrid powders with spherical and irregular shapes, *Adv. Mater. Process. Technol.* 8 (2020) 715–731. <https://doi.org/10.1080/2374068X.2020.1829960>.
- [144] M. Mehrabi, J. Gardy, F.A. Talebi, A. Farshchi, A. Hassanpour, A.E. Bayly, An investigation of the effect of powder flowability on the powder spreading in additive manufacturing, *Powder Technol.* 413 (2023) 1–13. <https://doi.org/10.1016/j.powtec.2022.117997>.
- [145] J. Varela, E. Arrieta, M. Paliwal, M. Marucci, J.H. Sandoval, J.A. Gonzalez, B. McWilliams, L.E. Murr, R.B. Wicker, F. Medina, Investigation of microstructure and mechanical properties for Ti-6Al-4V alloy parts produced using non-spherical precursor powder by laser powder bed fusion, *Materials (Basel)*. 14 (2021) 1–16. <https://doi.org/10.3390/ma14113028>.
- [146] Z. Wu, M. Asherloo, R. Jiang, M.H. Delpazir, N. Sivakumar, M. Paliwal, J. Capone, B. Gould, A. Rollett, A. Mostafaei, Study of printability and porosity formation in laser powder bed fusion built hydride-dehydride (HDH) Ti-6Al-4V, *Addit. Manuf.* 47 (2021) 1–13. <https://doi.org/10.1016/j.addma.2021.102323>.
- [147] H. Gu, H. Gong, J.J.S. Dilip, D. Pal, A. Hicks, H. Doak, B. Stucker, Effects of powder variation on the microstructure and tensile strength of Ti-6Al-4V parts fabricated by selective laser melting, *Int. J. Powder Metall.* 51 (2015) 35–42.

- [148] A. Simchi, The role of particle size on the laser sintering of iron powder, *Metall. Mater. Trans. B.* 35 (2004) 937–948. <https://doi.org/10.1007/s11663-004-0088-3>.
- [149] A.Y. Alfaify, J. Hughes, K. Ridgway, Critical evaluation of the pulsed selective laser melting process when fabricating Ti64 parts using a range of particle size distributions, *Addit. Manuf.* 19 (2018) 197–204. <https://doi.org/10.1016/j.addma.2017.12.003>.
- [150] M. Sinico, A. Witvrouw, W. Dewulf, Influence of the particle size distribution on surface quality of Maraging 300 parts produced by Laser Powder Bed Fusion, *Proc. Spec. Interes. Gr. Meet. Adv. Precis. Addit. Manuf.* (2019) 31–34.
- [151] M. Sinico, G. Cogo, M. Benettoni, I. Calliari, A. Pepato, Influence of powder particle size distribution on the printability of pure copper for selective laser melting, *30th Annu. Int. Solid Free. Fabr. Symp.* (2019) 1–11.
- [152] A.B. Spierings, G. Levy, Comparison of density of stainless steel 316L parts produced with selective laser melting using different powder grades, *20th Annu. Int. Solid Free. Fabr. Symp.* (2009) 342–353.
- [153] A. Soltani-Tehrani, M. Habibnejad-Korayem, S. Shao, M. Haghshenas, N. Shamsaei, Ti-6Al-4V powder characteristics in laser powder bed fusion: The effect on tensile and fatigue behavior, *Addit. Manuf.* 51 (2022) 1–17. <https://doi.org/10.1016/j.addma.2021.102584>.
- [154] M. Simonelli, D.G. McCartney, P. Barriobero-vila, N.T. Aboulkhair, Y.Y. Tse, A. Clare, R. Hague, The Influence of Iron in Minimizing the Microstructural Anisotropy of Ti-6Al-4V Produced by Laser Powder-Bed Fusion, *Metall. Mater. Trans. A.* 51 (2020) 2444–2459. <https://doi.org/10.1007/s11661-020-05692-6>.
- [155] M.J. Bermingham, D. Kent, H. Zhan, D.H. Stjohn, M.S. Dargusch, Controlling the microstructure and properties of wire arc additive manufactured Ti-6Al-4V with trace boron additions, *Acta Mater.* 91 (2015) 289–303. <https://doi.org/10.1016/j.actamat.2015.03.035>.
- [156] P.K. Verma, S. Warghane, U. Nichul, P. Kumar, A. Dhole, V. Hiwarkar, Effect of boron addition on microstructure, hardness and wear performance of Ti-6Al-

4V alloy manufactured by laser powder bed fusion additive manufacturing, *Mater. Charact.* 172 (2021) 1–11. <https://doi.org/10.1016/j.matchar.2020.110848>.

- [157] B. Vrancken, L. Thijs, J.P. Kruth, J. Van Humbeeck, Microstructure and mechanical properties of a novel β titanium metallic composite by selective laser melting, *Acta Mater.* 68 (2014) 150–158. <https://doi.org/10.1016/j.actamat.2014.01.018>.
- [158] M. Chen, S. Van Petegem, Z. Zou, M. Simonelli, Y.Y. Tse, C.S.T. Chang, M.G. Makowska, D. Ferreira Sanchez, H. Moens-Van Swygenhoven, Microstructural engineering of a dual-phase Ti-Al-V-Fe alloy via in situ alloying during laser powder bed fusion, *Addit. Manuf.* 59 (2022) 1–10. <https://doi.org/10.1016/j.addma.2022.103173>.
- [159] A. Hattal, T. Chauveau, M. Djemai, J.J. Fouchet, B. Bacroix, G. Dirras, Effect of nano-yttria stabilized zirconia addition on the microstructure and mechanical properties of Ti6Al4V parts manufactured by selective laser melting, *Mater. Des.* 180 (2019) 1–10. <https://doi.org/10.1016/j.matdes.2019.107909>.
- [160] C. Cai, J.C.D. Qiu, T.W. Shian, C. Han, T. Liu, L.B. Kong, N. Srikanth, C.-N. Sun, K. Zhou, Laser powder bed fusion of Mo₂C/Ti-6Al-4V composites with alternately laminated α' / β phases for enhanced mechanical properties, *Addit. Manuf.* 46 (2021) 1–13. <https://doi.org/10.1016/j.addma.2021.102134>.
- [161] Y. Liu, S. Li, R.D.K. Misra, K. Geng, Y. Yang, Planting carbon nanotubes within Ti-6Al-4V to make high-quality composite powders for 3D printing high-performance Ti-6Al-4V matrix composites, *Scr. Mater.* 183 (2020) 6–11. <https://doi.org/10.1016/j.scriptamat.2020.03.009>.
- [162] S.F. Li, Y. Liu, Y.F. Yang, Q.S. Zhu, K. Kondoh, R.D.K. Misra, C. Tan, C.Q. Hu, Y. Ge, Activating Trace Fe Impurity as Catalyst to Plant Carbon Nanotubes Within Ti-6Al-4V Powders for High-Performance Ti Metal Matrix Composites, *Metall. Mater. Trans. A Phys. Metall. Mater. Sci.* 50 (2019) 3975–3979. <https://doi.org/10.1007/s11661-019-05321-x>.
- [163] C. Qiu, A. Fones, H.G.C. Hamilton, N.J.E. Adkins, M.M. Attallah, A new approach to develop palladium-modified Ti-based alloys for biomedical applications, *Mater. Des.* 109 (2016) 98–111.

<https://doi.org/10.1016/j.matdes.2016.07.055>.

- [164] P. Krakhmalev, I. Yadroitsev, I. Yadroitsava, O. de Smidt, Functionalization of Biomedical Ti6Al4V via In Situ Alloying by Cu during Laser Powder Bed Fusion Manufacturing, *Materials* (Basel). 10 (2017) 1–14. <https://doi.org/10.3390/ma10101154>.
- [165] A. Macpherson, X. Li, P. McCormick, L. Ren, K. Yang, T.B. Sercombe, Antibacterial Titanium Produced Using Selective Laser Melting, *JOM*. 69 (2017) 2719–2724. <https://doi.org/10.1007/s11837-017-2589-y>.
- [166] A.M. Vilardell, I. Yadroitsev, I. Yadroitsava, M. Albu, N. Takata, M. Kobashi, P. Krakhmalev, D. Kouprianoff, G. Kothleitner, A. du Plessis, Manufacturing and characterization of in-situ alloyed Ti6Al4V(ELI)-3 at.% Cu by laser powder bed fusion, *Addit. Manuf.* 36 (2020) 1–14. <https://doi.org/10.1016/j.addma.2020.101436>.
- [167] L. Wang, Z. Song, X. Zhang, J. Park, J. Almer, G. Zhu, Y. Chen, Q. Li, X. Zeng, Y. Li, Developing ductile and isotropic Ti alloy with tailored composition for laser powder bed fusion, *Addit. Manuf.* 52 (2022) 1–12. <https://doi.org/10.1016/j.addma.2022.102656>.
- [168] Z. Song, X. Zeng, L. Wang, Laser additive manufacturing of titanium alloys with various Al contents, *Mater. Res. Lett.* 11 (2023) 391–398. <https://doi.org/10.1080/21663831.2023.2165418>.
- [169] S.A. Etesami, B. Fotovvati, E. Asadi, Heat treatment of Ti-6Al-4V alloy manufactured by laser-based powder-bed fusion: Process, microstructures, and mechanical properties correlations, *J. Alloys Compd.* 895 (2022) 1–15. <https://doi.org/10.1016/j.jallcom.2021.162618>.
- [170] B. Vrancken, L. Thijs, J.P. Kruth, J. Van Humbeeck, Heat treatment of Ti6Al4V produced by Selective Laser Melting: Microstructure and mechanical properties, *J. Alloys Compd.* 541 (2012) 177–185. <https://doi.org/10.1016/j.jallcom.2012.07.022>.
- [171] S. Cao, Q. Hu, A. Huang, Z. Chen, M. Sun, J. Zhang, C. Fu, Q. Jia, C.V.S. Lim, R.R. Boyer, Y. Yang, X. Wu, Static coarsening behaviour of lamellar

- microstructure in selective laser melted Ti–6Al–4V, *J. Mater. Sci. Technol.* 35 (2019) 1578–1586. <https://doi.org/10.1016/j.jmst.2019.04.008>.
- [172] ASTM F1472-14, Standard Specification for Wrought Titanium-6Aluminum-4Vanadium Alloy for Surgical Implant Applications (UNS R56400), (2014).
- [173] P. Kumar, U. Ramamurty, Microstructural optimization through heat treatment for enhancing the fracture toughness and fatigue crack growth resistance of selective laser melted Ti–6Al–4V alloy, *Acta Mater.* 169 (2019) 45–59. <https://doi.org/10.1016/j.actamat.2019.03.003>.
- [174] J. Haubrich, J. Gussone, P. Barriobero-Vila, P. Kürnsteiner, E.A. Jäggle, D. Raabe, N. Schell, G. Requena, The role of lattice defects, element partitioning and intrinsic heat effects on the microstructure in selective laser melted Ti-6Al-4V, *Acta Mater.* 167 (2019) 136–148. <https://doi.org/10.1016/j.actamat.2019.01.039>.
- [175] M.T. Tsai, Y.W. Chen, C.Y. Chao, J.S.C. Jang, C.C. Tsai, Y.L. Su, C.N. Kuo, Heat-treatment effects on mechanical properties and microstructure evolution of Ti-6Al-4V alloy fabricated by laser powder bed fusion, *J. Alloys Compd.* 816 (2020) 1–6. <https://doi.org/10.1016/j.jallcom.2019.152615>.
- [176] M. Kusano, S. Miyazaki, M. Watanabe, S. Kishimoto, D.S. Bulgarevich, Y. Ono, A. Yumoto, Tensile properties prediction by multiple linear regression analysis for selective laser melted and post heat-treated Ti-6Al-4V with microstructural quantification, *Mater. Sci. Eng. A.* 787 (2020) 1–10. <https://doi.org/10.1016/j.msea.2020.139549>.
- [177] G.M. Ter Haar, T.H. Becker, Selective laser melting produced Ti-6Al-4V: Post-process heat treatments to achieve superior tensile properties, *Materials (Basel)*. 11 (2018) 1–15. <https://doi.org/10.3390/ma11010146>.
- [178] S. Miyazaki, M. Kusano, D.S. Bulgarevich, S. Kishimoto, A. Yumoto, M. Watanabe, Image Segmentation and Analysis for Microstructure and Property Evaluations on Ti-6Al-4V Fabricated by Selective Laser Melting, *Mater. Trans.* 60 (2019) 561–568. <https://doi.org/10.2320/matertrans.MBW201806>.
- [179] C. Su, H. Yu, Z. Wang, J. Yang, X. Zeng, Controlling the tensile and fatigue properties of selective laser melted Ti–6Al–4V alloy by post treatment, *J. Alloys*

- Compd. 857 (2021) 1–12. <https://doi.org/10.1016/j.jallcom.2020.157552>.
- [180] N. Stefansson, S.L. Semiatin, Mechanisms of globularization of Ti-6Al-4V during static heat treatment, *Metall. Mater. Trans. A.* 34 A (2003) 691–698. <https://doi.org/10.1007/s11661-003-0103-3>.
- [181] J. Bustillos, J. Kim, A. Moridi, Exploiting lack of fusion defects for microstructural engineering in additive manufacturing, *Addit. Manuf.* 48 (2021) 1–9. <https://doi.org/10.1016/j.addma.2021.102399>.
- [182] D. Herzog, K. Bartsch, B. Bossen, Productivity optimization of laser powder bed fusion by hot isostatic pressing, *Addit. Manuf.* 36 (2020) 1–9. <https://doi.org/10.1016/j.addma.2020.101494>.
- [183] A. du Plessis, E. Macdonald, Hot isostatic pressing in metal additive manufacturing: X-ray tomography reveals details of pore closure, *Addit. Manuf.* 34 (2020) 1–12. <https://doi.org/10.1016/j.addma.2020.101191>.
- [184] C. Qiu, N.J.E. Adkins, M.M. Attallah, Microstructure and tensile properties of selectively laser-melted and of HIPed laser-melted Ti-6Al-4V, *Mater. Sci. Eng. A.* 578 (2013) 230–239. <https://doi.org/10.1016/j.msea.2013.04.099>.
- [185] M. Zhang, C.H. Ng, A. Dehghan-Manshadi, C. Hall, M.J. Bermingham, M.S. Dargusch, Towards isotropic behaviour in Ti-6Al-4V fabricated with laser powder bed fusion and super transus hot isostatic pressing, *Mater. Sci. Eng. A.* 874 (2023) 1–7. <https://doi.org/10.1016/j.msea.2023.145094>.
- [186] M. Tarik Hasib, H.E. Ostergaard, X. Li, J.J. Kruzic, Fatigue crack growth behavior of laser powder bed fusion additive manufactured Ti-6Al-4V: Roles of post heat treatment and build orientation, *Int. J. Fatigue.* 142 (2021) 1–13. <https://doi.org/10.1016/j.ijfatigue.2020.105955>.
- [187] S. Cao, Z. Chen, C.V.S. Lim, K. Yang, Q. Jia, T. Jarvis, D. Tomus, X. Wu, Defect, Microstructure, and Mechanical Property of Ti-6Al-4V Alloy Fabricated by High-Power Selective Laser Melting, *JOM.* 69 (2017) 2684–2692. <https://doi.org/10.1007/s11837-017-2581-6>.
- [188] G. Kasperovich, J. Hausmann, Improvement of fatigue resistance and ductility of TiAl6V4 processed by selective laser melting, *J. Mater. Process. Technol.* 220

- (2015) 202–214. <https://doi.org/10.1016/j.jmatprotec.2015.01.025>.
- [189] H. Masuo, Y. Tanaka, S. Morokoshi, H. Yagura, T. Uchida, Y. Yamamoto, Y. Murakami, Influence of defects, surface roughness and HIP on the fatigue strength of Ti-6Al-4V manufactured by additive manufacturing, *Int. J. Fatigue*. 117 (2018) 163–179. <https://doi.org/10.1016/j.ijfatigue.2018.07.020>.
- [190] B. Naab, M. Celikin, The role of microstructural evolution on the fatigue behavior of additively manufactured Ti–6Al–4V alloy, *Mater. Sci. Eng. A*. 859 (2022) 1–11. <https://doi.org/10.1016/j.msea.2022.144232>.
- [191] A. du Plessis, S.M.J. Razavi, D. Wan, F. Berto, A. Imdaadulah, C. Beamer, J. Shipley, E. MacDonald, Fatigue performance of shelled additively manufactured parts subjected to hot isostatic pressing, *Addit. Manuf.* 51 (2022) 1–8. <https://doi.org/10.1016/j.addma.2022.102607>.
- [192] Z. Zou, M. Simonelli, J. Katrib, G. Dimitrakis, R. Hague, Refinement of the grain structure of additive manufactured titanium alloys via epitaxial recrystallization enabled by rapid heat treatment, *Scr. Mater.* 180 (2020) 66–70. <https://doi.org/10.1016/j.scriptamat.2020.01.027>.
- [193] Z. Zou, M. Simonelli, J. Katrib, G. Dimitrakis, R. Hague, Microstructure and tensile properties of additive manufactured Ti-6Al-4V with refined prior- β grain structure obtained by rapid heat treatment, *Mater. Sci. Eng. A*. 814 (2021) 1–11. <https://doi.org/10.1016/j.msea.2021.141271>.
- [194] R. Sabban, S. Bahl, K. Chatterjee, S. Suwas, Globularization using heat treatment in additively manufactured Ti-6Al-4V for high strength and toughness, *Acta Mater.* 162 (2019) 239–254. <https://doi.org/10.1016/j.actamat.2018.09.064>.
- [195] C.L. Li, J.K. Hong, P.L. Narayana, S.W. Choi, S.W. Lee, C.H. Park, J.T. Yeom, Q. Mei, Realizing superior ductility of selective laser melted Ti-6Al-4V through a multi-step heat treatment, *Mater. Sci. Eng. A*. 799 (2021) 1–8. <https://doi.org/10.1016/j.msea.2020.140367>.
- [196] R.X. Zhao, J. Wang, T.W. Cao, T. Hu, S.S. Shuai, S.Z. Xu, M. Qian, C.Y. Chen, Z.M. Ren, Additively manufactured Ti–6Al–4V alloy by high magnetic field heat treatment, *Mater. Sci. Eng. A*. 871 (2023) 1–16.

<https://doi.org/10.1016/j.msea.2023.144926>.

- [197] P.P. Dhekne, T. Vermeij, V. Devulapalli, S.D. Jadhav, J.P.M. Hoefnagels, M.G.D. Geers, K. Vanmeensel, Micro-mechanical deformation behavior of heat-treated laser powder bed fusion processed Ti-6Al-4V, *Scr. Mater.* 233 (2023) 1–7. <https://doi.org/10.1016/j.scriptamat.2023.115505>.
- [198] S. Wei, G. Zhu, C.C. Tasan, Slip-twinning interdependent activation across phase boundaries: An in-situ investigation of a Ti-Al-V-Fe ($\alpha+\beta$) alloy, *Acta Mater.* 206 (2021) 1–14. <https://doi.org/10.1016/j.actamat.2020.116520>.
- [199] L. Lei, Y. Zhao, Q. Zhao, C. Wu, S. Huang, W. Jia, W. Zeng, Impact toughness and deformation modes of Ti-6Al-4V alloy with different microstructures, *Mater. Sci. Eng. A.* 801 (2021) 1–12. <https://doi.org/10.1016/j.msea.2020.140411>.
- [200] J.W. Won, S. Lee, W.C. Kim, Y.T. Hyun, D.W. Lee, Significantly increased twinning activity of pure titanium during room-temperature tensile deformation by cryogenic-deformation treatment, *Mater. Sci. Eng. A.* 862 (2023) 1–5. <https://doi.org/10.1016/j.msea.2022.144453>.
- [201] S. Xu, L.S. Toth, C. Schuman, J.S. Lecomte, M.R. Barnett, Dislocation mediated variant selection for secondary twinning in compression of pure titanium, *Acta Mater.* 124 (2017) 59–70. <https://doi.org/10.1016/j.actamat.2016.10.063>.
- [202] D.G.L. Prakash, R. Ding, R.J. Moat, I. Jones, P.J. Withers, J.Q. da Fonseca, M. Preuss, Deformation twinning in Ti-6Al-4V during low strain rate deformation to moderate strains at room temperature, *Mater. Sci. Eng. A.* 527 (2010) 5734–5744. <https://doi.org/10.1016/j.msea.2010.05.039>.
- [203] Z.W. Huang, S.B. Jin, H. Zhou, Y.S. Li, Y. Cao, Y.T. Zhu, Evolution of twinning systems and variants during sequential twinning in cryo-rolled titanium, *Int. J. Plast.* 112 (2019) 52–67. <https://doi.org/10.1016/j.ijplas.2018.08.008>.
- [204] F. Cheng, H. Wang, Z. Li, X. Cheng, D. Zheng, S. Zhang, X. Hu, H. Zhang, M. Liu, Dynamic compression deformation behavior of laser directed energy deposited $\alpha + \beta$ duplex titanium alloy with basket-weave morphology, *Addit. Manuf.* 61 (2023) 1–10. <https://doi.org/10.1016/j.addma.2022.103336>.
- [205] P. Wang, X. Tan, M.L.S. Nai, J. Wu, J. Wei, Deformation induced nanoscale

- twinning improves strength and ductility in additively manufactured titanium alloys, *Mater. Sci. Eng. A.* 833 (2022) 1–8. <https://doi.org/10.1016/j.msea.2021.142568>.
- [206] K. Chen, H. Li, D.J. Huang, X. Shen, N. Jia, Avoiding oxygen-induced early fracture in titanium with high strength via entangled grains through laser powder bed fusion, *Scr. Mater.* 222 (2023) 1–9. <https://doi.org/10.1016/j.scriptamat.2022.115051>.
- [207] ISO 13322-1, Particle size analysis by Image analysis methods, Part 1: Static image analysis methods, (2014).
- [208] A. Mazzoli, O. Favoni, Particle size, size distribution and morphological evaluation of airborne dust particles of diverse woods by Scanning Electron Microscopy and image processing program, *Powder Technol.* 225 (2012) 65–71. <https://doi.org/10.1016/j.powtec.2012.03.033>.
- [209] ASTM B213-20, Standard Test Methods for Flow Rate of Metal Powders Using the Hall Flowmeter Funnel, (2020).
- [210] P. Li, N.T. Aboulkhair, J. Wu, K.L. Leng, D. Yang, A.T. Clare, X. Hou, F. Xu, Tailoring the in-situ formation of intermetallic phases in the self-lubricating Al–WS₂ composite for enhanced tribological performance with wear track evolution analysis, *J. Mater. Res. Technol.* 27 (2023) 4891–4907. <https://doi.org/10.1016/j.jmrt.2023.10.157>.
- [211] L. Parry, Investigation of residual stresses in selective laser melting, PhD Thesis. (2015).
- [212] J.P. Kruth, J. Deckers, E. Yasa, R. Wauthlé, Assessing and comparing influencing factors of residual stresses in selective laser melting using a novel analysis method, *Proc. Inst. Mech. Eng. Part B J. Eng. Manuf.* 226 (2012) 980–991. <https://doi.org/10.1177/0954405412437085>.
- [213] R.R.J. Sélo, S. Catchpole-Smith, I. Maskery, I. Ashcroft, C. Tuck, On the thermal conductivity of AlSi10Mg and lattice structures made by laser powder bed fusion, *Addit. Manuf.* 34 (2020) 1–8. <https://doi.org/10.1016/j.addma.2020.101214>.
- [214] V. Lindström, O. Liashenko, K. Zweiacker, S. Derevianko, V. Morozovych, Y.

- Lyashenko, C. Leinenbach, Laser powder bed fusion of metal coated copper powders, *Materials* (Basel). 13 (2020) 1–12. <https://doi.org/10.3390/MA13163493>.
- [215] L. Newton, N. Senin, C. Gomez, R. Danzl, F. Helml, L. Blunt, R. Leach, Areal topography measurement of metal additive surfaces using focus variation microscopy, *Addit. Manuf.* 25 (2019) 365–389. <https://doi.org/10.1016/j.addma.2018.11.013>.
- [216] L.H. Qian, S.C. Wang, Y.H. Zhao, K. Lu, Microstrain effect on thermal properties of nanocrystalline Cu, *Acta Mater.* 50 (2002) 3425–3434. [https://doi.org/10.1016/S1359-6454\(02\)00155-6](https://doi.org/10.1016/S1359-6454(02)00155-6).
- [217] ASTM E8 E8M-16a, Standard Test Methods for Tension Testing of Metallic Materials, (2016).
- [218] K. Darvish, Z.W. Chen, T. Pasang, Reducing lack of fusion during selective laser melting of CoCrMo alloy: Effect of laser power on geometrical features of tracks, *Mater. Des.* 112 (2016) 357–366. <https://doi.org/10.1016/j.matdes.2016.09.086>.
- [219] R. Esmailizadeh, U. Ali, A. Keshavarzkermani, Y. Mahmoodkhani, E. Marzbanrad, E. Toyserkani, On the effect of spatter particles distribution on the quality of Hastelloy X parts made by laser powder-bed fusion additive manufacturing, *J. Manuf. Process.* 37 (2019) 11–20. <https://doi.org/10.1016/j.jmapro.2018.11.012>.
- [220] S.A. Khairallah, A.A. Martin, J.R.I. Lee, G. Guss, N.P. Calta, J.A. Hammons, M.H. Nielsen, K. Chaput, E. Schwalbach, M.N. Shah, M.G. Chapman, T.M. Willey, A.M. Rubenchik, A.T. Anderson, Y. Morris Wang, M.J. Matthews, W.E. King, Controlling interdependent meso-nanosecond dynamics and defect generation in metal 3D printing, *Science.* 368 (2020) 660–665. <https://doi.org/10.1126/science.aay7830>.
- [221] A.R. Nassar, M.A. Gundermann, E.W. Reutzel, P. Guerrier, M.H. Krane, M.J. Weldon, Formation processes for large ejecta and interactions with melt pool formation in powder bed fusion additive manufacturing, *Sci. Rep.* 9 (2019) 1–11. <https://doi.org/10.1038/s41598-019-41415-7>.

- [222] G. Zhang, J. Chen, M. Zheng, Z. Yan, X. Lu, X. Lin, W. Huang, Elemental Vaporization of Ti-6Al-4V during Selective Laser Melting, *Metals* (Basel). 10 (2020) 1–14. <https://doi.org/10.3390/met10040435>.
- [223] T. Mukherjee, J.S. Zuback, A. De, T. DebRoy, Printability of alloys for additive manufacturing, *Sci. Rep.* 6 (2016) 1–8. <https://doi.org/10.1038/srep19717>.
- [224] M. Taheri, R. Dehghani, M.R. Karamooz-ravari, A study on the effect of energy input on spatter particles creation during selective laser melting process, *Addit. Manuf.* 20 (2018) 33–43. <https://doi.org/10.1016/j.addma.2017.12.009>.
- [225] A. Ladewig, G. Schlick, M. Fisser, V. Schulze, U. Glatzel, Influence of the shielding gas flow on the removal of process by-products in the selective laser melting process, *Addit. Manuf.* 10 (2016) 1–9. <https://doi.org/10.1016/j.addma.2016.01.004>.
- [226] X. Zhang, B. Cheng, C. Tuffile, Simulation study of the spatter removal process and optimization design of gas flow system in laser powder bed fusion, *Addit. Manuf.* 32 (2020) 1–17. <https://doi.org/10.1016/j.addma.2020.101049>.
- [227] A.B. Spierings, N. Herres, G. Levy, Influence of the particle size distribution on surface quality and mechanical properties in AM steel parts, *Rapid Prototyp. J.* 17 (2011) 195–202. <https://doi.org/10.1108/13552541111124770>.
- [228] U. Ali, R. Esmailizadeh, F. Ahmed, D. Sarker, W. Muhammad, A. Keshavarzkermani, Y. Mahmoodkhani, E. Marzbanrad, E. Toyserkani, Identification and characterization of spatter particles and their effect on surface roughness, density and mechanical response of 17-4 PH stainless steel laser powder-bed fusion parts, *Mater. Sci. Eng. A.* 756 (2019) 98–107. <https://doi.org/10.1016/j.msea.2019.04.026>.
- [229] X. Chen, C. Qiu, In-situ development of a sandwich microstructure with enhanced ductility by laser reheating of a laser melted titanium alloy, *Sci. Rep.* 10 (2020) 1–12. <https://doi.org/10.1038/s41598-020-72627-x>.
- [230] M. Sangali, J.F.Q. Rodrigues, K.N. Campo, L.F. Starck, A. Cremasco, R.J. Contieri, R. Caram, Fine-layered CP-Ti /Ti–6Al–4V composites by laser powder bed fusion, *Vacuum.* 220 (2024) 1–6.

<https://doi.org/10.1016/j.vacuum.2023.112831>.

- [231] M.H. Mosallanejad, B. Niroumand, A. Aversa, A. Saboori, In-situ alloying in laser-based additive manufacturing processes: A critical review, *J. Alloys Compd.* 872 (2021) 1–19. <https://doi.org/10.1016/j.jallcom.2021.159567>.
- [232] D. Gu, Y.C. Hagedorn, W. Meiners, G. Meng, R.J.S. Batista, K. Wissenbach, R. Poprawe, Densification behavior, microstructure evolution, and wear performance of selective laser melting processed commercially pure titanium, *Acta Mater.* 60 (2012) 3849–3860. <https://doi.org/10.1016/j.actamat.2012.04.006>.
- [233] S.L. Lu, C.J. Todaro, Y.Y. Sun, T. Song, M. Brandt, M. Qian, Variant selection in additively manufactured alpha-beta titanium alloys, *J. Mater. Sci. Technol.* 113 (2022) 14–21. <https://doi.org/10.1016/j.jmst.2021.10.021>.
- [234] Y. Yang, Y.J. Liu, J. Chen, H.L. Wang, Z.Q. Zhang, Y.J. Lu, S.Q. Wu, J.X. Lin, Crystallographic features of α variants and β phase for Ti-6Al-4V alloy fabricated by selective laser melting, *Mater. Sci. Eng. A.* 707 (2017) 548–558. <https://doi.org/10.1016/j.msea.2017.09.068>.
- [235] T. Zhang, J. Zhu, T. Yang, J. Luan, H. Kong, W. Liu, B. Cao, S. Wu, D. Wang, Y. Wang, C.T. Liu, A new $\alpha + \beta$ Ti-alloy with refined microstructures and enhanced mechanical properties in the as-cast state, *Scr. Mater.* 207 (2022) 1–5. <https://doi.org/10.1016/j.scriptamat.2021.114260>.
- [236] J. Ju, J. Li, C. Yang, K. Wang, M. Kang, J. Wang, Evolution of the microstructure and optimization of the tensile properties of the Ti-6Al-4V alloy by selective laser melting and heat treatment, *Mater. Sci. Eng. A.* 802 (2021) 1–9. <https://doi.org/10.1016/j.msea.2020.140673>.
- [237] J. Liu, Q. Sun, C. Zhou, X. Wang, H. Li, K. Guo, J. Sun, Achieving Ti6Al4V alloys with both high strength and ductility via selective laser melting, *Mater. Sci. Eng. A.* 766 (2019) 1–8. <https://doi.org/10.1016/j.msea.2019.138319>.
- [238] <https://www.slm-solutions.com> [Accessed on 8 June 2023].
- [239] L. Liu, C. Chen, R. Zhao, X. Wang, H. Tao, S. Shuai, J. Wang, H. Liao, Z. Ren, In-situ nitrogen strengthening of selective laser melted Ti6Al4V with superior

- mechanical performance, *Addit. Manuf.* 46 (2021) 1–12. <https://doi.org/10.1016/j.addma.2021.102142>.
- [240] A. Gullane, J.W. Murray, C.J. Hyde, S. Sankare, A. Evirgen, A.T. Clare, On the use of multiple layer thicknesses within laser powder bed fusion and the effect on mechanical properties, *Mater. Des.* 212 (2021) 1–14. <https://doi.org/10.1016/j.matdes.2021.110256>.
- [241] Y. Xu, D. Zhang, Y. Guo, S. Hu, X. Wu, Y. Jiang, Microstructural tailoring of As-Selective Laser Melted Ti6Al4V alloy for high mechanical properties, *J. Alloys Compd.* 816 (2020) 1–13. <https://doi.org/10.1016/j.jallcom.2019.152536>.
- [242] M. Simonelli, N.T. Aboulkhair, P. Cohen, J.W. Murray, A.T. Clare, C. Tuck, R.J.M. Hague, A comparison of Ti-6Al-4V in-situ alloying in Selective Laser Melting using simply-mixed and satellited powder blend feedstocks, *Mater. Charact.* 143 (2018) 118–126. <https://doi.org/10.1016/j.matchar.2018.05.039>.
- [243] E.G. Brodie, A.E. Medvedev, J.E. Frith, M.S. Dargusch, H.L. Fraser, A. Molotnikov, Remelt processing and microstructure of selective laser melted Ti25Ta, *J. Alloys Compd.* 820 (2020) 1–15. <https://doi.org/10.1016/j.jallcom.2019.153082>.
- [244] A. Kumar, M. Sapp, J. Vincelli, M.C. Gupta, A study on laser cleaning and pulsed gas tungsten arc welding of Ti-3Al-2.5V alloy tubes, *J. Mater. Process. Technol.* 210 (2010) 64–71. <https://doi.org/10.1016/j.jmatprotec.2009.08.017>.
- [245] H.J. Yi, Y.J. Lee, K.O. Lee, Influences of the welding heat input and the repeated repair welding on Ti-3Al-2.5V titanium alloy, *Acta Metall. Sin. English Lett.* 28 (2015) 684–691. <https://doi.org/10.1007/s40195-015-0248-2>.
- [246] J. Zhang, Y. Liu, M. Bayat, Q. Tan, Y. Yin, Z. Fan, S. Liu, J.H. Hattel, M. Dargusch, M.X. Zhang, Achieving high ductility in a selectively laser melted commercial pure-titanium via in-situ grain refinement, *Scr. Mater.* 191 (2021) 155–160. <https://doi.org/10.1016/j.scriptamat.2020.09.023>.
- [247] H. Attar, M. Calin, L.C. Zhang, S. Scudino, J. Eckert, Manufacture by selective laser melting and mechanical behavior of commercially pure titanium, *Mater. Sci. Eng. A.* 593 (2014) 170–177. <https://doi.org/10.1016/j.msea.2013.11.038>.

- [248] C. Qiu, Q. Liu, R. Ding, Significant enhancement in yield strength for a metastable beta titanium alloy by selective laser melting, *Mater. Sci. Eng. A.* 816 (2021) 1–7. <https://doi.org/10.1016/j.msea.2021.141291>.
- [249] S. Chen, Q. Yu, The role of low angle grain boundary in deformation of titanium and its size effect, *Scr. Mater.* 163 (2019) 148–151. <https://doi.org/10.1016/j.scriptamat.2018.10.054>.
- [250] G.H. Zhao, X.Z. Liang, B. Kim, P.E.J. Rivera-Díaz-del-Castillo, Modelling strengthening mechanisms in beta-type Ti alloys, *Mater. Sci. Eng. A.* 756 (2019) 156–160. <https://doi.org/10.1016/j.msea.2019.04.027>.
- [251] M.A. Galindo-fernández, K. Mumtaz, P.E.J. Rivera-díaz-del-castillo, E.I. Galindo-nava, H. Ghadbeigi, A microstructure sensitive model for deformation of Ti-6Al-4V describing Cast-and-Wrought and Additive Manufacturing morphologies, *Mater. Des.* 160 (2018) 350–362. <https://doi.org/10.1016/j.matdes.2018.09.028>.
- [252] J.Y. He, H. Wang, H.L. Huang, X.D. Xu, M.W. Chen, Y. Wu, X.J. Liu, T.G. Nieh, K. An, Z.P. Lu, A precipitation-hardened high-entropy alloy with outstanding tensile properties, *Acta Mater.* 102 (2016) 187–196. <https://doi.org/10.1016/j.actamat.2015.08.076>.
- [253] R. Duan, S. Li, B. Cai, W. Zhu, F. Ren, M.M. Attallah, A high strength and low modulus metastable β Ti-12Mo-6Zr-2Fe alloy fabricated by laser powder bed fusion in-situ alloying, *Addit. Manuf.* 37 (2021) 1–15. <https://doi.org/10.1016/j.addma.2020.101708>.
- [254] L. Bolzoni, E.M. Ruiz-Navas, E. Gordo, Investigation of the factors influencing the tensile behaviour of PM Ti-3Al-2.5V alloy, *Mater. Sci. Eng. A.* 609 (2014) 266–272. <https://doi.org/10.1016/j.msea.2014.05.017>.
- [255] J. Kwame, E. Yakushina, P. Blackwell, Influence of Sheet Conditions on In-Plane Strain Evolution via Ex-Situ Tensile Deformation of Ti-3Al-2.5V at Room Temperature, *J. Mater. Appl.* 10 (2021) 15–26. <https://doi.org/10.32732/jma.2021.10.1.15>.
- [256] X. Wu, D. Zhang, Y. Guo, T. Zhang, Z. Liu, Microstructure and mechanical

- evolution behavior of LPBF (laser powder bed fusion)-fabricated TA15 alloy, *J. Alloys Compd.* 873 (2021) 1–10. <https://doi.org/10.1016/j.jallcom.2021.159639>.
- [257] T. Vilaro, C. Colin, J.D. Bartout, As-fabricated and heat-treated microstructures of the Ti-6Al-4V alloy processed by selective laser melting, *Metall. Mater. Trans. A.* 42 (2011) 3190–3199. <https://doi.org/10.1007/s11661-011-0731-y>.
- [258] R. Williams, M. Bilton, N. Harrison, P. Fox, The impact of oxidised powder particles on the microstructure and mechanical properties of Ti-6Al-4 V processed by laser powder bed fusion, *Addit. Manuf.* 46 (2021) 1–14. <https://doi.org/10.1016/j.addma.2021.102181>.
- [259] C. Pauzon, K. Dietrich, P. Forêt, S. Dubiez-Le Goff, E. Hryha, G. Witt, Control of residual oxygen of the process atmosphere during laser-powder bed fusion processing of Ti-6Al-4V, *Addit. Manuf.* 38 (2021) 1–10. <https://doi.org/10.1016/j.addma.2020.101765>.
- [260] K. Dietrich, J. Diller, S. Dubiez-Le Goff, D. Bauer, P. Forêt, G. Witt, The influence of oxygen on the chemical composition and mechanical properties of Ti-6Al-4V during laser powder bed fusion (L-PBF), *Addit. Manuf.* 32 (2020) 1–12. <https://doi.org/10.1016/j.addma.2019.100980>.
- [261] S. Zaefferer, A study of active deformation systems in titanium alloys: Dependence on alloy composition and correlation with deformation texture, *Mater. Sci. Eng. A.* 344 (2003) 20–30. [https://doi.org/10.1016/S0921-5093\(02\)00421-5](https://doi.org/10.1016/S0921-5093(02)00421-5).
- [262] S. Huang, Q. Zhao, C. Lin, C. Wu, Y. Zhao, W. Jia, C. Mao, In-situ investigation of tensile behaviors of Ti-6Al alloy with extra low interstitial, *Mater. Sci. Eng. A.* 809 (2021) 1–12. <https://doi.org/10.1016/j.msea.2021.140958>.
- [263] D. Guan, B. Wynne, J. Gao, Y. Huang, W.M. Rainforth, Basal slip mediated tension twin variant selection in magnesium WE43 alloy, *Acta Mater.* 170 (2019) 1–14. <https://doi.org/10.1016/j.actamat.2019.03.018>.
- [264] S. Cao, R. Chu, X. Zhou, K. Yang, Q. Jia, C.V.S. Lim, A. Huang, X. Wu, Role of martensite decomposition in tensile properties of selective laser melted Ti-6Al-4V, *J. Alloys Compd.* 744 (2018) 357–363.

<https://doi.org/10.1016/j.jallcom.2018.02.111>.

- [265] E. Sallica-Leva, R. Caram, A.L. Jardini, J.B. Fogagnolo, Ductility improvement due to martensite α' decomposition in porous Ti-6Al-4V parts produced by selective laser melting for orthopedic implants, *J. Mech. Behav. Biomed. Mater.* 54 (2016) 149–158. <https://doi.org/10.1016/j.jmbbm.2015.09.020>.
- [266] E. Wielewski, C.R. Siviour, N. Petrinic, On the correlation between macrozones and twinning in Ti-6Al-4V at very high strain rates, *Scr. Mater.* 67 (2012) 229–232. <https://doi.org/10.1016/j.scriptamat.2012.04.026>.
- [267] H. Qin, J.J. Jonas, H. Yu, N. Brodusch, R. Gauvin, X. Zhang, Initiation and accommodation of primary twins in high-purity titanium, *Acta Mater.* 71 (2014) 293–305. <https://doi.org/10.1016/j.actamat.2014.03.025>.
- [268] Z. Huang, D. Wen, X. Hou, Y. Li, B. Wang, A. Wang, Grain size and temperature mediated twinning ability and strength-ductility correlation in pure titanium, *Mater. Sci. Eng. A.* 849 (2022) 1–8. <https://doi.org/10.1016/j.msea.2022.143461>.
- [269] B. Wang, H. Liu, Y. Zhang, B. Zhou, L. Deng, C. Wang, J. Chen, Y. Zhang, Effect of grain size on twinning behavior of pure titanium at room temperature, *Mater. Sci. Eng. A.* 827 (2021) 1–13. <https://doi.org/10.1016/j.msea.2021.142060>.
- [270] B. Zhou, R. Yang, B. Wang, L. Deng, Y. Zhang, Twinning behavior of pure titanium during rolling at room and cryogenic temperatures, *Mater. Sci. Eng. A.* 803 (2021) 1–11. <https://doi.org/10.1016/j.msea.2020.140458>.
- [271] X. Li, J. Li, B. Zhou, M. Yu, M. Sui, Interaction of $\{11\bar{2}2\}$ twin variants in hexagonal close-packed titanium, *J. Mater. Sci. Technol.* 35 (2019) 660–666. <https://doi.org/10.1016/j.jmst.2018.09.049>.
- [272] X.D. Ren, W.F. Zhou, F.F. Liu, Y.P. Ren, S.Q. Yuan, N.F. Ren, S.D. Xu, T. Yang, Microstructure evolution and grain refinement of Ti-6Al-4V alloy by laser shock processing, *Appl. Surf. Sci.* 363 (2016) 44–49. <https://doi.org/10.1016/j.apsusc.2015.11.192>.
- [273] D. Zhang, L. Jiang, B. Zheng, J.M. Schoenung, S. Mahajan, E.J. Lavernia, I.J. Beyerlein, J.M. Schoenung, E.J. Lavernia, Deformation Twinning (Update), Ref.

Modul. Mater. Sci. Mater. Eng. (2016) 1–24. <https://doi.org/10.1016/b978-0-12-803581-8.02878-2>.

- [274] A. Zafari, M.R. Barati, K. Xia, Controlling martensitic decomposition during selective laser melting to achieve best ductility in high strength Ti-6Al-4V, *Mater. Sci. Eng. A.* 744 (2019) 445–455. <https://doi.org/10.1016/j.msea.2018.12.047>.
- [275] A. Fitzner, D.G.L. Prakash, J.Q. Da Fonseca, M. Thomas, S.Y. Zhang, J. Kelleher, P. Manuel, M. Preuss, The effect of aluminium on twinning in binary alpha-titanium, *Acta Mater.* 103 (2016) 341–351. <https://doi.org/10.1016/j.actamat.2015.09.048>.
- [276] V.M. Kaoushik, U. Nichul, V. Chavan, V. Hiwarkar, Development of microstructure and high hardness of Ti6Al4V alloy fabricated using laser beam powder bed fusion: A novel sub-transus heat treatment approach, *J. Alloys Compd.* 937 (2023) 1–12. <https://doi.org/10.1016/j.jallcom.2022.168387>.
- [277] F. An, B. Zhang, Y. Yan, L. Wang, Effect of vanadium contents on microstructure and mechanical properties of Ti-6Al-xV components produced by wire + arc additive manufacturing, *Mater. Trans.* 62 (2021) 1071–1078. <https://doi.org/10.2320/matertrans.MT-M2021031>.